



**A study of the Synthesis of Natisite and its Zirconium  
Doped Analogues as Solid Ion-Exchangers for the  
Remediation of Nuclear Waste.**

**by**

**Reece M. Hall**

A thesis submitted in partial fulfilment for the requirements for the degree of  
Doctor of Philosophy at the University of Central Lancashire

School of Physical Sciences and Computing

June 2017

# STUDENT DECLARATION FORM



Type of Award:                      Doctor of Philosophy  
School:                                  Physical Sciences and Computing

**1. Concurrent registration for two or more academic awards**

I declare that while registered as a candidate for the research degree, I have not been a registered candidate or enrolled student for another award of the University or other academic or professional institution

**2. Material submitted for another award**

I declare that no material contained in the thesis has been used in any other submission for an academic award and is solely my own work

**3. Collaboration**

Where a candidate's research programme is part of a collaborative project, the thesis must indicate in addition clearly the candidate's individual contribution and the extent of the collaboration. Please state below:

**4. Use of a Proof-reader**

No proof-reading service was used in the compilation of this thesis.

Signature of Candidate: *Reece M. Hall*

Print name: Reece M. Hall

# *ABSTRACT*

Unlike zeolites which contain  $\text{SiO}_4$  and  $\text{AlO}_4$  tetrahedra, microporous titanium silicates display  $\text{SiO}_4$  in tetrahedral coordination and  $\text{TiO}_6$  octahedra and therefore display a wider range of possible structures which can result in different properties. Doping different transition metals into existing titanium silicate structures can lead to significant changes in the structure which lead to differences in the materials ion-exchange chemistry. Sitenakite,  $\text{KNa}_2\text{Ti}_4\text{Si}_2\text{O}_{13}(\text{OH})\cdot 4\text{H}_2\text{O}$ , and the synthetic niobium doped analogue (IONSIV-911) is one example of a doped titanium silicate which is used as an ion-exchanger for the removal of  $\text{Cs}^+$  and  $\text{Sr}^{2+}$  from nuclear waste.

Natisite,  $\text{Na}_2\text{TiSiO}_5$ , crystallises in the tetragonal space group  $P4/n\ m\ m$  and is a layered titanium silicate with titanium in an unusual 5 coordinate square pyramidal environment. Little previous work has been conducted on this material, with any published work focusing on synthesis and characterisation of the structure. No work to date has been conducted on the modification of the framework or any tests on natisites ion-exchange chemistry. Preliminary results have found that increasing the levels of zirconium doping has significant effects on the materials ion-exchange chemistry. Such differences include a faster rate of exchange for Co, increased affinity for Sr and Cs and, a slight increase in the level of exchange with respect to Ce and Nd (used as inactive surrogates for Pu and U respectively).

Ti Edge XAS data has been investigated and shown significant changes in the XANES region upon ion-exchange. The presence of Zr within the natisite framework has a significant

effect on the materials ion-exchange chemistry but the changes in the Ti XAS data suggests that the exchanged cations prefer sites closer to titanium rather than zirconium.

Cerium ion-exchanges shows the formation of CeO<sub>2</sub> nanoparticles between the layers. X-Ray diffraction shows that the layers themselves are still intact but the stacking has been disrupted by the introduction of these CeO<sub>2</sub> nanoparticles with X-Ray Absorption Spectroscopy (XAS) used to identify the Ce phase.

The work presented here will focus on the differences between 0, 10% and 20% Zr doped natisite and the effect this has on the materials ion-exchange chemistry both with single and competitive ion-exchanges. These results will be compared to clinoptilolite which is used as the industrial standard material for treatment of radioactive liquid waste via the SIXEP process. Clinoptilolite sourced from Sellafield has undergone ion-exchanges under controlled conditions with the capacity directly compared to that of natisite, 10% Zr natisite and 20% Zr natisite.

Results have shown that natisite has superior performance towards Ce, Nd, Co, both in the single exchanges and in the presence of competing ions such as Ca, Mg and K. Also the zirconium doped analogues of natisite has a comparable exchange capacity towards Cs and Sr to that of clinoptilolite.

# *Acknowledgements*

First and foremost, I would like to thank my supervisor Dr Jenny Readman for her unrelenting help and support not just throughout my PhD, but my entire time under her supervision. There is no doubt in my mind that I would not be where I am today if it were not for the invaluable knowledge, advice and countless coffee breaks you provided. I am extremely appreciative for everything you have done for me and it is something of which I won't soon forget. Thank you!

My gratitude goes to the Nuclear Decommissioning Authority for the funding of this project and Dr Thomas Carey (National Nuclear Laboratories) for the supervision, help and insight into the nuclear industry. Also, my thanks go to the ICDD for awarding me the Ludo Frevel crystallography scholarship.

Next I would like to thank my family and friends for their reassurance and help during the production of this work. Thank you to all the technical staff that have helped over the years, in particular, Jim, Tamar, Beth and finally Sal, who has always been there to provide help and advice, even from the first year of my undergraduate degree.

Finally, my heartfelt appreciation goes to Damian Bennison. Thank you for putting up with me during the past three years. Your support and encouragement cannot be understated. Thank you for everything babs!

# *CONTENTS*

<b>Chapter One: Introduction</b> .....	1
1.1: Background.....	1
1.2: Zeolites .....	8
1.2.1: Löwenstein’s Rule.....	11
1.2.2: Zeolites as drying agents .....	11
1.2.3: Molecular sieves.....	12
1.2.4: Catalysis.....	13
1.3: Zeotypes .....	15
1.3.1: Titanium silicates.....	16
1.3.2: Sitalakite.....	17
1.3.3: ETS-4.....	18
1.3.4: ETS-10.....	19
1.3.5: TS-1.....	20
1.3.6: Natisite .....	20
1.4: Ion-exchangers .....	21
1.5: SIXEP process.....	24
1.6: Aim of Work.....	25
<b>Chapter Two: Experimental Techniques</b> .....	27
2.1: Synthesis.....	27
2.1.1: Hydrothermal synthesis .....	27
2.1.2: Microwave synthesis .....	28
2.2: Crystallography and diffraction.....	29
2.2.1: Introduction to crystallography.....	29
2.2.2: Powder X-ray diffraction (XRD) .....	31
2.2.3: Generation of X-rays.....	34
2.2.4: Rietveld Refinement.....	36

2.2.5: Laboratory instrumentation .....	36
2.3: Synchrotron radiation .....	37
2.3.1: X-ray absorption spectroscopy (XAS) .....	39
2.3.2: Analysis of a XAS spectrum (Muffin tin potential) .....	45
2.4: X-ray fluorescence (XRF).....	46
2.4.1: Laboratory instrumentation .....	48
2.5: Scanning electron microscopy (SEM) & Energy dispersive X-ray analysis (EDX) ....	49
2.5.1: Energy dispersive X-ray analysis (EDX).....	50
2.5.2: Laboratory instrumentation .....	52
2.6: Inductively coupled plasma mass spectrometry (ICP-MS) .....	52
2.6.1: Laboratory instrumentation .....	53
<b>Chapter Three: Synthesis and characterisation of Natisite.....</b>	<b>55</b>
3.1: Introduction.....	55
3.2: Sample preparation .....	57
3.3: Characterisation .....	57
3.3.1: Indexing and unit cell refinement .....	57
3.3.2: SEM EDX .....	62
3.3.3: Microwave synthesis .....	64
3.4: Ion-exchange .....	66
3.4.1: Sample preparation .....	66
3.4.2: Analysis.....	67
3.4.2.1: XRD .....	67
3.4.2.2: XRF .....	71
3.4.2.3: SEM.....	73
3.4.2.4: ICP-MS .....	74
3.5: Summary.....	78
<b>Chapter Four: Synthesis and characterisation of zirconium doped natisite .....</b>	<b>79</b>
4.1: Introduction.....	79

4.2: Sample preparation .....	80
4.3: Characterisation .....	80
4.3.1: Unit cell refinement.....	80
4.3.2: SEM EDX .....	85
4.3.3: XAS.....	86
4.3.3.1: Experimental parameters.....	87
4.3.3.2: XAS results .....	87
4.4: Ion-exchange .....	98
4.4.1: Sample preparation .....	98
4.4.2: Analysis.....	98
4.4.2.1: XRD .....	98
4.4.2.2: XRF.....	107
4.4.2.3: SEM.....	110
4.4.2.4: ICP-MS .....	112
4.4.2.5: XAS.....	114
4.5: Summary.....	123
<b>Chapter Five: Competitive ion-exchanges.....</b>	<b>124</b>
5.1: Introduction.....	124
5.2: Competitive ion-exchanges .....	124
5.2.1: Sample Preparation .....	125
5.2.2: Analysis.....	125
5.2.2.1: ICP-MS .....	125
5.2.2.2: XRD .....	132
5.2.2.3: XRF.....	136
5.3: Summary.....	137
<b>Chapter Six: Variable pH ion-exchanges.....</b>	<b>139</b>
6.1: Introduction.....	139
6.2: Acidic pH ion-exchange .....	140

6.2.1: Sample preparation .....	140
6.2.2: Analysis .....	140
6.2.2.1: XRD .....	140
6.2.2.2: ICP-MS .....	145
6.3: Basic pH ion-exchange.....	146
6.3.1: Sample preparation .....	146
6.3.2: Analysis.....	146
6.3.2.1: XRD .....	146
6.3.2.2: ICP-MS .....	149
6.4: Summary.....	149
<b>Chapter Seven: Clinoptilolite.....</b>	<b>150</b>
7.1: Introduction.....	150
7.2: Clinoptilolite Ion-exchange.....	151
7.2.1: Sample preparation .....	152
7.2.2: Analysis.....	152
7.2.2.1: SEM-EDX .....	152
7.2.2.2: XRD .....	153
7.2.2.3: ICP-MS .....	156
7.3: Summary.....	158
<b>Chapter Eight: Conclusions and future work .....</b>	<b>160</b>
8.1: Conclusions.....	160
8.2: Future Work .....	163
8.2.1: Ion-exchange mechanism future work .....	163
8.2.2: Geological disposal .....	165
<b>References .....</b>	<b>167</b>

# *List of Abbreviations*

<b>CPS</b>	<b>Counts Per Second</b>
<b>EBR-1</b>	<b>Experimental Breeder Reactor 1</b>
<b>EDX</b>	<b>Energy Dispersive X-rays</b>
<b>EXAFS</b>	<b>Extended X-ray Absorption Fine Structure</b>
<b>FCC</b>	<b>Fluid Catalytic Cracking</b>
<b>GLEEP</b>	<b>Graphite Low Energy Experimental Pile</b>
<b>HIPing</b>	<b>Hot Isostatic Pressing</b>
<b>ICP-MS</b>	<b>Inductively Coupled Plasma Mass Spectrometry</b>
<b>SEM</b>	<b>Scanning Electron Microscopy</b>
<b>SIXEP</b>	<b>Sellafield Ion Exchange Effluent Plant</b>
<b>TS-1</b>	<b>Titanium Silicate 1</b>
<b>XRD</b>	<b>X-ray Diffraction</b>
<b>XRF</b>	<b>X-ray Fluorescence</b>
<b>XAS</b>	<b>X-ray Absorption Spectroscopy</b>
<b>XANES</b>	<b>X-ray Absorption Near Edge Structure</b>
<b>8MR</b>	<b>Eight Membered Ring</b>

# *LIST OF FIGURES*

Figure 1.1: Decay Products from $^{238}\text{U}$ with down arrows showing $\alpha$ -decays and upward arrows showing $\beta$ -decays .....	4
Figure 1.2: $[\text{AlO}_4]$ or $[\text{SiO}_4]$ tetrahedra building blocks. Single 4 and single 6 rings. Double 4 and double 6 rings .....	9
Figure 1.3: Crystal structure of sitinakite with Ti in octahedral coordination and Si in tetrahedral coordination. ....	17
Figure 1.4: Crystal structure of ETS-4 with Ti in octahedral coordination (grey) and Si in tetrahedral coordination (green).....	18
Figure 1.5: Crystal structure of ETS-10 with Ti in octahedral coordination (grey) and Si in tetrahedral coordination (green).....	19
Figure 1.6: Crystal structure of TS-1 with Ti in tetrahedral coordination.....	20
Figure 1.7: Crystal structure of natisite with Ti (grey) in square pyramidal coordination, Si (green) in tetrahedral coordination.....	20
Figure 1.8: Schematic of the SIXEP process. ....	24
Figure 1.9: Cs discharges following the construction of SIXEP .....	25
Figure 2.1: Representation of hydrothermal synthesis of zeolites.....	28
Figure 2.2: The derivation of Bragg's law .....	33
Figure 2.3: A schematic of the important features of a synchrotron .....	39
Figure 2.4: Typical X-ray absorption spectroscopy beamline set up.....	39
Figure 2.5: A typical X-ray absorption spectrum .....	44
Figure 2.6: Atoms showing various different scattering pathways .....	45
Figure 2.7: Generation of XRF spectral lines.....	47
Figure 2.8: Emission signals from an irradiated sample in SEM/TEM .....	50
Figure 2.9: Example of an EDX spectrum.....	51
Figure 2.10: Example of a typical ICP-MS schematic .....	52
Figure 2.11: ICP-MS sample preparation method .....	54
Figure 3.1: Titanium in square pyramidal coordination, as found in the natisite structure ...	56

Figure 3.2: Natisite chain showing coordination environments. Ti (grey), Si (green) O (red).	56
Figure 3.3: Crystal structure of natisite. Corner sharing layers of SiO <sub>4</sub> (green) and TiO <sub>5</sub> (grey) extending in the <i>ab</i> plane are separated by charge balancing cations (blue).....	56
Figure 3.4: Diffraction Pattern of natisite with main peaks labelled with their corresponding 2-Theta value .....	58
Figure 3.5: Observed and calculated profiles for the Rietveld refinement of natisite with the bottom curve showing the difference. Tick marks show calculated peak positions.....	60
Figure 3.6: SEM image for natisite .....	62
Figure 3.7: Diffraction patterns of microwave and hydrothermally synthesised natisite.....	64
Figure 3.8: SEM image of microwave synthesised natisite .....	65
Figure 3.9: XRD patterns of ion-exchanged natisite .....	68
Figure 3.10: Pawley peak fitting of (A)Ce (B)Co (C)Cs (D)Nd (E)Sr ion-exchanged natisite.....	70
Figure 3.11: XRF spectrum for natisite .....	71
Figure 3.12: XRF spectra for ion-exchanged natisite .....	72
Figure 3.13: SEM micrographs of ion-exchanged natisite .....	73/74
Figure 3.14: Calibration curve for Na ion used in ICP-MS.....	75
Figure 4.1: XRD patterns of 10% and 20% Zr-doped natisite .....	81
Figure 4.2: Observed and calculated profiles for the Pawley refinement of 10% Zr (top) and 20% Zr Natisite (bottom), with the bottom curve showing the difference. Tick marks show calculated peak positions.....	82
Figure 4.3: SEM image of (A) 10% and (B) 20% Zr-doped natisite.....	85
Figure 4.4: Ti-edge X-ray absorption spectra of natisite, 10% Zr and 20% Zr natisite .....	90
Figure 4.5: Fourier Transform of figure 4.3, detailing relative atomic distances .....	91
Figure 4.6: Zr K edge X-ray absorption spectra for 10% Zr and 20% Zr natisite .....	92
Figure 4.7: Fourier Transform of figure 4.6, detailing relative atomic distances .....	93
Figure 4.8: Fit of Ti-edge data for natisite .....	94
Figure 4.9: Fit of Ti-edge data for 10% Zr doped natisite .....	95
Figure 4.10: Fit of Ti-edge data for 20% Zr doped natisite .....	95
Figure 4.11: (A) Co-exchanged natisite (B) Co-exchanged 20% Zr natisite .....	99
Figure 4.12: XRD patterns of ion-exchanged 10% Zr natisite .....	101

Figure 4.13: Pawley phase fitting of (A) Ce (B) Co (C) Cs (D) Nd (E) Sr ion-exchanged 10% Zr-natisite .....	103
Figure 4.14: XRD patterns of ion-exchanged 20% Zr natisite .....	104
Figure 4.15: Pawley phase fitting of (A) Ce (B) Co (C) Cs (D) Nd (E) Sr ion-exchanged 20% Zr-natisite .....	106
Figure 4.16: XRF spectra of ion-exchanged 10% Zr natisite .....	108
Figure 4.17: XRF spectra of ion-exchanged 20% Zr natisite .....	109
Figure 4.18: SEM micrographs of 10% Zr natisite ion exchanged (left) and 20% Zr natisite (right) .....	110
Figure 4.19: Calculated percentage ion-exchange from ICP-MS results for natisite, 10% Zr and 20% Zr natisite .....	114
Figure 4.20: Ti-edge XANES region of natisite, 10% Zr and 20% Zr Co-exchanged natisite ..	117
Figure 4.21: Fourier Transform of figure 4.20, detailing relative atomic distances .....	118
Figure 4.22: Zr-edge XANES region of natisite, 10% Zr and 20% Zr Co-exchanged natisite .....	119
Figure 4.23: Fourier transform of figure 4.22, detailing relative atomic distances.....	120
Figure 4.24: XAS spectra of Co edge 20% Zr-natisite against (Top) 4-coordinate (Middle) 5-coordinate (Bottom) 6 coordinate Co standards.....	121
Figure 4.25: XAS spectra of Ce edge natisite against (Top) CeO <sub>2</sub> (middle) CeCl <sub>3</sub> (bottom) CeVO <sub>4</sub> .....	122
Figure 5.1: XRD pattern of Ce/Cs competitive ion-exchange with pure Ti-natisite .....	133
Figure 5.2: Pawley fit of Ce/Cs competitive ion-exchange with pure Ti-natisite .....	134
Figure 5.3: Pawley fit of Co/K competitive ion-exchange with 20% Zr natisite .....	134
Figure 5.4: Pawley fit of Cs/Sr competitive ion-exchange with 10% Zr natisite.....	135
Figure 5.5: Pawley fit Nd/Sr competitive ion-exchange with 10% Zr natisite .....	136
Figure 5.6: XRD spectra of (left) 10% Zr natisite Ce/Sr exchange and (right) 10% Zr natisite Ce/Cs .....	136
Figure 6.1: XRD patterns of ion-exchanged natisite at pH 7 .....	141
Figure 6.2: XRD patterns of ion-exchanged natisite at pH 3 .....	141
Figure 6.3: Pawley fits of (A) Ce pH 3 (B) Co pH 3 (C) Cs pH 3 (D) Nd pH 3 (E) Sr pH 3 exchanged natisite .....	143
Figure 6.4: XRD patterns of ion-exchanged 10% Zr natisite at pH 3.....	144

Figure 6.5: XRD patterns of ion-exchanged 20% Zr natisite at pH 3.....	144
Figure 6.6: XRD patterns of ion-exchanged natisite at pH 10 .....	147
Figure 6.7: XRD patterns of ion-exchanged 10% Zr natisite at pH 10.....	148
Figure 6.8: XRD patterns of ion-exchanged 20% Zr natisite at pH 10.....	148
Figure 7.1: SEM image for clinoptilolite.....	152
Figure 7.2: Pawley fit of clinoptilolite .....	154
Figure 7.3: Pawley fit of ion-exchanged clinoptilolite (A) Ce (B) Co (C) Cs (D) Nd (E) Sr .....	155
Figure 7.4: Comparison table of the percentage ion-exchange of each cation .....	158

# *List of Tables*

Table 1.1: Principle oxidation states of the main actinides. * indicating those oxidation states of interest in nuclear fuel recycling .....	6
Table 2.1: Table showing the seven crystal systems and their related unit cell lengths and angles .....	30
Table 3.1: Peak list for as synthesised natisite with corresponding <i>h k l</i> , 2-theta and relative intensities values displayed .....	59
Table 3.2: Rietveld refinement of natisite .....	61
Table 3.3: Bond distances and angles of natisite.....	62
Table 3.4: Elemental composition acquired from EDX.....	63
Table 3.5: Microwave synthesis times and products formed.....	65
Table 3.6: Pawley peak fitting of ion-exchanged natisite.....	69
Table 3.7: Calculated percentage ion-exchange from ICP-MS results of Ti-natisite .....	77
Table 4.1: Pawley refinement of 10% Zr and 20% Zr natisite.....	83
Table 4.2: Peak list with corresponding <i>h k l</i> , 2-theta and relative intensities values displayed .....	84
Table 4.3: Elemental composition of 10% Zr natisite acquired from EDX.....	86
Table 4.4: Elemental composition of 20% Zr natisite acquired from EDX.....	86
Table 4.5: Refined contact distances for natisite (Ti-edge).....	96
Table 4.6: Refined contact distances for 10% Zr natisite (Ti-edge).....	97
Table 4.7: Refined contact distances for 20% Zr natisite (Ti-edge).....	97
Table 4.8: Refined lattice parameters of ion-exchanged 10% Zr natisite .....	102
Table 4.9: Refined lattice parameters of ion-exchanged 20% Zr natisite .....	105
Table 4.10: Calculated percentage ion-exchange from ICP-MS results for 10% Zr natisite..	112
Table 4.11: Calculated percentage ion-exchange from ICP-MS results for 20% Zr natisite..	113
Table 5.1: ICP-MS results showing percentage exchange. (Ce% / competing ion %) .....	126
Table 5.2: ICP-MS results showing percentage exchange. (Co% / competing ion %) .....	128
Table 5.3: ICP-MS results showing percentage exchange. (Cs% / competing ion %).....	130

Table 5.4: ICP-MS results showing percentage exchange. (Nd% / competing ion %)	131
Table 5.5: ICP-MS results showing percentage exchange. (So% / competing ion %)	131
Table 6.1: Refined lattice parameters of ion-exchanged natisite at pH 3	142
Table 6.2: Comparison of percentage exchange for natisite, 10% Zr and 20% Zr natisite at pH 3	145
Table 6.3: Refined lattice parameters of ion-exchanged natisite at pH 10	147
Table 7.1: Elemental composition of clinoptilolite acquired from EDX	153
Table 7.2: Refined lattice parameters of clinoptilolite and ion-exchanged clinoptilolite	154
Table 7.3: Calculated percentage ion-exchange from ICP-MS results for clinoptilolite	156
Table 7.4: Optimum ion-exchange material for each of the ions of interest	159

# *CHAPTER ONE*

## *Introduction*

### 1.1: Background

Electricity generated by nuclear power was developed via the need for the production of plutonium for nuclear weapons. The world's first nuclear reactor achieved criticality in 1942 where simple reactors housed uranium in graphite blocks from which plutonium was chemically extracted and used in atomic bombs.<sup>[2]</sup>

The Manhattan project was tasked with developing a nuclear program for the sole purpose of developing the United States of America's nuclear arsenal.<sup>[3]</sup> The research produced by this project showed that heat was produced during nuclear fission, a process where a heavy nucleus splits on impact with a neutron. The heat from this process could be exploited to heat water into steam, driving turbines and generating electricity or even to provide propulsion for submarines and large aircraft carriers. The first nuclear reactor whose sole purpose was for the production of electricity provided enough energy to power 4 light bulbs and was named the "Experimental Breeder Reactor" (EBR-1) and was built in Idaho in 1951, 9 years after the Manhattan project achieved criticality.<sup>[2]</sup> EBR-1 was seen as the inspiration for fast breeder reactors which were designed to run on the plutonium extracted from spent fuel from a traditional reactors developed during the Manhattan project. So effectively, nuclear power plants were generating electricity as a by-product as part of their nuclear weapons program.

In 1945, the UK's atomic bomb committee agreed upon a programme for the construction of nuclear reactors. The first nuclear reactor in Western Europe was the "Graphite Low Energy Experimental Pile" (GLEEP) in Harwel, Oxfordshire. It took 2 years for GLEEP to become operational and was mainly used for research in reactor design and operation as part of a weapons program.<sup>[4]</sup>

In 1950, the Windscale piles in Cumbria achieved criticality with their simple graphite block reactors. In 1952, the spent fuel from these reactors was reprocessed to extract weapons grade plutonium on site. The Windscale reactors were air cooled by blowing air directly through the piles and vented it through tall stacks back into the atmosphere with no treatment. This initiated massive research and development in nuclear science in the UK for both military and civilian uses.

It is abundantly clear that without the need for a nuclear weapons program there would be no civilian nuclear industry. It was by changing the design of the reactors that allowed the heat from nuclear fission reactions to generate electricity. Nuclear power is recognised as the only large scale CO<sub>2</sub> emission free power source compared to the traditionally used depleting fossil fuels. The majority of nuclear power plants produce electricity from uranium fuel. The fission of a uranium nucleus can generate up to 200 MeV of energy<sup>[5]</sup> compared to 4 eV per atom in the oxidation of carbon to CO<sub>2</sub>.<sup>[6]</sup> Despite some high profile incidents, nuclear power still remains the safest method of electricity generation. In 2016 13 countries relied on nuclear energy to supply at least one-quarter of their total electricity with 72.3% of the total energy production in France being produced by nuclear power. As of April 2007, 30 countries worldwide are operating 449 nuclear reactors.<sup>[7]</sup>

It was not until decades after the wide scale adoption of nuclear power, that issue of how to deal with the waste generated in a safe and effective manner was first discussed. Waste is generated at every stage of the nuclear fuel cycle and disposing of all the waste generated is still seen as one of the most difficult problems and often referred to as the “Achilles Heel” of nuclear energy.<sup>[8]</sup>

To produce the fuel for the reactors, uranium is extracted from crushed ore by treatment with sulphuric acid or a sodium carbonate solution via a leaching process. Most of the decay products, from radon and below, are classed as waste “tailings”.<sup>[9]</sup> These tailings are a high volume low activity waste, currently around 940 Mt have been created containing around 75% of the original radioactivity of the uranium ore.<sup>[10, 11]</sup>

There are three naturally occurring isotopes of uranium,  $^{234}\text{U}$ ,  $^{235}\text{U}$  and,  $^{238}\text{U}$  with the early generation reactors focusing on the chemical neutron fission of the  $^{235}\text{U}$  isotope (0.72 atom %). However, the dominant  $^{238}\text{U}$  atom, also referred to as the “fertile isotope”, can be converted into artificial isotopes, in particular the thermally fissile  $^{239}\text{Pu}$  which can also be used in energy production. As plutonium and other fissile isotopes are produced during the irradiation of the  $^{238}\text{U}$  isotope, they can also be exploited for energy production though *in-situ* consumption. In a typical uranium fuelled reactor, approximately 40% of the total energy produced is derived from the fission of plutonium isotopes produced *in-situ*.

As the fuel is irradiated the proportion of useful fissile material is reduced and the amount of fission products increases. These fission products are very effective neutron absorbers and essentially poison the fuel by limiting the amount of neutrons available. Figure 1.1 shows the nuclear decay series of the  $^{238}\text{U}$  isotope.<sup>[12]</sup> After approximately 3 years of

irradiation the efficiency of the fuel is deemed to be too low and the “spent fuel” is removed from the reactor despite the percentage of fissile fuel still being above 90%.<sup>[13]</sup>

Advances in reactor design however could combat this issue, ultimately reducing the amount of waste produced and therefore limiting the environmental impact of spent fuel.

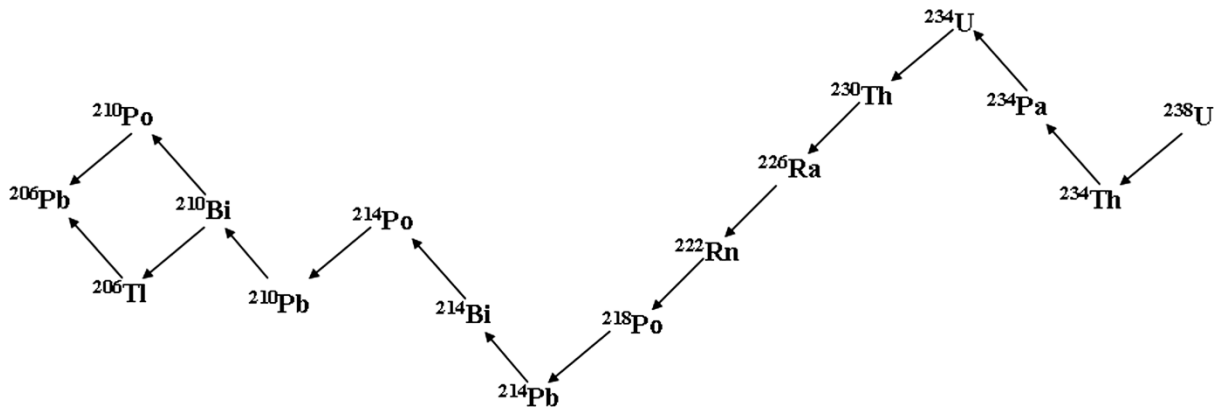


Figure 1.1 – Decay products from  $^{238}\text{U}$  with down arrows showing  $\alpha$ -decays and upward arrows showing  $\beta$ -decays.

In addition, as high-level waste produces heat, a larger amount of space is needed to store them in order to reduce heat load. Storage facilities have legal limits on the amount of waste they can store.

Uranium/plutonium fast reactors are a potential solution to reduce the amount of problem waste isotopes however, issues associated with the cooling processes have slowed progress in this area. Neutrons produced in fast reactors have an energy up to 1 MeV and can fission the  $^{238}\text{U}$  isotope effectively. High energy fission events triggered by fast neutrons in turn produce more neutrons in comparison to thermal reactors (approximately 100 times larger than is available in a thermal reactor).<sup>[14]</sup> There is therefore a surplus of neutrons, which can be used to change a fertile material (breeder reactor) or destroy problem waste products.

However, there are significant problems associated with the storage of waste generated from nuclear power plants. There is a massive accumulation of nuclear waste worldwide which poses a significant threat not only to the environment but to the general population. Currently nuclear waste is held in temporary storage facilities across the globe. This short-term fix does not rectify the problem of what to do with the waste.  $^{90}\text{Sr}$  ( $\beta$  emitter),  $^{137}\text{Cs}$  ( $\beta$  emitter) and  $^{60}\text{Co}$  ( $\gamma$  emitter) are just three radioactive isotopes commonly found in waste streams from, but not limited to, the decontamination of instruments and clothes. Significant amounts of research have focused on the safe capture and storage of these isotopes.

A key example of this is the Hanford nuclear facility in Washington, USA. During the 40 years of uranium and plutonium production a large amount of radioactive waste was generated and stored in 177 underground tanks on site, amongst this was the storage of low-level waste in burial trenches. It has been reported that 67 of the single-shell carbon-steel tanks have leaked over  $10^6$  cubic inches of  $^{137}\text{Cs}$  into underground soil. The waste solutions have been shown to contain concentrated sodium hydroxide (up to 8 M or higher).<sup>[15]</sup> At the Hanford site, there were several different nuclear processes for the production of weapons resulting in a variety of the nuclear waste generated in both volume and chemical composition further complicating the remediation process of the waste. The radiochemical composition of the waste varies over time due to the differing half-lives of the radionuclides, for instance  $^{135}\text{Cs}$  (half-life of  $3 \times 10^6$  years),  $^{137}\text{Cs}$  (half-life 30.1 years),  $^{90}\text{Sr}$  (half-life 28.78 years) and  $^{129}\text{I}$  (half-life  $1.57 \times 10^7$  years). Therefore, the separation of radionuclides from waste is an important factor to consider prior to any permanent disposal. All large scale separations depend on the diverse redox chemistry of the mid actinides (U, Np, Pu, Am).

These elements (mainly  $\alpha$  emitters) have substantial chemical differences between the linear dioxo “actinyl” ions  $\text{MO}_2^{+2+}$  (including solubility in aqueous and non-aqueous solvents and affinity for a complexant) formed by the oxidation states of V and VI, and the simple  $\text{M}^{3+/4+}$  ions formed by lower oxidation states. Table 1.1 displays the oxidation states of the mid actinides. The highly radioactive waste and spent fuel is seen as the most problematic waste forms to dispose of due to their toxicity and long half-lives.

**Table 1.1 – Principle oxidation states of the mid actinides. \* indicating those oxidation states of interest in nuclear fuel recycling.**

<i>U</i>	<i>Np</i>	<i>Pu</i>	<i>Am</i>
<i>III</i>	<i>III</i>	<i>III*</i>	<i>III*</i>
<i>IV*</i>	<i>IV*</i>	<i>IV*</i>	<i>IV</i>
<i>V</i>	<i>V*</i>	<i>V</i>	<i>V</i>
<i>VI*</i>	<i>VI*</i>	<i>VI</i>	<i>VI</i>
	<i>VII</i>	<i>VII</i>	

There are four categories of nuclear waste (UK definitions and state activity limits):

- High level waste - This only accounts for 3% of the world’s nuclear waste but contributes 95% of the radioactivity. This level waste is generated by the reprocessing of spent nuclear fuel. Not only does it require shielding to contain the radioactivity but also some form of cooling as it still produces heat. (State activity level – heat producing)
- Intermediate level waste - This only accounts for 7% for the overall volume and 4% of the radioactivity. Materials such as the metal cladding surrounding the reactors are

classed as intermediate level waste. (State activity higher than LLW, not heat generating)

- Low level waste - This accounts for 90% of the total volume but only 1% of the total radioactivity. Materials such as paper, tools and protective clothing all come under the low level waste category. <sup>[10]</sup> (state activity limit 4BG/t a, 12 BGq/t/g)
- Very low level waste - This is the least radioactive category. This type of waste typically consists of rubble and scrap metal which have been in contact with radioactive products and have been made weakly radioactive by irradiation of neutrons.

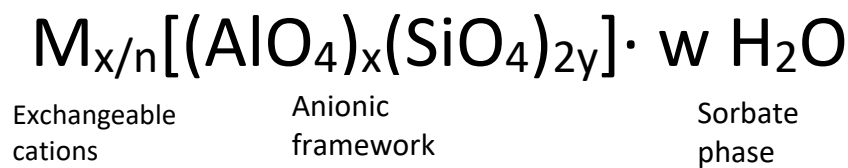
The earliest suggestion of dealing with waste generated from the nuclear fuel cycle was to simply dispose of the waste in the sea. The preferred option proposed by many countries now is to dispose of nuclear waste in facilities built in rock formations hundreds of metres underground. Currently only Finland has started the production of this type of facility<sup>[16]</sup> with Sweden having just agreed on a location for theirs. The U.S., who have the most radioactive waste, voted against an underground facility in Nevada, despite over two decades of research, over \$3 billion in costs and having over 70,000 tonnes of nuclear waste stored on nuclear sites across the country.<sup>[17, 18]</sup>

Nuclear disasters at Chernobyl, Three Mile Island and most recently Fukushima have all demonstrated the dangerous consequences of nuclear power. With the extension of Hinkley power plant in the United Kingdom to be completed by 2025, the issue of how to safely deal with the waste materials generated has again been a key issue. A material which could effectively remove radioactive isotopes from nuclear waste with minimal leaching back into the environment or that could be used in the event of accident release into water streams would have significant applications within the nuclear industry.

## 1.2: Zeolites

Zeolites by definition are a family of crystalline aluminosilicates whose chemical and physical properties are dependent on their unit cell and cavity dimensions. Discovered in 1756 by the Swedish mineralogist Alex Cronstedt. It was discovered that these materials have the ability to reversibly release adsorbed water upon heating. This discovery led to their name “zeolites” (ζειν=zein and λίθος=lithos) meaning “boiling stones”.<sup>[19]</sup> To date there are over 40 naturally occurring zeolites and over 200 different synthetic structures recognised by the International Zeolite Association.<sup>[20]</sup>

Zeolites follow the general formula:



(Equation 1.1)<sup>[21]</sup>

where M is a cation of valence +n. Zeolites can be reversibly dehydrated with little to no effect to the framework. This can result in these materials being used in solvent exchange or have other species absorbed in the place of framework coordinated water. The framework should be described as somewhat flexible with zeolite frameworks adapting to the application of heat and guest species.<sup>[22]</sup>

Zeolites have a three-dimensional framework consisting of  $[SiO_4]^{4-}$  and  $[AlO_4]^{5-}$  tetrahedra linked by sharing two, three or all four corners (figure 1.2). It is this formation of oxygen bridges between the Si and Al tetrahedron which creates large interconnected voids and channels.

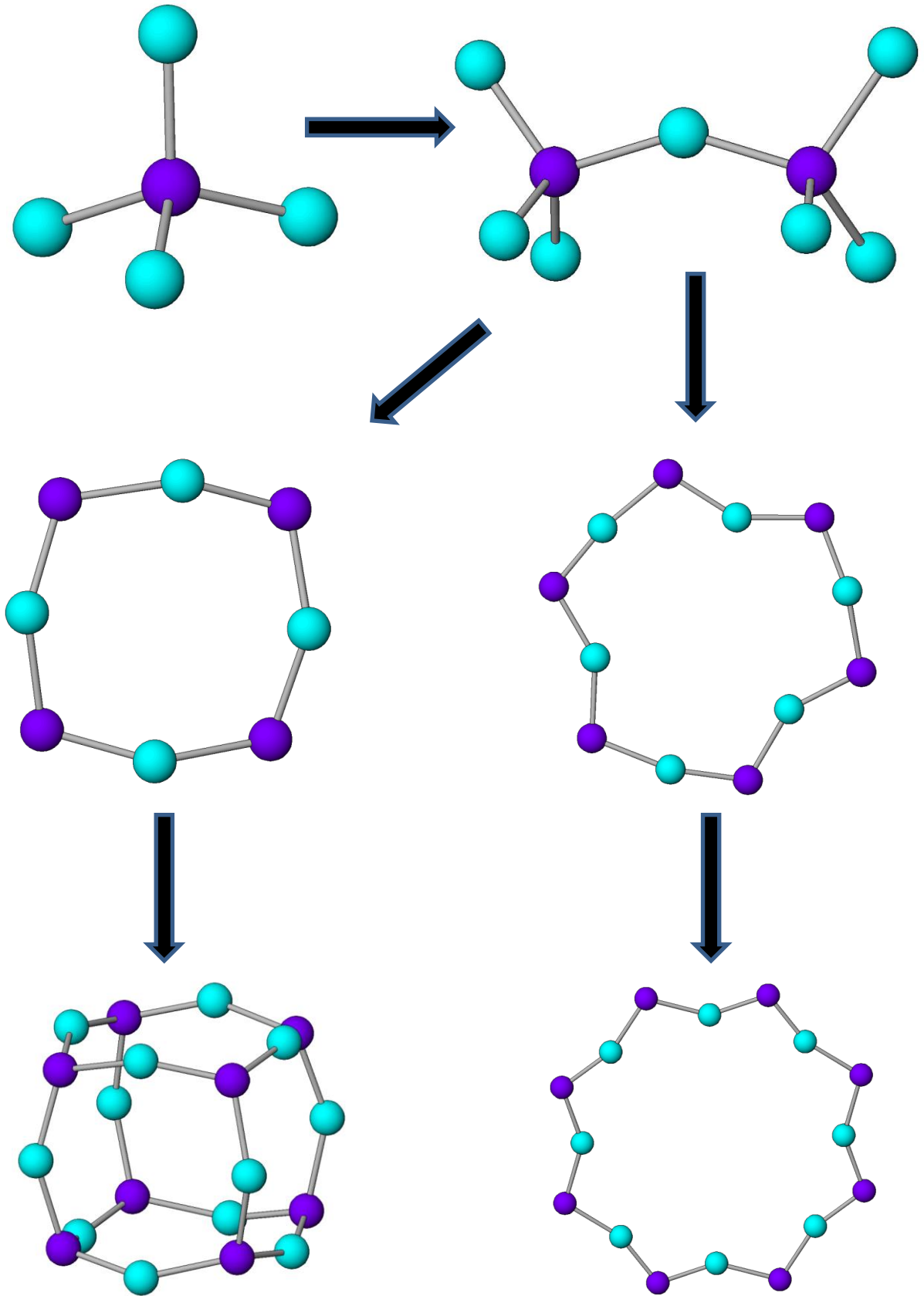


Figure 1.2 -  $[\text{AlO}_4]$  or  $[\text{SiO}_4]$  tetrahedra building blocks. Single 4 and single 6 rings. Double 4 and double 6 rings.

The presence of  $\text{AlO}_4$  causes the framework to have a net negative charge, which is balanced by counter ions, such as  $\text{Na}^+$ . These cations are loosely coordinated to the framework and preserve the electroneutrality of the material. The highly mobile nature of these cations means they can undergo reversible exchange. It is this property which has led to their use as detergent additives. The number of cations present within the extra-framework cavities is determined by the number of  $[\text{AlO}_4]^{5-}$  tetrahedra in the framework.

Naturally occurring zeolites are said to have formed through geochemical hydrothermal processes. These materials are found in a variety of geological locations mainly from volcanic debris, usually in megaton quantities, and have long been recognised of having a series of industrially useful properties which could be exploited either as ion-exchangers, in catalysis or as drying agents. It was not until the 1950's that large minable quantities of chabazite, clinoptilolite and mordenite were found throughout western America. During the 1940's and 1950's the conditions needed to synthesise zeolites were replicated in the laboratory. By the 1980's synthetic zeolites were used as molecular sieves with a large interest in ZSM-5 and ZSM-11 due to their hydrophobic surface leading to new possibilities in the separation of organic matter from aqueous solutions.<sup>[23]</sup>

Despite extensive knowledge of natural zeolites, their use over the past 50 years has been limited in comparison to the commercial use for synthetic zeolites whose output is approximately 500,000 metric tonnes annually in the U.S. alone.<sup>[24]</sup>

### 1.2.1: Löwenstein's rule

It would be anticipated that the distribution of Al throughout the zeolite framework would be random, however, this is not the case. Löwenstein's rule forbids the Al-O-Al linkage due to electrostatic effects, stating that the ratio of Si and Al molecules must be greater than or equal to 1. A lower ratio would imply more Al than Si meaning there would be some degree of Al-O-Al linkage within the structure, something which has never been experimentally observed. A ratio of 1:1 means there is strict alternation of Si and Al throughout the structure implying that the ordering of  $\text{SiO}_4$  and  $\text{AlO}_4$  tetrahedra in the zeolite framework is not random (figure 1.2). Altering the Si:Al ratio and substituting framework heteroatoms are two ways in which to synthesise new microporous compounds. These include aluminophosphates (AlPOS), silicoaluminophosphates (SAPOS), gallophosphates (GaPOS), zincophosphates, titanium silicates, metal substituted zeolites and phosphates.

### 1.2.2: Zeolites as drying agents

Zeolites with low Si:Al ratios or aluminophosphates have strong interactions with polar molecules and are therefore generally used as drying agents. This is achieved by dehydrating the zeolites, usually under vacuum, meaning the cations settle in sites with a lower coordination number. The removal of water can be more difficult in some zeolites than others with a positive correlation between framework density and energy required for water diffusion. The external presence of water will therefore rehydrate the zeolite meaning the cations will move back to their preferred higher coordinated state. The dehydration and subsequent rehydration of zeolites has little to no effect on the anionic framework and results in large empty pores in which substances other than water can be adsorbed. Pore size is

dependent on the number of oxygen molecules in the rings with 8-, 10- and 12- membered rings having typical sizes of  $\sim 4.5 \text{ \AA}$ ,  $\sim 6.3 \text{ \AA}$  and  $\sim 8.0 \text{ \AA}$  respectively.<sup>[25]</sup> As a result of the removal of coordinated water and the migration of cations to lower coordination sites dehydrated zeolites have a very open and porous structures.<sup>[21]</sup>

### 1.2.3: Molecular sieves

Zeolites, carbons, glasses and oxides are all used as molecular sieves. Due to the uniform pore size observed in zeolites, these materials are the most commonly used. The location of the charge balancing cations can partially block the pores in these materials reducing the overall size. Using this principle, ion-exchanging zeolites is an extremely effective way of tailoring pore sizes within zeolites. Larger cations will take up more pore space meaning the absorption of smaller molecules will be preferred. Cations of different sizes will occupy a different amount of space within a unit cell. The adjustable pore sizes make zeolites ideal materials as molecular sieves. Substances other than water can be adsorbed into the large empty pore of the dehydrated zeolites.

For example, the pore size of dehydrated zeolite-A is approximately  $4.7 \text{ \AA}$  however, the sodium cations reduce the pore size down to  $4 \text{ \AA}$ . By exchanging the sodium ions for calcium ions the pore size is changed from  $4 \text{ \AA}$  to  $5 \text{ \AA}$ . Calcium exchanged zeolite-A (known as zeolite 5A) has many industrial applications and is often used as a molecular sieve as it allows the absorption of n-alkanes but does not admit those that are branched or cyclic.

Zeolite 3A, the potassium form of zeolite-A, and 4A, the sodium form of zeolite-A, are commonly used worldwide as drying agents for liquid hydrocarbons with propane gas and natural gas being the most commonly treated. Where 3A is preferred in the treatment of

cracked gas such as ethylene and methanol, 4A is more commonly used for drying alcohols and benzene.

An alternative method to alter the pore sizes is to change the Si:Al ratio. An increase in the quantity of Si within a zeolite decreases the size of the unit cell due to the differences between the average lengths of Si-O and Al-O being 1.61Å and 1.75Å respectively.<sup>[26]</sup> This therefore alters the overall size of the cavities. Zeolites with higher quantities of Si require a lower amount of charge balancing cations needed to produce an over neutral charge on the framework meaning the pores are less restricted by cations. It is therefore possible to synthesise zeolites with specific pore sizes to allow adsorption of molecules tailored for their industrial use. There are four arbitrary categories of aluminosilicate zeolites; low, intermediate, high silica zeolites and silica molecular sieves.

The increase of silica in the framework causes the zeolites to have a certain set of properties including a higher thermal stability, a more hydrophobic surface selectivity and an increase in acidity. Since their introduction, the commercial use of zeolites and molecular sieves has grown vastly with their annual use being estimated at \$1.6-1.7 billion worldwide in 1998.<sup>[27]</sup>

#### 1.2.4: Catalysis

The characteristics of aluminium-containing zeolites make them excellent materials for use in catalysis due to their three-dimensional porous structure which creates a material with a very large surface area. These materials display important and useful catalytic properties which are not found in traditional amorphous catalysts. The isomorphic substitution of aluminium atoms creates a negatively charged framework which is overcome

by a counter ion. When this counter ion is a proton a Brønsted acid site is created. Normal synthetic zeolites contain sodium as a counter ion which can be exchanged for a proton by a simple reaction with an acid. This reaction will yield Si-OH and Al-OH hydroxyl groups on the surface of the framework. Zeolites which are unstable in acidic conditions due to dealumination, will be unable to undergo this reaction. It is still possible to generate these sites by reacting the zeolite with a  $\text{NH}_4^+$  salt and calcining the resulting product at high temperature. This effectively removes the ammonia leaving the proton. This is the preferred technique as it ensures that, if done correctly, dealumination (the stripping of aluminium from the framework) does not occur. Acid sites in zeolites can be Brønsted or Lewis in nature. In order to generate a Lewis acid site the material is further heated thereby removing the framework coordinated water from the Brønsted site, leaving a tricoordinated aluminium ion. The number of Brønsted acid sites is dependent on the framework composition. Those with a lower Si:Al ratio will give rise to a greater number of protons.

The selectivity of chemical reactions involving zeolitic catalysts can be increased by three mechanisms:

- Reactant shape selectivity - where large molecules in the mixture will be unable to enter the restrictive size of the pore and therefore unable to react.
- Product shape selectivity - where several products are formed within the zeolite but only one product is able to leave, or one product leaves at a much faster rate.
- Transition shape-selectivity - where the dimensions of the pore/active site inhibits the production of a certain product or transition state leading to the formation of other products. [28]

Therefore, the molecular sieve properties of these zeolites can provide extremely useful in only allowing certain molecules to access or exit the active site, properties which are not found in traditional catalysts.

Zeolites have many industrial uses as catalysts but perhaps their main industrial application is that in fluid catalytic cracking (FCC). Before the introduction of zeolites, the traditional method was to use thermal techniques via a complex free radical reaction pathway to obtain lighter petroleum products. It was not until the 1960's where it was shown by Plank and Rosiknski that the use of Zeolite-X and -Y were shown to be  $10^4$  times more active than the traditional amorphous silica-alumina catalysis. This was attributed to the higher concentration of active sites within the pores. Today, zeolite-Y and ZSM-5 are the two main zeolites used within fluid catalytic cracking and their inclusion within this process has been attributed to saving the petrochemical industry billions of dollars since their first use. [29]

### 1.3: Zeotypes

A new name is needed when dealing with materials that do not fit the strict definition of a zeolite but still have similar properties that make them applicable in zeolite science. Microporous materials, which contain metal cations coordinated to oxygen, are given the name "Zeotypes". Zeotypes are able to structurally form like zeolites and as such display similar chemical and physical properties. These include aluminophosphates (ALPOs), silico-aluminophosphates (SAPOs) and metallosilicates.

Mixed coordination inorganic frameworks exhibit metal cations in octahedral and tetrahedral coordination sites. Predominantly the silicate groups are tetrahedral with the larger metal cations being in an octahedral coordination environment. These cations can be

readily exchanged with the first row transition metal elements and those of groups III and IV heavier than aluminium and silicon. It has also been observed in some porous frameworks that the cations can be entirely in geometries that are neither tetrahedral nor octahedral. Aluminium, for example, can be coordinated four-, five- and six- fold with some frameworks such as UT-6, exhibiting aluminium in a mixture of these coordinations.<sup>[30]</sup> Metallosilicates are microporous frameworks in which the metal cations are octahedrally coordinated. These octahedra have been observed to exist as layers between porous silicates or isolated within the silicate framework with all the oxygens shared with the  $[\text{SiO}_4]^{4-}$  tetrahedra.

### 1.3.1: Titanium silicates

One of the most widely studied families of mixed coordination materials are titanium silicates. The synthesis of microporous materials which contain titanium instead of aluminium was attempted as early as 1967 however it was not until 1983 that the first crystalline titanium silicate was discovered. The substitution of silicon(IV) by titanium(IV) was attempted by Taramasso, Perego and Notari who discovered a new material with the composition:  $x\text{TiO}_2(1-x)\text{SiO}_2$  where  $(0.0 \leq x \leq 0.04 M)$ .<sup>[31]</sup>

It was widely believed that the substitution of framework silicon by titanium does not occur in aluminosilicates. This led to the belief that titanium had a preference to be octahedrally coordinated rather than tetrahedrally bound. Lone *et al.* in 1985 supported this argument by applying the Pauling rule of coordination. This was based on the ratio of ionic radii of the cation and anion and was found that the titanium(IV) and oxygen fell well outside the expected range for tetrahedral coordination.

The unusual properties of titanium silicates have been attributed to the presence of titanium(IV) within the silicon-oxygen lattice. There is a limit to how much titanium can be substituted within this  $\text{SiO}_2$  lattice. If titanium is in excess however there is a possibility of  $\text{TiO}_x$  nanophases being formed meaning the characterisation of the material is very difficult.<sup>[32]</sup>

Microporous titanium silicates display different structural characteristics compared to conventional zeolites including increased acidic stability. These differences allow the titanium silicates to be subjected to more extreme conditions, such as those found in the treatment of nuclear waste. Crystalline zeotypes such as sitinakite ( $\text{Na}_2\text{Ti}_2\text{O}_3\text{SiO}_4 \cdot 2\text{H}_2\text{O}$ ) are often used due to the higher stability in acidic conditions. Unlike aluminium, which only coordinates tetrahedrally in zeolites, titanium can have both octahedral and tetrahedral coordination leading to a wider range of possible structures also meaning that Löwensteins rule no longer applies, as there can now be some degree of Ti-O-Ti linkage within the zeotype framework. These new structures could lead to new materials exhibiting useful ion-exchange properties where traditional zeolites would be unstable, most notably in acidic conditions.

### 1.3.2: Sitinakite

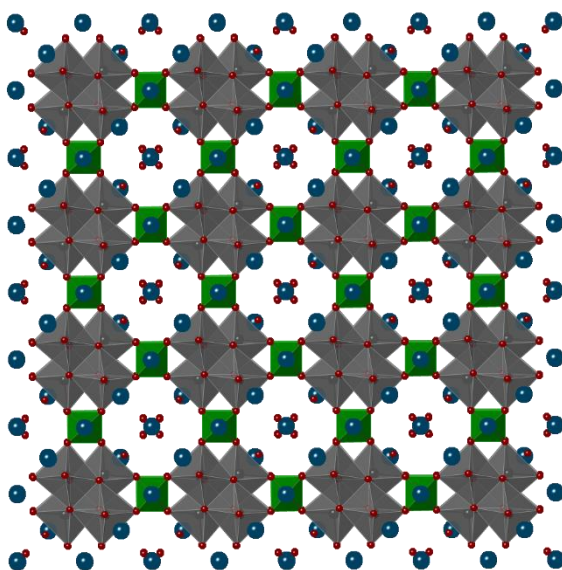


Figure 1.3 - Crystal structure of sitinakite with Ti in octahedral coordination and Si in tetrahedral coordination.

Sitinakite,  $\text{KNa}_2\text{Ti}_4\text{Si}_2\text{O}_{13}(\text{OH}) \cdot 4\text{H}_2\text{O}$ ,  $a = b = 7.81 \text{ \AA}$   $c = 12.09 \text{ \AA}$ , crystallises in the tetragonal spacegroup  $P4_2/mcm$  with the structure consisting of  $\text{Ti}_4\text{O}_4$  cube-like units which are linked together by silicate groups.

These form together to build a cube with the cube like groups linked together by oxo-groups<sup>[33]</sup>.

Sitinakite (figure 1.3) is considered one of the baseline materials for caesium removal and is considered of great importance due to the materials tuneable ion-exchange properties. The framework substitution of hetero atoms ( $\text{Nb}^{5+} \leftrightarrow \text{Ti}^{4+}$ ) does not change the structure significantly but does create differences in the materials ion-exchange chemistry. It was shown by Rietveld analysis of the powder diffraction patterns that caesium and strontium lay in different coordination environment depending on whether there was any niobium present within the framework.<sup>[34]</sup> This change was attributed to the population of water and sodium ions in the channels resulting in different hydration environments of caesium and strontium. This therefore changed the materials pore size in such a way as to increase the materials overall affinity for caesium and strontium.<sup>[33]</sup> Microporous titanium silicates such as sitinakite and the synthetic niobium doped analogue are being used as ion-exchange materials for the removal of  $\text{Cs}^+$  and  $\text{Sr}^{2+}$  from nuclear waste, referred to industrially as IONSIV-911<sup>®</sup>.<sup>[35, 36]</sup>

### 1.3.3: ETS-4

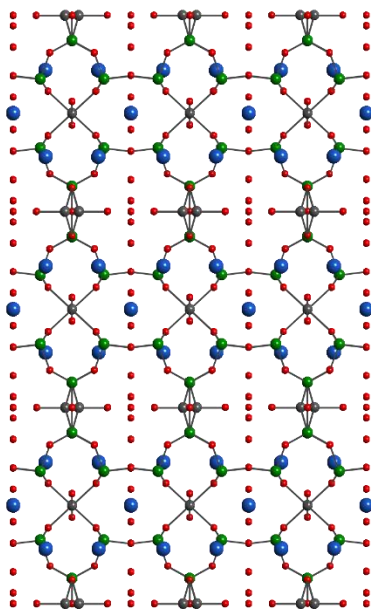


Figure 1.4 – Crystal structure of ETS-4 with Ti in octahedral coordination (grey) and Si in tetrahedral coordination (green).

ETS-4 (figure 1.4) crystallises in the orthorhombic space group  $Cmm$ ,  $a = 23.2 \text{ \AA}$   $b = 7.17 \text{ \AA}$   $c = 6.97 \text{ \AA}$  with the ideal formula of  $\text{Na}_8(\text{Ti}_5\text{H}_2\text{Si}_{12}\text{O}_{39})8.45(\text{H}_2\text{O})$ . The pore sizes in the material ETS-4 can be altered by dehydrating the material at high temperatures allowing the access to the interior of the crystal. This dehydration technique allows the effective tailoring of adsorption properties

making ETS-4 a commercially viable material for gas separations throughout the 3-4 Å size range.<sup>[37]</sup> ETS-4 has a mixed octahedral/tetrahedral framework with access to crystal interior occurring through narrow eight membered rings (8MRs).

The negative charge on the framework is balanced by sodium cations but derivatives such as Sr-ETS-4 has also been reported<sup>[38]</sup>. Careful heating shows that ETS-4 undergoes negative thermal expansion meaning as the material is heated there is a decrease of lattice size in all directions along with gradual loss of crystallinity. Strontium (and other cations) can increase the thermal stability of ETS-4 (up to 350°C for Sr exchanged, compared to 200°C for as synthesised Na- ETS-4).<sup>[39]</sup>

#### 1.3.4: ETS-10

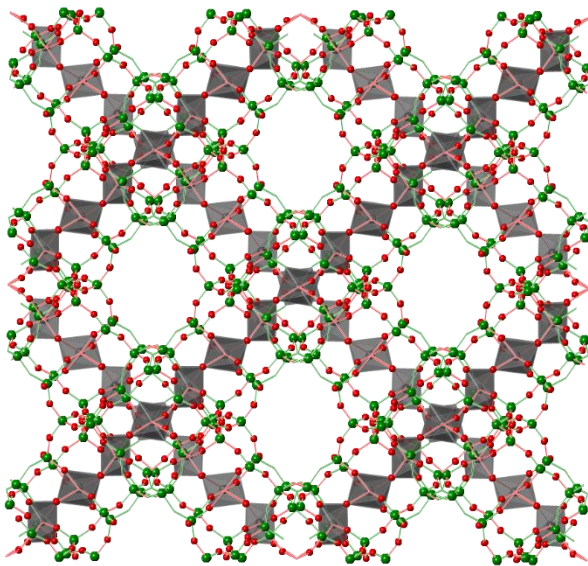


**Figure 1.5 - Crystal structure of ETS-10 with Ti in octahedral coordination (grey) and Si in tetrahedral coordination (green).**

ETS-10 (figure 1.5) is a crystalline highly disordered wide pore microporous material with the ideal formula  $\text{Na}_2\text{TiSi}_5\text{O}_{13} \cdot n\text{H}_2\text{O} \cdot 3$

The disorder is due to the introduction of stacking faults. ETS-10 is a large pore solid consisting of chains of corner sharing  $\text{TiO}_6$  octahedra which share 4 oxygens with the  $\text{SiO}_4$  tetrahedra.<sup>[40]</sup> The charge balancing cations are found in sites

next to the Ti-O-Ti-O chains. ETS-10 crystallises in the monoclinic space group  $C2/c$  with  $a = b = 21.00\text{Å}$ ,  $c = 14.51\text{Å}$  and  $\beta = 112.12^\circ$ . ETS-10 is commonly used as a basic catalyst and has

been studied as a possible material in the removal of  $\text{Cs}^+$  and  $\text{Sr}^{2+}$  from contaminated waste.<sup>[41]</sup>

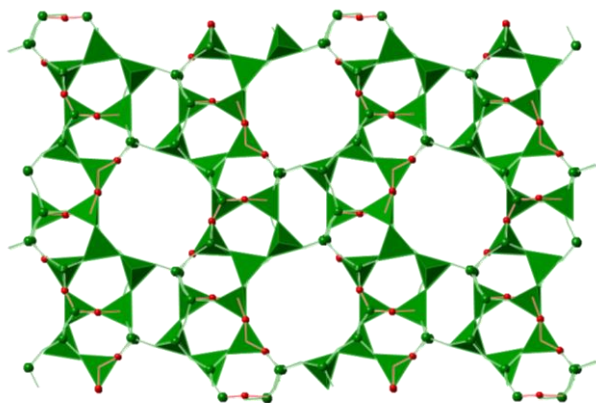


Figure 1.6 – Crystal structure of TS-1 with Ti in tetrahedral coordination.

### 1.3.5: TS-1

Titanium silicate 1 (TS-1) (figure 1.6) is a medium pore sized titanium silicate belonging to the MFI structure group with

the ideal formula  $\text{TiSi}_2\text{O}_6$ . First synthesised in 1983 by Taramasso *et al* TS-1 consists of both

sinusoidal and straight 10-membered rings of around  $5.5\text{\AA}$ . TS-1 is a particularly useful titanium silicate due to its interesting catalytic properties especially in the production of many organic compounds including in the hydroxylation of phenol, benzene and alkanes. It is believed that the titanium atoms in the isolated  $\text{Ti}^{4+}$  lattice positions are the active sites in selective oxidation reactions.

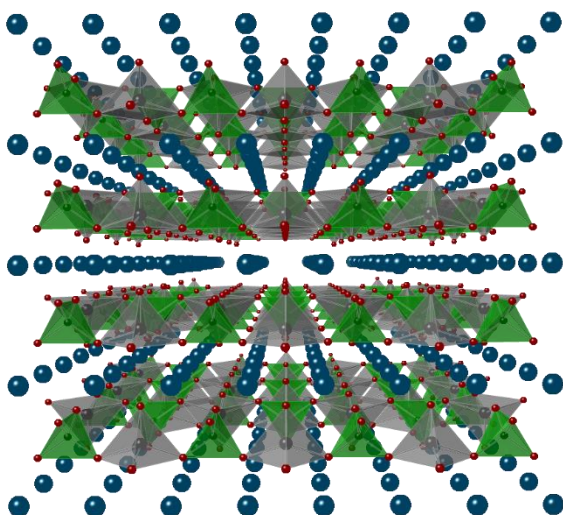


Figure 1.7 - Crystal structure of natisite with Ti (grey) in square pyramidal coordination, Si (green) in tetrahedral coordination.

### 1.3.6: Natisite

Natisite (figure 1.7) is a layered titanium silicate with the ideal formula  $\text{Na}_2\text{TiSiO}_5$ . The structure consists of titanium in an unusual 5- coordinate square pyramidal environment with the sodium charge balancing cations located between the layers.

The square pyramidal  $\text{TiO}_5$  units alternate with  $\text{SiO}_4$  tetrahedra. Natisite crystallises in

the tetragonal space group  $P4/n m m$  with  $a = b = 6.4967(8) \text{ \AA}$  and  $c = 5.0845(11) \text{ \AA}$ .<sup>[42]</sup> Little previous work has been conducted on this material, with any published work focusing on synthesis and characterisation of the structure. Kostov-Kytin and Ferdov focused on the successive transformation of paranatisite into natisite<sup>[43]</sup> with Peng and Liu investigating the FT-IR and XRD of heat treated natisite.<sup>[44]</sup> No work to date has been conducted on the modification of the framework or any tests on the materials ion-exchange chemistry.

## 1.4: Ion-Exchangers

Ion-exchangers by definition are insoluble solids which contain exchangeable cations or anions with those which are capable of both cation and anion exchange being called amphoteric ion-exchangers. Zeolites are the most widely used ion-exchange material due to the wide range of possible structures they exhibit. They are classed as microporous materials, meaning the diameter of the pore size is less than  $20 \text{ \AA}$ . Charge balancing cations, which are usually loosely coordinated to the framework, have high levels of mobility and can be readily exchanged with other cations in a surrounding solution. The exchange of ions is mostly stoichiometric, reversible and essentially a diffusion process meaning that chemical kinetics usually have little relation to the process as a whole. Zeolites are particularly suitable ion-exchanges as the charge balancing cations released during ion-exchange are commonly found and harmless to humans and aquatic life.

It was not until 1850 that Thompson and Way, studied the exchangeability of cations by clays and aluminosilicate precipitates. These experiments consisted of passing solutions containing common salts, including  $\text{NH}_4^+$ ,  $\text{K}^+$ ,  $\text{Na}^+$ ,  $\text{Mg}^{2+}$  and  $\text{Ca}^{2+}$ , through columns containing these solids. Their results showed that these solids had the ability to exchange cations by stating “...it was observed that the liquid which first ran though no longer contained any of the

*ammonia or other salt employed*". Lemberg and Weigner were able to correctly identify the identity of the solid with the first synthesis of an inorganic ion-exchanger being achieved by Ham and Rumpler.

There are two main types of ion-exchange material, either inorganic zeolites and clays or organic resins. Zeolites have a well-ordered structure and techniques such as X-ray diffraction (XRD) can be utilised in order to characterise the material. Organic resins however are amorphous and often irregular, complicating any analysis of their structure.

This pore size will determine what ions can be exchanged as some will be too large to fit through the pore. The advantage of using zeolites over traditional organic ion-exchangers is their ability to retain their structure in extreme conditions including elevated temperatures and strong radiation.

The specific ion-exchange nature of the materials is dependent on the amount of  $\text{AlO}_4$  tetrahedra as the number of these dictate the amount of charge balancing cations required. <sup>[45]</sup> Cations are not a structural part of the framework meaning they can be removed with no effect to the framework. However, the size and position of the cation has significant implications to the materials property. A change in the cationic occupancy will significantly affect the size of molecules which can be adsorbed as these cations have the ability to either partially or fully block the channels and pores of the material.<sup>[21]</sup>

A rise in temperature and concentration of the effluent will have an effect on the rate of exchange. A raise in temperature is likely to increase the diffusion process due to both the framework and the cation both being electrically charged. Higher concentrations of effluent should increase the level of exchange to a point however, it is worth noting that the total level

of exchange will remain fixed due to the limited number of cations coordinated to the framework. Once all the cations have been exchanged, increasing the concentration will have no further effect.<sup>[27]</sup> The following factors will all effect the amount of exchange: pH, temperature, pressure, and amount of contact time between the effluent and the ion-exchange material.

A typical **cation** exchange



(equation 1.2)

A typical **anion** exchange



(equation 1.3)

with **X** representing the structural unit of the ion-exchanger.

The general reaction (equation 1.2) was first exploited commercially in the early 1900's when it was observed that the  $\text{Na}^+$  form of zeolite-A can be used as a water softener as the  $\text{Na}^+$  ions would readily exchange with the  $\text{Ca}^{2+}$  ions which were responsible for hard water. As with most ion-exchange reactions, the process is completely reversible. Zeolite-A can be regenerated once all the  $\text{Na}^+$  ions have been exchanged by simply passing it through a solution containing a sodium salt. Some zeolites will have a natural affinity towards certain cations with clinoptilolite being a significant natural zeolite used in the nuclear industry to remove  $\text{Cs}^+$  from waste streams.

## 1.5: SIXEP Process

The Sellafield Ion Exchange Effluent Plant (SIXEP) is an effluent treatment plant located in Sellafield, UK, which is used to remove radioactivity from liquid waste feeds. A schematic of the SIXEP process is shown in figure 1.8.

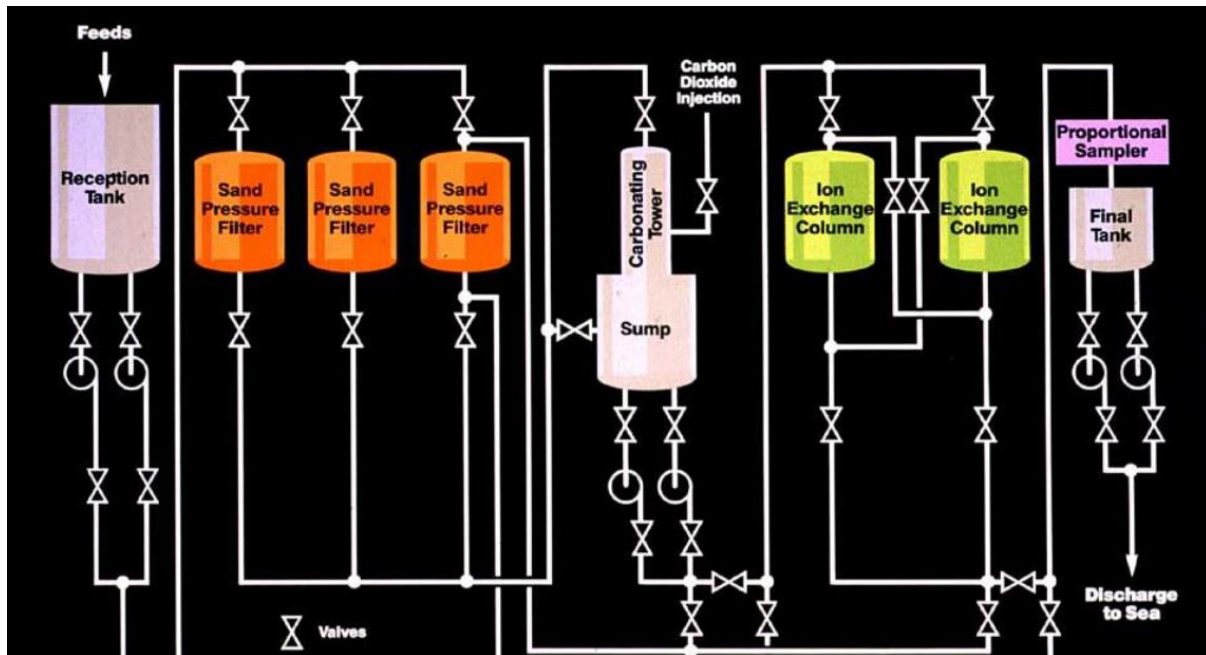


Figure 1.8 – Schematic of the SIXEP process.

Design and development of the SIXEP process began in the 1970's and became operational in 1985. The plant receives waste effluent from several facilities across the Sellafield site and first allows solid sediment to settle in the bulk storage tanks. Following this the waste effluent is filtered using sand bed filtration to remove the coarse particulate and is put through a carbonation process to neutralise the alkaline feed. Clinoptilolite, a naturally occurring zeolite, is then used as an ion-exchanger to remove radionuclides, mainly strontium and caesium. The clinoptilolite is replaced on average every 77 days in order to ensure high levels of radionuclide exchange and avoid breakthrough. During the 22 years in which SIXEP has been operational, 18.5 million cubic meters of water has been treated removing over

85,000 TBq of beta radioactivity and approximately 80 TBq of alpha activity.<sup>[46, 47]</sup> This is a significant success story for the nuclear industry and demonstrates a significant improvement to activity released prior to the construction of the facility (figure 1.9). However, reprocessing operations are due to cease at the Sellafield plant within the decade which will be followed by a phase of Post Operational Clean Out (POCO). Waste effluent streams with different compositions to those which SIXEP has traditionally faced are expected to arise throughout decommissioning. Consequently, alternative sorption materials may be required to manage the new effluent challenges ahead and are subject of much interest.

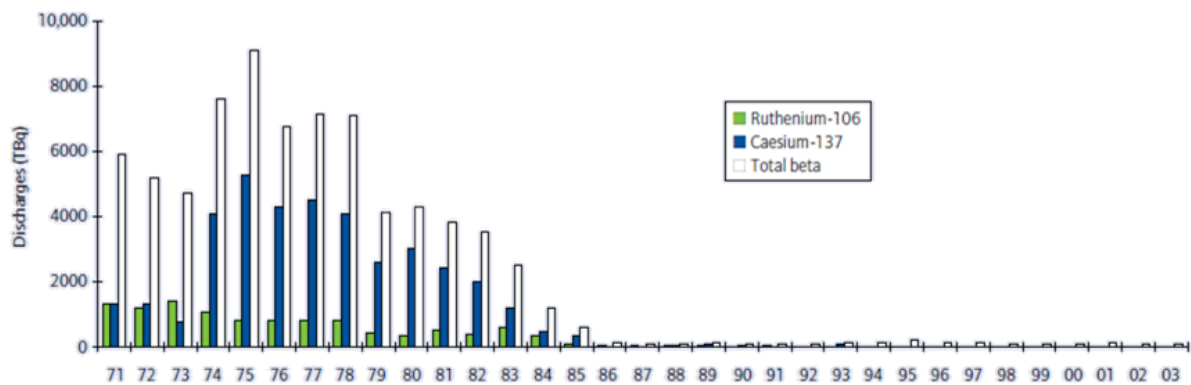


Figure 1.9 – Cs discharges following the construction of SIXEP.

## 1.6: Aim of Work

The aim of this work is to investigate a potential new ion-exchange material for the remediation of problem waste radionuclides from solution. Inspiration was drawn from sitinakite and its synthetic niobium doped analogue (IONSIV® 911). The niobium doped sitinakite was shown to have significant differences in the materials ion-exchange chemistry, in particular the increase in uptake of  $\text{Cs}^+$  from solution, in comparison to the parent material. It was hoped that synthesising natisite and a zirconium doped natisite that differences in the materials ion-exchange chemistry could be investigated and compared.

The aim of this work was to synthesis a series of natisite samples with different levels of zirconium substitution up to 20% and to investigate how this introduction changes the materials ion-exchange chemistry. Determining the structure is crucial to understanding how the introduction of zirconium into the structure affects the materials ion-exchange chemistry. The structure of natisite and zirconium doped natisite were investigated using a variety of solid state characterisation techniques including powder X-ray diffraction (XRD), X-ray fluorescence (XRF), scanning electron microscope (SEM), X-ray absorption spectroscopy (XAS) and pair distribution function analysis (PDF).

Another primary aim was to ion-exchange the pure natisite and Zr-doped natisite and to investigate any differences in the selectivity and capacity for certain cations. This was achieved again by using Inductively Coupled Plasma Mass Spectrometry (ICP-MS) to analyse waste effluent.

Finally, these ion-exchange results will be compared with the naturally occurring zeolite clinoptilolite. Clinoptilolite is commercially used in the SIXEP process at Sellafield for the removal of  $\text{Cs}^+$  and  $\text{Sr}^{2+}$  from solution. By conducting both single and competitive ion-exchange experiments in the same laboratory environment, a direct comparison can be drawn. Therefore, we can conclude the material which is superior for the removal of certain radionuclides, and if natisite has any commercial value.

# *CHAPTER TWO*

## *Experimental Techniques*

The main characterisation techniques used in this work were powder X-ray diffraction (XRD), X-ray fluorescence (XRF), X-ray absorption spectroscopy (XAS), Inductively Coupled Plasma Mass Spectrometry (ICP-MS), and scanning electron microscopy (SEM).

### 2.1: Synthesis

Throughout this work, a single method was used to synthesis the materials. Crystalline natisite ( $\text{Na}_2\text{TiSiO}_5$ ) and partially zirconium-doped natisite were both prepared hydrothermally using stainless steel autoclaves lined with a Teflon™ reaction vessel.

#### 2.1.1: Hydrothermal Synthesis

Hydrothermal synthesis has provided a way of successful reducing reaction times for the synthesis of microporous materials (figure 2.1). A typical hydrothermal synthesis for zeolites includes mixing amorphous reagents containing silicon and aluminium together with a cation source in a basic solution. This mixture is heated typically above 100°C in a sealed autoclave. After a certain amount of time the amorphous material being turned into crystalline zeolite product until essentially all the material is approximately an equal mass of crystalline product. This insoluble product is then recovered by filtration washing and drying.<sup>[1]</sup> Molar ratios of the precursors are added to the Teflon™ liner which is used due to its ability to withstand high pressures up to 150 bar and temperatures up to 270°C.

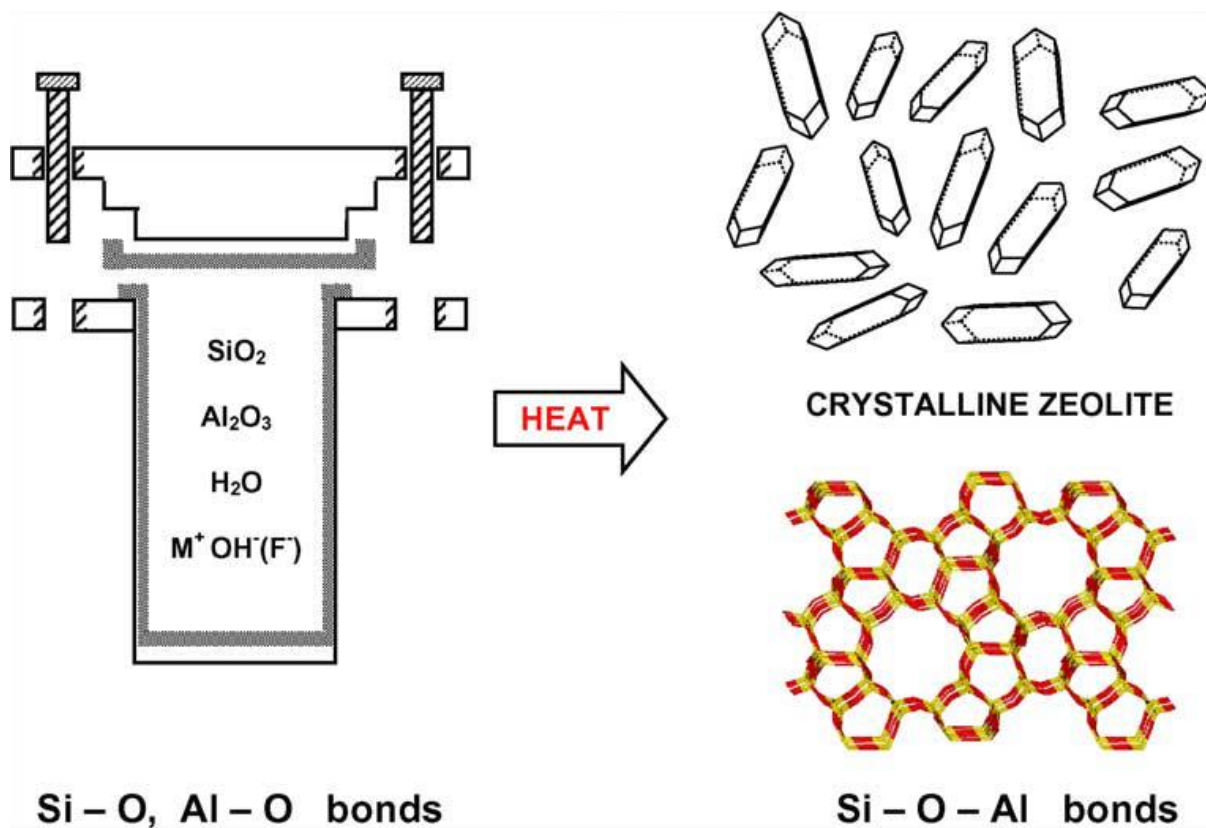


Figure 2.1 – Representation of hydrothermal synthesis of zeolites.<sup>[1]</sup>

Natisite and its zirconium doped analogue were both synthesised using hydrothermal methods. A highly alkaline solution ( $\sim$  pH 14) is necessary for formation of a highly pure product. Hydrothermal synthesis was carried out using acid digestion vessels (Parr, model 4744 capacity 45 ml) and (Parr, model 4748 capacity 125 ml) with a Teflon™ liner.

### 2.1.2: Microwave Synthesis

A review on microwave syntheses has shown that it is able to reduce reaction times from a matter of days down to several hours producing highly pure products with narrow particle size distribution.<sup>[48]</sup> The driving of chemical reactions by microwave irradiation is becoming increasingly popular in all fields of chemistry, especially in the synthesis of zeolites and related materials whose synthesis times can be reduced significantly. Microwave heating

holds several advantages over conventional heating. As conventional heating requires an outside heat source transferring the heat to the surface of the material and conducting that heat to the middle of the material, microwave heating has a much more instantaneous heating with no wall or heat diffusion effects. This coupled with much higher heating rates yields much faster reaction times. To date several zeolites/zeotypes have been successfully synthesised by microwave irradiation. Previous work has shown that the microporous materials ZSM-5<sup>[49]</sup>, TS-1<sup>[50]</sup>, TS-2<sup>[51]</sup> and Zeolite A<sup>[52]</sup> can all be successfully synthesised at lower temperatures and reaction times compared to that of the hydrothermal method. In particular Linde Type N which is used within the petroleum and petrochemical industry, in either catalytic or adsorbent based processes, has been shown to be successfully synthesised by microwave irradiation after as little as 1 hour with no organic structure directing agent.

Microwave samples are prepared in the same way as the hydrothermal synthetic route, but instead are placed in a 25mL microwave vessel set at 200 psi and 200°C for typically 18 hours using a CEM DISCOVER-S microwave.

## 2.2: Crystallography and Diffraction

### 2.2.1: Introduction to Crystallography

Crystallography is the study of the arrangement of atoms in crystalline solids and is used to determine the structures of unknown materials. It can provide information on the shape and size of a unit cell, giving details on how the atoms or molecules pack together. In addition, it provides information on the location and nature of atoms, bond distances and angles, from which; bond strengths, oxidation states and distortions can be inferred. A detailed understanding of how atoms pack together and interact in the solid state is crucial

in the study of many important inorganic materials, including zeolites, superconductors and nanomaterials, as there is a relationship between the structure of a material and its physiochemical properties.

Crystals are solids with repeating units of atoms, with the smallest arrangement that can convey the full symmetry of the crystal structure being referred to as the unit cell. The lengths of the unit cells are given as  $a$ ,  $b$  and  $c$  with the angles between the unit cells given as  $\alpha$ ,  $\beta$ , and  $\gamma$ . The relationships between lattice parameters (Table 2.1) form the basis of the seven crystal systems: triclinic, monoclinic, orthorhombic, tetragonal, trigonal, hexagonal and cubic.

**Table 2.1 – Table showing the seven crystal systems and their related unit cell lengths and angles.**

<i>Crystal System</i>	<i>a b c</i>	<i><math>\alpha \beta \gamma</math></i>
<i>Cubic</i>	$a = b = c$	$\alpha = \beta = \gamma = 90^\circ$
<i>Hexagonal</i>	$a = b \neq c$	$\alpha = \beta = 90^\circ \gamma = 120^\circ$
<i>Trigonal</i>	$a = b = c$	$\alpha = \beta = \gamma \neq 90^\circ$
<i>Tetragonal</i>	$a = b \neq c$	$\alpha = \beta = \gamma = 90^\circ$
<i>Orthorhombic</i>	$a \neq b \neq c$	$\alpha = \beta = \gamma = 90^\circ$
<i>Monoclinic</i>	$a \neq b \neq c$	$\alpha = \gamma = 90^\circ \beta \neq 90^\circ$
<i>Triclinic</i>	$a \neq b \neq c$	$\alpha \neq \beta \neq \gamma \neq 90^\circ$

These crystal structures can combine with one of the lattice centring, either primitive (P), body-centred (I), face-centred (F), or side-centred (C) generate the 14 Bravais lattices (Figure 2.2) which describe the arrangement of atoms in a unit cell. Unit cells by definition are the smallest repeatable unit by translational motion only. However, other symmetry operations have to be considered such as rotations and reflections. These symmetry

operations can therefore generate the whole unit cell with fewer atoms, referred to as an asymmetric unit. Combining the fourteen Bravais lattices with all the possible symmetry elements gives a total of 230 space groups.

### 2.2.2: Powder X-ray diffraction (XRD)

X-ray diffraction is the main and most useful solid-state analytical technique in the structural analysis of crystalline materials. X-rays are electromagnetic radiation with an energy range of 500 eV to 500 KeV, or wavelengths from  $\sim 25 \text{ \AA}$  to  $0.25 \text{ \AA}$ .

X-rays are generated when high-energy electrons bombard a metal source, usually copper, with the consequent loss of energy given out as X-rays. Less than 1% of the electron beam is converted into X-rays, with the majority dissipated as heat. The electrons ionise the inner core 1s electrons of the metal source, creating a vacancy in this shell. This vacancy is then filled by an electron in a higher energy shell with the difference in energy emitted as X-rays of a characteristic wavelength that varies with differing metal sources. The most common being Cu, with a wavelength of  $1.5418 \text{ \AA}$ .

Diffraction occurs when X-rays interact with the three-dimensional array of atoms (or rather the electrons of the atoms) within a crystal and are subsequently scattered in all directions. The three-dimensional array of atoms or molecules are in a fixed position and due to the repetition, can act as a diffraction grating for incident X-rays.

Two factors determine the appearance of an X-ray diffraction pattern:

- 1) The symmetry and size of the unit cell, which gives both the number and position of the peaks.

2) The positions of the atoms in the unit cell and the atomic numbers, which dictate the intensity of the peaks.

Diffraction patterns can be used to determine a structural model where either the Laue equations or Braggs law can be used.

The Laue equations treat diffraction of crystalline materials in a similar way as diffraction of light by an optical grating. In a hypothetical 1D crystal consisting of a row of atoms, the following equation is given:

$$a \sin \phi = n \lambda$$

(Equation 2.1)

For 3D materials however, three equations must be given in order to correspond to the three crystallographic axis:

$$a_1 \sin \phi_1 = n \lambda$$

$$a_2 \sin \phi_2 = n \lambda$$

$$a_3 \sin \phi_3 = n \lambda$$

(Equation 2.2)

For diffraction to occur all three equations must be satisfied simultaneously. Despite the Laue equations being mathematically correct they are extremely complicated to use and therefore are rarely used.

Braggs law however treated 3D crystals as a build of layers/plains, with these layers/planes acting as semi-transparent mirrors. As X-rays interact with the material, some are reflected off the plains with the angle of reflectance equalling the angle of incidence,  $\theta$ , whereas the rest are transmitted to be reflected by succeeding layers.

This leads to the Bragg equation,

$$n\lambda = 2d\sin\theta$$

(Equation 2.3)

$\lambda$  = wavelength of radiation used  
 $n$  = integer  
 $d$  = perpendicular distance between the lattice plains  
 $\theta$  = angle of incidence

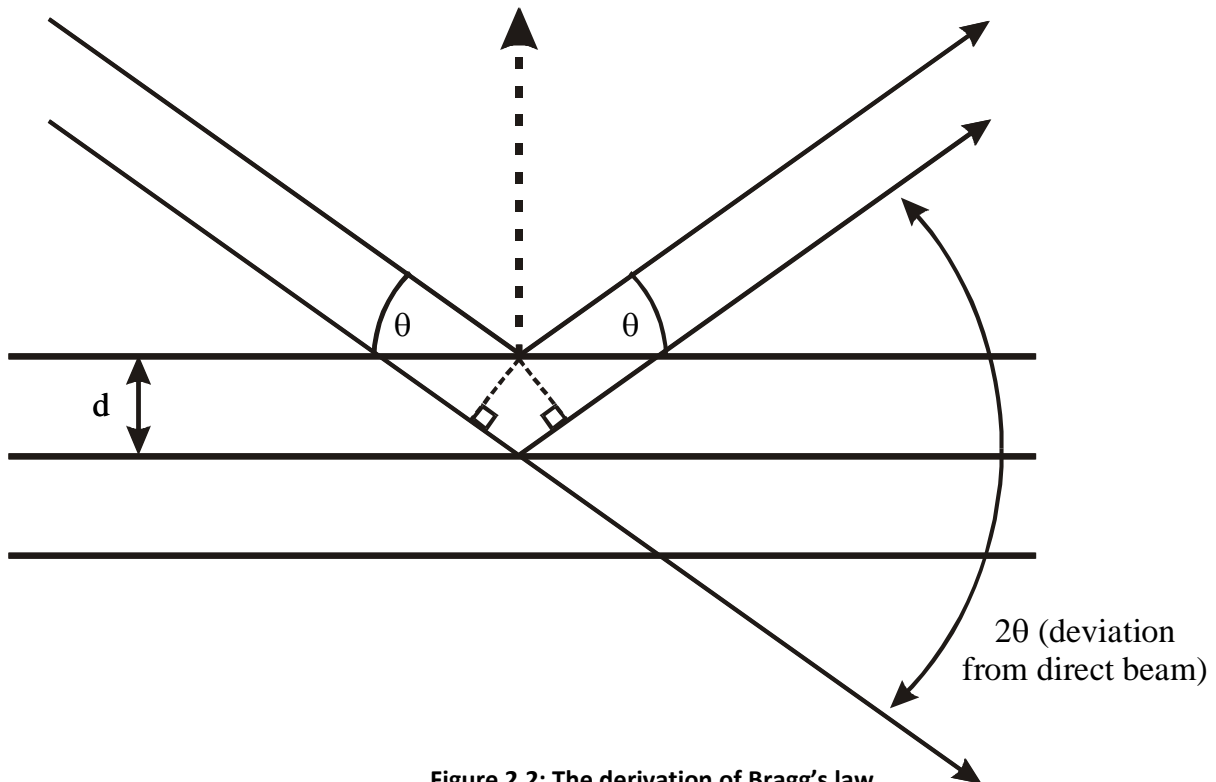


Figure 2.2: The derivation of Bragg's law.

The path difference must be an integer number of wavelengths in order to satisfy the equation. Bragg's law (figure 2.2) sets a strict definition on angles at which reflections occur (~tenths of a degree tolerance). When Bragg's law is satisfied, the reflected beams are in phase and interfere constructively. At angles other than the incidence angle, the beams are out of phase and therefore interfere destructively. It should be noted that the atoms do not reflect X-rays, rather they scatter/diffract them in all directions. Real crystals contain thousands of planes therefore due to the random orientation of crystallites in powders, there should always be a crystallite which satisfies Bragg's law.

The distance between two adjacent parallel planes of atoms with the same Miller Indices is known as interplaner spacing (d-spacing). The interplaner spacing in tetragonal materials is given by the equation:

$$\frac{1}{d^2} = \frac{h^2 + k^2}{a^2} + \frac{l^2}{c^2}$$

(Equation 2.4)

### 2.2.3: Generation of X-rays

Laboratory XRDs contain a metal target housed under vacuum in an “X-ray Tube”. A large voltage, usually around 40kV is generated between the filament and the water-cooled X-ray tube. This produces high-energy electrons traveling in the direction of the metal source. Once the X-rays have been generated, they leave the tube through a beryllium window. Be is virtually transparent to X-rays due to its low atomic number, and allows X-rays to be emitted from the tube whilst maintaining the vacuum.

Most laboratory diffractometers use copper as the metal source. As this copper source is bombarded with electrons the electrons in the copper 1s shell are ionised leaving a vacancy in the orbital. The most favourable transition is the 2p → 1s transition, where electrons from the higher energy 2p shell fill the vacancy in the 1s orbital with excess energy given out by a characteristic wavelength of X-ray energy. This yields the most common CuK $\alpha$  radiation line. As electrons have two spin states, this transition appears as a doublet. Monochromators (usually germanium) are needed within diffractometers to select only the K $\alpha_1$  as the two spin states of electrons yields radiation at both  $\lambda=1.54051\text{\AA}$  and  $\lambda=1.54433\text{\AA}$  for K $\alpha_1$  and K $\alpha_2$  - respectively.

Despite copper being the most common metal target it is not the only option with chromium, iron, cobalt, molybdenum and silver also being used. X-rays are also generated from Bremsstrahlung, meaning breaking radiation. This involves the rapid deceleration of electrons as they interact with a metal source. Bremsstrahlung, also known as white radiation, has a continuous spectrum, however characteristic radiation is more useful in diffraction.

The intensity of the diffraction peaks are determined by the arrangement of atoms in the entire crystal with the quantitative measurements of XRD intensities being crucial to determining crystal structures.

$$I_{hkl} = K(Lp)_{hkl} j_{hkl} F_{hkl}^2 e^{-2w} \cdot A_{hkl}$$

(Equation 2.4)

$K$  = scale factor, normalising experimentally observed intensities with calculated intensities.

$(LP)_{hkl}$  = Lorentz-Polarisation factor. This contains two parts, the Lorentz factor and the polarisation factor.

$j_{hkl}$  = multiplicity of the  $[hkl]$  planes.

$W$  = Debye temperature correction factor.  $\left(-\frac{B_{iso} \sin^2 \theta}{\lambda^2}\right)$

$A_{hkl}$  = absorption factor.

$F_{hkl}$  = structure factor.

Two main factors affect the intensity of peaks in X-ray diffraction. The atomic number of the atoms, which is taken into account in the intensity equation and the orientation of the particles in a powdered sample. Generally, the heavier the element the more electrons it has

and the stronger is scatters X-rays. It is assumed in powdered samples the crystallites are in a random orientation. Some crystallites may be needle like and therefore orientate themselves in a certain direction, having a very strong effect on the intensity of some peaks, known as preferred orientation.

#### 2.2.4: Rietveld Refinement

In the 1960's Rietveld had developed a method for analysing complex powder patterns by minimising the difference between the observed and calculated diffraction patterns. The difference between the observed and calculated patterns were then used to refine the atomic coordinates of a starting model. Careful examination of observed, calculated and difference plots is the best way of following a least-squares refinement.

Numerical values can also be calculated to indicate the "goodness of fit". The weighted profile R-value ( $R_{wp}$ ), R-value ( $R_p$ ) and goodness of fit ( $\chi^2$ ) are defined as:

$$R_{wp} = \sqrt{\frac{\sum W_m (Y_{o,m} - Y_{c,m})^2}{\sum W_m Y_{o,m}^2}} \quad R_p = \sqrt{\frac{\sum |Y_{o,m} - Y_{c,m}|}{\sum Y_{o,m}}} \quad \chi^2 = \sqrt{\frac{\sum W_m (Y_{o,m} - Y_{c,m})^2}{M - P}}$$

#### 2.2.5: Laboratory Instrumentation

The Bruker D2 Phaser used in this work utilises a LYNXEYE 1-dimensional detector eliminating the need for a secondary monochromator by suppressing sample fluorescence. A Ni filter removes  $K\beta$  signal and Soller slits are used on the detector. The diffractometer operates in  $\theta$ - $\theta$  geometry and generates X-rays at 30kV /10 mA. Powder samples were analysed using a Bruker zero background sample holder, which consists of a thin wafer of silicon along the (1 0 0) plane.

## 2.3: Synchrotron Radiation

Synchrotrons are a source of extremely powerful X-ray radiation. The tuneable beams of electromagnetic radiation mean that anything from far Infra-red to hard X-rays can be used at one facility. The first observation of synchrotron radiation was on the 24<sup>th</sup> April 1947 at the General Electric Research Laboratory in Schenectady, New York.<sup>[53]</sup>

The mass of particles increases and the energy increases towards the relativistic range. The heavy particles then arrive too late at the electrode for the radio frequency (RF) voltage, used to further accelerate the particles, therefore limiting the maximum particle energy. It was found that particles which are too fast get less acceleration from the RF accelerators and slow down compared to the particles which are too slow which get more acceleration and speed up producing a stable bunch of particles which are accelerated together. At GE, researchers tested this theory, and saw a bright arc of light being produced from the electron beam. Langmuir was credited as recognising this as synchrotron radiation.

Intensities of X-rays at synchrotrons (measured in flux/brilliance) is many magnitudes higher, around  $10^{14}$ , than those found in laboratory diffractometers. Synchrotrons consist of five main components (figure 2.4):

1. Electron source – Electrons are produced from thermionic emission from a hot filament in an electron gun. The electrons are accelerated to around 100 MeV using a linear accelerator (LINAC). A constant supply of electrons is needed, as some are lost in collisions with gas particles in the storage ring.

2. Booster ring – Electrons are now further accelerated to the same energy as found in the storage ring. These electrons are periodically injected into the storage ring in order to maintain the current.
3. Storage Ring – Contains high-energy electrons, traveling in bunches which are kept on a closed path by magnets. The storage ring consists of both straight and curved sections. Dipole or bending magnets are used to change the path of the electrons at the curved sections. Quadropole magnets are used to focus the electron beam, with sextupole magnets correcting for chromatic aberrations caused by quadropole magnets.
4. Radio Frequency (RF) supply – As the electrons travel around the ring, some energy is lost due to emission of synchrotron energy. The RF supply provides electrons with just enough extra energy to make it around the storage ring and prevent electrons from spiralling into the walls of the ring.
5. Beamlines – These beamlines are located tangentially to the storage ring and along the axis of insertion devices and off tangents to bending magnets. Beamlines are split into two parts;
  - i. The front end – Where the majority of the safety features are located. This acts to isolate the beamline vacuum from the storage ring vacuum. In addition, the beam is then focused and/or monochromated in the optics hutch depending on the experimental conditions required.
  - ii. The experimental hutch – High-energy beamlines have thick lead lined concrete walls to protect from X-rays and gamma radiation.

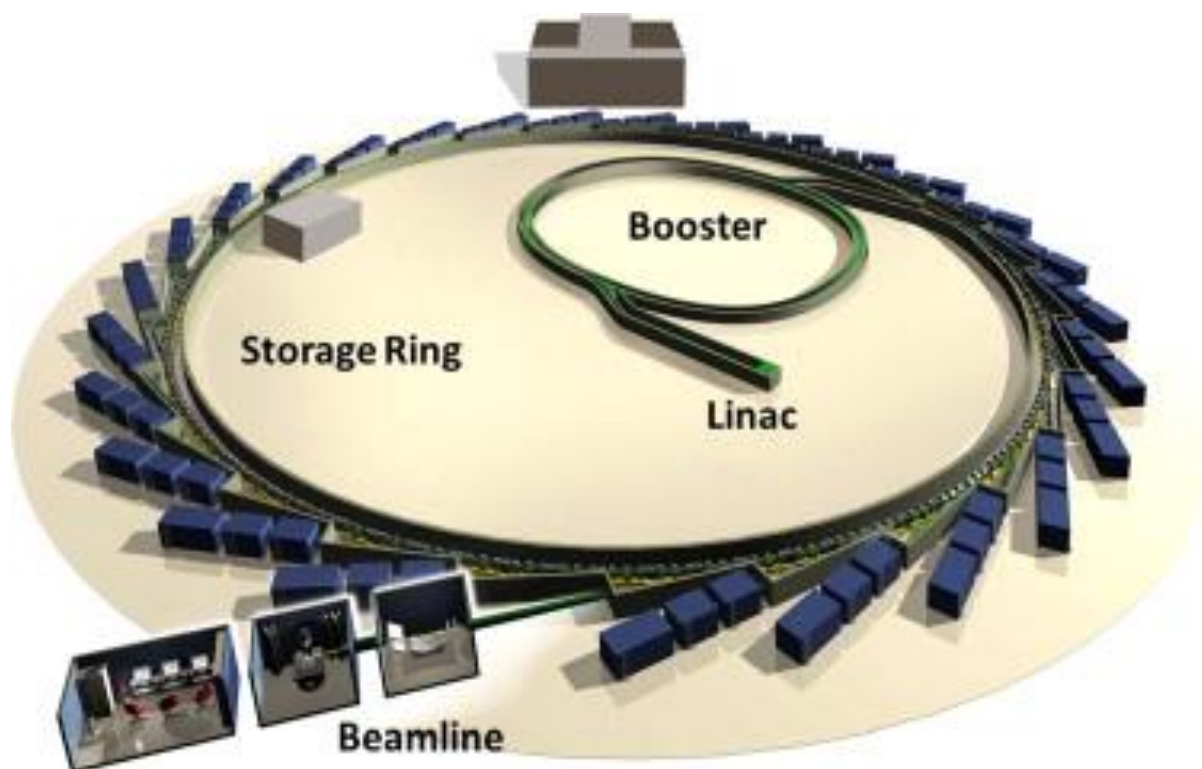


Figure 2.3 – A schematic of the important features of a synchrotron.

### 2.3.1: X-ray Absorption Spectroscopy (XAS)

X-ray absorption spectroscopy is a technique designed to analyse the local short-range order of atoms, typically around the  $10 \text{ \AA}$  length scale and details the absorption of X-rays by atoms near and above the atoms core binding energy. Figure 2.5 shows an example of a schematic of an XAS beamline.

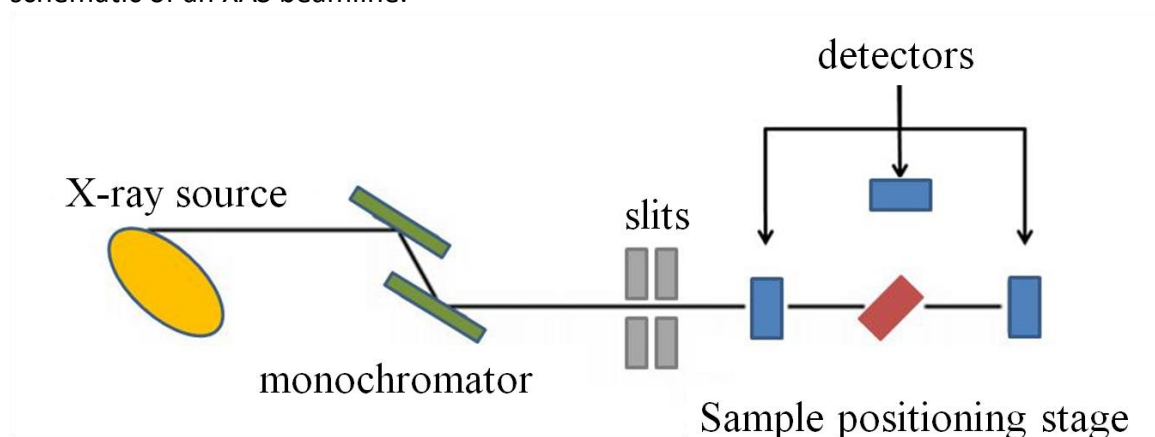


Figure 2.4 – Typical X-ray absorption spectroscopy beamline set up.

Equation 2.5 shows the EXAFS equation. This equation attempts to incorporate changes in disorder, multiple atoms around the absorber, multiple scattering pathways and phenomena that removes signal from the main channel. <sup>[54]</sup>

$$X(k) = S_0^2 \sum N_i \frac{f_i}{kD_i^2} e^{-\frac{2D_i}{\lambda(k)}} e^{-2k^2\sigma_i^2} \sin(2kD_i + \delta_i(k))$$

(Equation 2.5)

D = Half path length

N = Degeneracy

$\sigma^2$  = Mean square relative displacement (MSRD)

$S_0^2$  = Amplitude reduction factor

$E_0$  = Edge Energy

$\lambda(k)$  = Mean free path

X-ray radiation is absorbed by an electron in a defined quantum core level (e.g. 1s, 2p, 2s) of an atom. When the binding energy of this quantum core level is less than the energy of the incident X-ray beam, the X-ray is absorbed and energy, which is excess of the core binding energy, is released from the atom as a photoelectron radiating out in all directions. As this electron wave propagates out, it can scatter off nearby atoms returning to the original absorbing atom, where the wave can interfere both constructively and destructively. If the waves are in phase and interfere constructively the electron density around the absorbing atom is now increased. Therefore, the probability of finding this state after measurement is increased, rather than the state where a photon continues without being absorbed.

Constructive interference at the location of the absorbing atom happens when the photoelectron wave travels a whole number of wavelengths.

$$2D = n\lambda$$

(Equation 2.6)

$D$  = Distance from absorbing atom to scattering atom

$n$  = An integer

$\lambda$  = Wavelength

The primary concern when dealing with XAS is the absorption coefficient,  $\mu$ , which gives the probability that X-rays will be absorbed according to Beer's Law:

$$I = I_0 e^{-\mu t}$$

(Equation 2.7)

$I$  = Intensity of X-rays transmitted through sample

$I_0$  = Intensity of incident X-rays

$\mu$  = Absorption coefficient

$t$  = Sample Thickness

As the absorption coefficient depends on an available electronic state, the presence of a photo-electron scattered back from a neighbouring atom will alter the value of  $\mu$ . X-ray absorption is the transition between two quantum states:

1. Initial state – An X-ray, a core electron and no photo-electron

## 2. Final state – No X-ray, a core hole and a photo-electron

$\mu$  can therefore be described with Fermi's Golden Rule to give:

$$\mu(E) \propto |\langle i|H|f\rangle|^2$$

(Equation 2.8)

$\mu(E)$  = Absorption Coefficient

$\langle i|$  = Initial State

$H$  = Interaction term

$|f\rangle$  = Final State

The close analysis of a XAS spectrum can yield information on the atoms formal oxidation state, coordination, distances, coordination number and species of atoms immediately surrounding the chosen element. As XAS is an atomic probe, all types of samples, both crystalline and amorphous solids and liquids, can be analysed.

As all atoms have core electrons, XAS provides an effective way of measuring most elements on the periodic table. In addition, crystallinity is not required in order to generate an XAS spectra making it one of only a few structural techniques for non-crystalline and highly disordered materials, including solutions. X-rays by nature are very penetrating meaning that XAS is not a surface sensitive technique. However, by changing the setup of the beamline, surface sensitivity can be increased, if desired. XAS can measure elements that are of a trace amount in a sample, making it a unique technique of measuring chemical and physical properties of dilute species in systems.

Absorption can be quantified by measuring the difference in energy of the incident beam and the transmitted beam, measuring the fluorescence given off by excited atoms or

by measuring ejected electrons as core holes are filled. Once absorption has been determined, the energy of the incident X-rays is changed slightly and the process repeated producing a spectrum with four common features:

- An almost linear downward trend towards lower absorption with energy,
- A sharp rise in absorption above incident energy,
- Several small peaks and shoulders near and above the peak of absorption
- A general oscillation up and down following a downwards trend.

The probability of absorption of photons decreases as the energy of X-rays increases, although there are exceptions to this general rule. Figure 2.6 shows a typical XAS spectra. <sup>[55]</sup>

1. Background – The background follows a general rule: The probability of absorption decreases as the energy of the photons increases. Although, there are exceptions to this rule.
2. The edge – The edge starts at energies below the energy needed to excited core electrons. Whilst above this energy, they have enough energy producing a sharp increase in absorption
3. X-ray Absorption Near Edge Structure (XANES)– Peaks, shoulders and other features near or on the edge are referred to as the XANES region. XANES is very sensitive to oxidation states and coordination chemistry.
4. Extended X-ray Absorption Fine Structure (EXAFS) – Gradual oscillations above the edge are referred to as the EXAFS region. EXAFS region is used to determine distances, coordination number and species of neighbouring atoms.

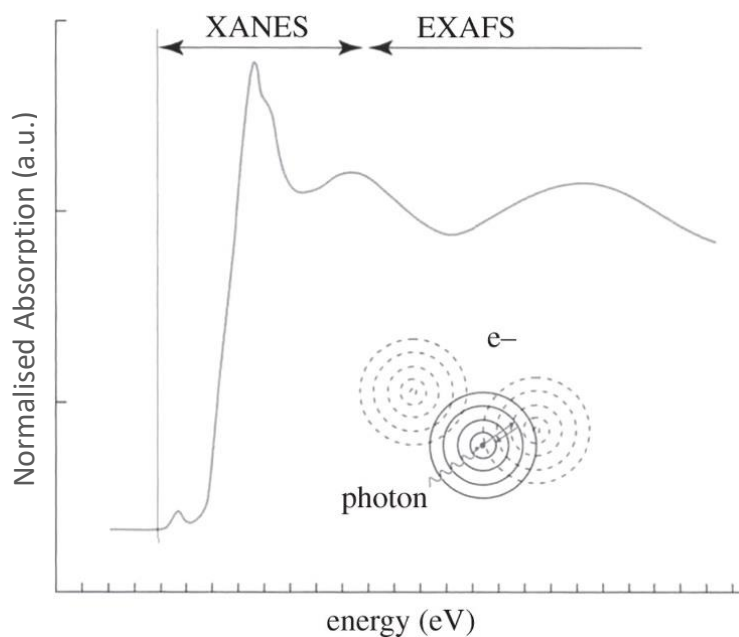


**Figure 2.5 – A typical X-ray absorption spectrum.**

The simplest method for the analysis of an XAS spectrum is through matching with empirical standards, mainly for the XANES region. As the features of an XAS spectra provides information about coordination environments and oxidation states, comparing with standards of a known composition can help to identify species in an unknown sample. Another more in depth analytical method is through the modelling of experimental obtained EXAFS data. XAS experiments measures the probability that X-rays will be absorbed by a sample.

The energy of the X-ray beam is increased through the use of a monochromator, and starts below the binding energy of the element of interest. Once the energy reaches this binding energy and surpasses it, the probability of the photon being detected increases dramatically. After an atom absorbed the incident X-ray, it propagates out as a spherical wave, with the propagation between the electrons of differing atoms referred to as the path length. Each path begins and ends at the central atom ensuring the paths are always closed. In the analysis of XAS closed paths are only considered.

Figure 2.7 shows various different scattering pathways.<sup>[56]</sup> Path 1 shows a single scattering pathway. Paths 2 and 3 shows double scattering pathways and 4 – 6 showing triple scattering pathways.

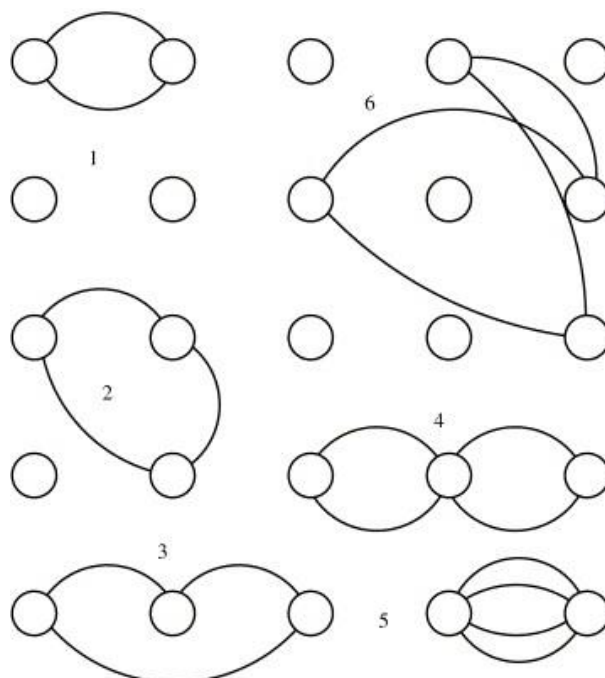


Figure 2.6 – Atoms showing various different scattering pathways.

### 2.3.2: Analysis of a XAS Spectrum (Muffin Tin Potential)

In order to analyse the multiple scattering pathways a FEFF calculation can be run which is performed on the Fourier transformed data after background removal and weighting. FEFF<sup>[57]</sup> is a computer program, which can calculate the spectroscopic properties of EXAFS, generating theoretical standards. FEFF incorporates the full multiple scattering technique to give information on scattering factors and mean-free-path for a given coordination shell. Once these theoretical scattering pathways have been calculated, they can be incorporated into the EXAFS equation (equation 2.5) in order to refine structural parameters from experimentally obtained data. FEFF incorporates the electronic configurations of free atoms by placing them in positions specified on input. A calculation starts by generating the

potentials and calculating the scattering phase shifts. Atoms are treated as localised spherical potentials, which can be treated in three ways: not touching, barely touching and overlapping. Meaning that in any circumstance there will be space that is not assigned to any atom. The interstitial potential in this space is assumed to be constant. This result is referred to as the muffin tin potential where there are circular regions, some of which overlap slightly in which the potential drops.

The software packages used in the analysis of XAS spectra in this work were Athena, Artemis and Hephaestus using IFEFFIT.<sup>[58]</sup>

## 2.4: X-ray Florescence (XRF)

X-ray Florescence is a non-destructive emission technique used for elemental analysis of bulk samples. XRF works on the principle that when a sample is exposed to high energy X-rays, inner core electrons ionise, leaving a vacancy in the 1s shell for example, however it is not just restricted to this transition. During the relaxation process electrons from higher energy subshells moves down to fill the vacancy with the emission of a quantised X-ray photon. Any electrons from the outer shells can drop down to fill the vacancy, meaning there are multiple transitions that occur, with each transition having its own specific energy. The three main lines produced are labelled K, L or M depending on which shell the electron initial drops down from (figure 2.8).<sup>[59]</sup>

Each element gives a characteristic emission spectrum composed of a set of sharp peaks. These peaks are different for each element due to the energy difference between the shells which is dependent on atomic number:

$$\lambda^{-1/2} = C(Z - \sigma)$$

(Equation 2.10)

Where C and  $\sigma$  are constants. Therefore, wavelength of lines decreases with increasing atomic number (Z) and the energy will increase.

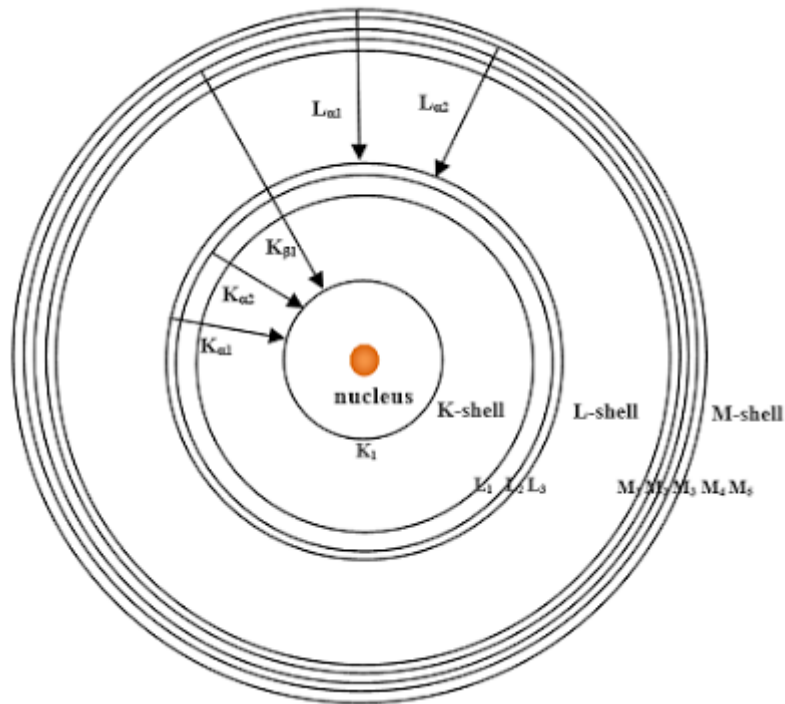


Figure 2.7 – Generation of XRF spectral lines.

Fluorescence can be measured using two systems, Wavelength Dispersive (WDXRF), which separates X-rays according to their wavelength, or Energy Dispersive (EDXRF), which directly measure the energy of the emitted X-rays from the sample.

In wavelength dispersive XRF all elements within the sample are excited simultaneously. The different characteristic energies emitted from the sample are diffracted in different directions along an analysing crystal or monochromator. By placing a detector at a certain angle, intensities can be measured. There are two types of detectors commonly used with WDXRF:

- Sequential Spectrometer – Move through an angular range with the use of a goniometer to measure intensities of many different wavelengths.
- Simultaneous Spectrometer – A fixed set of detection systems where each measures the radiation of a specific element.

In energy dispersive XRF again all the elements are simultaneously excited. An energy dispersive detector with a multi-channel analyser is used to collect fluorescence radiation directly from the elements within the sample. Both WD and ED XRF systems consist of a metal source, usually Rhodium, and a filament, usually tungsten wire. Thermal electrons are released from the filament and upon contact with the anode; Bremsstrahlung and characteristic X-rays of the anode are emitted and released through a beryllium window.

As the primary radiation penetrates into the sample it is absorbed, emitting characteristic X-rays which are then detected, forming the basis of an XRF spectrum. However, these characteristic X-rays can also be absorbed in the sample before reaching the detection system. Characteristic X-rays of higher energy can act to enhance intensity of lower energy X-rays. This phenomenon is referred to as Matrix effects and is separated into elastic or inelastic scattering.

#### 2.4.1: Laboratory Instrumentation

A Bruker Tracer IV-SD hand-held XRF used in this work utilises a 1kW Rh X-ray tube. The XRF uses a 10 mm<sup>2</sup> XFlash<sup>®</sup> solid state detector producing a resolution of 145 eV at 100,000 cps. Data were typically collected using a 25kV accelerating voltage.

## 2.5: Scanning Electron Microscopy (SEM) & Energy Dispersive X-ray Analysis (EDX)

Scanning electron microscopy (figure 2.9) is the primary method for obtaining information on specimen surfaces and morphology over a wide magnification range. SEM uses electrons to image the sample in a similar way as optical microscopes use photons, albeit at a much higher resolution. The electrons have wavelengths over 100,000 times smaller than that of visible light significantly increasing the resolution resulting in magnifications of up to 1,000,000x being achieved. Electron beams are accelerated through 1-200 kV with electric and magnetic fields used to focus the beam. When the electron beam interacts with the sample (figure 2.1.10), various signals are emitted from the surface and used to express different types of information.

As electrons interact strongly with matter, the thicker the samples are, the less transmission of electrons through the sample is likely. Therefore, in transmission mode, the samples are required to be much thinner than would be necessary in reflection mode. Higher voltage instruments (1 MV) can also be used if absorption of the electron beam is still occurring, as this high voltage beam will be much more penetrating. This will also help to reduce background scatter and produce higher resolution images at higher magnifications.

SEM in reflection mode covers the magnification range between the lower resolution limit of an optical microscope ( $\sim 1 \mu\text{m}$ ) to the upper limit of TEM ( $\sim 0.1 \mu\text{m}$ ). In reflection mode, it is important that samples are conductive in order to prevent a build-up of electrons on the surface resulting in a blurring of the image produced. It is therefore necessary to coat the

materials in a fine layer of metal, usual gold or carbon, in order to increase the conductivity on the surface.

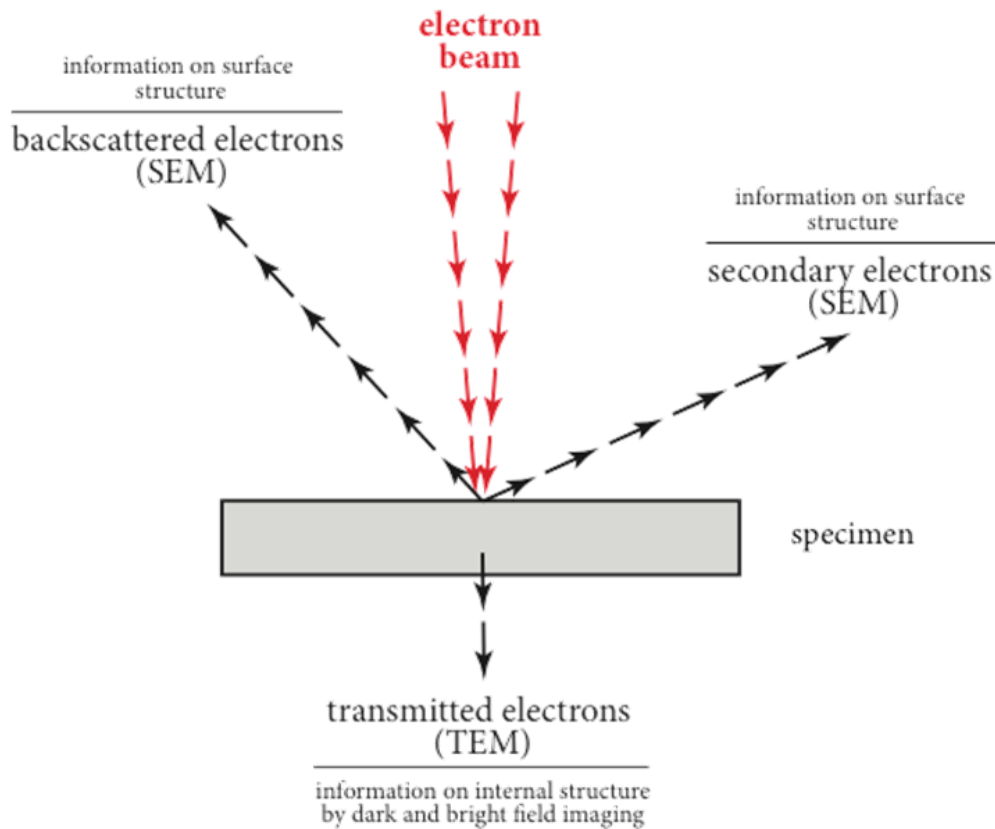


Figure 2.8 – Emission signals from an irradiated sample in SEM/TEM.

### 2.5.1: Electron Dispersive X-ray Analysis (EDX)

As well as imaging samples, the electron beam can also be used to quantify elemental composition of the sample. As the high-energy beam interacts with the sample, electrons within are excited and ejected. The difference between the ground state and excited state can be emitted as characteristic X-rays, allowing the identification of specific elements based on this emission.(figure 2.9)

Accuracy of an EDX spectrum however can be affected by several factors. Most elements have overlapping peaks, for example the Ti  $K_{\beta}$  and the V  $K_{\alpha}$  at 4.931 keV and 4.952 keV respectively, meaning that some basic understanding of elemental composition is imperative in the correct analysis of the results. In addition, the probability of an X-ray leaving the sample and being detected is dependent on the sample density.

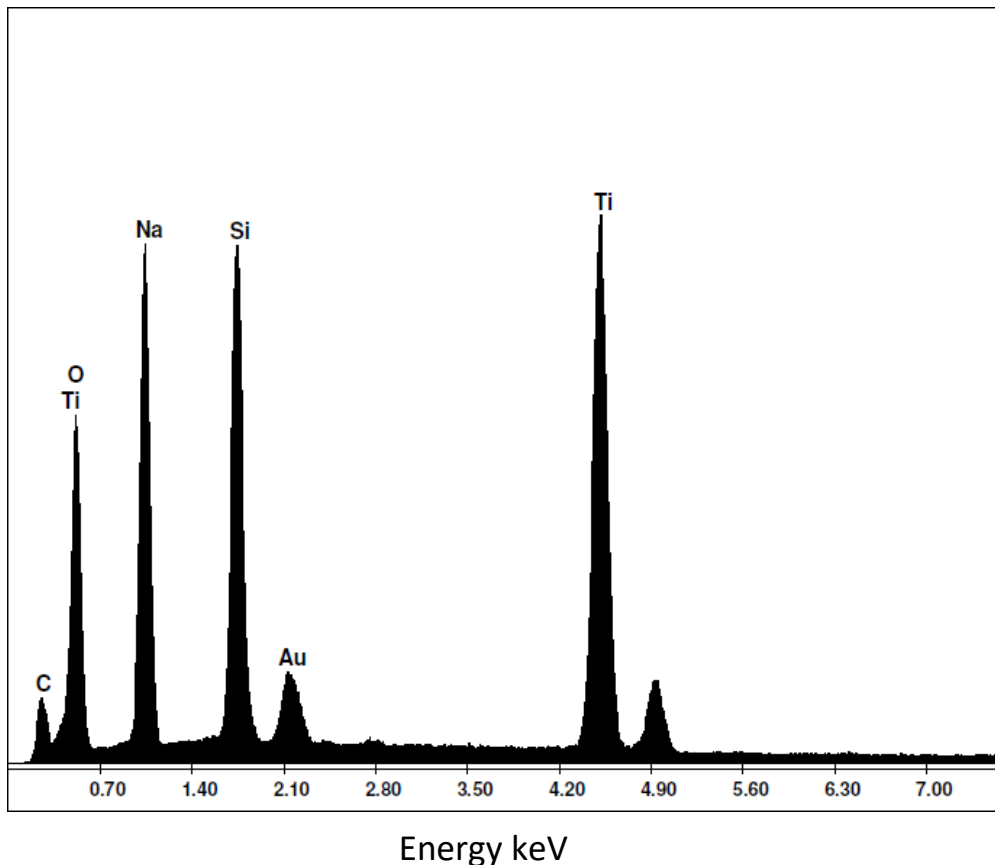


Figure 2.9 – Example of an EDX spectrum.

Samples that are inhomogeneous, dense or rough can scatter these X-rays in such a way that does not allow for their detection, reducing accuracy of the results. Also, the results can be affected by the resolution of the detector system.

## 2.5.2: Laboratory Instrumentation

A FEI Quanta 200 SEM and EDAX microanalysis EDX system was used in the work to determine surface morphology and elemental composition in atomic percent. A working distance of 10mm and spot size of 5 were used. The accelerating voltage was set to 20 kV and the samples splutter coated with gold to increase conductivity.

## 2.6: Inductively Coupled Plasma Mass Spectrometry (ICP-MS)

Inductively Coupled Plasma Mass Spectrometry (ICP-MS) is an analytical technique used to determine elemental concentrations within samples. ICP-MS is a combination two instruments, a high temperature ICP that converts the atoms of the elements in the sample to ions, which are then detected by a mass spectrometer.

Argon gas flows inside a narrow quartz tube surrounded by a radio frequency coil which, when power is supplied to the coil, oscillating magnetic and electric fields are

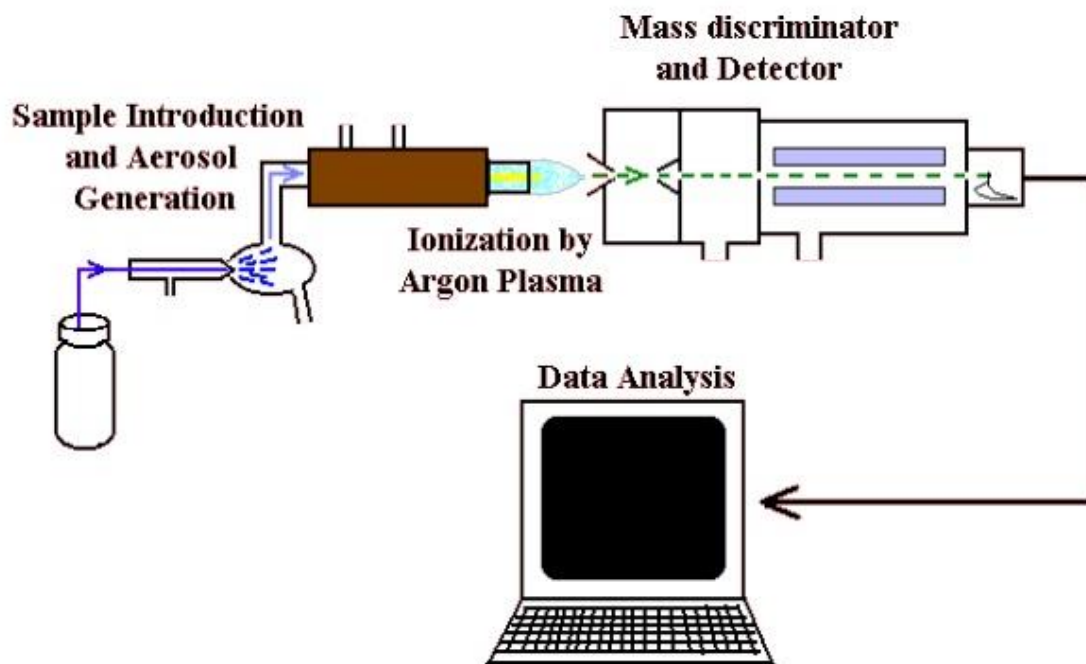


Figure 2.10 – Example of a typical ICP-MS schematic.

produced. A spark then causes the electrons to be stripped of the argon gas, forming argon ions, which are then caught by the electric and magnetic fields where they collide creating an argon discharge or plasma.

A sample is introduced into the ICP as an aerosol through the aspiration of a liquid. Once the aerosol is exposed to the plasma, it is completely desolvated leaving just the elements in the aerosol. These are then converted first into gaseous atoms and then ionised towards the end of the plasma. The ions are then sent to the mass spectrometer and separated by their mass-to-charge ratio. The intensity of emission is proportional to the amount of species present and can be used to measure concentration. However, the ICP-MS does not give a direct concentration, rather a calibration curve of known concentrations must be made with the unknown samples compared against it.

The ICP plasma temperature can be anywhere from 6000 K to 10,000 K meaning that even stable elements can be analysed. The plasma is an excellent source of ions but also tends to produce typically positive  $M^+$  or  $M^{+2}$  ions. It is for this reason that it is difficult to determine atoms that have a tendency to form negative ions (Cl, I, F etc.).

### 2.6.1: Laboratory Instrumentation

The Thermo Scientific X Series ICP-MS used in this work is a high signal-to-noise quadrupole ICP-MS providing precise analysis and quantification of trace elements in liquid samples. The concentration range investigated in this work was 0 ppm to 12 ppm range required the liquid samples to be diluted 200-fold before analysis using ICP-MS. Each sample was collected three times and the results averaged. The results were compared to a

calibration curve made up from a multi-element standard of known concentration of 1000 ppm used for Na, Ca, Ce, Co, Cs, K, Mg, Nd, Sr.

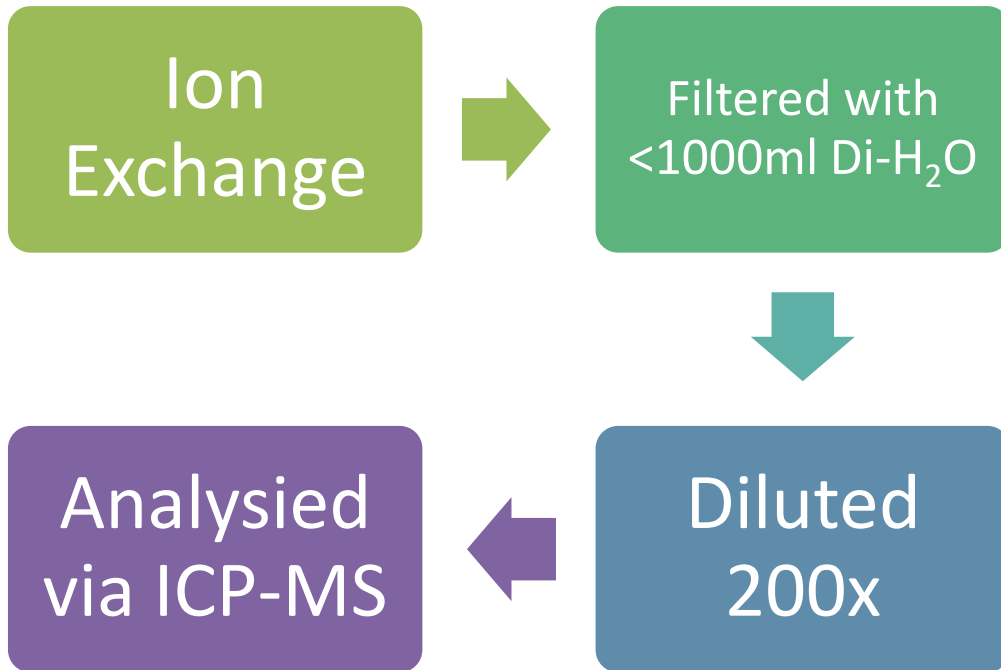


Figure 2.11 – ICP-MS sample preparation method.

# CHAPTER THREE

## *Synthesis and Characterisation of Natisite*

### 3.1: Introduction

Natisite, first discovered in 1975, is a naturally occurring mineral, mined from Kola peninsula, Russia and crystallises in the tetragonal (ditetragonal dipyramidal) space group  $P4/n m m$  with  $a = b = 6.4967(8) \text{ \AA}$  and  $c = 5.0845(11) \text{ \AA}$ .

The material is a layered titanium silicate where titanium is in an unusual square pyramidal coordination (Figure 3.1) included in a water-free framework. Usually titanium in crystalline oxygen containing materials forms a six-coordinate complex. The titanium coordination polyhedra consists of four Ti-O bonds at (1.990 Å) and one titanyl Ti=O bond at (1.695 Å). The corner sharing layers of SiO<sub>4</sub> tetrahedra and TiO<sub>5</sub> square pyramid extend in the *ab* plane and are separated by one crystallographically unique Na cation which compensates the charge. <sup>[60]</sup>

Much of the previous work conducted on this material has focused on the synthesis and characterisation. Peng *et al.* <sup>[61]</sup> investigated the Infrared absorption of natisite, showing sharp characteristic peaks of IR absorption at 725 and 624 cm<sup>-1</sup>. These peaks represent the internal vibration of the TiO<sub>5</sub> and SiO<sub>4</sub> structural units respectively.

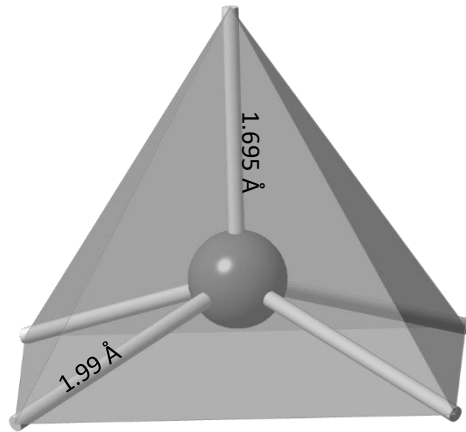


Figure 3.1 – Titanium in square pyramidal coordination, as found in the natisite structure.

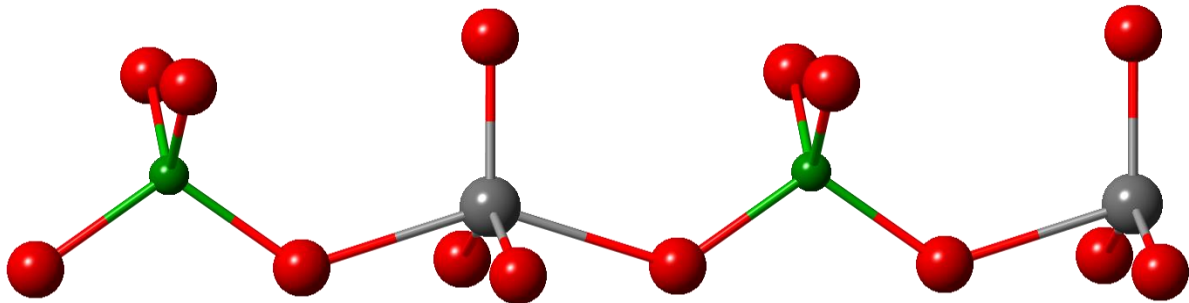


Figure 3.2 - Natisite chain showing coordination environments. Ti (purple), Si (cyan) O (red).

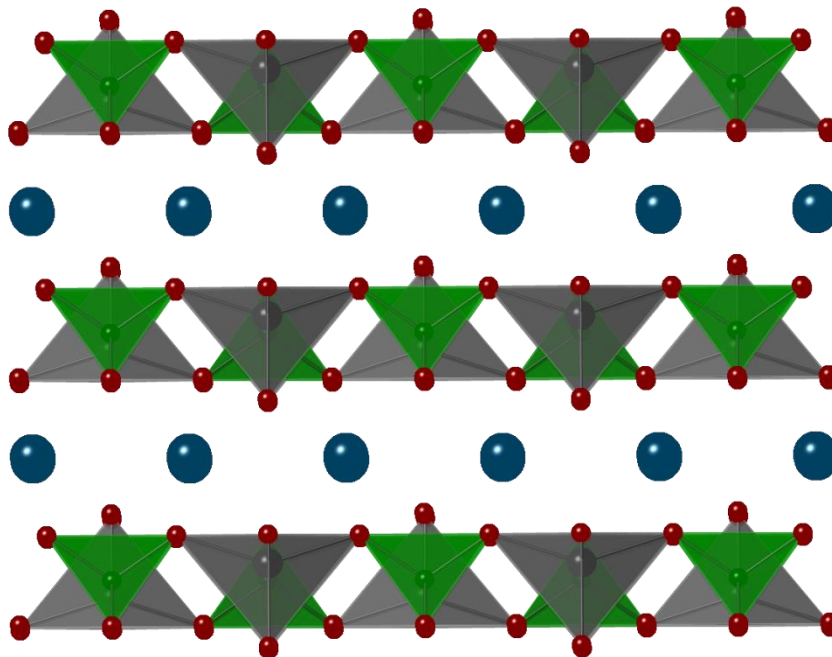


Figure 3.3 - Crystal structure of natisite. Corner sharing layers of  $\text{SiO}_4$  (green) and  $\text{TiO}_5$  (grey) extending in the  $ab$  plane are separated by charge balancing cations (blue).

## 3.2: Sample Preparation.

Natisite was synthesised hydrothermally modified from a previously reported procedure for the titanium silicate, sitinakite.<sup>[62]</sup> 3.3 g of sodium hydroxide (NaOH) was added to 25 ml of deionised water and stirred until all the NaOH had dissolved. To this solution, 2.28 g of titanium isopropoxide ( $\text{Ti}[\text{OCH}(\text{CH}_3)_2]_4$ ) was added along with 1.665 g of Tetraethylorthosilicate (TEOS). The resulting solution was stirred at ambient temperature for one hour. The solution was transferred into a 45 mL Teflon™ liner filled no more than 60% full at 200°C for 5 days. The resulting solution was cooled to room temperature with a white solid being collected after filtration and washing with copious amounts of deionised water until the pH dropped below eight.

## 3.3: Characterisation

### 3.3.1: Indexing and Unit Cell Refinement

The natisite sample was indexed from a 30-minute powder XRD pattern. Figure 3.4 shows the powder XRD pattern of phase pure tetragonal natisite with a peak match shown in table 3.1. The Bruker TOPAS<sup>[63]</sup> software package was used to perform Rietveld refinements of the observed pattern against the known structure reported by Nyman *et al.*<sup>[64]</sup> A summary of the results are showed in table 3.2. The final refinement shows a good agreement between the calculated and observed patterns, with a refined long Ti-O bond distance of 2.002 Å and short Ti-O bond distance of 1.687 Å. Both bond distances are slightly longer than those found in literature. The refined lattice parameters are now  $a = b = 6.48493(2)$  Å and  $c = 5.0936(2)$  Å. The  $ab$  parameter being slightly shorter than the literature value with the  $c$  parameter slightly longer.

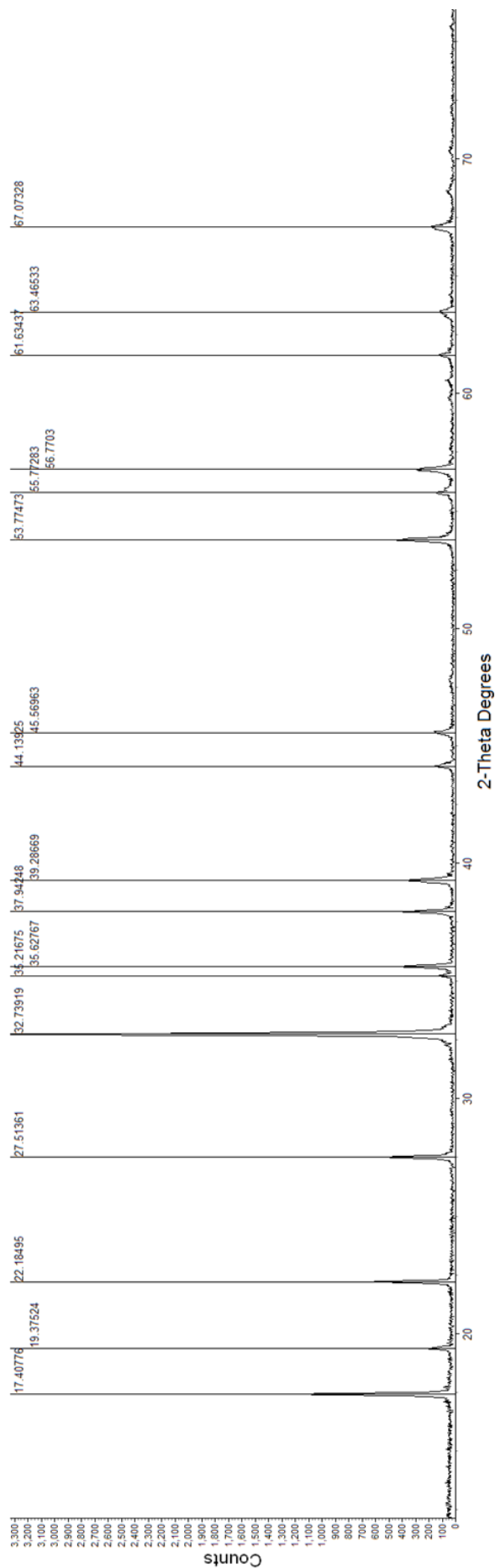


Figure 3.4 – Diffraction pattern of natisite with main peaks labelled with their corresponding 2-Theta value.

Table 3.1 – Peak list for as synthesised natisite with corresponding h k l, 2-theta and relative intensities values displayed.

<i>Peak</i>	<i>h</i>	<i>k</i>	<i>l</i>	<i>2-Theta</i> $\vartheta^\circ$	<i>Relative Intensity</i> %
1	0	0	1	17.38701	31.7
2	1	1	0	19.32859	6.4
3	0	1	1	22.16123	13.9
5	0	2	0	27.4676	18.2
6	0	2	1	32.69267	100
7	0	0	2	35.1913	1.6
8	2	1	1	35.57075	11
9	0	1	2	37.90314	6.7
10	2	2	0	39.23633	12.6
11	3	1	0	44.09562	4.4
12	0	3	1	45.51924	4.6
13	2	2	2	53.71686	11.4
14	0	3	2	55.69529	2.9
15	0	4	0	56.69559	9.6
16	0	2	3	61.5726	1.9
17	3	3	1	63.44663	3.5
18	4	2	1	67.00398	5.3
19	0	4	2	68.51118	1

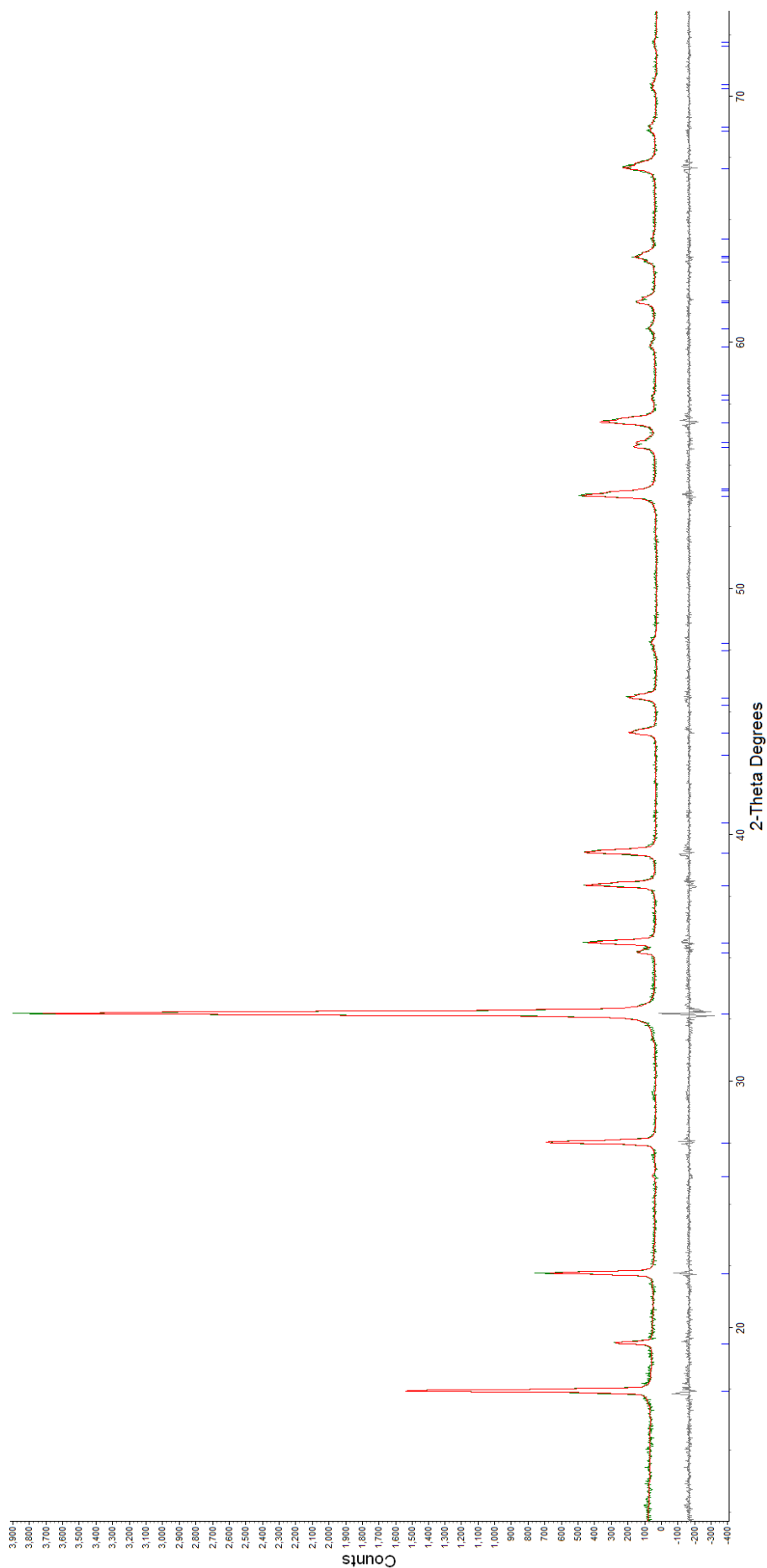


Figure 3.5 – Observed and calculated profiles for the Rietveld refinement of natisite, with the bottom curve showing the difference. Tick marks show calculated peak positions. Page | 60

Table 3.2 – Rietveld refinement of natisite.

<b>Atom</b>	<b><i>x/a</i></b>	<b><i>y/a</i></b>	<b><i>z/a</i></b>	<b>Fractional Occupancy</b>	<b><math>U_{iso}(x10^2)\text{\AA}^2</math></b>
<i>Ti</i>	0.5	0	0.9357 (6)	1	3.38 (11)
<i>Na</i>	0.25	0.25	0.5	1	4.05(15)
<i>Si</i>	0	0	0	1	2.80(12)
<i>O(1)</i>	0	0.20715(9)	0.1857(7)	1	2.78(13)
<i>O(2)</i>	0.5	0	-0.7332 (7)	1	2.24(26)

<b>Space Group</b>	<b>P4/nmm</b>
<i>a</i>	6.48493(2) Å
<i>b</i>	6.48493(2) Å
<i>c</i>	5.0936(2) Å
$\alpha$	90°
$\beta$	90°
$\gamma$	90°
Volume (Å <sup>3</sup> )	214.207519(14)
Formula Unit	Na <sub>2</sub> TiSiO <sub>5</sub>
Wavelength	1.54060 Å
2 $\theta$ range	5-80°
Step-Scan increment (2 $\theta$ ), deg	0.02°
Step-scan time, s	0.45
No of data point	3715
Profile Function	Pseudo-Voight
R <sub>wp</sub> %	12.807
R <sub>p</sub> %	9.407

Table 3.3 – Bond distances and angles of natisite.

<i>Bond</i>	<i>Distance Å</i>	<i>Angle°</i>
<i>Ti-O1</i>	<i>1.9984(35)</i>	<i>O1-Ti-O2 108.08(13)</i>
<i>Ti-O2</i>	<i>1.6885(95)</i>	<i>Ti-O2-Na 117.48(12)</i>
<i>Ti-Si</i>	<i>3.259(34)</i>	<i>Ti-O1-Si 125.310(58)</i>
<i>Ti-Na</i>	<i>3.192(22)</i>	<i>Ti-O1-Na 94.28(17)</i>

### 3.3.2: SEM EDX

SEM and EDX analysis was performed in order to determine the morphology and the elemental composition of the synthesised natisite sample. An image typical of the show sample is are shown in figure 3.6.

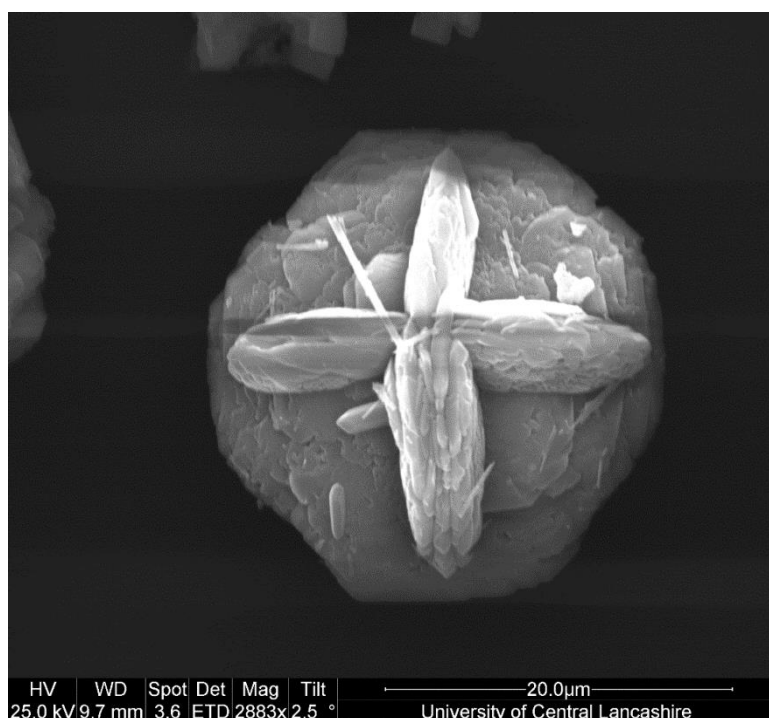


Figure 3.6 – SEM Image for natisite.

The SEM results at 2883x magnification shows microcrystalites of approximately 20µm with a protruding cross on the face. EDX was performed on figure 3.6 and the results shown in table 3.4.

The Si:Ti ratio is slightly higher than the ideal value of one could indicate the presence of a small impurity phase, which could not be distinguished in the XRD pattern. Also the Si:O ratio is again lower than the ideal value of 5 at 3.86.

Table 3.4 – Elemental composition acquired from EDX.

<i>Element</i>	<i>Measure Weight</i> %	<i>Measured Atom</i> %	<i>Measured Molar ratio</i> <i>(normalised to Si)</i>	<i>Molar ratio</i> <i>(expected)</i>
<i>Na</i>	19.18	23.41	1.95	2
<i>Ti</i>	27.68	16.22	1.35	1
<i>Si</i>	11.98	11.97	1	1
<i>O</i>	26.40	46.30	3.86	5

This can be explained by the relative inaccuracy of determining O content within the sample. The O signal is of low energy and therefore difficult to measure accurately. These results present here however are not observed by S. Ferdov<sup>[65, 66]</sup> where it was found that the morphology of natisite could be varied by the composition of the precursor gel. A different synthetic route was taken in the work presented by S. Ferdov, where TiCl<sub>4</sub> was used instead of Ti-isopropoxide, and a crystallisation time of 24 hours instead of the 120 hour crystallisation time used in this work.

Despite five different morphology's investigated by Ferdov's work, none matched the morphology found in figure 3.6. This indicates that the morphology is extremely susceptible to change not only through initial composition of the precursor gel but also through other experimental variables such as time and temperature.

### 3.3.3: Microwave Synthesis

Phase pure natisite can also be successfully synthesised under microwave irradiation after 18 hours. Figure 3.7 shows the diffraction pattern of the microwave and hydrothermally synthesised natisite.

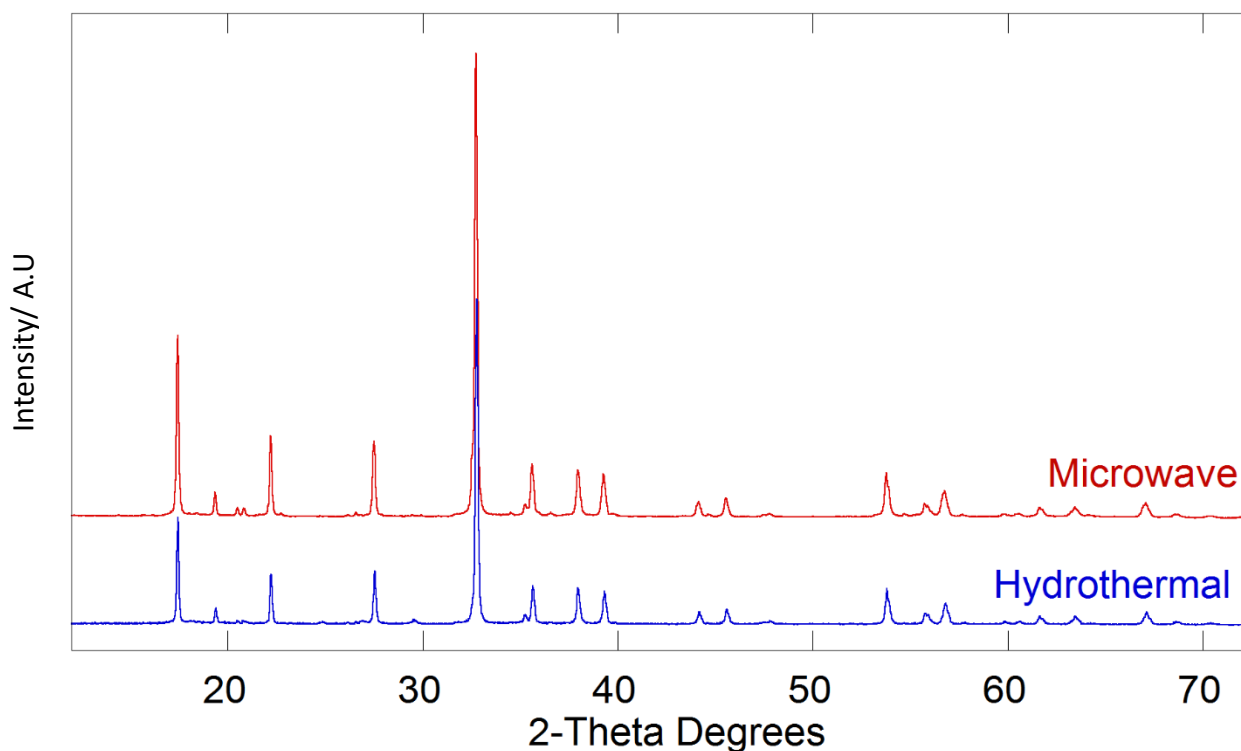


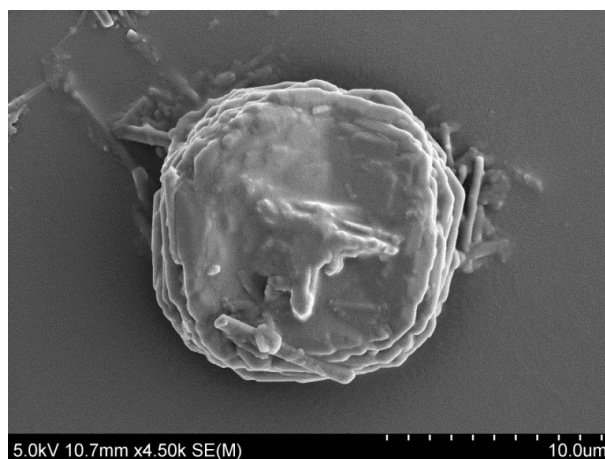
Figure 3.7 – Diffraction patterns of microwave and hydrothermally synthesised natisite.

The diffraction pattern of the microwave synthesised natisite sample is almost indistinguishable to that of the hydrothermal natisite sample. Table 3.4 shows the microwave synthesis times and resulting products formed. Before 6 hours an amorphous diffraction pattern is obtained. The formation of a multi-phase product appears as soon as 6 hours. From this we can already see the formation of paranatisite, a less thermodynamically stable precursor to natisite.

**Table 3.7 –Microwave synthesis times and resulting products formed.**

Synthesis Time	Product
1 hour	Amorphous
2 hours	Amorphous
4 hours	Amorphous
6 hours	Dihydrogen silicodititanate dehydrate [ $\text{H}_2\text{SiTi}_2\text{O}_7(\text{H}_2\text{O})_2$ ] + Paranatisite [ $\text{Na}_2(\text{TiO})\text{SiO}_4$ ] + Silicon Oxide [ $\text{SiO}_2$ ]
8 hours	Silicon Oxide [ $\text{SiO}_2$ ] + Dihydrogen silicodititanate dehydrate [ $\text{H}_2\text{SiTi}_2\text{O}_7(\text{H}_2\text{O})_2$ ]
10 hours	Natisite [ $\text{Na}_2\text{TiSiO}_5$ ] + Silicon Oxide [ $\text{SiO}_2$ ]
14 hours	Natisite [ $\text{Na}_2\text{TiSiO}_5$ ] + Silicon Oxide [ $\text{SiO}_2$ ]
16 hours	Natisite [ $\text{Na}_2\text{TiSiO}_5$ ] + Silicon oxide [ $\text{SiO}_2$ ]
18 hours	Natisite [ $\text{Na}_2\text{TiSiO}_5$ ]
20 hours	Sitinakite [ $\text{Na}_2(\text{Ti}_2\text{O}_3(\text{SiO}_4))(\text{H}_2\text{O})_2$ ]

As soon as 10 hours we can see that natisite is being formed along with a silicon oxide impurity. Heating for 14 hours and 16 hours produce a highly crystalline sample of natisite which is virtually indistinguishable from the reported ideal diffraction pattern. However, there is still some level of silicon oxide present. It is not until 18 hours that a phase pure natisite is obtained. Figure 3.8 shows the SEM image of microwave synthesised natisite. Further heating to 20 hours results in the formation of sitinakite.

**Figure 3.8 –Scanning electron micrograph of microwave synthesised natisite.**

The SEM image is similar again to that of hydrothermally synthesised natisite, with a uniform morphology of around 10  $\mu\text{m}$ . Despite not being fully formed there is also evidence of the protruding cross seen in the natisite samples. Further strengthening the argument that natisite can be successfully synthesised by microwave synthetic route.

### 3.4: Ion-Exchange

To date no ion-exchange work has been carried out on Natisite. In this part of the work, the ion-exchange selectivity and capacity for individual ions commonly found within nuclear waste streams, using natisite as an insoluble ion-exchanger was investigated. Firstly, ion-exchanges were conducted with ions at a neutral pH with no competing ions. These were conducted in order to determine the materials baseline affinity towards certain ions before changing conditions. These ions included;  $\text{Cs}^+$ ,  $\text{Co}^{2+}$ ,  $\text{Sr}^{2+}$  also,  $\text{Ce}^{4+}$ ,  $\text{Nd}^{3+}$  which were used as inactive surrogates for  $\text{Pu}^{3/4+}$  and  $\text{U}^{4/6+}$  respectively. Competitive ion-exchanges were also conducted with ions commonly found in water.  $\text{K}^+$ ,  $\text{Ca}^{2+}$ ,  $\text{Mg}^{2+}$  were chosen to act as competing ions in order to determine if natisite could selectively remove the ions of choice whilst leaving competing ions in solution. This will be discussed in a later chapter.

#### 3.4.1: Sample Preparation

A 0.1 M solution of each nitrate ion was prepared in 125 ml di-water at room temperature. Each solution was mechanically stirred at 300 rpm with the use of a glass coated magnetic follower. 0.5 g of natisite was added to the ion containing solution and left for a period of 18 hours. The resulting powder was collected by filtration and washed with copious amounts of di-water.

## 3.4.2: Analysis

### 3.4.2.1: XRD

XRD patterns of the single ion-exchanges is shown in figure 3.7 with Pawley phase fitting being performed on the ion-exchanged samples shown in table 3.5 and figure 3.8. There is a loss of crystallinity associated with the Ce-exchanged sample. There is a clear peak at  $27^\circ$  and a series of small, unresolved peaks at  $19.4^\circ 2\theta$  and  $44^\circ 2\theta$ . The  $h k l$  values of these peaks show the  $l$  value to be 0. Indicating that the layers of natisite remain intact, but the actual stacking of the layers was disrupted by the presence of the large  $Ce^{4+}$  ion. The  $Co^{2+}$  exchanged sample showed a high background associated with fluorescence of the sample due to the copper sourced X-ray beam. Despite the higher than normal background, changes in the diffraction pattern can be seen, showing that the uptake of  $Co^{2+}$  from solution has been successful. There was also the presence of an unusual green colour post Co-exchange suggesting the cobalt could be in an unexpected coordination environment. Similarly, this was the case with the  $Sr^{2+}$  and  $Nd^{3+}$  exchanges. No changes were observed in peak position or relative intensity in the  $Cs^+$  exchanged diffraction pattern, indicating there was little uptake of  $Cs^+$  ions from solution. This is further supported by the very small changes in the lattice parameters of the  $Cs^+$  exchanged sample. The largest changes in the lattice parameters seen by  $Co^{2+}$  and  $Nd^{3+}$  can be attributed to the lack of crystallinity. Figure 3.8 D shows three broad peaks, indicating small particle size, which do not fit to that of the natisite structure. These match to  $Nd(OH)_3$  [67] indicating that this Nd species is being formed from Nd nitrate used as the Nd source in this work.

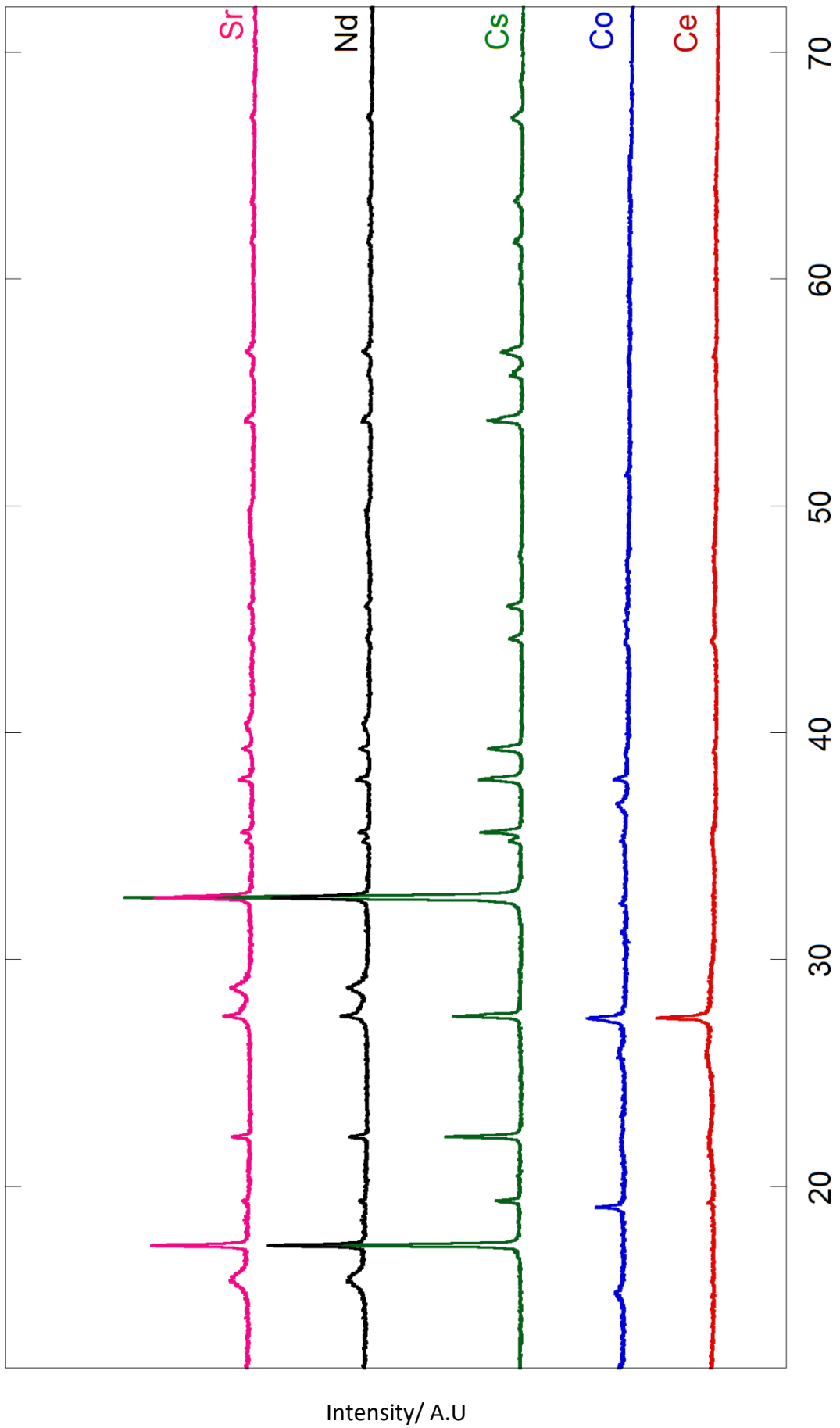
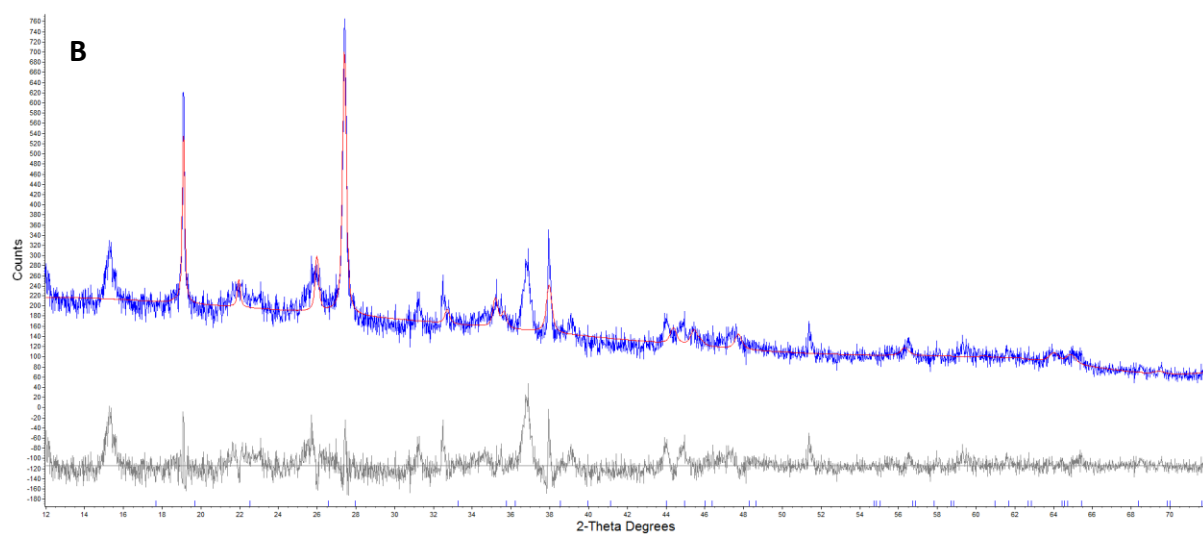
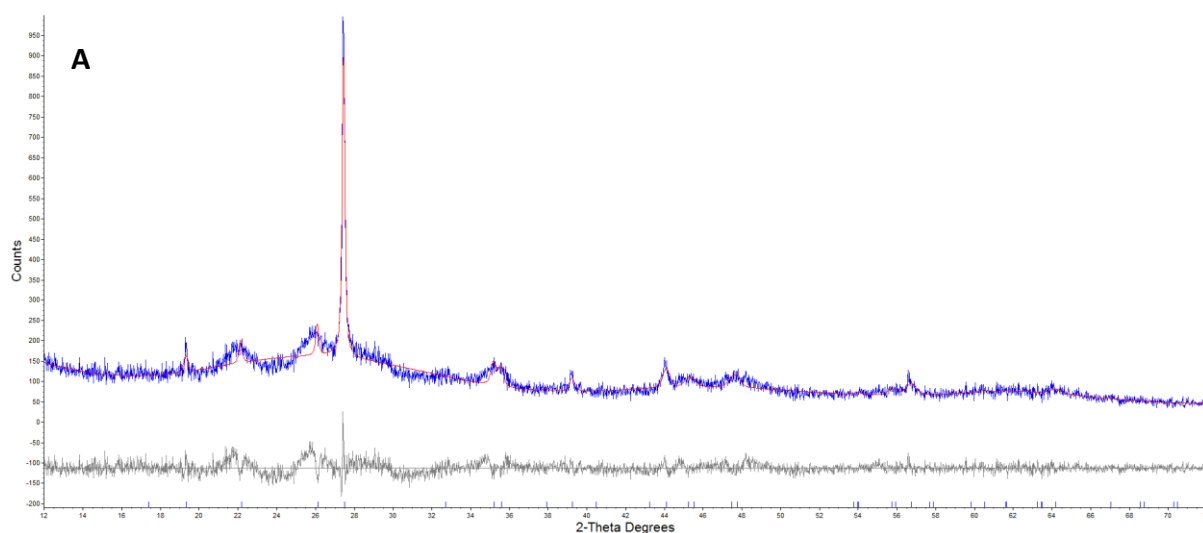


Figure 3.9 – XRD patterns of ion-exchanged natisite.

Table 3.6 – Pawley peak fitting of ion-exchanged natisite.

Ion	<i>ab</i>	<i>c</i>	RwP %	Difference to Synthesised Natisite	
				<i>a</i> /Å	<i>c</i> /Å
Natisite	6.4849(2)	5.0936(2)	12.807	-	-
Ce	6.4894(33)	5.0936(31)	11.085	0.0045	0.00003
Co	6.36744(29)	5.0146(19)	12.052	-0.11749	-0.07908
Cs	6.48323(2)	5.09316(4)	10.210	-0.0017	-0.00044
Nd	6.48059(7)	5.09498(10)	17.354	-0.00435	0.05537
Sr	6.4833(2)	5.0927(2)	9.766	-0.00164	-0.00091



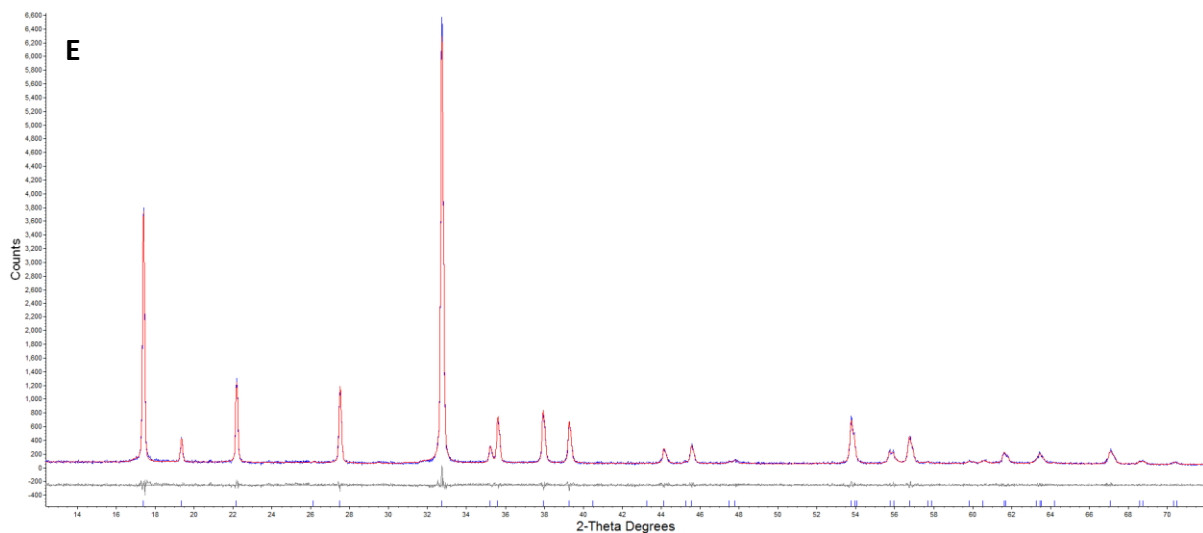
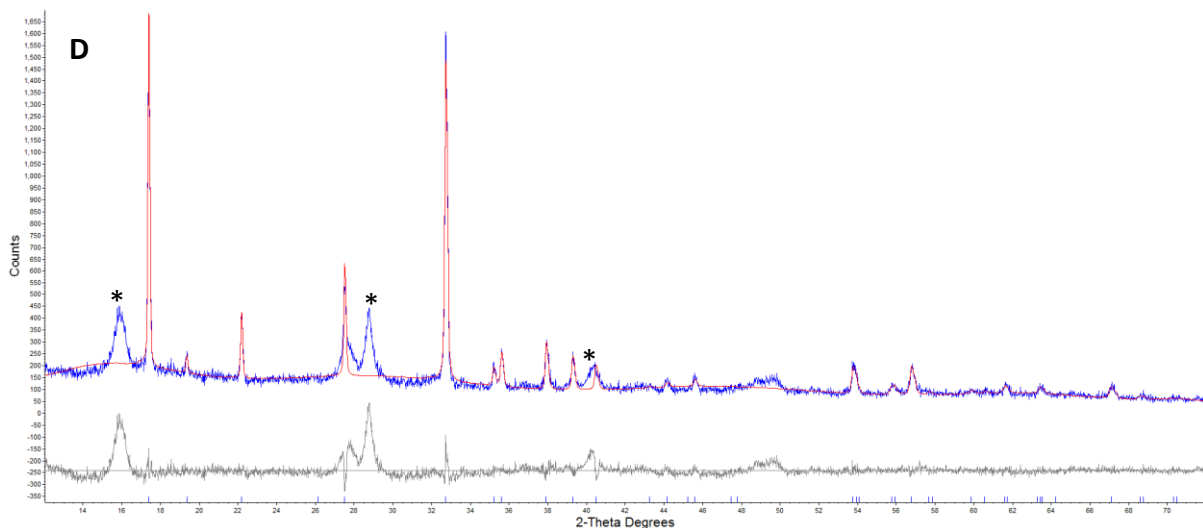
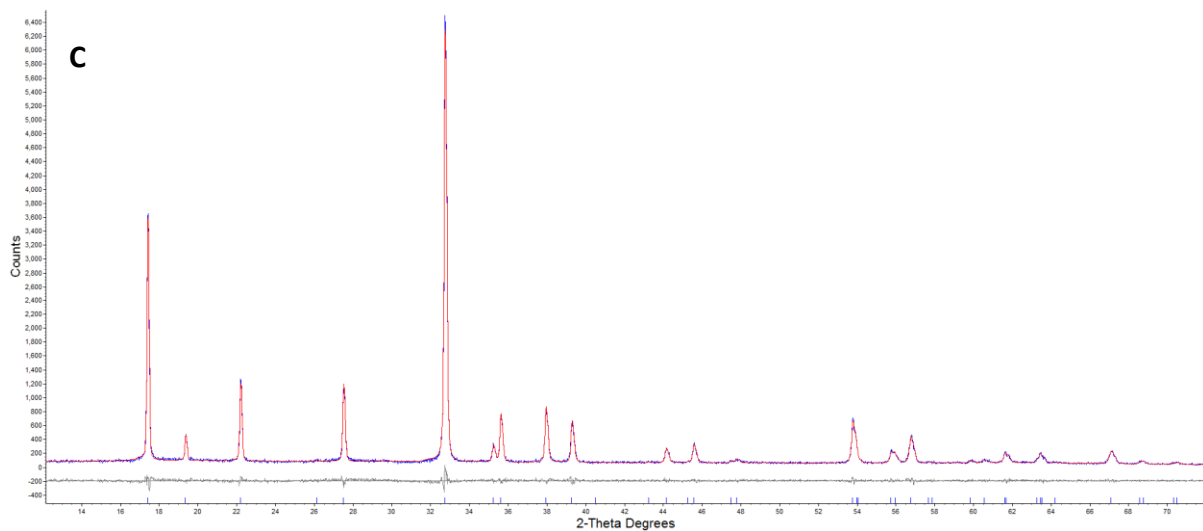


Figure 3.10 – Pawley peak fitting of (A) Ce (B) Co (C) Cs (D) Nd (E) Sr ion-exchanged natisite.

### 3.4.2.2: XRF

A bulk powder sample was placed in an XRF sample cup lined with Mylar film. The sample was run at 25 kV for 15 seconds at 20.0854 eV per channel. XRF was solely used as a qualitative technique in this work. The XRF spectrum (figure 3.10) shows a well-resolved peak at 4.51 keV, indicating the presence of Ti within the sample. Si (only visible in an inert atmosphere), Na and O are of too low energy to be seen in the XRF spectrum.

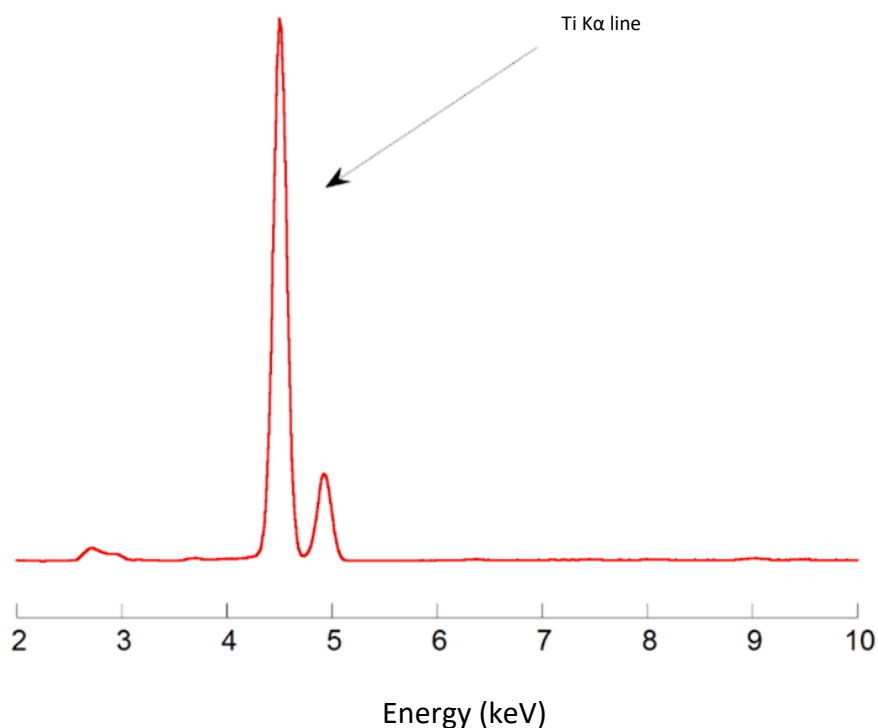


Figure 3.11 – XRF spectrum for natisite.

XRF provided qualitative results on the ion-exchanged samples shown in figure 3.12. The spectra show that each sample has successfully been exchanged. The XRF spectra show the presence of each of the ions indicating successful removal of the ions from solution with the exception of Cs. The Cs L line, located at 4.28 keV overlaps with the Ti K line at 4.51 keV. It was therefore difficult to determine by XRF alone if Cs ions had been taken up by the material. There is however, the presence of a shoulder on the Ti K line, which could be attributed to

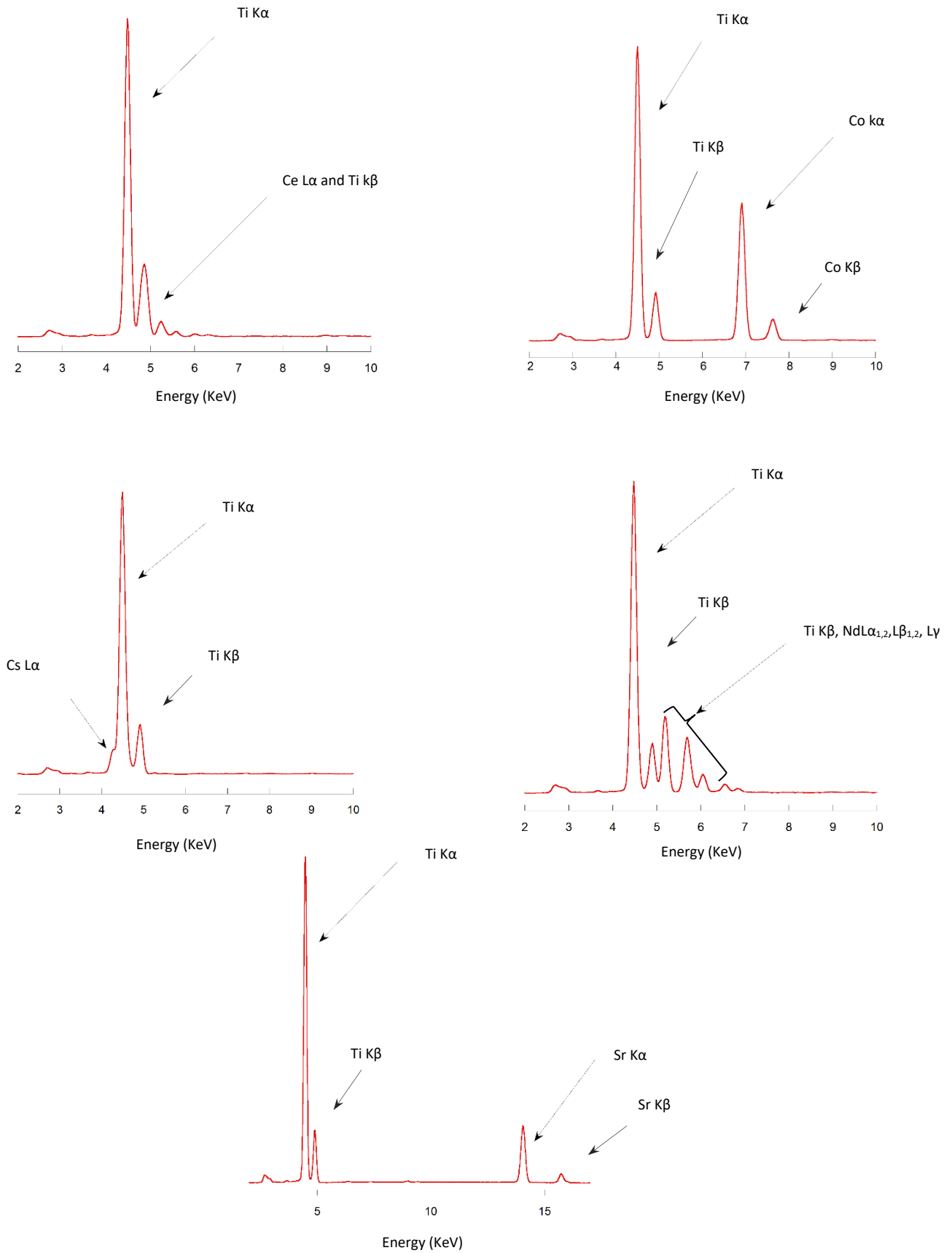


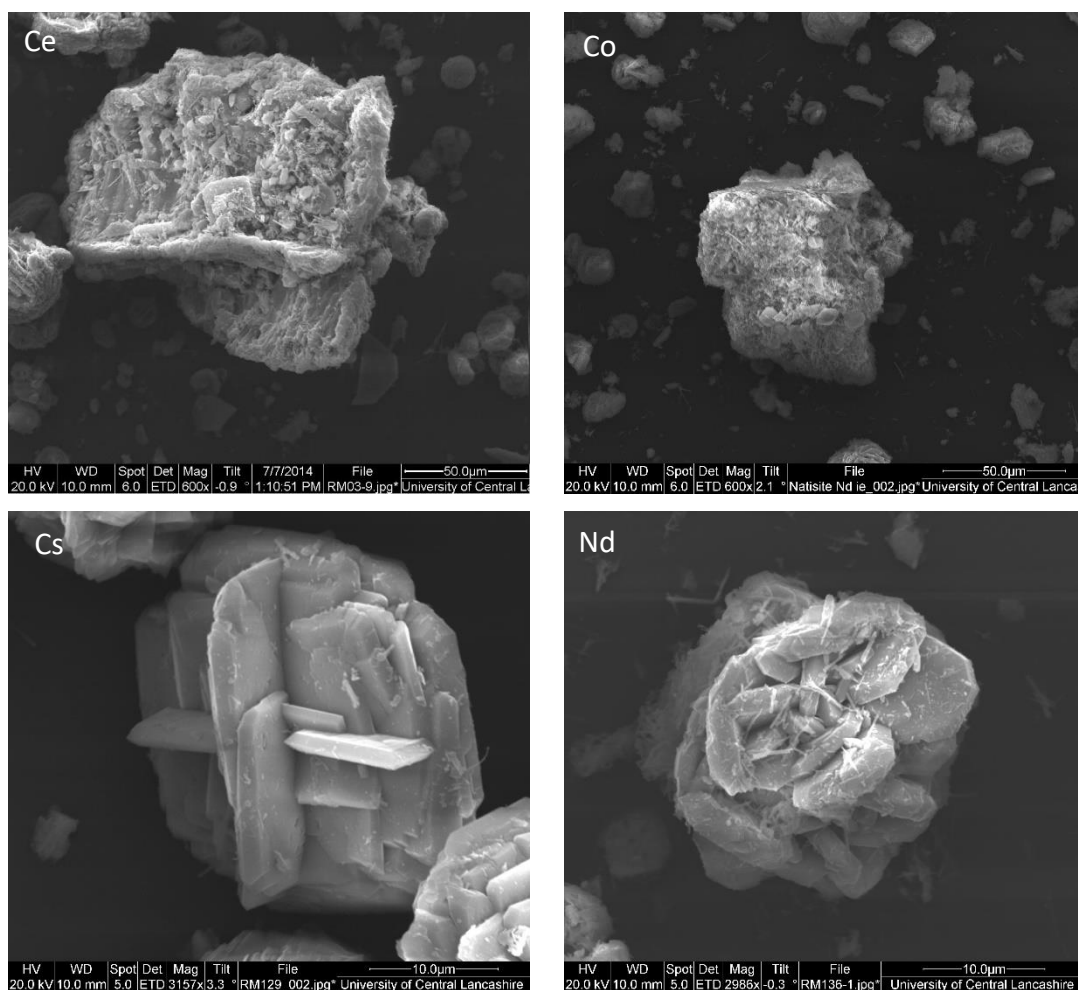
Figure 3.12 – XRF spectra for ion-exchanged natisite.

the Cs L Line. The XRF used in this work was unable to detect energies above 25 keV, therefore the Cs K line was unable to be investigated.

As there are very little changes in the Cs-exchanged diffraction pattern and lattice parameters, indicating low levels of exchange, we would not expect a large signal from the XRF.

### 3.4.2.3: SEM

SEM images were taken to determine changes in morphology associated with ion-exchange and are shown in figure 3.13.



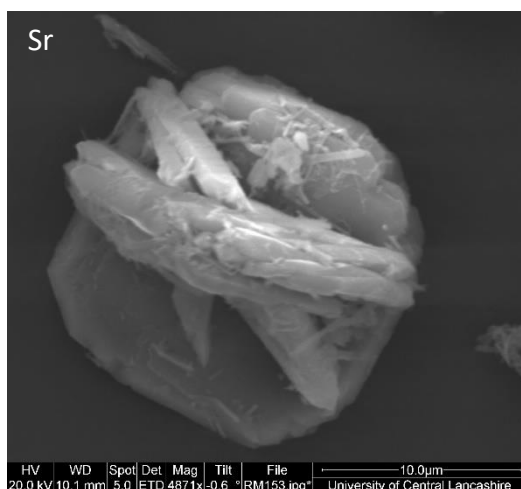


**Figure 3.13 – SEM micrographs of ion-exchanged natisite.**

The SEM images show differences in morphology post ion-exchange. Few differences are observed with the Cs ion-exchange, again indicating that natisite has a relatively low affinity towards Cs. More significant changes in morphology were seen with regards to Ce, Co and Sr, with a complete loss of particle morphology seen with Nd, which is in agreement with the XRD pattern loss of crystallinity. XRF and XRD both show clear differences compared to Na-natisite, showing again that ion-exchange had been successful.

#### 3.4.2.4: ICP-MS

In order to quantitatively determine the level of exchange of each ion, ICP-MS was performed on the waste solution post exchange. By knowing the initial concentration, the amount of liquid after filtration and the dilution factor from the ICP-MS, a percentage level of exchange can be calculated. Initial standards of known concentration were made up to produce a calibration curve showing in figure 3.14.

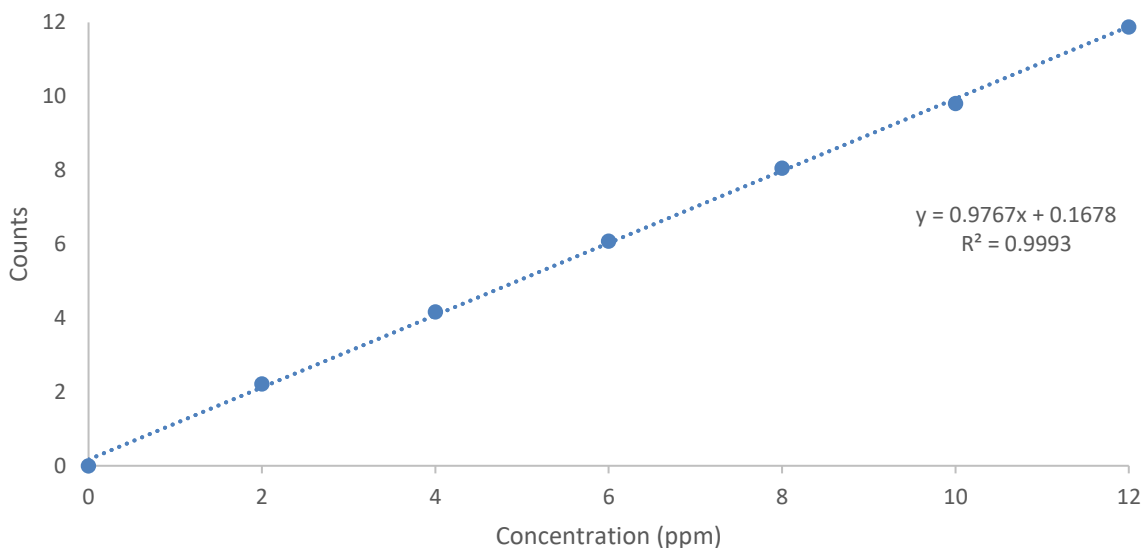


Figure 3.14 – Calibration curve for Na ion used for ICP-MS analysis.

By determining the maximum amount of moles of Na in natisite, we can therefore determine, in terms of moles, the maximum amount of exchange of each ion possible.

RMM of natisite:  $\text{Na}_2\text{TiSiO}_5$  ( $46 + 47.9 + 28 + (5 \times 16)$ ) = 201.9 g/mol. 0.5 g of natisite used per ion-exchange.

$$\frac{0.5}{201.9} = 2.476472.47647 \times 10^{-3} \text{ moles of natisite}$$

Have 2 x Na per mole of natisite therefore:

$$2 \times 2.47647 \times 10^{-3} \times 2 = 4.9529 \times 10^{-3}$$

$4.9529 \times 10^{-3}$  per 125 ml therefore:

$$4.9529 \times 10^{-3} \times 8 = 0.03962 \text{ M}$$

The maximum available Na to be exchanged is therefore 0.03962 M.

The results obtained from the ICP-MS are reported in parts per million (PPM), it is therefore necessary to convert PPM into M in order to calculate % exchange.

$$ppm = mg/L$$

Worked example for Ce exchange:

Na concentration from ICP-MS = 0.447

$$ppm = mg/l \rightarrow 0.447 \text{ mg/l of Na}$$

RAM of Na = 23 g/mol

$$\frac{0.447}{23 \times 1000} = 1.9434 \times 10^{-5}$$

Sample was diluted 200 fold in order to be analysed by the ICP-MS. Sample had a total volume of 660 ml before analysis.

$$1.9434 \times 10^{-5} \times 200 = 0.00388 \text{ M in } 660 \text{ ml}$$

$$C_1 \times V_1 = C_2 \times V_2$$

$$0.00388 \text{ M} \times 660 \text{ mL} = C_2 \times 125 \text{ mL}$$

$$C_2 = \frac{0.003887 \times 660}{125} = 0.0205 \text{ M Na}$$

$$\frac{0.0178}{0.03962} \times 100 = 51.7 \% \text{ Exchange}$$

Table 3.7 –Calculated percentage ion-exchange from ICP-MS results of Ti-natisite.

Ion	ppm of Na released from natisite	Percentage exchange/ %
Ce	0.447	52
Co	0.167	19
Cs	0.03	4
Nd	0.229	27
Sr	0.046	6

When analysing the level of ion-exchange, it is important to remember that the ions will be replacing the Na which has a +1 charge. Therefore Ce<sup>4+</sup> will replace four Na<sup>+</sup> ions upon exchange. Co<sup>+</sup> and Sr<sup>+</sup> will replace two Na<sup>+</sup> with Nd<sup>+</sup> and Cs<sup>+</sup> replacing three and one Na<sup>+</sup> respectively. Therefore, upon analysis of results obtained from the ICP-MS results are doubled, tripled or quadrupled depending on the charge of the ion.

From the results, we can determine an order of affinity. Cs < Sr < Co < Nd < Ce. Natisite has the highest affinity for Ce by removing 52% of the Ce from the solution. This is supported by the strong signal in the XRF and causing a complete loss of long range order with the XRD pattern. Cs and Sr have a lowest levels of exchange at 4% and 6% respectively. This is again supported by the XRD data showing little changes post exchange.

### 3.5: Summary

Crystalline natisite,  $\text{Na}_2\text{TiSiO}_5$ , can be successfully synthesised using hydrothermal methods without the presence of impurity. Synthesis of the material was investigated using XRD, XRF, SEM, EDX and Rietveld refinement all of which provided a good agreement with previously published work, with the exception of SEM where the morphology was slightly different.

From the ion-exchange studies, it was found that Ce had the highest affinity, this was despite the complete lack of crystallinity in the XRD patterns. This lack of crystallinity is associated with the large  $\text{Ce}^{4+}$  ions causing faults in the way the layers stack. This is supported by XRD in the way that  $h k 0$  peaks are present. The lowest affinity was towards Cs and Sr, the lack of changes in the XRD pattern supported the low percentage exchange results obtained from the ICP-MS.

SEM images showed that morphology remains fairly consistent with that seen with natisite with the exceptions of Ce, Nd and Co.

After 18 hours, the highest level of exchange was 52%. The optimisation of ion-exchange conditions still needs to be investigated further in order to determine the maximum level of exchange possible.

# *CHAPTER FOUR*

## *Synthesis and Characterisation of Zirconium Doped Natisite*

### 4.1: Introduction

As previously stated, no previous work had been carried out on the structural modification of natisite. Inspiration for this work was drawn from the material Sitinakite,  $\text{KNa}_2\text{Ti}_4\text{Si}_2\text{O}_{13}(\text{OH})\cdot 4\text{H}_2\text{O}$ , where unmodified, the materials selectivity towards Cs was low. When the framework was substituted with 20% Nb in place of Ti, the presence of this Nb not only altered the framework charge but also altered the shape and size of the pores in such a way that increased the materials affinity towards Cs and Sr. It was hoped that by modifying the framework of natisite by substituting in another metal in place of titanium, the order of affinity towards certain ions could be changed and tailored for use within the nuclear industry.

In this work, Zr was chosen to substitute for Ti in the framework, as the slightly larger metal ion of Zr with the same oxidation state should affect the structure of the layers in such a way that the materials ion-exchange chemistry is altered without changing the charge balancing. Understanding how the introduction of Zr into the framework effects the materials ion-exchange chemistry is crucial. The ability to tailor an ion-exchange material to a specific application will depend on a thorough understanding of the materials ion-exchange chemistry. Also, as Zr is less expensive than Nb (used in the synthesis of the industrially used

IONSIV-911®), if the material was to be ever adopted commercially, the financial benefits of a cheaper dopant metal would be advantageous.

## 4.2: Sample Preparation

A 10% Zr and 20% Zr natisite containing sample were synthesised hydrothermally using the procedure detailed in chapter three, with calculated amounts of Zr added and Ti removed in order to achieve the desired level of doping.

## 4.3: Characterisation

### 4.3.1: Unit Cell Refinement

Both the 10% and 20% containing sample were indexed from a 30-minute powder XRD scan. Figure 4.1 shows the powder XRD pattern of natisite, 10% Zr-natisite and 20% Zr-natisite.

The Bruker TOPAS software package was used to run Pawley refinements of the observed pattern against the pattern of Rietveld refined synthesised natisite, detailed in chapter three. A summary of the results are shown in table 4.1. The Pawley fit shown in figure 4.2 shows an overall good agreement with the natisite structure. There are now several additional peaks which do not match to that of natisite. These additional peaks can be attributed to a zirconium containing impurity phase,  $\text{Na}_2\text{ZrSiO}_5$  [68] (labelled \*) which is not believed to have a significant effect on the ion-exchange chemistry. However, changes in the relative intensities and slight changes in peak positions indicate that some zirconium has successfully been doped onto titanium sites within the natisite structure.

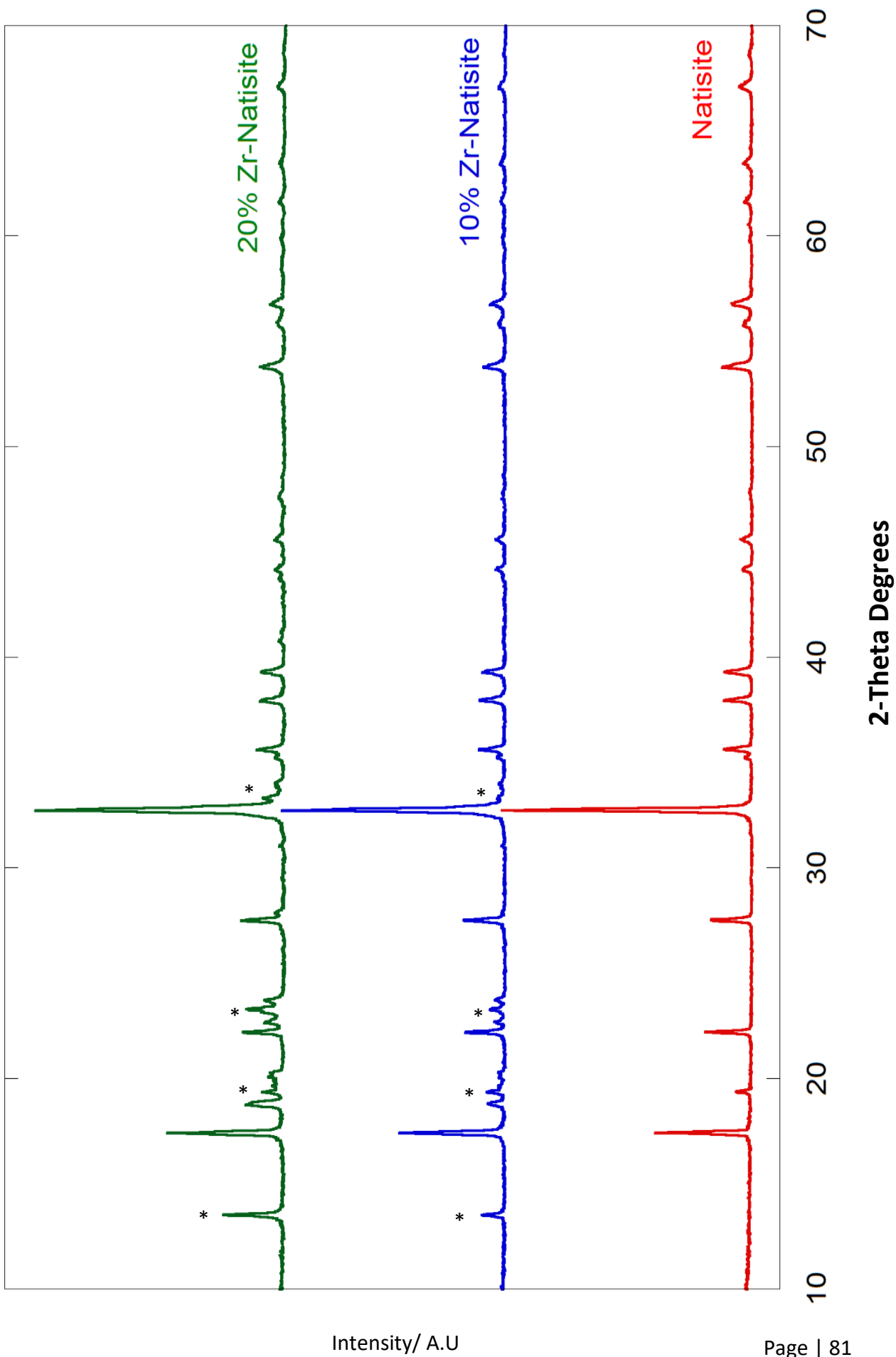


Figure 4.1 – XRD patterns of 10% and 20% Zr-doped natisite.

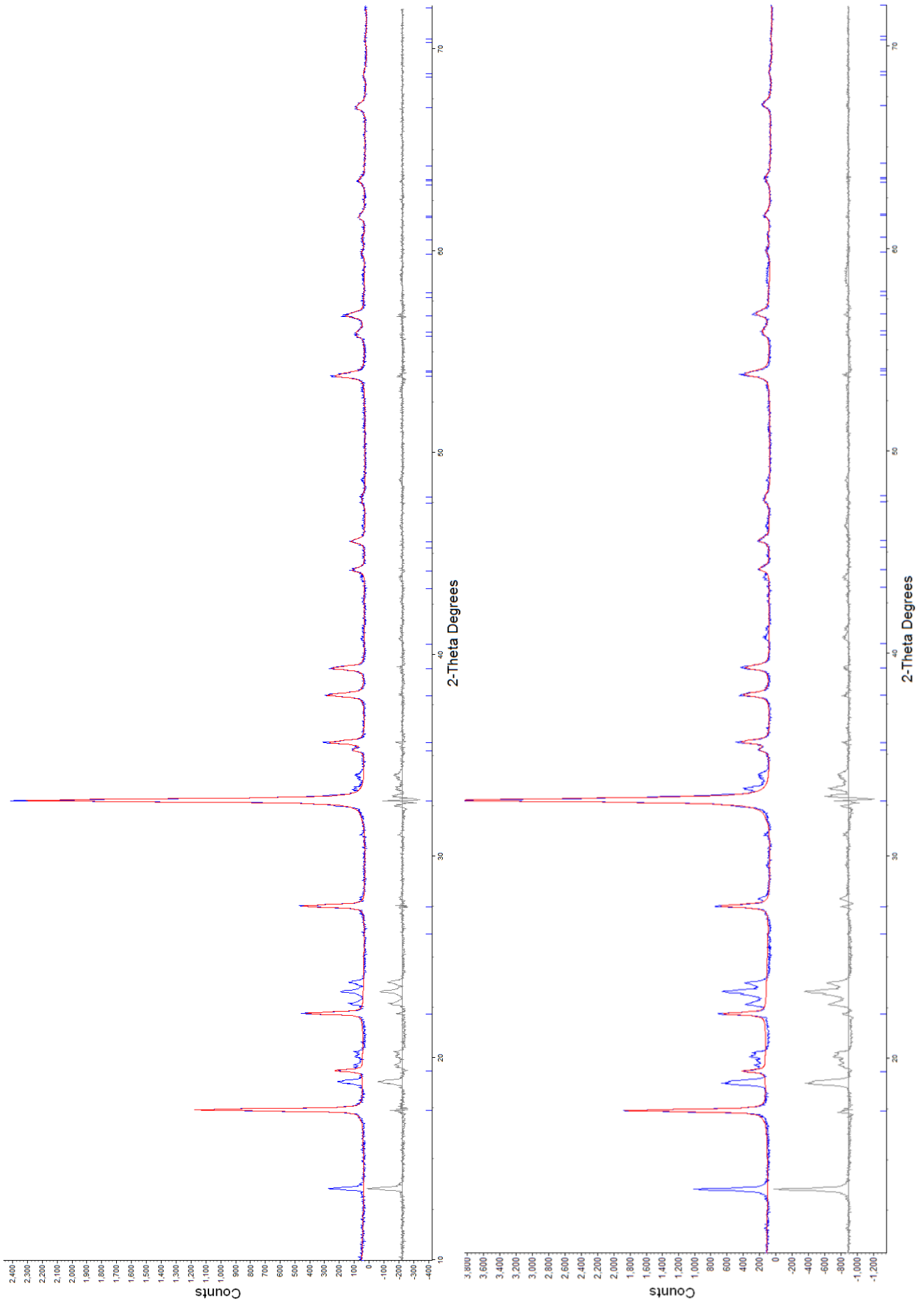


Figure 4.2 – Observed and calculated profiles for the Pawley refinement of 10% Zr (top) and 20% Zr Natisite (bottom), with the bottom curve showing the difference. Tick marks show calculated peak positions.

Table 4.1 – Pawley refinement of 10% Zr and 20% Zr Natisite.

Parameters	10% Natisite	20% Natisite
Space Group	<i>P4/nmm</i>	<i>P4/nmm</i>
<i>a</i>	6.4838 (5)Å	6.4825 (5)Å
<i>b</i>	6.4838 (5)Å	6.4825 (5)Å
<i>c</i>	5.0917 (7)Å	5.0933 (14)Å
$\alpha$	90°	90°
$\beta$	90°	90°
$\gamma$	90°	90°
Volume (Å <sup>3</sup> )	214.0504 (46)	214.03 (86)
Wavelength (Å)	1.54060	1.54060
2 $\theta$ range	5-80°	5-80°
Step-Scan increment (2 $\theta$ ), deg	0.02°	0.02°
Step-scan time, s	0.45	0.45
No of data points	3715	3715
Profile Function	Thompson-Cox-Hastings	Pseudo-Voight
R <sub>wp</sub> %	23.124	27.304
R <sub>p</sub> %	15.535	18.304

Table 4.2 – Peak list with corresponding h k l, 2-theta and relative intensities values displayed.

<i>Peak</i>	<i>h</i>	<i>k</i>	<i>l</i>	<i>2-Theta <math>\theta^\circ</math></i>	<i>Relative Intensity % (Natisite)</i>	<i>Relative Intensity % (10% Zr Natisite)</i>	<i>Relative Intensity % (20% Zr Natisite)</i>
1	0	0	1	17.38701	31.7	43.1	49.8
2	1	1	0	19.32859	6.4	5.8	7.5
3	0	1	1	22.16123	13.9	17.5	17.4
5	0	2	0	27.4676	18.2	16.7	19.1
6	0	2	1	32.69267	100	100	100
7	0	0	2	35.1913	1.6	2.4	2.4
8	2	1	1	35.57075	11	13	11.2
9	0	1	2	37.90314	6.7	11.8	9.7
10	2	2	0	39.23633	12.6	9.8	10.9
11	3	1	0	44.09562	4.4	2.9	4.2
12	0	3	1	45.51924	4.6	4.4	3.2
13	2	2	2	53.71686	11.4	9.5	10.3
14	0	3	2	55.69529	2.9	2.1	2.4
15	0	4	0	56.69559	9.6	4.5	5.7
16	0	2	3	61.5726	1.9	1.9	2.4
17	3	3	1	63.44663	3.5	2.5	1.4
18	4	2	1	67.00398	5.3	3.1	3.4
19	0	4	2	68.51118	1	1	1

### 4.3.2: SEM EDX

SEM and EDX analysis was performed in order to examine the morphology (figure 4.3) and determine the elemental composition of the Zr doped natisite samples. Compositional results are shown in table 4.3 and 4.4.

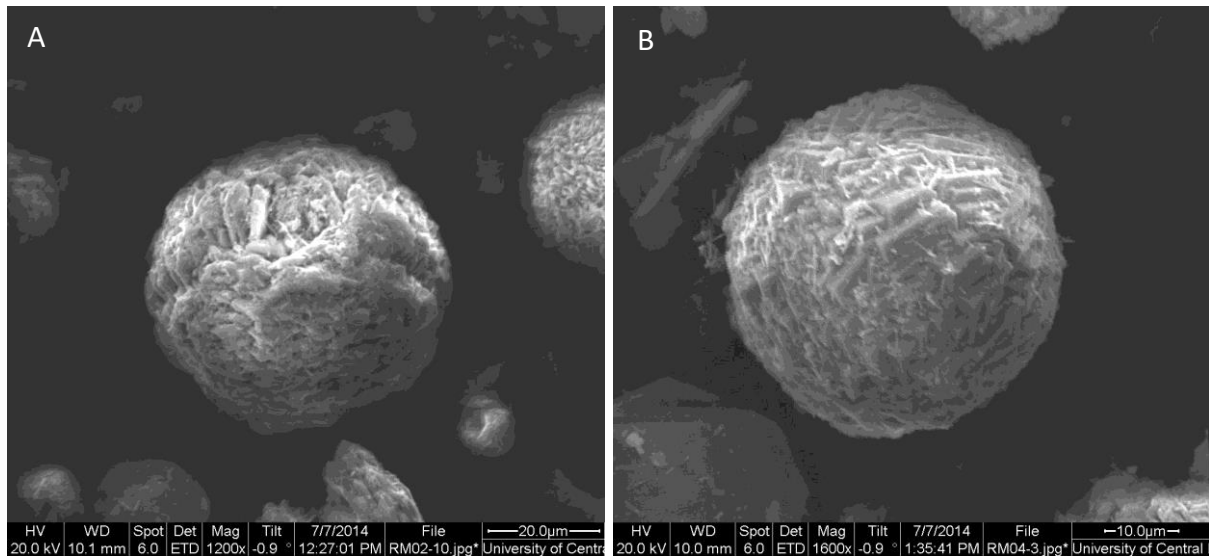


Figure 4.3 – SEM Image of (A) 10% and (B) 20% Zr-doped natisite.

The results for 10% Zr natisite at 1200x magnification shown in figure 4.3 shows spherical microcrystalites around 40 $\mu$ m to 60 $\mu$ m in diameter. This is larger than the original natisite (of approximately 20 $\mu$ m) indicating the presence of zirconium has had an effect on crystal growth and morphology. Again the 20% Zr containing sample at 1600x magnification is around 45 $\mu$ m in size. The distinctive protruding cross seen in the pure Ti-natisite has also been lost with the inclusion of Zr. As stated in chapter three, and supported by findings from Ferdov <sup>[65]</sup> the experimental procedure from the synthesis of natisite has a significant impact on morphology. One could assume that modification of the composition would alter the morphology of both the 10 and 20% samples significantly, which has been observed here and is further evidence that some Zr has been included in the natisite framework.

Table 4.3 – Elemental composition of 10% Zr- natisite acquired from EDX.

<i>Element</i>	<i>Measured Weight %</i>	<i>Measured Atom %</i>	<i>Molar ratio (expected)</i>	<i>Measured Molar ratio (Normalised to Si)</i>
<b>Na</b>	18.65	21.58	2	1.94
<b>Ti</b>	20.51	9.46	0.9	0.85
<b>Si</b>	14.13	11.12	1	1
<b>O</b>	47.80	66.03	5	5.93
<b>Zr</b>	2.09	0.98	0.1	0.08

Table 4.4 – Elemental composition of 20% Zr- natisite acquired from EDX.

<i>Element</i>	<i>Measured Weight %</i>	<i>Measured Atom %</i>	<i>Molar ratio (Expected)</i>	<i>Measured Molar ratio (Normalised to Si)</i>
<b>Na</b>	19.18	24.14	2	2.05
<b>Ti</b>	17.11	8.96	0.8	0.76
<b>Si</b>	13.14	11.73	1	1
<b>O</b>	41.09	64.41	5	5.49
<b>Zr</b>	8.35	2.29	0.2	0.19

### 4.3.3 XAS

X-Ray absorption spectroscopy was used to examine coordination environments and bond distances around both Ti and Zr atoms. XRD showed differences in diffraction patterns with increasing Zr doping. However, it was unable to provide detailed information on local coordination environments of Zr within the sample, as it is a long range order technique . It

was therefore necessary to use a local order technique to determine if there was any ordering of Zr in the framework or if it was randomly distributed, what the likely coordination environment was and finally the effect on the Ti environment.

#### 4.3.3.1: Experimental Parameters

XAS experiments were carried out at Diamond Light Source on beamline B18. As the elements to be investigated were in high concentration, the absorption measurements were carried out in transmission mode using ion chambers as detectors. Carefully calculated amounts of the powdered samples were thoroughly mixed with cellulose, used as a binding agent. The samples were then pressed into 13 mm pellets. For the Ti K edge measurements, a scan range of 4820 – 5816 eV, step size of 0.25 eV was used. The time for each scan was 173 seconds and each sample was collected three times and averaged post data collection using the Athena software.<sup>[58]</sup> For the Zr K edge measurements, a scan range of 11798 – 19300 eV and step size of 0.5 eV was used. Again, each sample was collected for 173 seconds, collected three times and averaged post data collection.

#### 4.3.3.2: XAS Results

Figure 4.4 shows the Ti-edge XAS spectra of natisite, 10% Zr and 20% Zr doped natisite. Background removal was performed prior to analysis. Also, the data was truncated at 5500 eV in order to extract statistically relevant data for further analysis. There is a distinctive pre edge feature (labelled A) for titanium located at 4968 eV and is characteristic of a titanium atomic coordinated to and oxygen and has been previously reported in literature.<sup>[69]</sup> However, despite this pre-edge feature commonly being used to identify tetrahedrally coordinated titanium with oxygen, it still remains present with the square pyramidal complex

seen in this material at a slightly lower energy, as supported by findings from P. Behrens *et al.* [70] who found square pyramidal coordinated Ti in the fresnoite structure at approximately 4 KeV, again lower than the 4.5 KeV found in tetrahedrally coordinated Ti in Ba<sub>2</sub>TiO<sub>4</sub> for example.[70]

This pre-edge feature decreases in amplitude with increasing Zr substitution, there is also a slight change in energy. This suggest a change in co-ordination number or potentially a change in the titanium oxidation state. This indicates that Zr is located within the Ti silicate layers, but that the presence of the slightly larger Zr atom is changing the co-ordination or geometry around Ti. Performing a Fourier transform on the spectra, gives information on coordination shells and interatomic distances. Figure 4.5 shows the Fourier transforms of the data presented in figure 4.4. Examination of this shows no discernible changes within the first shell, meaning that the short Ti-O bond remains unchanged albeit at a slightly shorter experimentally observed distance of 1.62 Å compared to the literature value of 1.69 Å.[71] Changes however are observed in the second shell and further out, indicating that the Ti-O-Si linkage is changing due to the inclusion of Zr. The pure natisite form and 10% Zr-doped form look similar before a switch to a new geometry indicated by the increase in amplitude of the second shell peak. The difference in the second shell radial distances can be attributed to the increase in the size of the Zr radii, reducing the oxygen bond angle.

The data for the Zr-edge again had the background removed and was truncated at 18499.81 eV. The Zr edge XANES profile are in good agreement to octahedrally coordinated Zr reported in literature.[72-75] The spectra show no notable differences between 10% and 20% doped samples. This suggests that the level of exchange does not alter the coordination or geometry around the zirconium. Work presented by G. Mountjoy *et al.* [73] however showed

that increasing Zr content should cause asymmetry in the Zr XANES profile, something of which has not been experimentally observed in this work. However, this could be due to the relatively small increase in Zr content. Increasing the Zr content further could cause this to occur. Very few changes are again observed in the XANES region and Fourier transformed data (figures 4.6 - 4.7), again further suggesting that the level of zirconium doping is not altering the immediate local geometry around zirconium. The lack of differences in the Zr-edge data indicates that the Zr groups are more rigid than the titanium groups.

Modelling of the XAS data reveals the local order around titanium. However, this is only possible to a relatively small distance from the scatterer due to the damping of the XAS signal from the framework at larger distances. Figure 4.8 shows the natisite fit using the Artemis XAS fitting program.<sup>[58]</sup> Table details the refined contact distances are presented in table 4.5. The fit shows an overall good agreement up to the fitting range of 4 Å. After this distance, as previously discussed, the outgoing and incoming XAS signal interfere destructively as a consequence of the structure, damping the XAS signal out at longer contact distances. The refined contact distances again show an overall good agreement to literature values.<sup>[44]</sup> When modelling the XAS data of the zirconium doped natisite samples the zirconium silicate zektzerite<sup>[76]</sup> was used in the FEFF calculation for to determine a Zr-O contact distance. This was necessary as the CIF file for natisite, and by consequence the Feff calculation did not contain any Zr. Also as the fit range is only to 4 Å and the relatively small amount of Zr in relation to Ti, it is reasonable to assume there will be no Zr-Zr interaction, therefore it is safe to assume one Zr site scatters against all other Ti. Tables 4.6 and 4.7 show the refined contact distances for 10% Zr natisite and 20% natisite respectively.

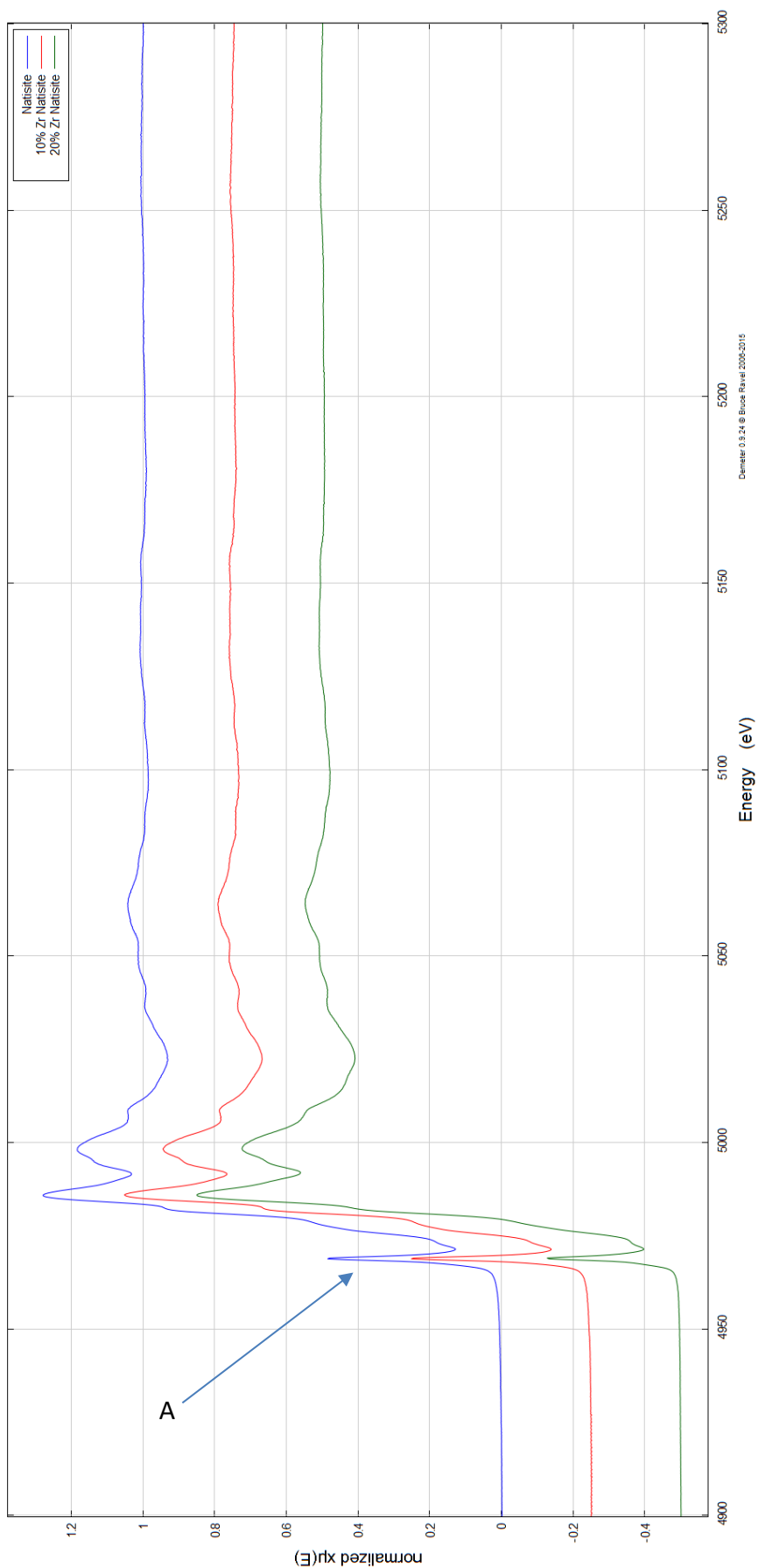


Figure 4.4 – Ti K-edge X-ray absorption spectra of natisite, 10% Zr and 20% Zr natisite. Page | 90

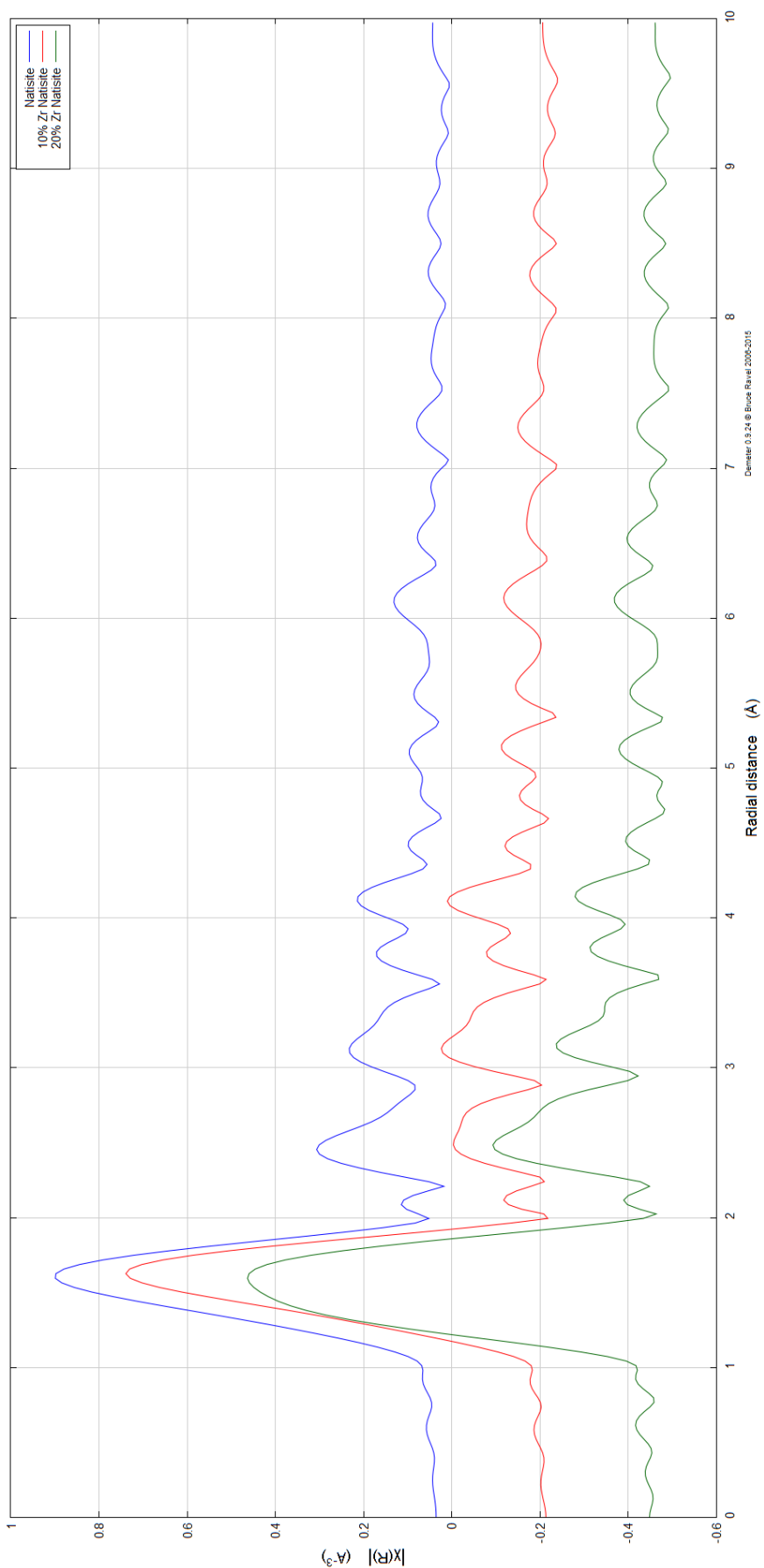


Figure 4.5 –Fourier Transform of figure 4.4, detailing relative atomic distances.

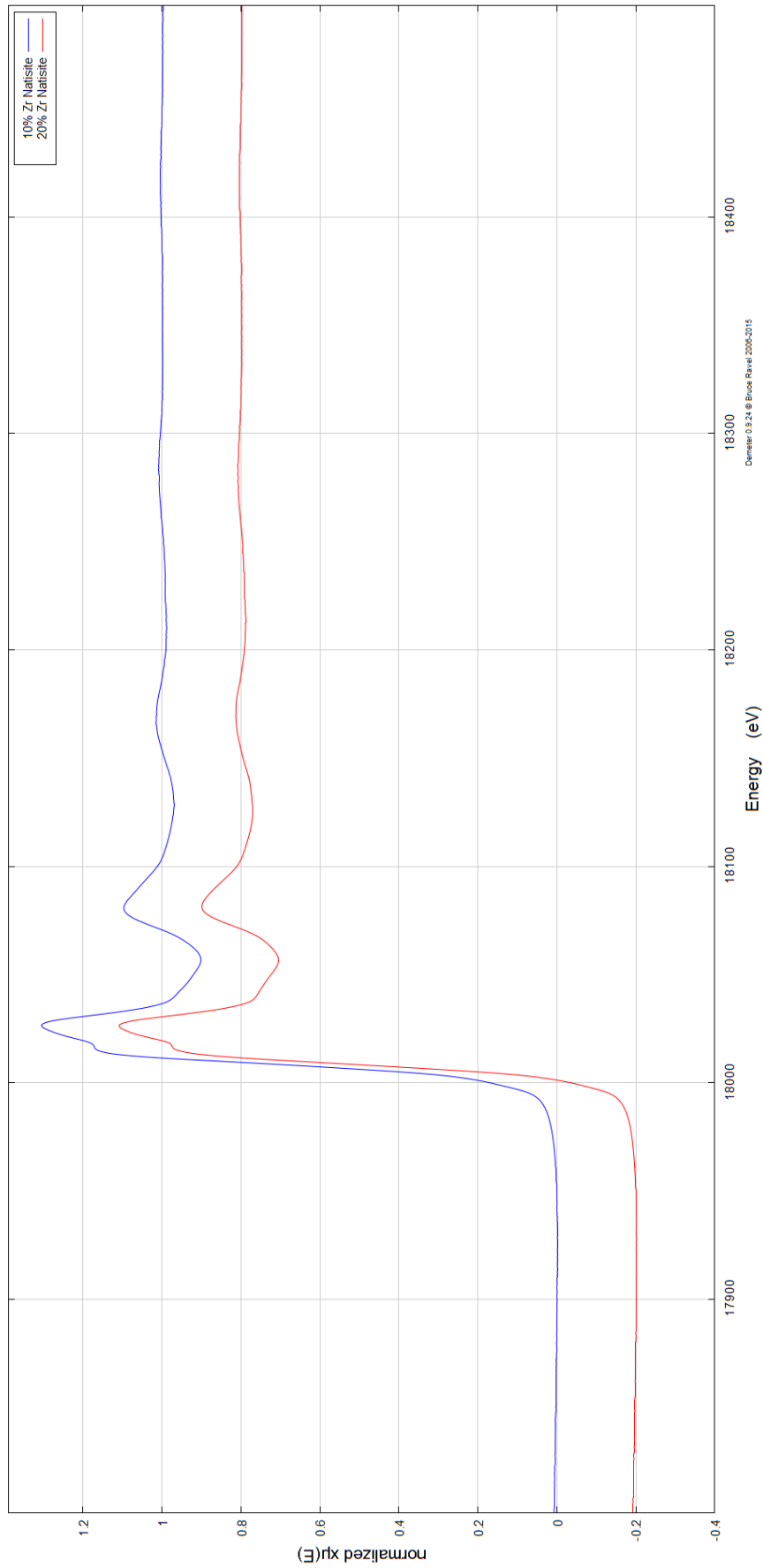


Figure 4.6 – Zr K edge X-ray absorption spectra of 10% Zr and 20% Zr natisite.

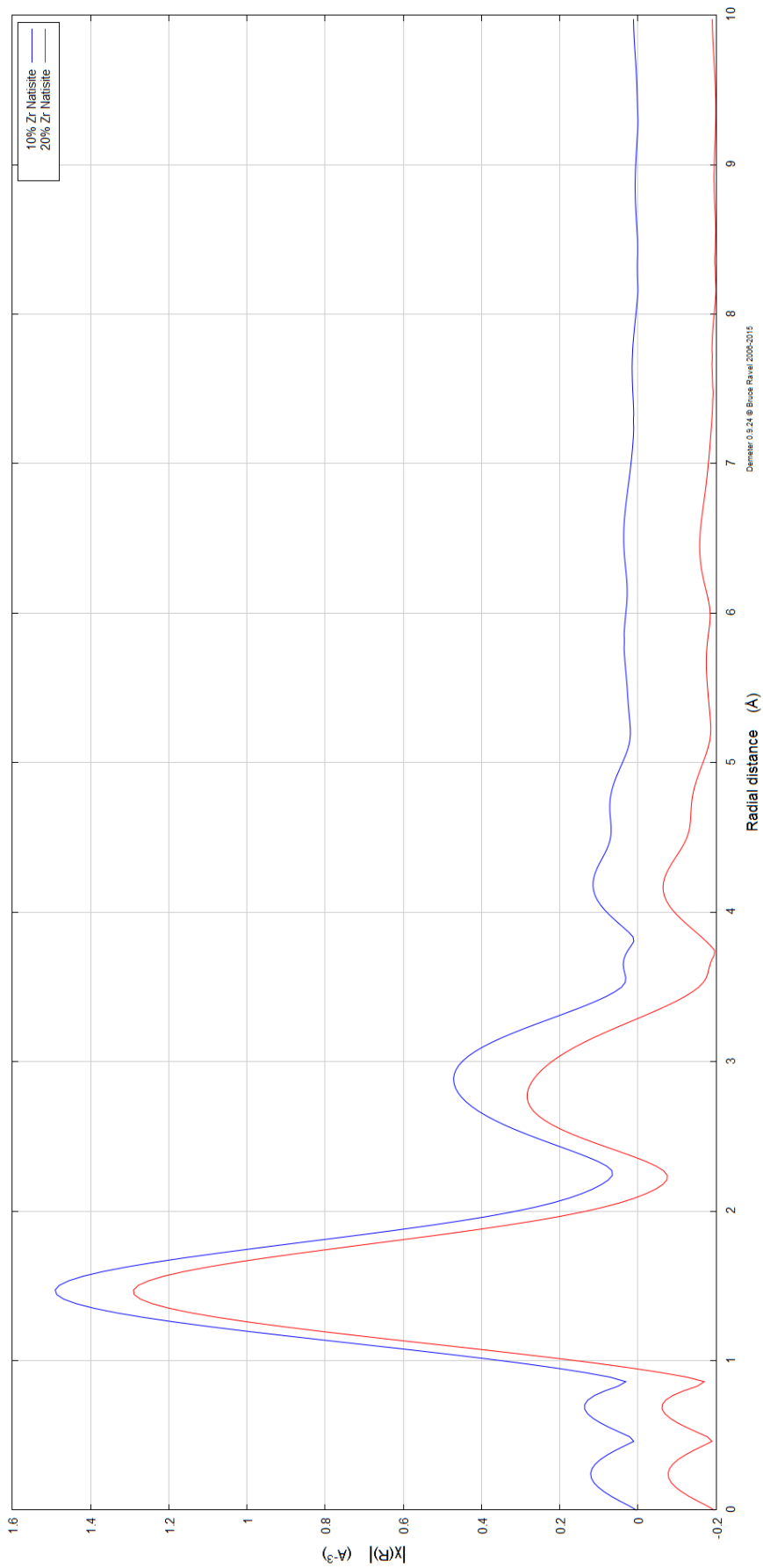


Figure 4.7 – Fourier Transform of figure 4.6, detailing relative atomic distances.

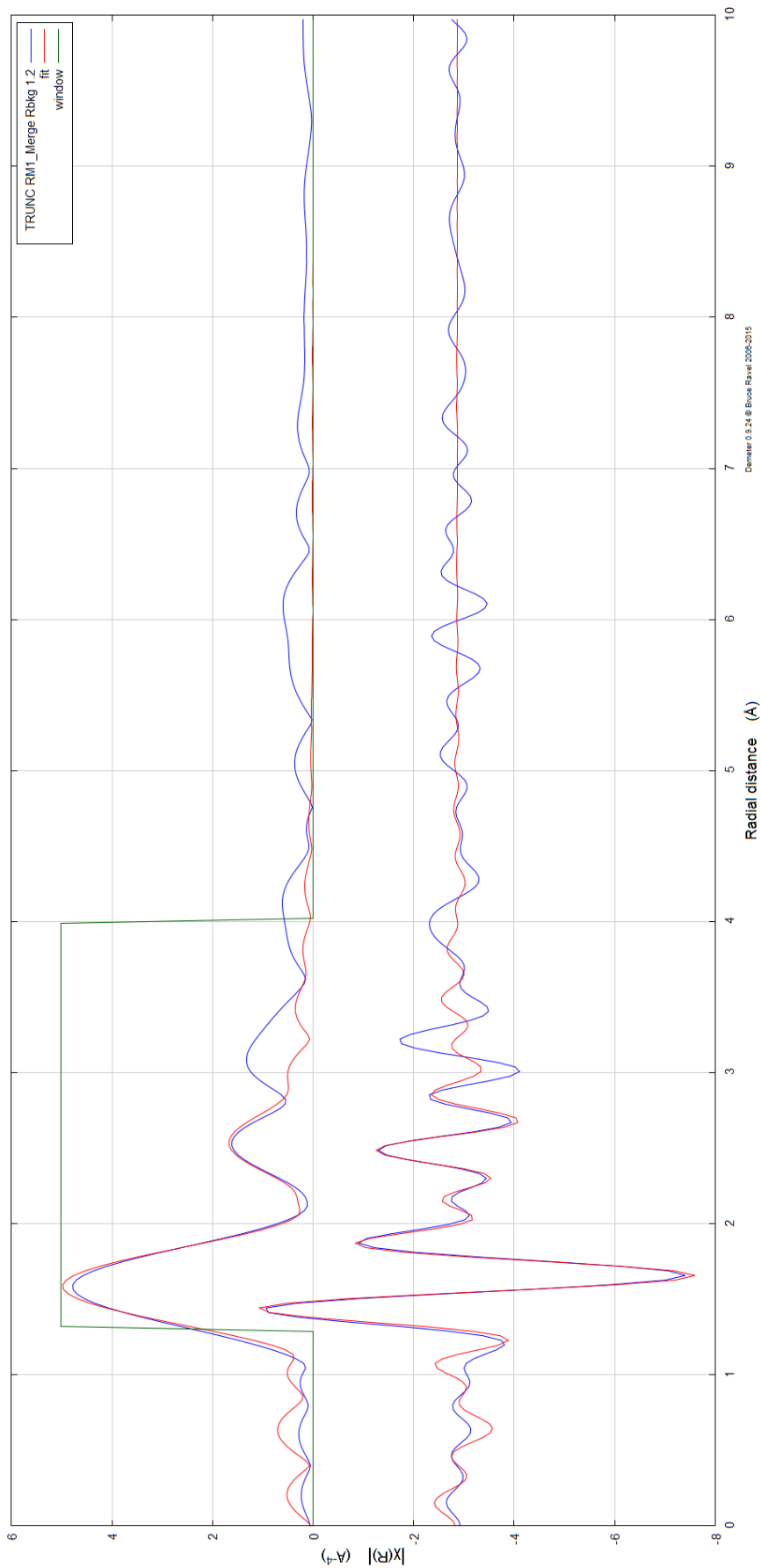


Figure 4.8 – Fit of Ti-edge data for natisite.

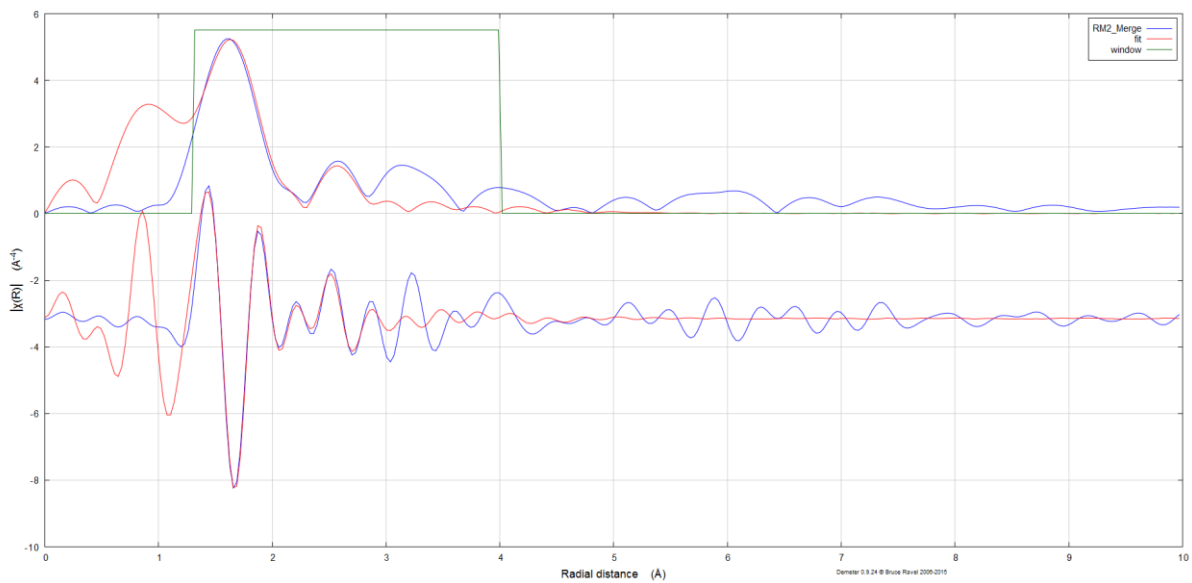


Figure 4.9 – Fit of Ti-edge data for 10% Zr doped natisite.

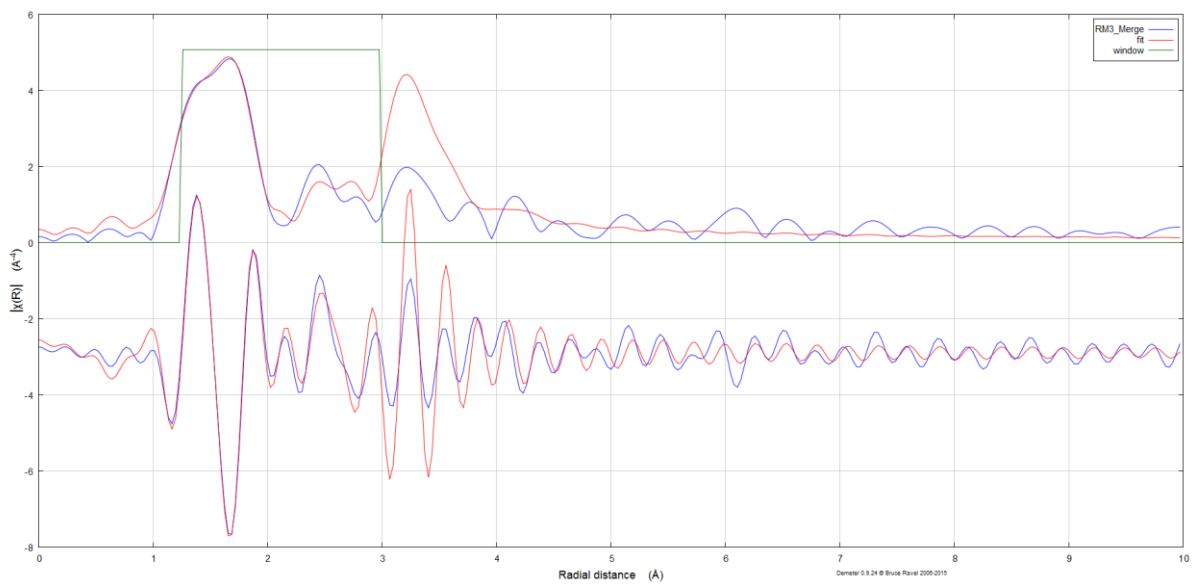


Figure 4.10 – Fit of Ti-edge data for 20% Zr doped natisite.

Table 4.5 – Refined contact distances for Natisite (Ti edge).

Scatterer	Reff/Å	R/Å	Delr
O2	1.69500	1.64034	-0.05466
O1	1.99040	2.00645	0.01605
Na1	3.18880	2.95846	-0.23034
Si1	3.25730	3.04810	-0.20921

Tables 4.6 and 4.7 show the refined contact distances for 10% Zr natisite and 20% natisite respectively. With the inclusion of Zr into the framework, contact distances have changed compared to Ti-natisite. The largest change in the 10% Zr natisite contact distance is the Ti1 – Na1 distance, which has decreased by 0.22111Å. This is potentially due to the presence of zirconium altering the bond angle in the layers, decreasing the distance between the two atoms. The 20% Zr natisite contact distances have also shifted, where the Ti1 – Si1 distance has increased by 0.3661Å. However, in the 10% Zr sample the Ti1 – Si1 distance had decreased by 0.19865 Å. This suggests that the inclusion of 10% Zr in the framework seems to be contacting the bond angles in such a way that it is decreasing contact distances. However, the 20% Zr samples are distorting the O coordination in a way that now increases the contact distance between Ti1 and Si1.

Table 4.6 – Refined contact distances for 10% Zr-Natisite (Ti edge).

Scatterer	Reff/Å	R/Å	Delr
O2	1.69500	1.44606	-0.24894
O1	1.99040	1.99406	0.00366
Na1	3.18880	2.96769	-0.22111
Si1	3.25730	3.05865	-0.19865
Zr1	2.06500	1.84947	-0.21553

Table 4.7 – Refined contact distances for 20% Zr Natisite (Ti edge).

Scatterer	Reff/Å	R/Å	Delr
O2	1.69500	1.53845	-0.15655
O1	1.99040	2.06566	0.07526
Na1	3.18880	3.02060	-0.16820
Si1	3.25730	3.62361	0.36631
Zr1	2.06500	2.01472	-0.05028

## 4.4: Ion-exchange

The substitution of framework Ti for Zr was performed in order to determine if the order of ion-exchange affinity could be changed and what effect the level of Zr substitution had on the materials ion-exchange chemistry. Both the 10% and 20% Zr containing natisite samples were exchanged with the cations of;  $\text{Cs}^+$ ,  $\text{Co}^{2+}$ ,  $\text{Sr}^{2+}$  and  $\text{Ce}^{4+}$ ,  $\text{Nd}^{3+}$  again used as inactive surrogates for Pu and U respectively.

### 4.4.1: Sample Preparation

A 0.1 M solution of each ion was prepared in 125 ml di-water. Each solution was mechanically stirred at 300 rpm with the use of a glass coated magnetic follower. 0.5 g of natisite was added to the ion containing solution and left for a period of 18 hours. The resulting powder was collected by filtration and washed with copious amounts of di-water.

### 4.4.2: Analysis

#### 4.4.2.1: XRD

XRD patterns of 10% Zr substituted natisite are shown in figure 4.12 with Pawley phase fitting performed on the ion-exchanged samples shown in table 4.8. As seen with pure natisite, there is a complete loss of crystallinity associated with the Ce-exchanged sample. There is a small peak at  $27^\circ 2\theta$  where the  $hkl$  value is  $020$ . This again suggests that the layers of natisite are remaining intact but the  $\text{Ce}^{4+}$  ion is introducing stacking faults or disrupting the long range order between the layers. The high background associated with the fluorescence of the Co-exchange means that subtle differences are difficult to detect. The Pawley phase fitting again shows very little difference between the ideal lattice parameter and the lattice

parameters post exchange. It is therefore difficult to detect by XRD alone the effect of Co exchange. As mentioned in the previous chapter, there is an unusual green colour associated with the Co exchanged sample (figure 4.11). This green colour was still present after exchange with 10% Zr-natisite. Above this, the rate of the Co exchange seemed to increase significantly with a near instant reaction, whereas the pure Ti-natisite needed upwards of 18 hours for the same level of exchange. This was evident by the white powder changing into the green colour upon instant contact with the Co containing solution, which was not observed with Ti-natisite.

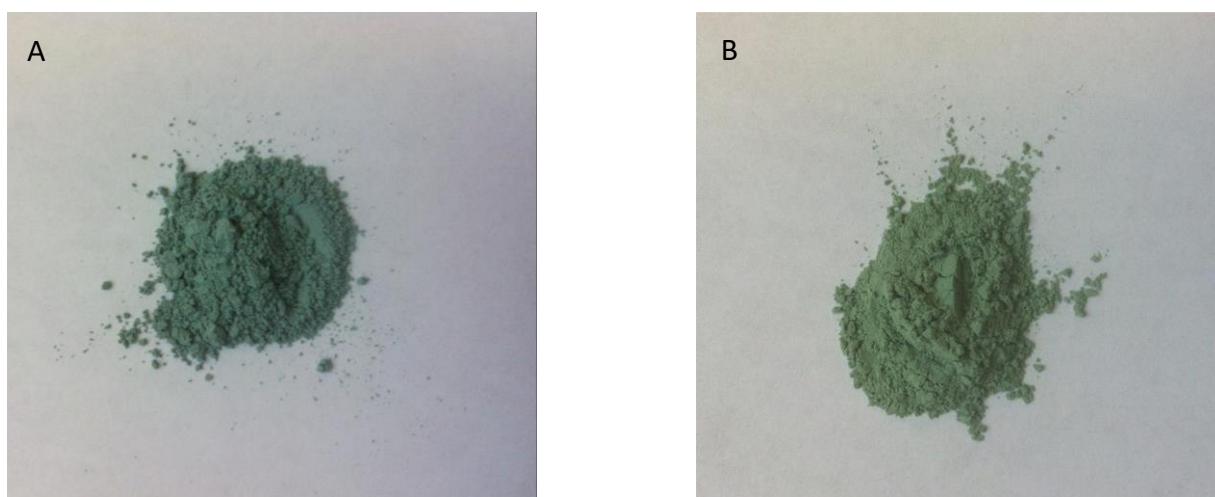


Figure 4.11 – (A) Co-exchanged natisite (B) Co-exchanged 20% Zr natisite.

There are few differences observed in the diffraction pattern with respect to Cs and Sr exchange, indicating that, from XRD alone, either the level of exchange is low, or the effect of exchange with these cations has very little effect on the structure of the material. The Nd exchanged sample shows a loss of crystallinity, with large changes in the materials lattice parameter. This again suggest that the larger cations of  $Ce^{4+}$  and  $Nd^{3+}$  are too large to be accommodated within the material without some form of stacking fault being introduced. This is supported from results found by J.J. Neeway *et al.*<sup>[77]</sup> where they detailed the ion-exchange of  $TcO_4^-$  from solution using a layered potassium metal sulphide. The XRD data post

exchange shows the loss of peaks indicative of the layered structure, supporting the idea the ion-exchange can introduce stacking faults and act to force layers apart.

Diffraction patterns of ion-exchanged 20% Zr natisite are shown in in figure 4.14. There are further changes in the diffraction patterns for the 20% substituted samples compared to the 10% containing sample. This is especially noticeable in the Co-exchanged sample. There is a much higher and nosier background compared to both the Ti-natisite and 10% containing analogue. This can be rationalised by the increased fluorescence of the sample, meaning that more Co must have been exchanged by the sample, causing this increase of fluorescence. Similar again to the Ti and 10% samples, Ce and Nd exchanges cause a loss of crystallinity. More changes are now being observed with respect to Cs and Sr, indicating that the increased level of Zr in the framework is now making ion-exchange of these cations more facile. Pawley fits of 20% Zr ion-exchanges are shown in in table 4.9 Again, the largest differences are observed in the Ce and Nd ion-exchanges. Also, changes are now observed in the Cs and Sr exchanged samples with larger changes to the lattice parameters compared to Ti-natisite and the 10% Zr doped sample. These changes further supports the idea that more Cs and Sr are being removed from solution compared to the undoped sample.

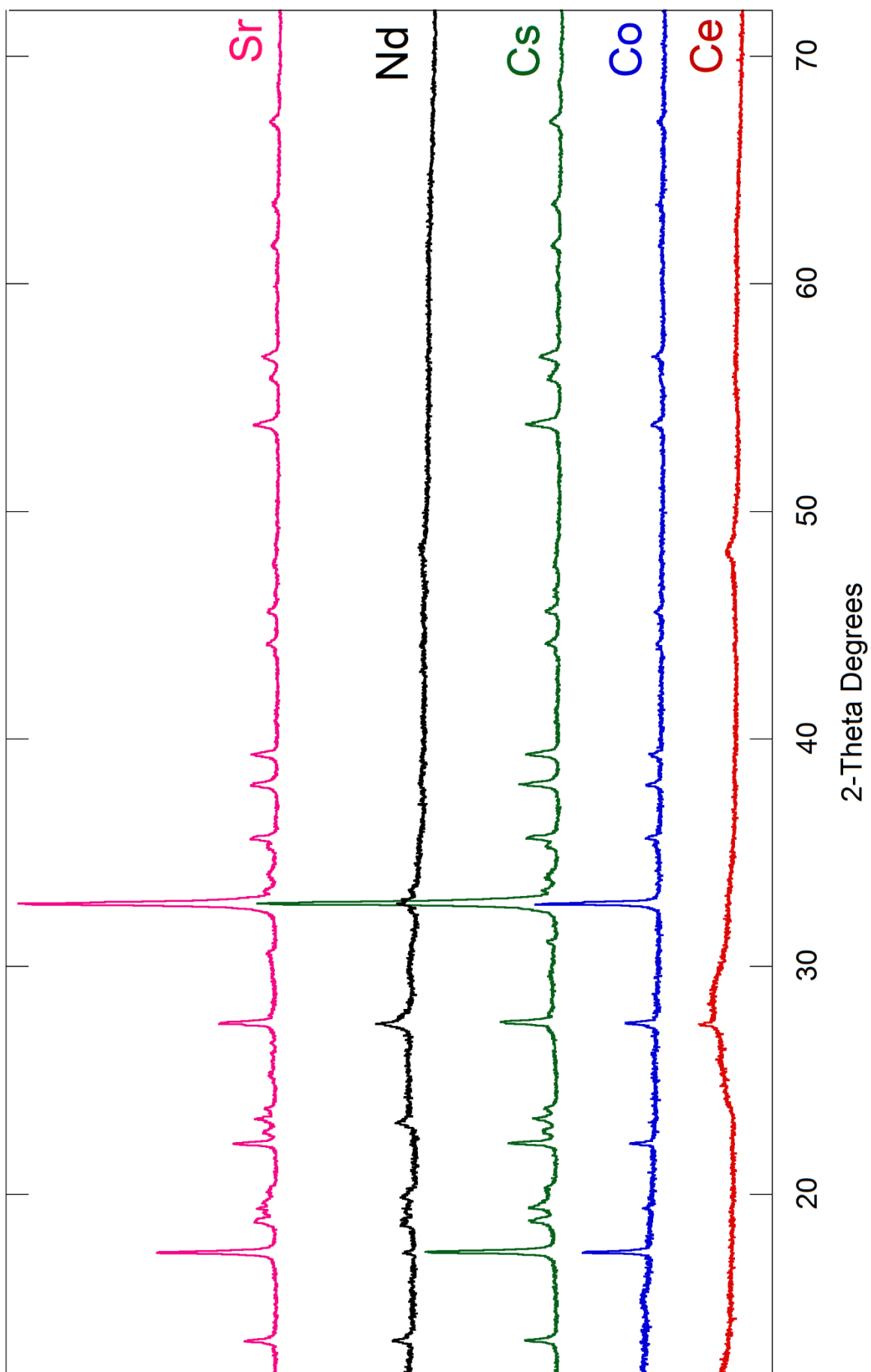
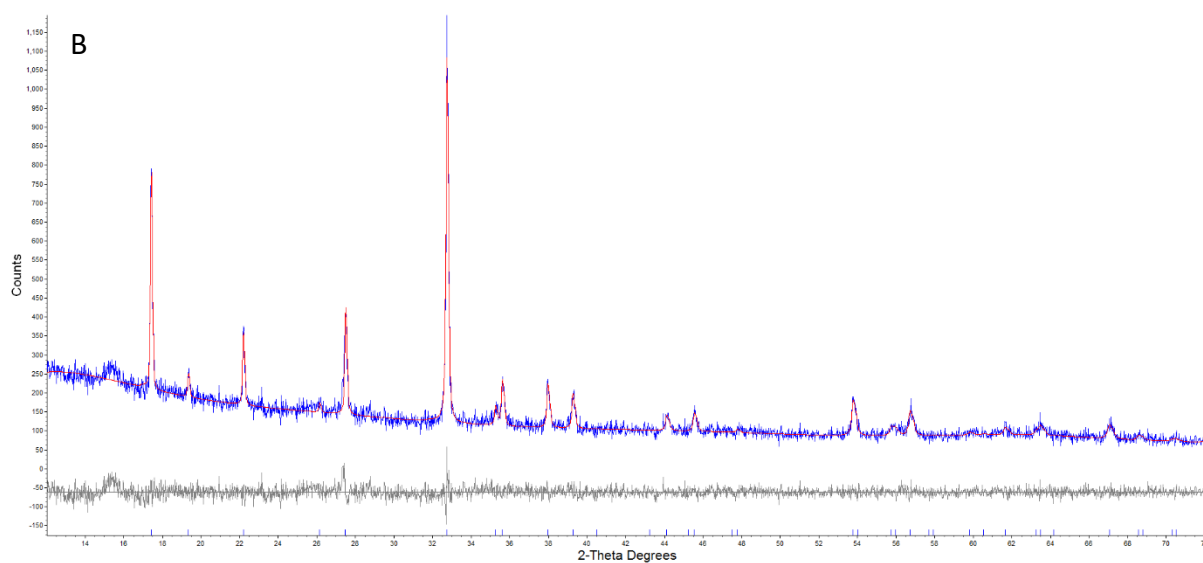
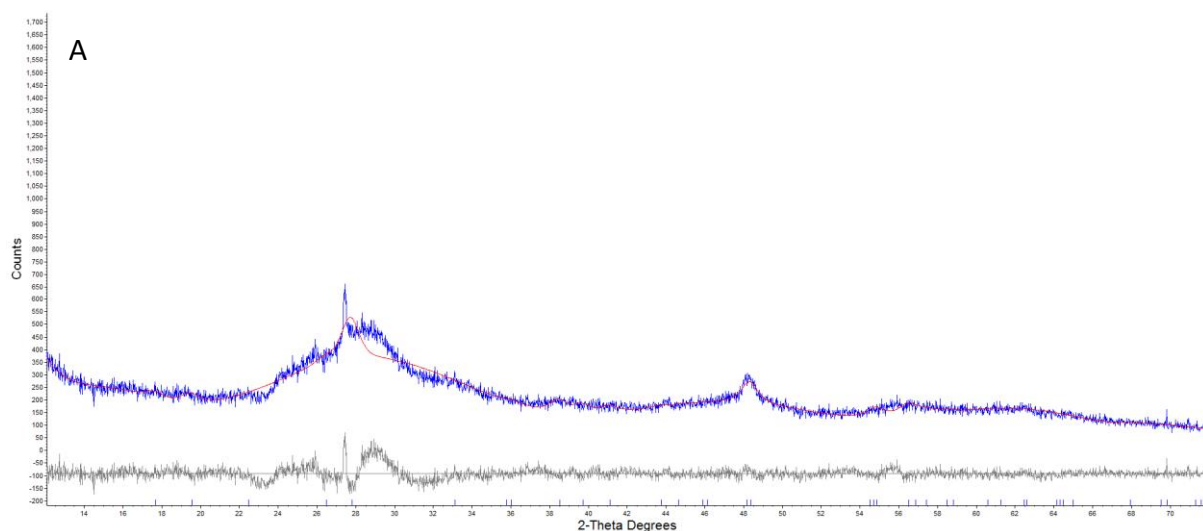


Figure 4.12 – XRD patterns of ion-exchanged 10% Zr-natisite.

Table 4.8 – Refined lattice parameters of ion-exchanged 10% Zr-natisite.

Ion	$ab / \text{\AA}$	$c / \text{\AA}$	Rwp %	Difference to 10% Zr Natisite	
				$a / \text{\AA}$	$c / \text{\AA}$
<b>10% Zr Natisite</b>	6.4838(5)	5.0917(7)	23.124	-	-
<b>Ce</b>	6.4119(198)	5.0131(130)	9.154	-0.07187	-0.07865
<b>Co</b>	6.4851(6)	5.0889(9)	9.136	0.00191	-0.000282
<b>Cs</b>	6.4855(6)	5.0922(8)	17.582	0.00168	0.00051
<b>Nd</b>	6.4390(70)	5.0280(62)	8.091	-0.04477	-0.0637
<b>Sr</b>	6.4845(6)	5.091(9)	17.954	0.00068	-0.00024



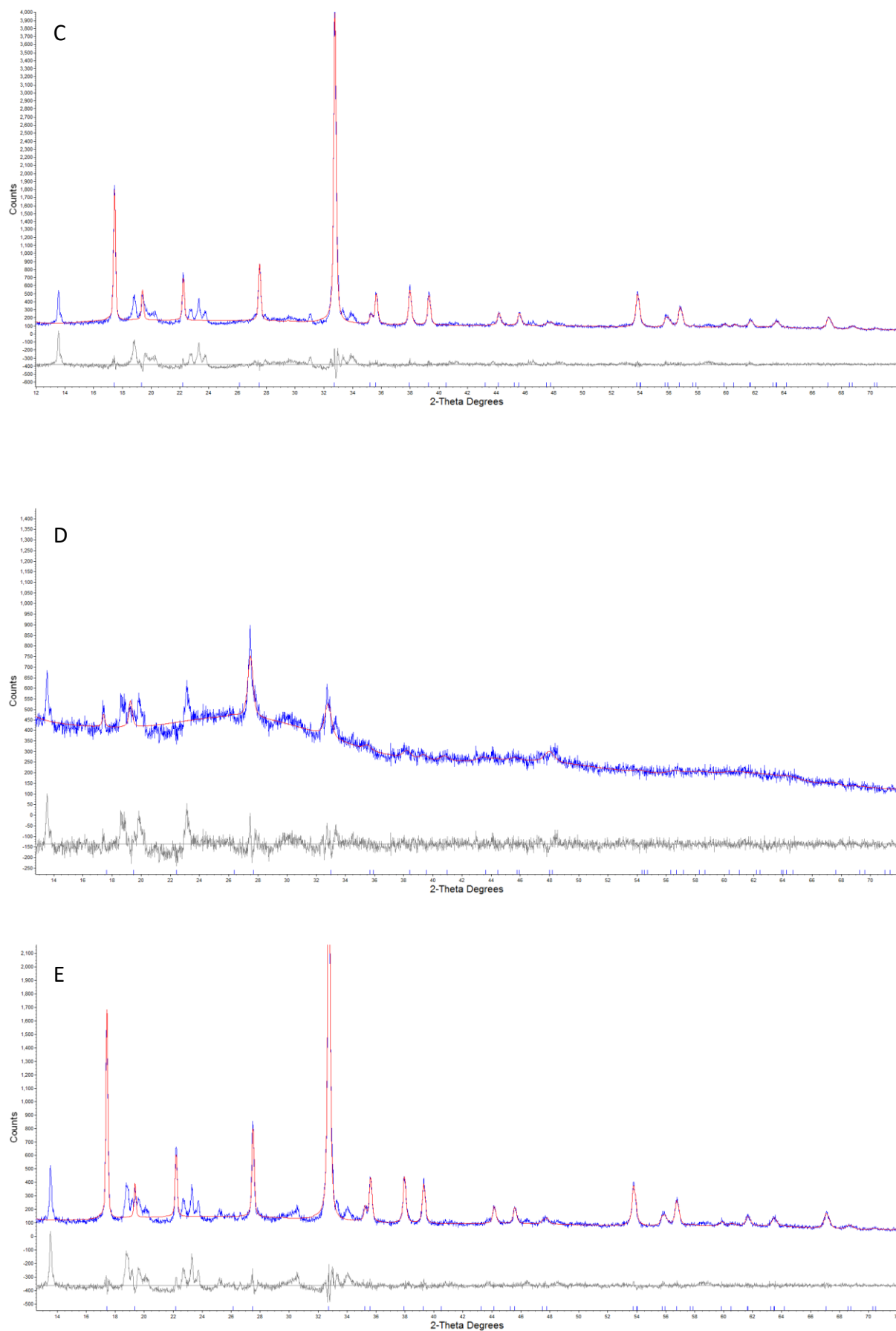


Figure 4.13 – Pawley fit of (A) Ce (B) Co (C) Cs (D) Nd (E) Sr exchanged 10% Zr-natisite.

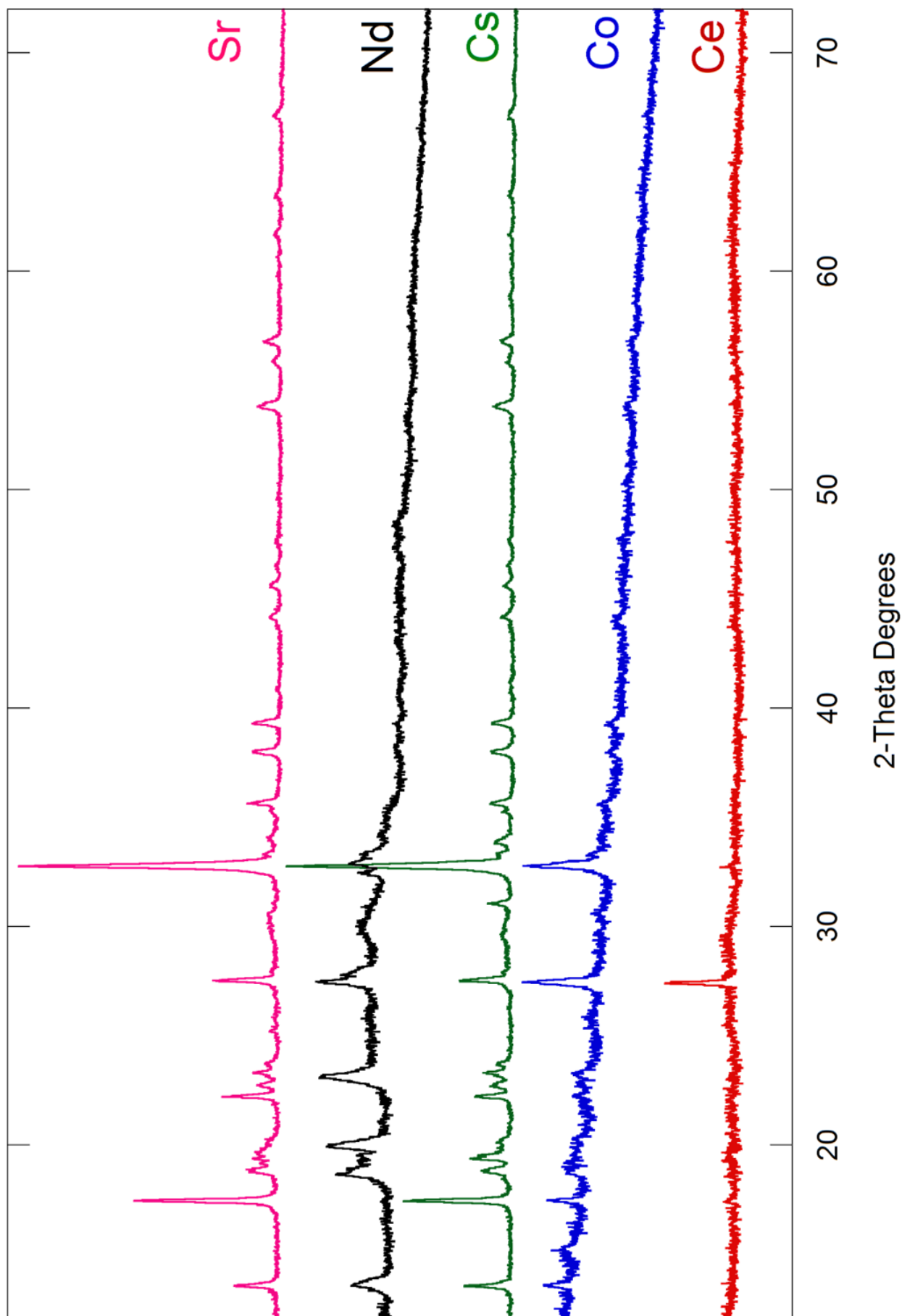
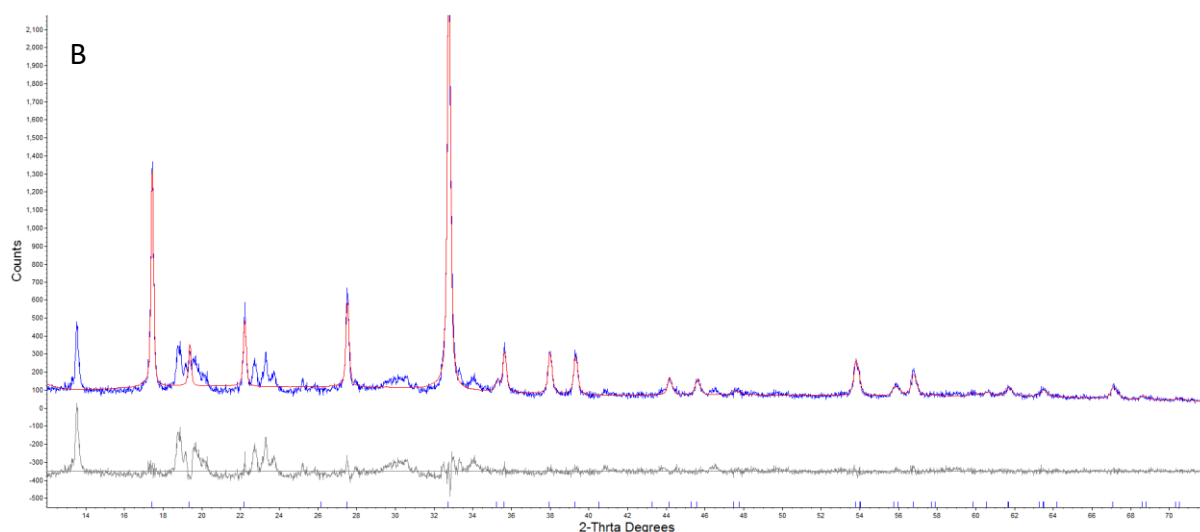
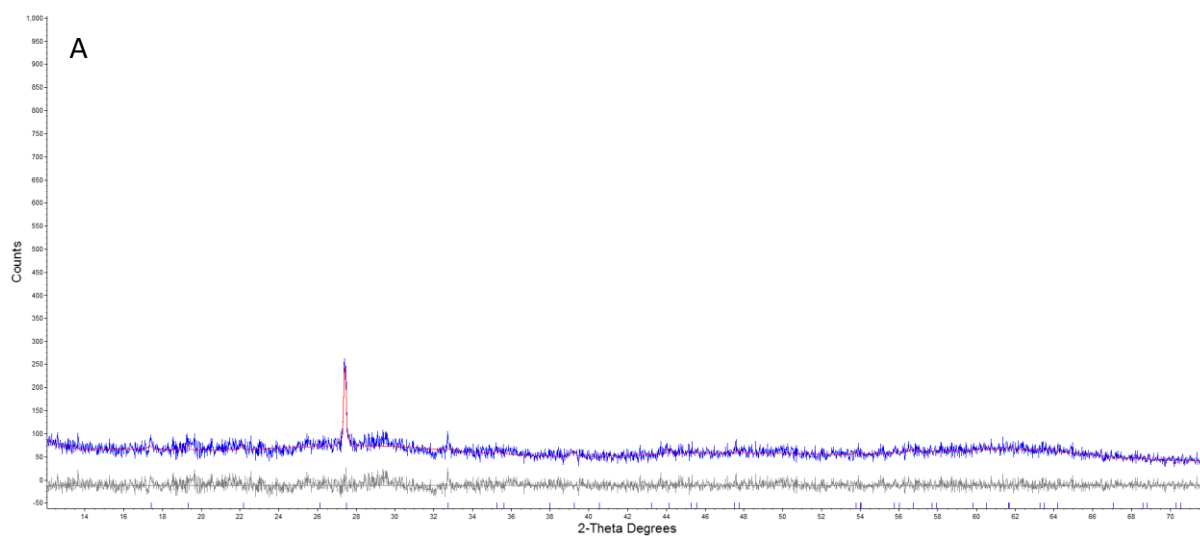


Figure 4.14 – XRD patterns of ion-exchanged 20% Zr-natisite.

Table 4.9 – Refined lattice parameters of ion-exchanged 20% Zr-natisite.

Ion	$ab / \text{Å}$	$c / \text{Å}$	Rwp %	Difference to 20% Zr Natisite	
				$a / \text{Å}$	$c / \text{Å}$
<b>20% Zr Natisite</b>	6.4838(5)	5.0917(7)	23.124	-	-
<b>Ce</b>	6.4855(69)	5.0865(86)	13.339	0.00305	-0.00673
<b>Co</b>	6.4630(35)	5.0314(33)	5.001	-0.01946	-0.06181
<b>Cs</b>	6.4856(10)	5.0951(14)	21.843	0.00319	0.00186
<b>Nd</b>	6.8011(52)	5.1163(47)	7.711	0.31862	0.0231
<b>Sr</b>	6.4840(8)	5.0904 (12)	20.089	0.00156	-0.00284



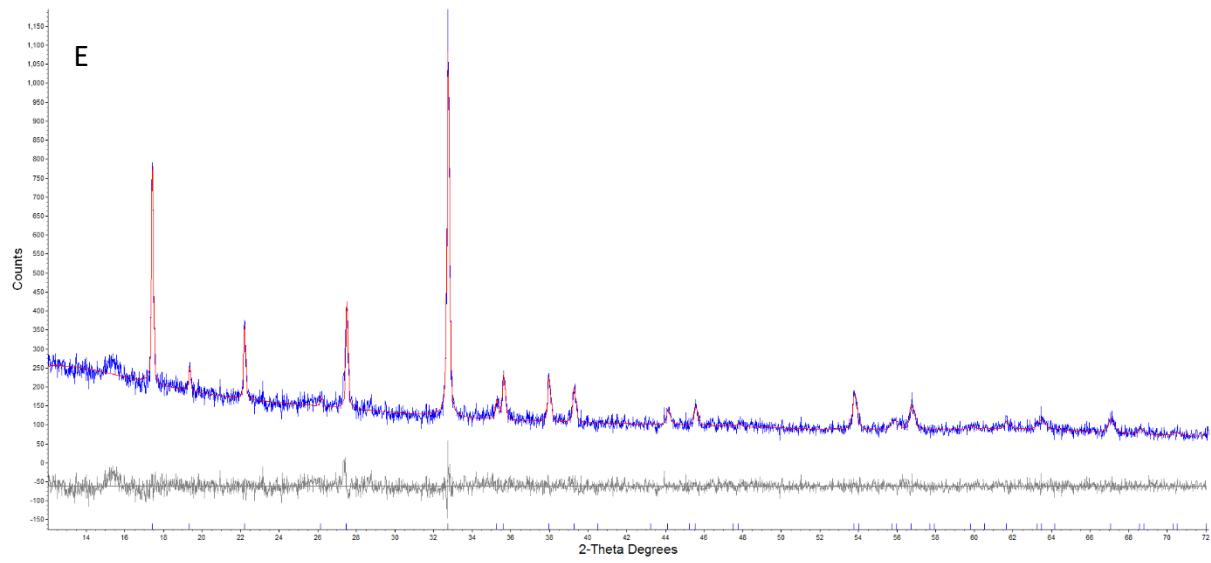
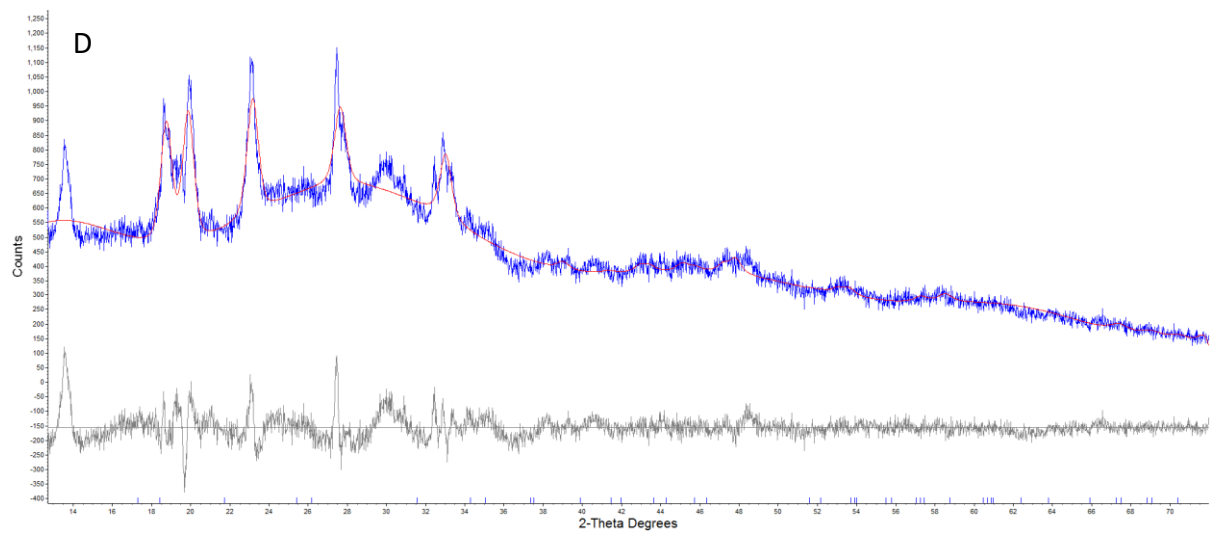
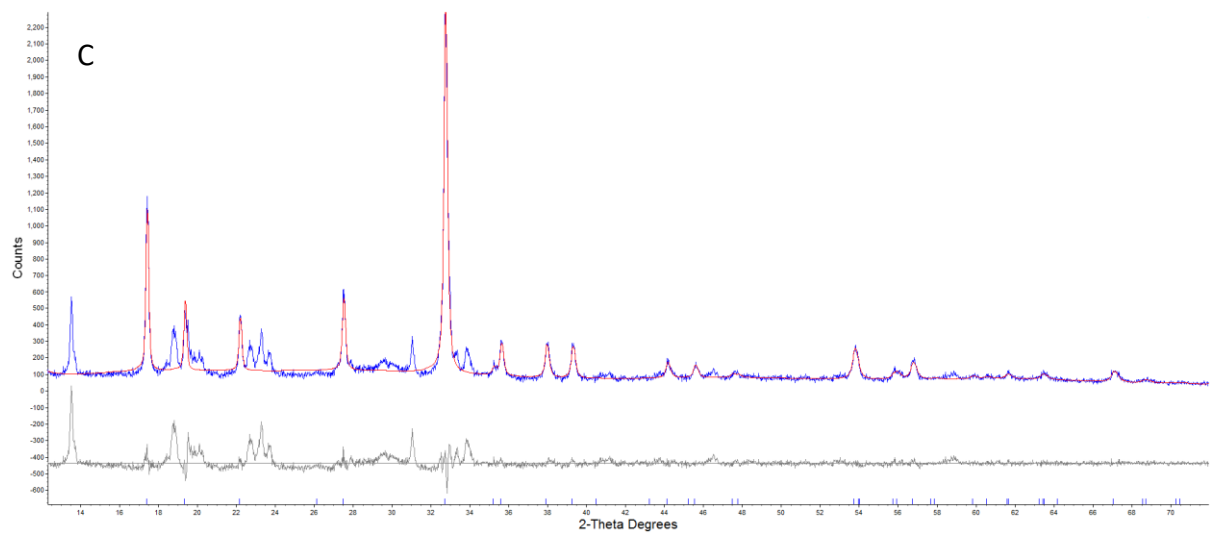


Figure 4.15 – Pawley phase fitting of (A) Ce (B) Co (C) Cs (D) Nd (E) Sr ion-exchanged 20% Zr-natisite.

#### 4.4.2.2: XRF

XRF provided qualitative results on the ion-exchanged samples of 10% Zr-natisite. The spectra are shown in figure 4.16. The same experimental method detailed in chapter three, was used here.

The results show signals from each of the respective elements, indicating detectable levels of exchange. Also, the XRF was able to detect a signal from the Zr L line, and a Ti signal with a lower intensity compared to that of the undoped natisite spectra.

A shoulder on the Ti K line is again observed at 4.28 keV. As the signal is originating from the Cs L line and only small changes are observed in the XRD data, these would contribute to a small signal observed in the XRF spectra

There are changes in the XRF spectra between 10% Zr and 20% Zr natisite. The Cs signal increases with the increase of Zr in the natisite framework and we can see that there is an increased Cs signal on the Cs-exchanged 20% Zr natisite XRF spectra compared to the 10% natisite Cs exchanged XRF spectra. Also, the relative intensities of the Co K line and the Ti K have changed from the 10% natisite to the 20% natisite samples. Indicating from XRF alone that the level of Co exchange has increased. The Sr signal however does not seem to increase or decrease significantly indicating that the level of Sr exchange is not dependent or affected by the increased level of Zr within the framework.

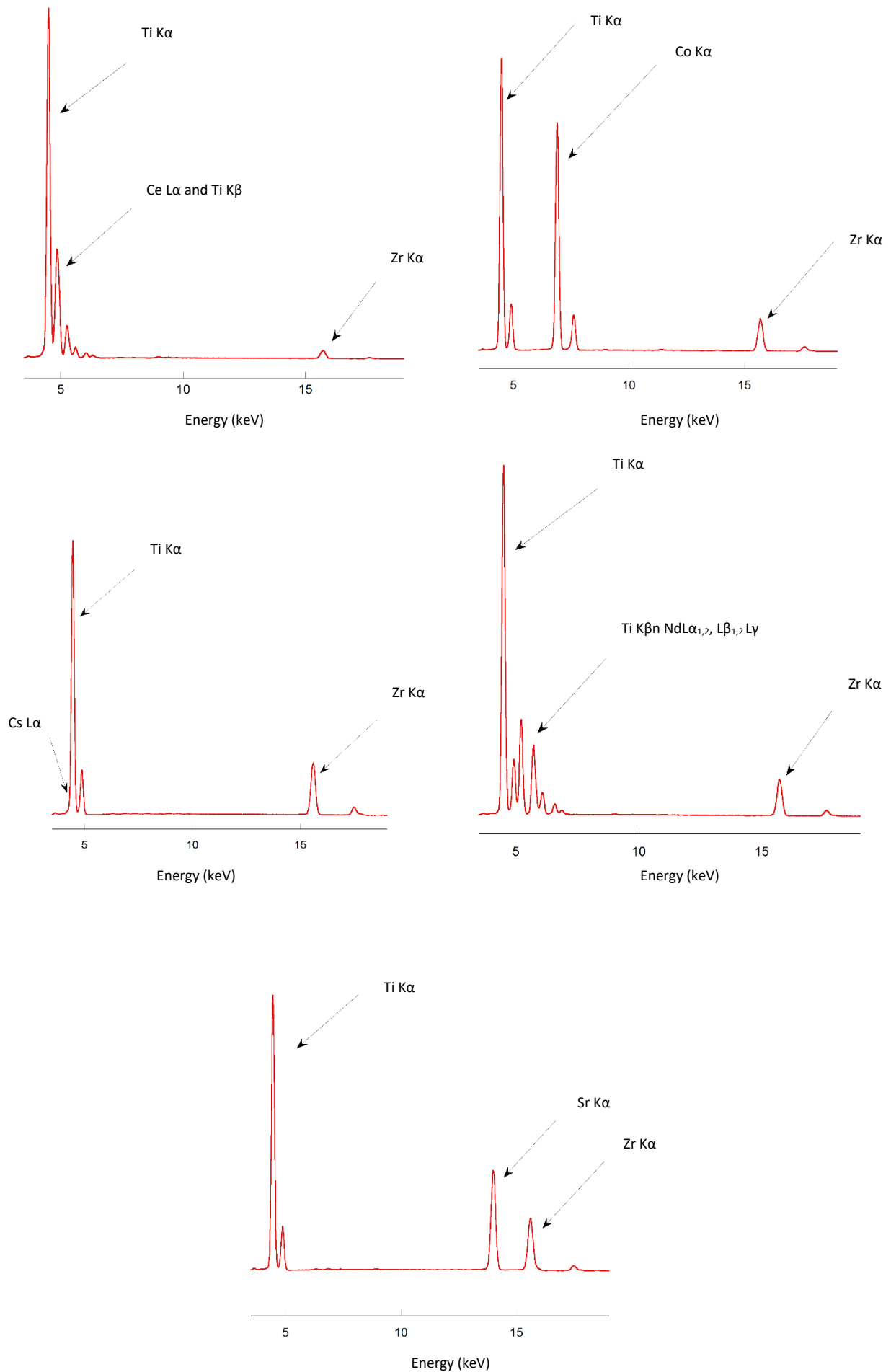


Figure 4.16 – XRF spectra of ion-exchanged 10% Zr natisite.

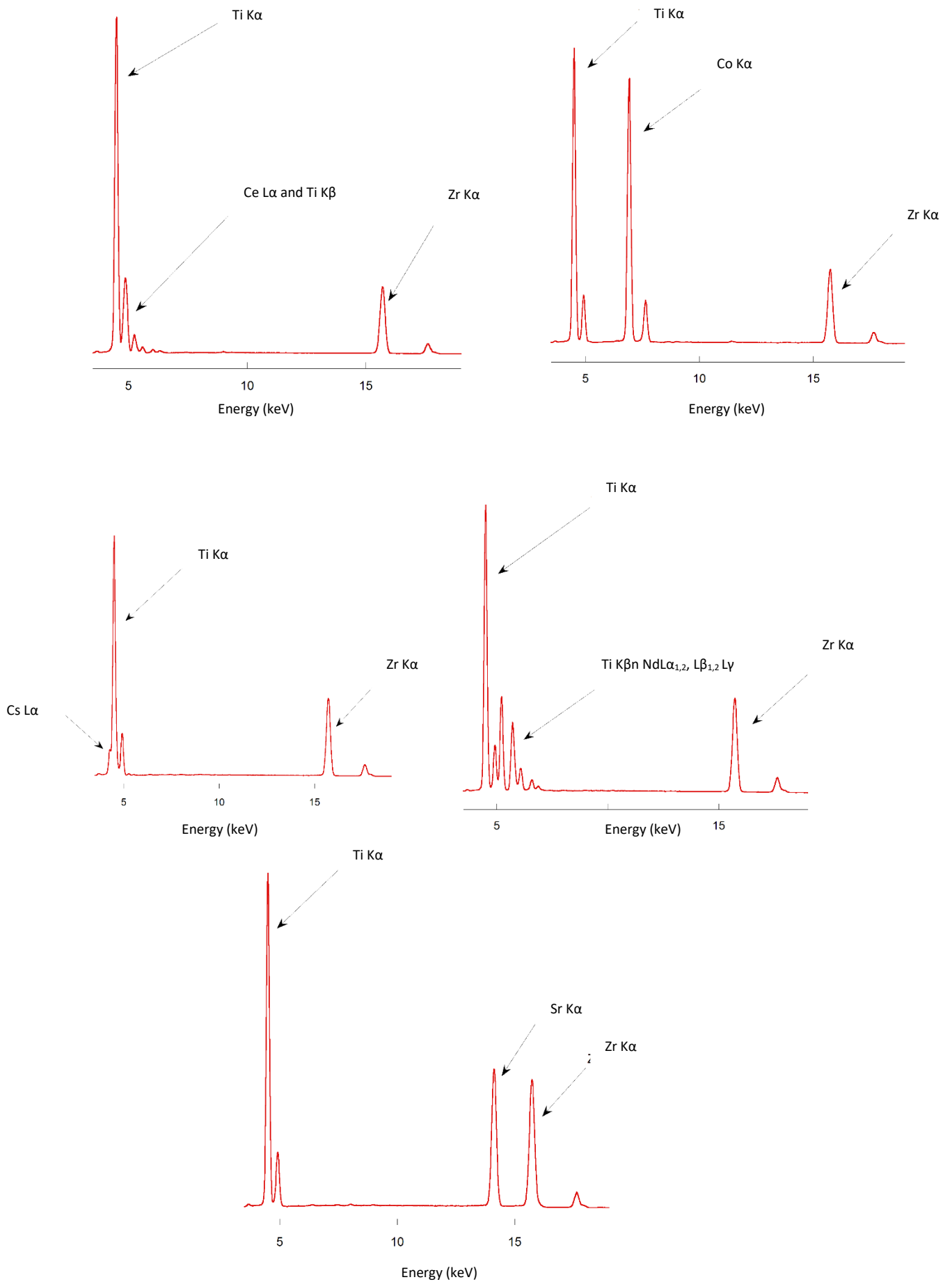
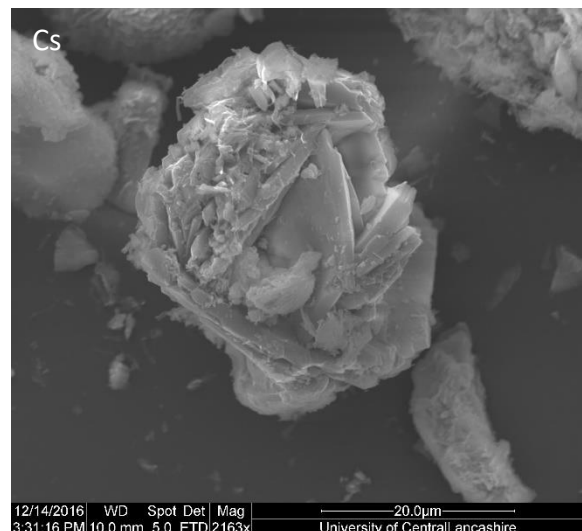
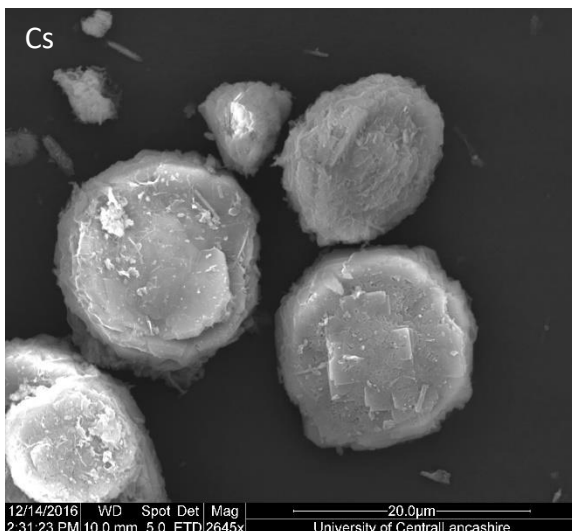
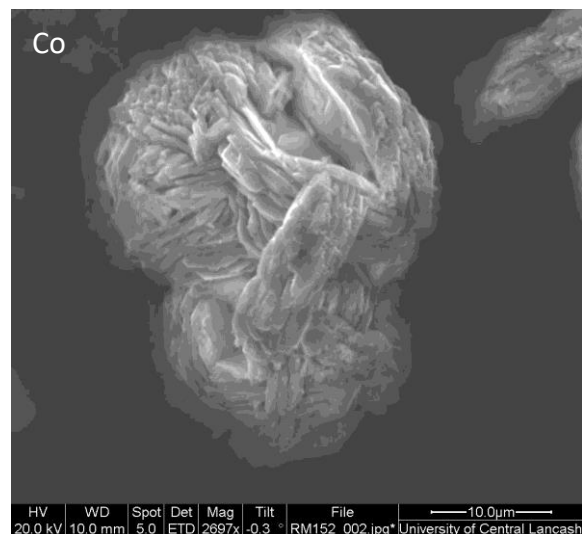
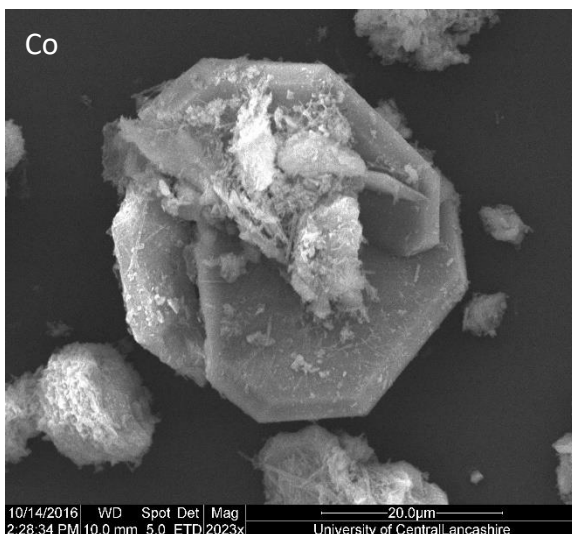
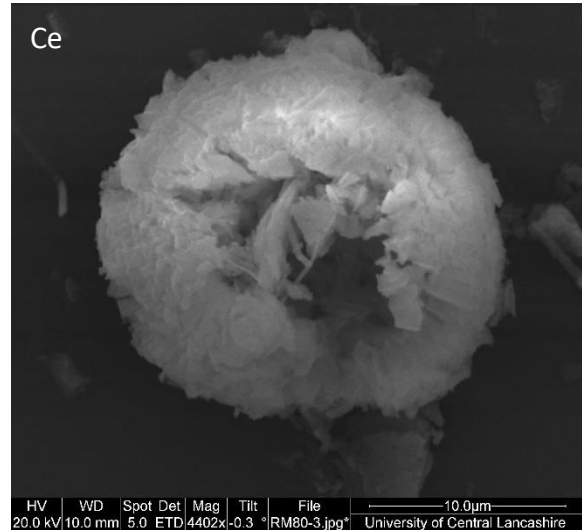
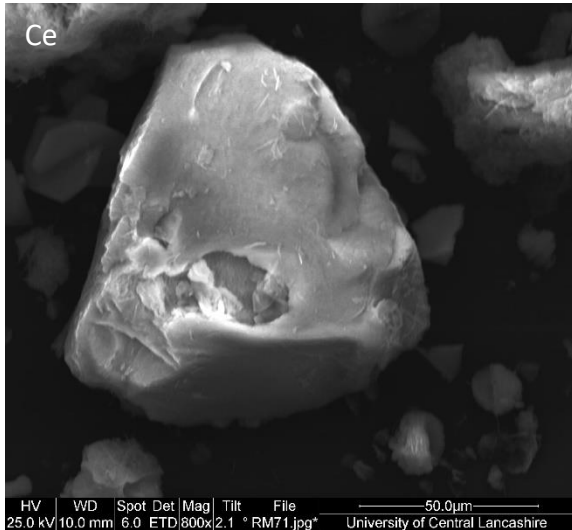


Figure 4.17 – XRF spectra of ion-exchanged 20% Zr-natisite.

### 4.4.2.3: SEM

SEM images were taken to determine any changes in morphology to the 10% and 20%

Zr doped natisite samples after ion-exchange shown in figure 4.18.



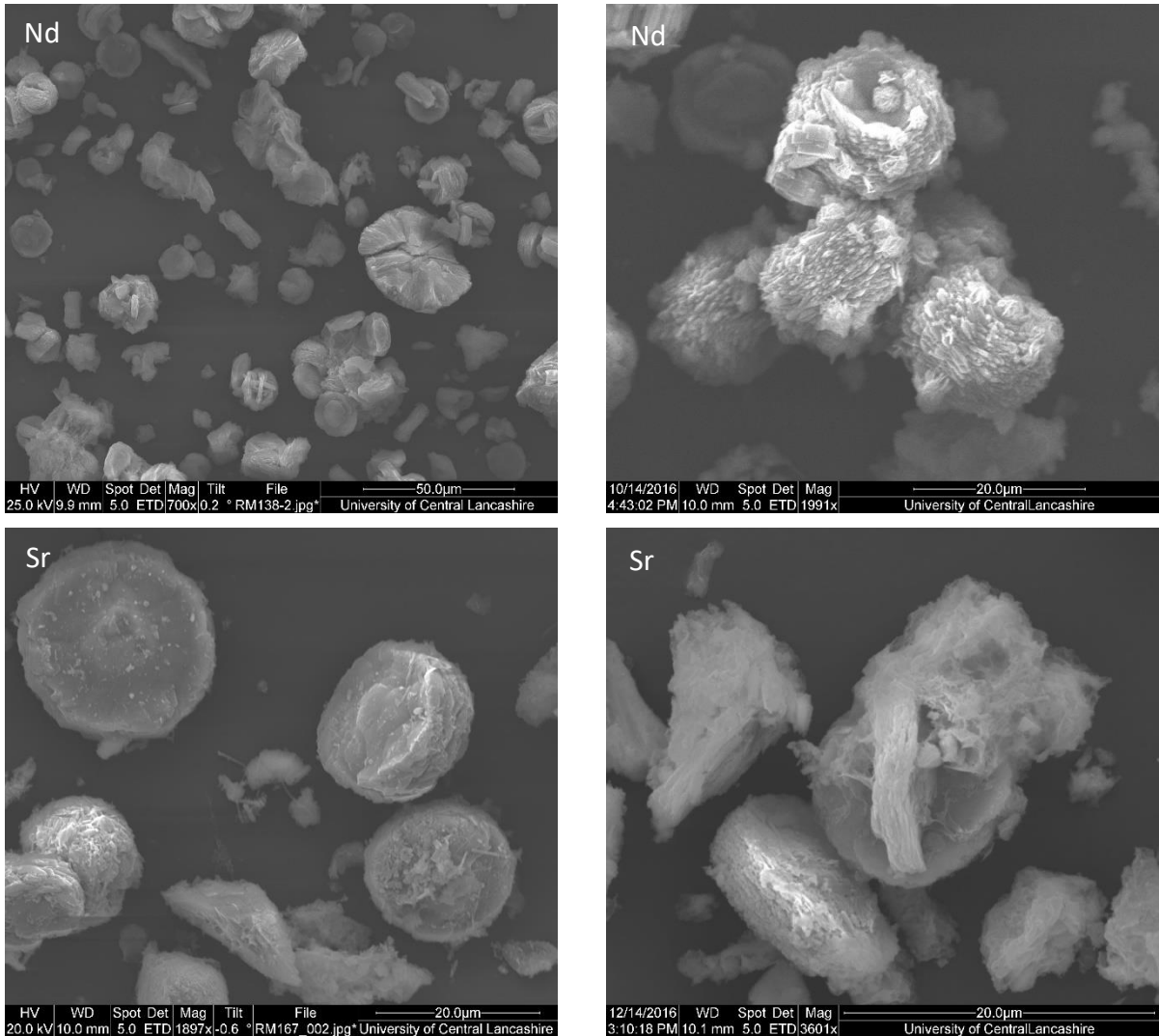


**Figure 4.18 – SEM micrographs of 10% Zr natisite ion exchanges (left) and 20% Zr natisite (right).**

The SEM images show distinct differences in morphology depending on the exchanged cation. Ce and Nd exchanged samples as expected showed partial destruction of particle morphology, unseen with any other exchanged cation. Particle size remains unchanged with each exchange with sizes around 20 µm, however these are smaller than the unexchanged 10% and 20% samples where sizes were observed at around 40-50 µm. Also differences are observed between the same cations of different level Zr doping. This is especially evident in the Ce exchanged samples with the 10% Zr natisite showing no resemblance to that of the

unexchanged sample. The 20% Zr Ce exchanged sample is similar in morphology to that of the unexchanged sample. However, we can see clearly that the microcrystalites have been broken down. This supports the XRD data which shows a complete loss of crystallinity post Ce exchange. The Nd exchanged sample again show that the morphology is has been modified, again supporting the results from the XRD and agaon the formation of Nd(OH)<sub>3</sub>.

The large changes in morphology between 10% and 20% exchanges samples and the changes observed in the XRD data indicate that the level of Zr substitution in the framework, does have a significant effect on the removal of cations from solution.

#### 4.4.2.4: ICP-MS

Quantitative analysis of the waste solutions was determined by ICP-MS. The results are shown in in table 4.10 and table 4.11.

**Table 4.10–Calculated percentage ion-exchange from ICP-MS results for 10% Zr natisite.**

<b>Ion</b>	<b>ppm Na<sup>+</sup></b>	<b>Percentage exchange/ ±1%</b>
Ce	0.477	60
Co	0.34	35
Cs	0.056	7
Nd	0.484	59
Sr	0.107	21

Table 4.11–Calculated percentage ion-exchange from ICP-MS results for 20% Zr natisite.

Ion	ppm Na <sup>+</sup>	Percentage exchange/ ±%
Ce	0.536	67
Co	0.281	42
Cs	0.26	39
Nd	0.357	47
Sr	0.109	18

The ppm results show the concentration of Na<sup>+</sup> found in solution after ion-exchange. As the initial concentration of Na<sup>+</sup> in solution pre-exchange is 0, any Na<sup>+</sup> found in solution post exchange is a result of the exchange out of the framework and can therefore be used quantitatively to determine the level of exchange of the cations exchanged onto the framework.

Both the 10% and 20% Zr containing samples have increased the percentage exchange of all the cations. From the results, we can now determine a new order of affinity for both the 10% and 20% Zr doped natisite

For 10%: Cs < Sr < Co < Nd < Ce

For 20%: Sr < Cs < Co < Nd < Ce

While the order of affinity has varied little from the pure Ti-natisite, it is the increase of the level of exchange which has shown the biggest difference (figure 4.19). The biggest difference being in the level of Cs removal with the 20% Zr containing natisite. While the 10% Zr natisite causes a slight increase in the level of Cs uptake, the presence of 20% Zr in the

natisite framework makes exchange of Cs much more facile and increases the level of exchange from 4% in Ti-natisite to 39% in 20% Zr natisite.

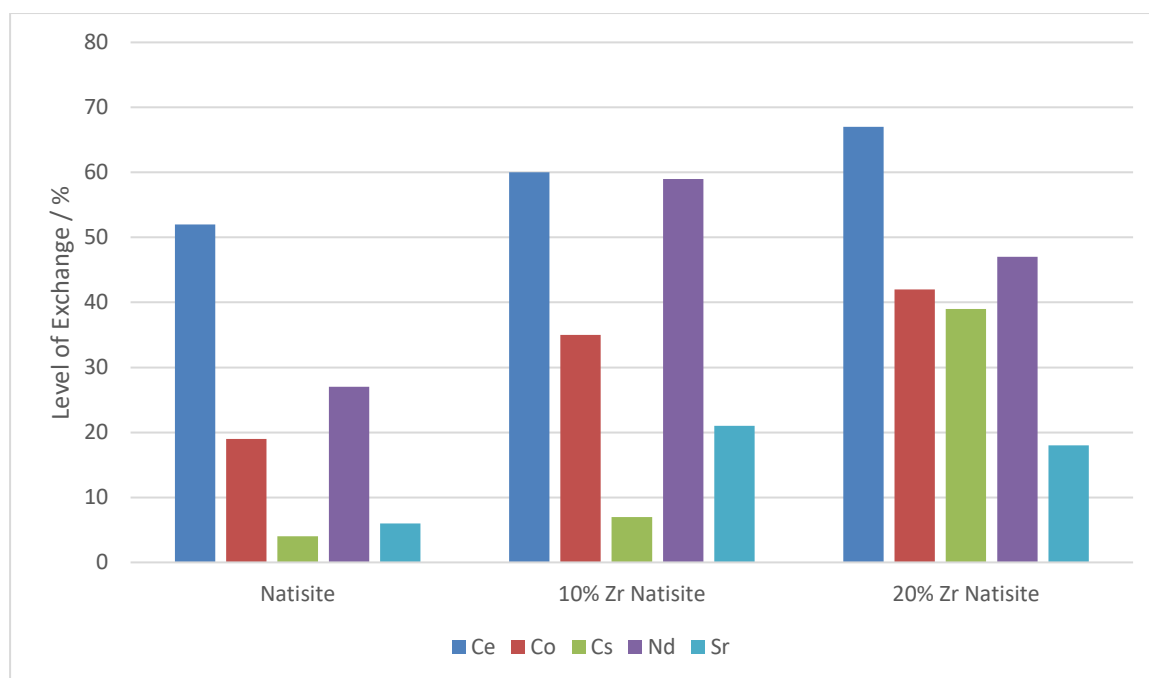


Figure 4.19 – Calculated percentage ion-exchange from ICP-MS results for natisite, 10% Zr and 20% Zr.

#### 4.4.2.5: XAS

From the diffraction data and ICP-MS results, it is clear that the introduction of Zr into the framework is having significant effects on the ion-exchange chemistry of the material. XAS can be used to determine the local coordination environments around both Ti and Zr to investigate how the exchanged cations are bound to the framework. Also by modelling the experimentally obtained data, it will provide refined contact distances detailing the effect on the local structure post ion-exchange.

The effect of Zr doping on the Co exchange was significant and therefore XAS was used to investigate the increase in the rate of exchange. Figure 4.20 shows the XANES profile for

Ti-edge Co-exchanged natisite and 10% and 20% Zr natisite with figure 4.21 showing the Fourier transform of data presented in figure 4.20. The data shows significant changes in the XANES region and Fourier Transformed data between the un-exchanged natisite and Co-exchanged samples. However, when comparing this with the Zr edge data presented in figures 4.22 and 4.23, there are relatively few observed changes with the exchanged samples. As stated previously, the inclusion of Zr into the framework speeds up the rate of Co exchange, therefore changes would have been expected around the Zr local environment. It is now believed that Zr alters the local coordination of the layers in such a way that allows for the easier exchange of not only Co, but all exchanged cations, to sites closer to Ti. Supported by the large changes in the Ti edge data and small changes around Zr.

The Co exchanged samples as mentioned previously displayed an unusual green colour indicating that perhaps the cobalt was in an unusual coordination environment. By comparing the XAS spectra against the Co spectra of known coordination environments, the determination of Co environment in the exchanged natisite can be achieved. Figure 4.24 shows the comparison of the Co K edge XAS comparison with four-<sup>[78]</sup> five-<sup>[79, 80]</sup> and six-<sup>[81]</sup> coordinate standards. From the spectra we can see that the tetrahedral coordination provides the best match, indicating that Co is in a tetrahedral coordination. However, this does not explain the green colour of the powder obtained post-exchange.

Investigating the Ce edge data as shown in in figure 4.25 a possible reason for the lack of crystallinity obtained can be explained. The Ce spectra was compared against Ce standards of known coordination,  $\text{CeCl}_3$   $\text{CeVO}_4$ <sup>[82]</sup> and  $\text{CeO}_2$ <sup>[82]</sup>. The diffraction data shows broad featureless peaks in positions similar to those of  $\text{CeO}_2$ . By investigating the Ce L edge and comparing with a  $\text{CeO}_2$  standard a good agreement between the spectra is achieved.

Thereby indicating that cerium oxide nanoparticles are formed in between the layers of natisite introducing stacking faults and loosing long range order. The formation of CeO<sub>2</sub> nanoparticles has been previously investigated by N.W. Pettinger<sup>[83]</sup> where it was found that the addition of cerium ammonium nitrate (CAN) (used as Ce source in this work) will spontaneously form CeO<sub>2</sub> in water without the addition of a strong base or heat. It is therefore possible that the same mechanism is occurring in the work and then the CeO<sub>2</sub> is adsorbing in between the layers. However, in the results presented by Pettinger, the conditions in which these CeO<sub>2</sub> particles formed was different to this work using only mM concentrations of CAN. In the work presented here, the concentrations were much higher in the order of 0.1 M, also the pH of the solution was tested upon the addition of the natisite and was observed at pH 7. This is again different to the pH value of 2 which Pettinger recorded.

In unpublished work conducted by the Readman group<sup>[84]</sup> using natural zeolites and microporous zirconium silicates, the formation of CeO<sub>2</sub> nanoparticles was not observed within a 3D pore structure but is being formed with a layered structure such as natisite. This indicates that natisite could possibly catalyse the formation of high concentrations of CAN into CeO<sub>2</sub> nanoparticles without the presence of heat or a highly basic solution and with respect to the natisite system adsorb these in between the layers.

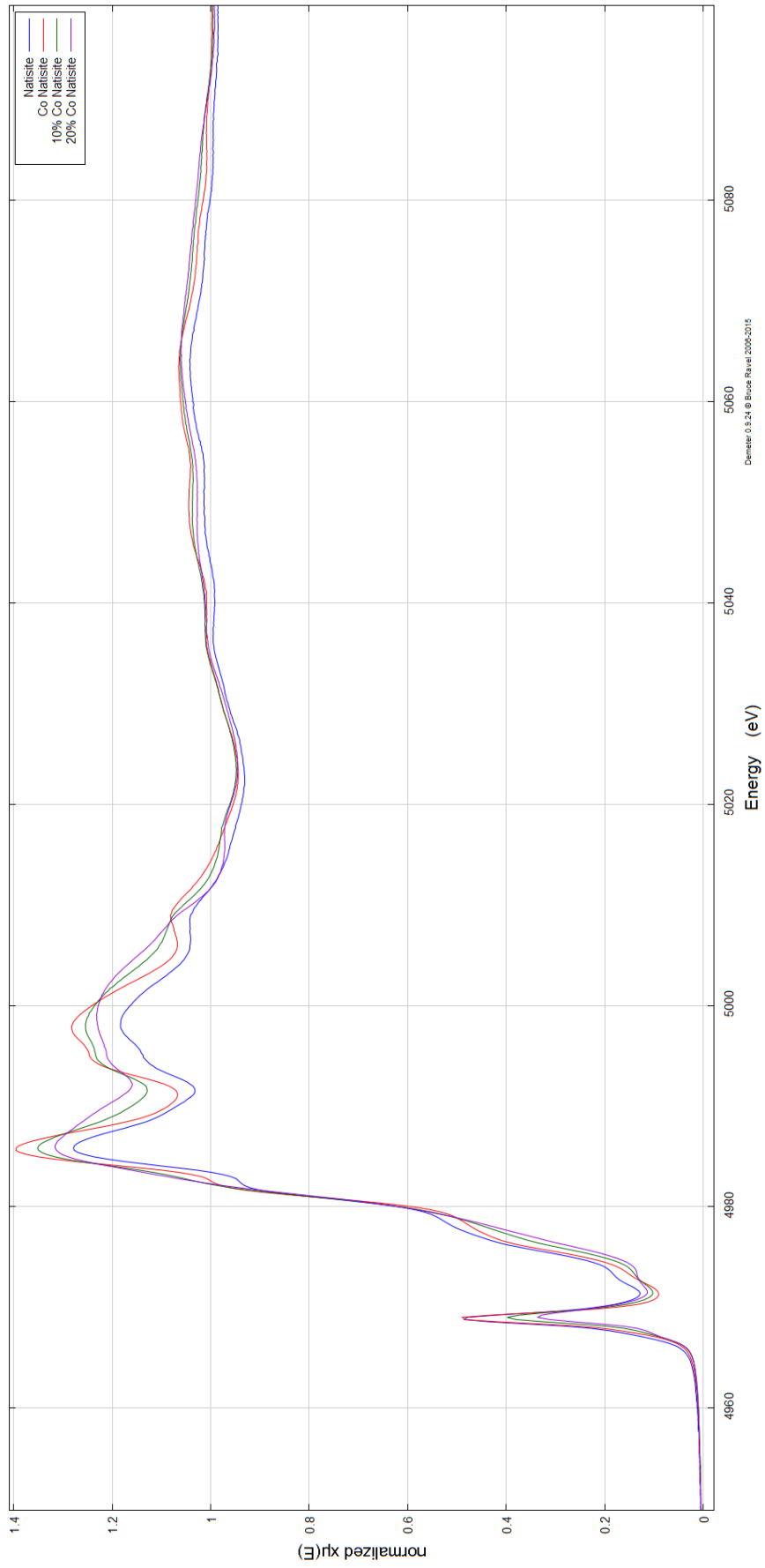


Figure 4.20 – Ti-edge XANES region of natisite, 10% Zr and 20% Zr Co-exchanged natisite.

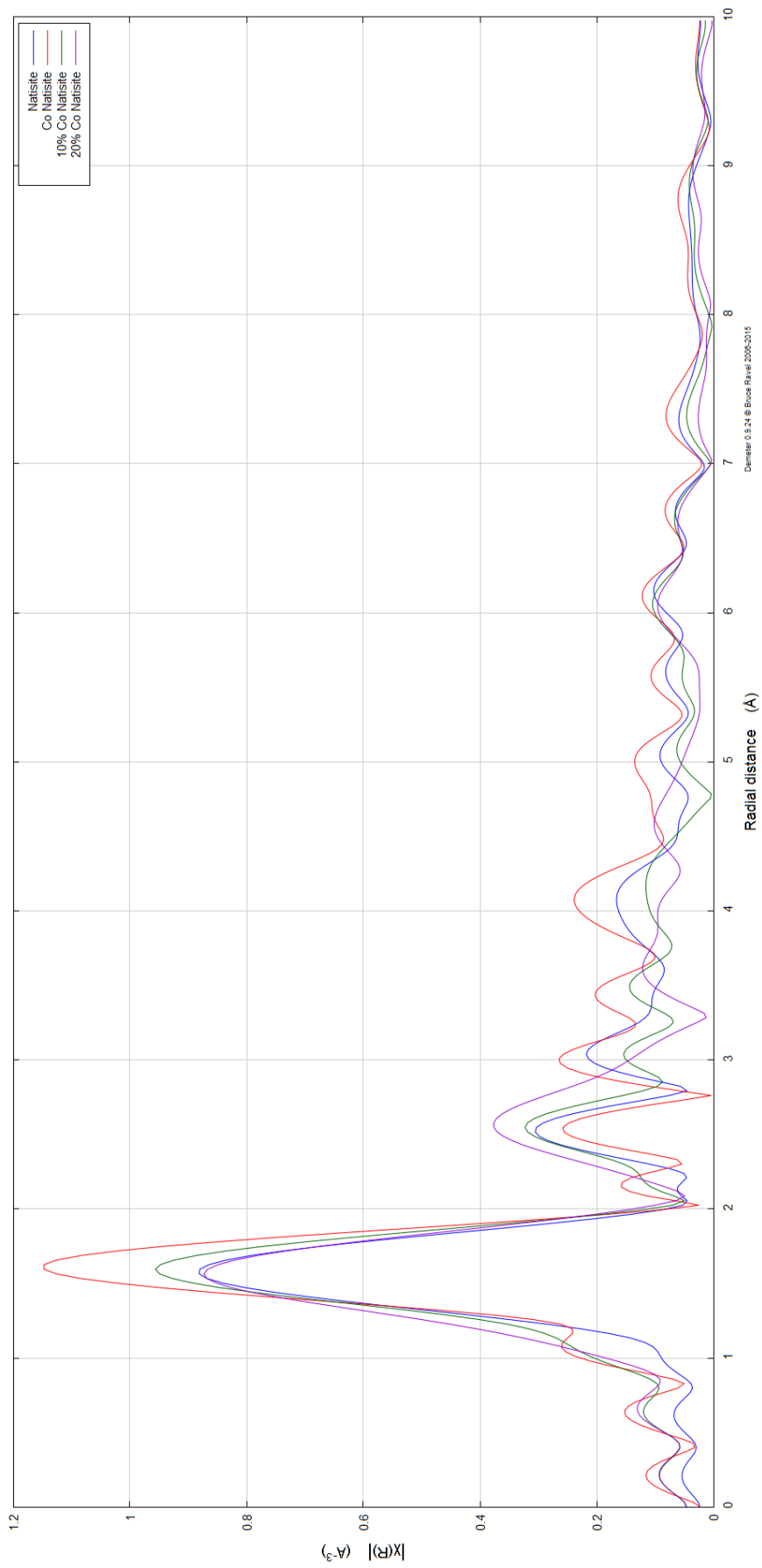


Figure 4.21 – Fourier Transform of figure 4.20, detailing relative atomic distances.

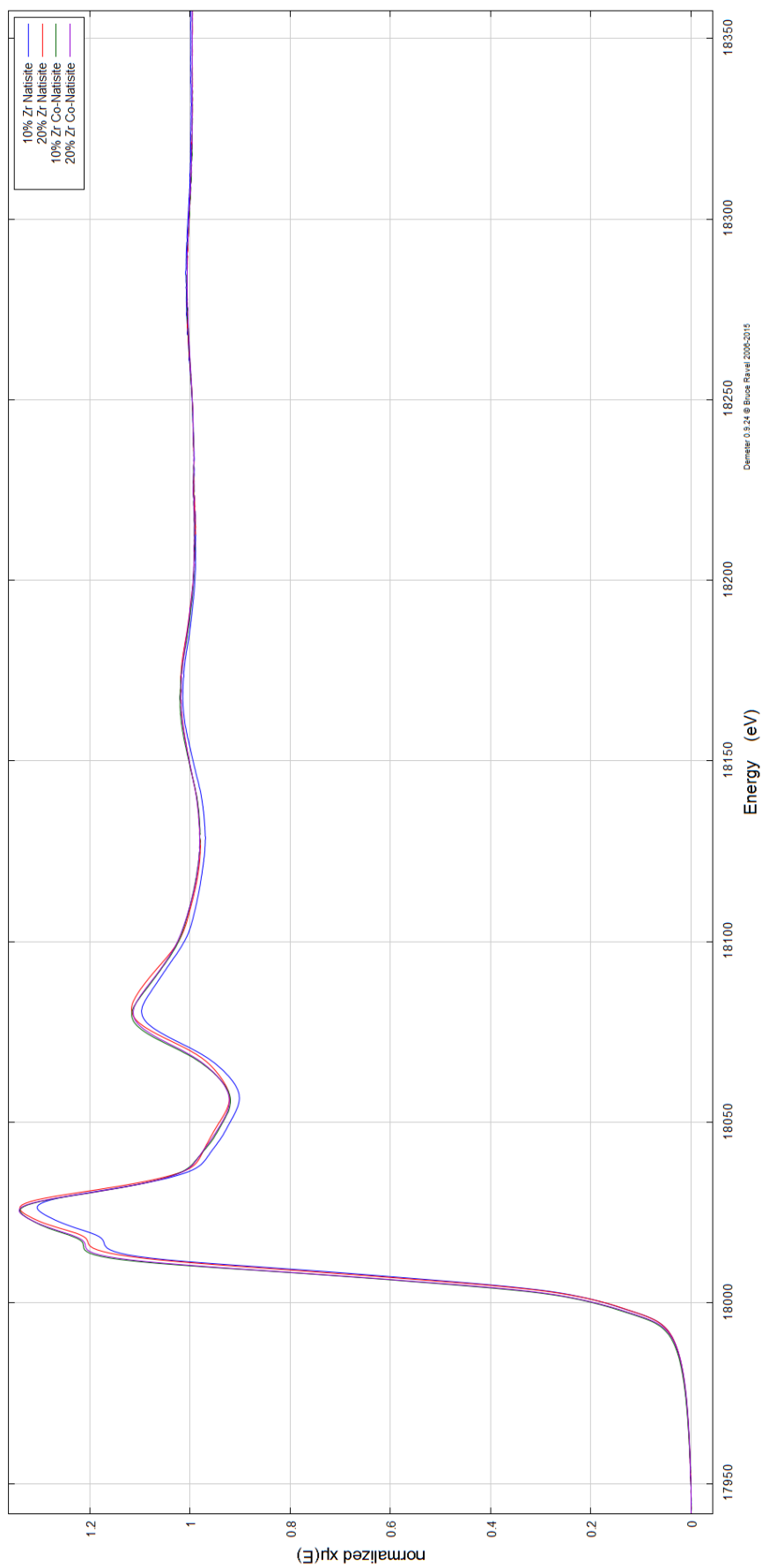


Figure 4.22 –Zr-edge XANES region of natisite, 10% Zr and 20% Zr Co-exchanged natisite.

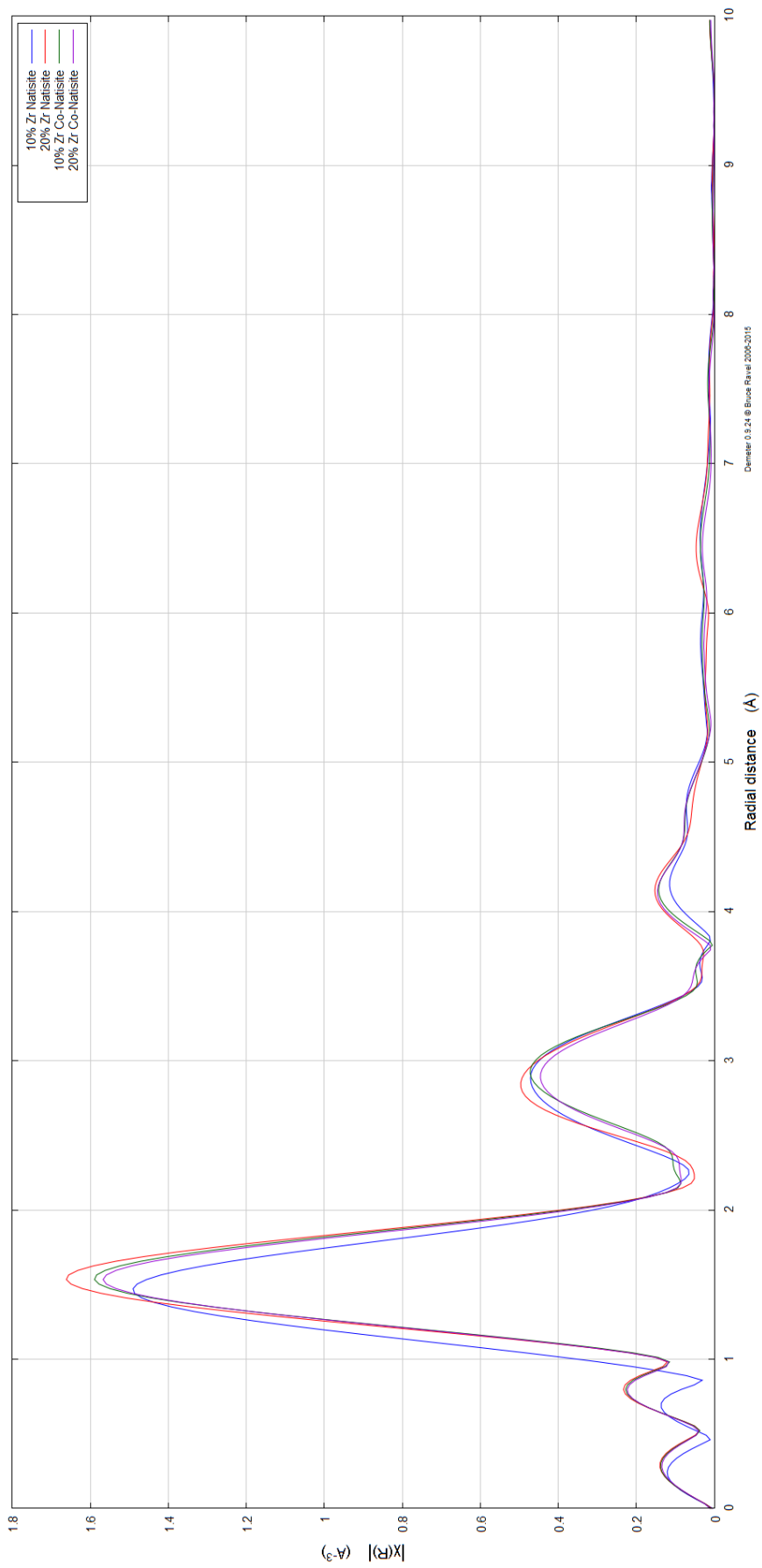
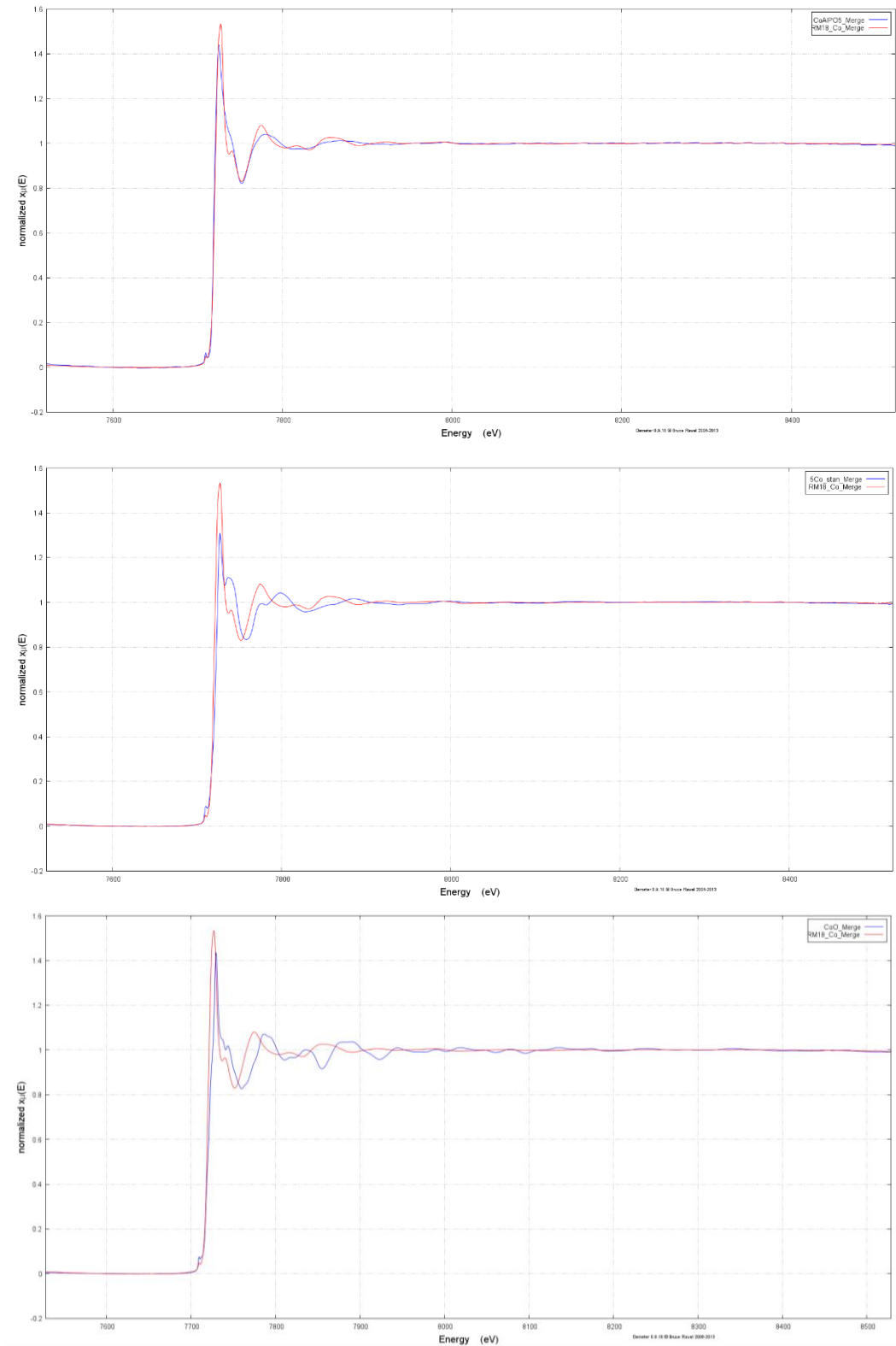
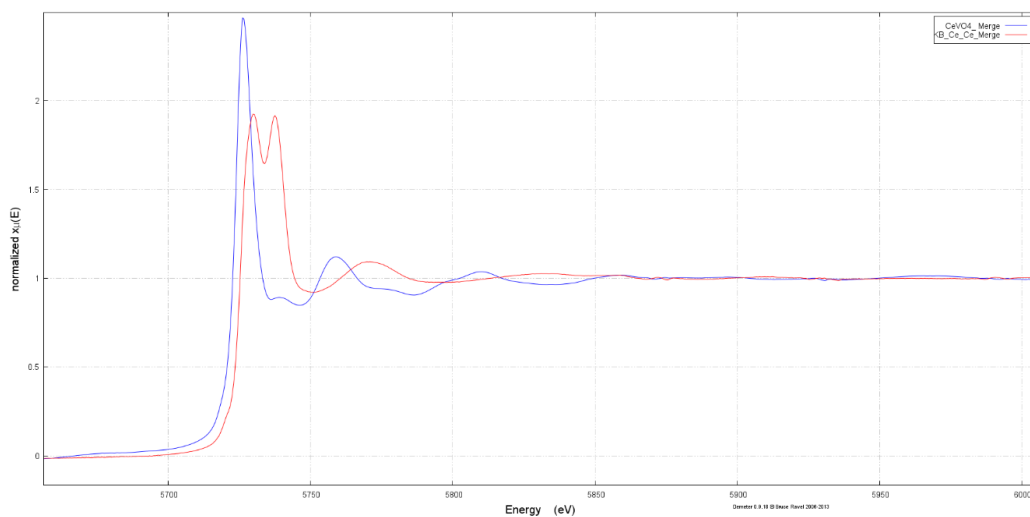
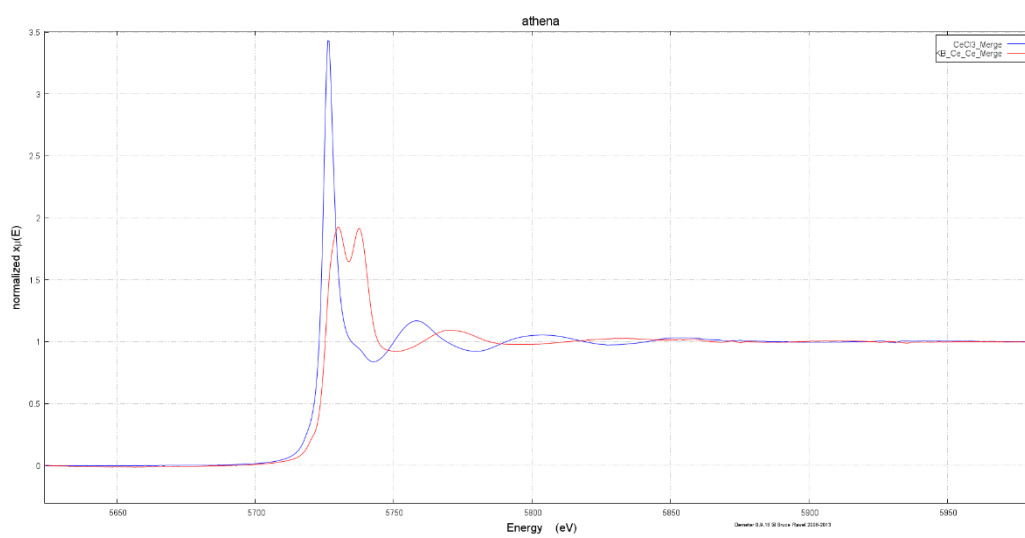
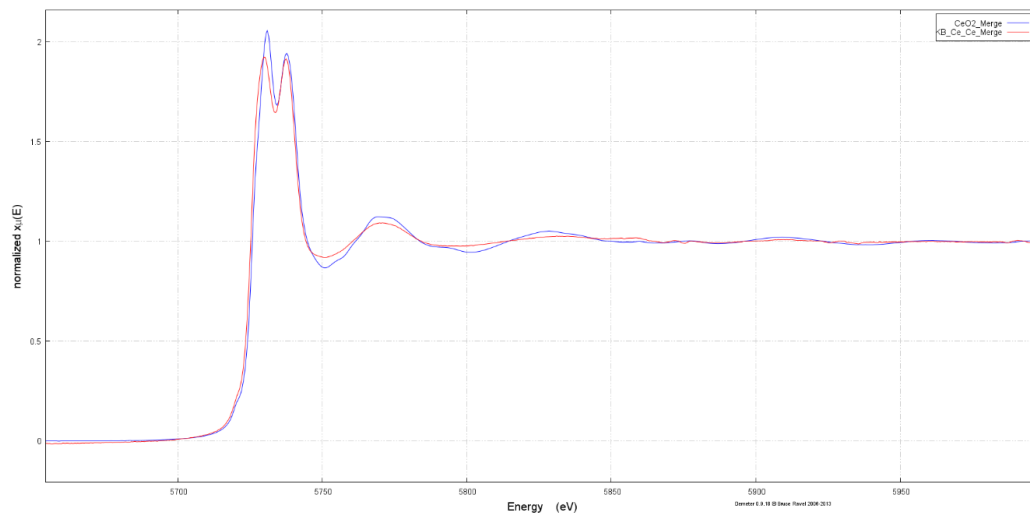


Figure 4.23 – Fourier transform of figure 4.22, detailing relative atomic distances.



**Figure 4.24 –XANES region of Co edge 20% Zr-natisite against (Top) 4-coordinate (Middle) 5-coordinate (Bottom) 6 coordinate Co standards.**



**Figure 4.25 –XANES region of Ce edge natisite against (Top) CeO<sub>2</sub> (Middle) CeCl<sub>3</sub> (Bottom) CeVO<sub>4</sub>.**

## 4.5: Summary

10% and 20% Zr natisite can both be successfully synthesised using hydrothermal methods with the small presence of a Zr containing impurity phase. It was determined that the impurity phase has no substantial ion-exchange capabilities and therefore does not significantly affect the ion-exchange results. This is supported by the Co ion-exchange results where the Zr doped analogous instantly all turns a green colour. If the ion-exchange results were being affected by the impurity phase, only 10% or 20% of the sample would have changed colour upon contact with the Co containing solution. Also, the SEM results do not show particles with two separate morphologies. Further indicating that there is some level of Zr substitution of Ti in the framework. However, it is noteworthy that the actual level of Zr in both the 10% and 20% Zr natisite samples will be slightly lower due to this impurity phase.

The XAS data used alongside the XRD patterns helps show that the substitution of framework Ti for Zr has been successful. This is shown by the decrease of amplitude of the Ti pre-edge feature and the changes in inter atomic distances. Results that would not be present if substitution had not occurred.

From the ion-exchange studies it was shown that the order of affinity was not altered in the 10% Zr natisite and in the 20% Zr natisite only Cs and Sr had been changed. However, the level of exchange of each ion that had increased, suggesting that the presence of Zr in the framework is making it easier for these cations to exchange with Na between the silicate layers. Again, a lack of crystallinity is seen with Ce and Nd XRD patterns, and the morphology of these again is inconsistent with that of the unexchanged samples. Fewer changes are observed with Co, Cs and Sr.

# *CHAPTER FIVE*

## *Competitive Ion-Exchanges*

### 5.1: Introduction

Previous chapters have described the ability of the materials to remove single cations from solution quantifying the level of exchange and providing an order of affinity. However, the composition of waste within the nuclear industry is unlikely to contain a single cationic species without any competing ions within the solution. It is much more likely that there will be a number of different cations within the waste, including ions such as of Ca, Mg and K found in natural water systems. It is therefore important to determine the effectiveness of the ion-exchange materials to selectively remove the cations of interest whilst leaving the competing ions in solution.

### 5.2: Competitive Ion-Exchange

This chapter details competitive ion-exchanges of each of the five cations of interest against the cations of Ca, K and Mg, commonly found in natural water. Na will be found in large quantities in natural water and also in waste streams but as it is the charge balancing cation in natasite, it has not been investigated as a competing ion in this work. Also, each of the main five cations ( $Ce^{4+}$ ,  $Co^{2+}$ ,  $Cs^{+}$ ,  $Nd^{3+}$  and  $Sr^{2+}$ ) are exchanged against each other to see if the order of affinity or level of exchange differs in the presence of other cations of interest.

### 5.2.1: Sample Preparation

The concentration of each nitrate ion in 125 ml of di-water at room temperature was 0.1M with a total concentration of 0.2 M. This solution was mechanically stirred at 300 rpm with the use of a glass coated magnetic follower. 0.5 g of natisite, 10% Zr or 20% Zr natisite was added to the mixed ion solution and left for a period of 18 hours. The resulting powder was collected by filtration and washed with copious amounts of di-water. A small sample of the waste solution was obtained for analysis.

### 5.2.2: Analysis

#### 5.2.2.1: ICP-MS

In order to quantitatively determine the level of exchange of each ion, ICP-MS was performed on the waste solution post exchange. By knowing the initial concentration, the amount of liquid after filtration and the dilution factor from the ICP-MS, a percentage level of exchange can be calculated for each of the ions in solution, therefore being able to provide quantitative results for the exchange of each ion.

As started previously the charge of each cation should be considered when replacing the Na +1 charge. The same calculation method detailed in chapter three was used to determine percentage exchange in this chapter.

Table 5.1 shows the ion-exchange of the Ce ion against other cations investigated in this work. The first trend noted is the level of Ce exchange is much lower than seen than the exchange with single ion-exchange experiments with natisite, 10% Zr and 20% Zr natisite

having percentage exchange values of 52%, 60% and 67% respectively in the single exchange experiments.

Table 5.1 –ICP-MS results showing percentage exchange. (Ce % / competing ion %).

<b>Ce Competitive Exchanges</b>	<b>Natisite</b>	<b>10% Zr Natisite</b>	<b>20% Zr Natisite</b>
Co	16/31	14/38	15/27
Cs	14/53	20/50	31/54
Nd	16/18	15/18	14/15
Sr	14/26	30/45	31/50
Ca	19/20	32/25	29/24
K	15/57	13/60	13/62
Mg	20/23	24/20	27/20

This can be explained by the presence of a competing ion in the solution. With a 1:1 solution it would be expected that 50% less exchange of both ions would take place if they had similar affinities therefore it would be expected that the level of any single cation would be lower in these competing ion-exchanges experiments. Another possible reason for the lower level of Ce exchange observed is due to the formation of CeO<sub>2</sub> nanoparticles allowing exchange of other ions. Without in-situ Ce ion-exchange work, the rate or mechanism of formation of the CeO<sub>2</sub> nanoparticles in this work is unknown. However, it is entirely possible that in a two-ion containing solution that the Ce mechanism is much slower than the exchange of the competing ion, therefore a reduced amount of Ce is able to exchange and adsorb to the natisite framework.

Levels of Cs exchange have also increased with the presence of Ce in the same solution from 4% exchange of Cs in the single ion-exchange experiments up to 53% when Ce is the competing ion. Despite Ce having a higher affinity for each of the natisite samples investigated in the single exchange experiments, in the competitive exchanges Cs is now exchanged at a higher amount compared to Ce. This could be due to the CeO<sub>2</sub> nanoparticles forcing the layers apart in such a way that makes Cs exchange much more facile. Either displacing some Ce adsorbed to the surface or not allowing the further exchange of Ce to levels seen within the single exchanges.

The Ce/Nd exchanges show lower levels of exchange for both ions compared to the single ion-exchange experiments with the level of exchange of both of the ions remaining similar despite the increasing Zr levels in ion exchange material.

With respect to the Ce/Sr exchange, the general trend of increased Sr uptake with increasing Zr content is again observed but similarly to that of the Ce/Cs exchanges where the Cs is at higher levels, again indicating that the presence of Ce is facilitating higher levels of exchange though the forcing of the natisite layers apart. The level of exchange for Ce against the ions of Ca and Mg is higher for the Zr containing natisite samples and only 11% and 4% lower for the unmodified natisite for Ca and Mg respectively.

The levels of exchange with regards to K however is very different. There are much higher levels of K uptake (up to 62%) than any other ion investigated. This could be due to the same plus 1 charge being on the K ion going in as the Na coming out. Also with the addition of Ce forcing the silicate layers apart allowing for the easier exchange of cations, could contribute to the high levels seen.

In general, the level of Ce exchange remains constant, at around 15%, though the competitive ion-exchange work regardless of the level of Zr doping. Increases in exchange of Cs and Sr could be due to the forcing a part of the silicate layers by the CeO<sub>2</sub> nanoparticles produced. Co and Nd levels of exchange are lower than seen in singles exchanges but could be due to slower uptake by the material and limited space due to CeO<sub>2</sub> uptake. *In-situ* ion-exchange experiments would need to be conducted to gain a clearer understanding of the ion-exchange mechanism with regards to the competitive ion-exchange experiments.

Table 5.2 shows the competitive ion-exchange results for Co against other competing ions. Ce is omitted from this table as the results have already been presented in table 5.1. The levels of Cs removal when in a Co containing solution is 33% lower for natisite, 9% lower for

Table 5.2 –ICP-MS results showing percentage exchange. (Co % / competing ion %).

Co Competitive	Natisite	10% Zr Natisite	20% Zr Natisite
Exchanges	±1%	±1%	±1%
Cs	21/20	26/41	24/44
Nd	28/18	30/18	32/18
Sr	28/24	29/25	30/26
Ca	27/22	30/24	33/23
K	25/20	28/18	35/15
Mg	29/25	28/21	30/20

10% Zr natisite and 10% lower for 20% Zr natisite than those found when Ce is the competing ion. The levels of exchange do increase with increasing Zr content following the

trend seen with the singles ion-exchanges. The levels of Co removal is uncorrelated to either the amount of Zr in the framework or amount of Cs exchanged.

The level of Nd exchange is unchanged in this series of competitive ion-exchanges, despite the increase of Zr. There is however a steady increase of Co uptake, although this is a relatively small increase and still lower than was observed with the single exchanges.

The Co/Sr levels of exchange are almost constant showing a slight increase of 1% with increasing Zr content. Natisite, 10% Zr and 20% Zr all have a higher affinity towards Co than the commonly found water ions. This was despite the trend seen with the Ce exchanges where the levels of K were much higher than seen in with the Co exchanges. As discussed previously, the introduction of Zr into the framework does not increase the affinity towards Co but does increase the rate of exchange. It is therefore possible that Co is exchanging into the material much faster than K, causing the levels of K to be much lower over the time period studied.

Table 5.3 shows the competitive ion exchange data for Cs against other competing ions. (Ce and Co have been omitted from this table). Similar to the trends seen in the Ce and Co series, the level of Cs exchange is much higher than seen in the single exchanges while the level of Nd exchange is much lower. Cs is seen to be the preferred cation over each of the competing ions in table 5.3, with the exception of K where levels are higher across all three natisite samples. Again, this could be due to the same charge and similar ionic size of the Na<sup>+</sup> (1.02 Å) and K<sup>+</sup> (1.38 Å) ions exchanging. The level of Cs exchange with respect to undoped natisite has increased from 4% in the single exchanges to a high of 35% in the competitive ion exchanges. The levels of Nd show a small decrease in percentage exchange compared to the values presented in table 5.1 and 5.2.

Table 5.3 –ICP-MS results showing percentage exchange. (Cs % / competing ion %).

Cs Competitive	Natisite	10% Zr Natisite	20% Zr Natisite
Exchanges	±1%	±1%	±1%
Nd	24/16	37/14	37/14
Sr	25/22	40/24	38/20
Ca	35/22	42/24	43/24
K	35/39	41/53	40/58
Mg	33/15	44/22	38/20

Both Ca and Mg levels of exchange are relatively low compared to Cs with the average percentage exchange difference over natisite, 10% Zr natisite and 20% Zr natisite being 16% for Ca and at 19% for Mg. The percentage exchange is similar to the values seen with the Ce and Co series of exchanges, indicating that all of the natisite samples have a lower affinity towards Mg and Ca regardless of the competing ion in solution.

Table 5.4 shows the competitive ion exchange data for Nd against other competing ions. (Ce, Co and Cs have been omitted from this table). The level of Nd exchange in the presence of a competing ion remains at a constant level of 14 - 16% but again lower than the levels seen with the singles exchanges where 27% exchange was observed. The level of K exchange is again higher than Ca or Mg (6% - 13% higher) following the trend observed with Ce, Co, and Cs. The level of Sr removal is at similar levels to those previous competitive exchanges with the exception of the Ce series.

Table 5.4 –ICP-MS results showing percentage exchange. (Nd % / competing ion %).

<b>Nd Competitive</b>	<b>Natisite</b>	<b>10% Zr Natisite</b>	<b>20% Zr Natisite</b>
<b>Exchanges</b>	<b>±1%</b>	<b>±1%</b>	<b>±1%</b>
Sr	15/20	15/28	13/18
Ca	14/22	14/21	14/24
K	15/30	16/32	16/30
Mg	15/22	15/21	14/19

Table 5.5 shows the competitive ion-exchange data for Sr against other competing ions. (Ce, Co, Cs and Nd have been omitted from this table). Following the trends seen with the other exchanges K exchange is still removed at a higher rate than either Ca or Mg. However, the level of Sr exchange with K as the competing ion produces higher levels of Sr exchange from a high of 19% with Ca or Mg to 32% Sr exchange with K as the competing ion. Indicating that the exchange of K is facilitating the exchange of Sr at higher levels than with Ca or Mg. This is despite K having a much larger ionic radius of 1.32 Å compared to Na at 1.02 Å, Sr at 1.18 Å, Ca at 1 Å and Mg at 0.72 Å.

Table 5.5 –ICP-MS results showing percentage exchange. (Sr % / competing ion %).

<b>Sr Competitive</b>	<b>Natisite</b>	<b>10% Zr Natisite</b>	<b>20% Zr Natisite</b>
<b>Exchanges</b>	<b>±1%</b>	<b>±1%</b>	<b>±1%</b>
Ca	22/17	19/15	21/19
K	28/32	27/35	30/35
Mg	26/14	26/16	25/19

Levels of exchange with two ions in solution shows successful exchange of each ion albeit at lower levels than observed with the single exchanges. It appears from the ICP-MS data that exchanges where one ion is Ce that this facilitates higher levels of exchanges compared to any other cation. Nd exchanges remain much lower than the single exchanges at around 15% compared to 27% in the singles exchange experiment, regardless of Zr doping or competing cation.

K is the most preferred competing ion in all competitive ion-exchange experiments, apart from those where Co is the competing ion, where it is believed the inclusion of Zr in the natisite framework is increasing the rate of Co exchange limiting the overall amount of K exchange possible.

#### 5.2.2.2: XRD

XRD analysis was performed on competitive ion-exchanges to investigate any differences in diffraction pattern and therefore any structural changes from the single ion-exchanges. Figure 5.1 shows a diffraction pattern from the natisite Ce/Cs competitive ion-exchange.

As observed with the single Ce ion-exchange there is a loss of crystallinity caused by a loss of long range order and a number of peaks which correspond to the layers of natisite remaining intact. Despite the level of Ce exchange in the competitive ion-exchanges being 36% lower, there is still a loss of long range order

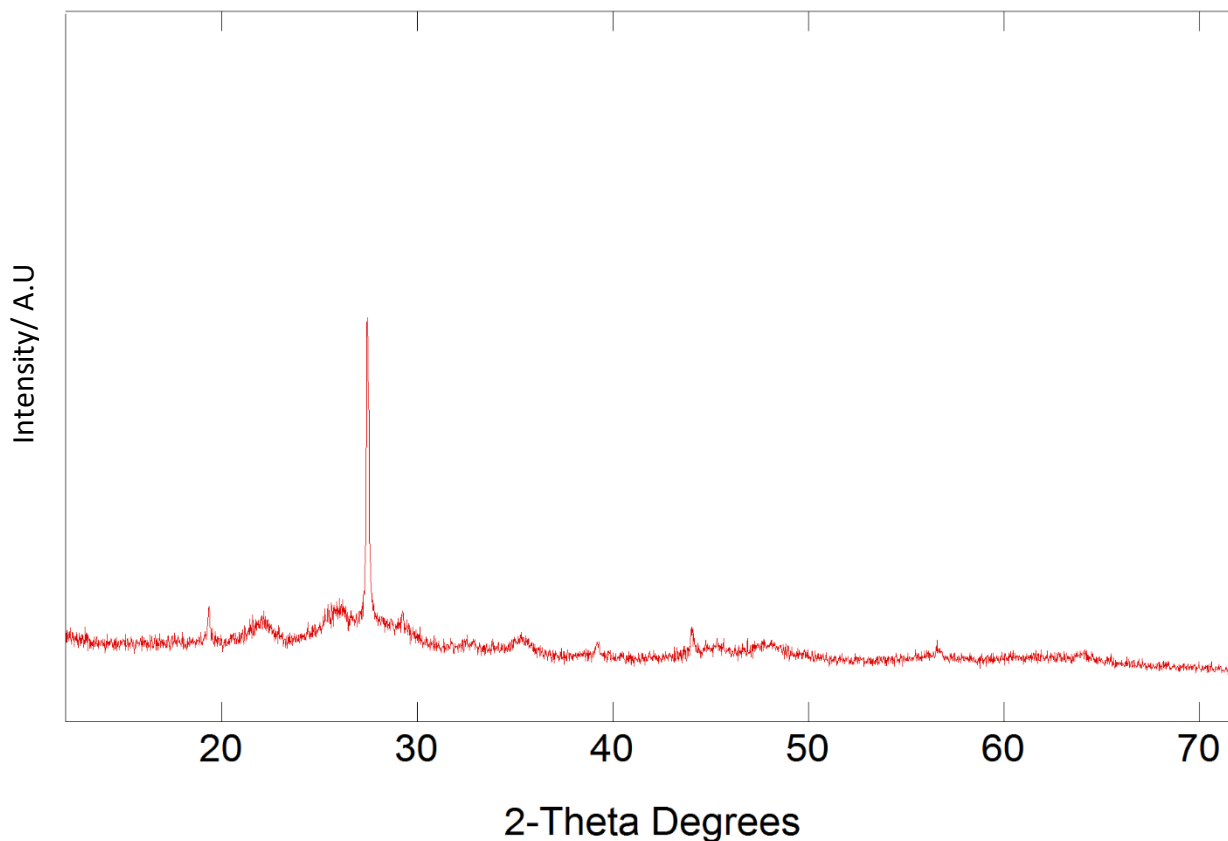


Figure 5.1 – XRD pattern of Ce/Cs competitive ion-exchange with pure Ti-natisite.

Figure 5.2 shows a Pawley fit of the Ce/Cs competitive ion-exchange. It is unknown from the diffraction pattern alone if the increased level of Cs exchange has had an effect on the crystallinity of the material however the lattice parameters has changed from  $a = b = 6.4894(33) \text{ \AA}$   $c = 5.0936(31) \text{ \AA}$  in the single Ce ion-exchange to  $a = b = 6.4978(27) \text{ \AA}$   $c = 5.0938(28) \text{ \AA}$  indicating that Cs is successfully exchanging and causing an effect on the lattice parameter.

It is mainly the  $ab$  parameter which is changing indicating that there are changes in the actual layer of the material. However, these cannot be investigated further using traditional diffraction methods alone.

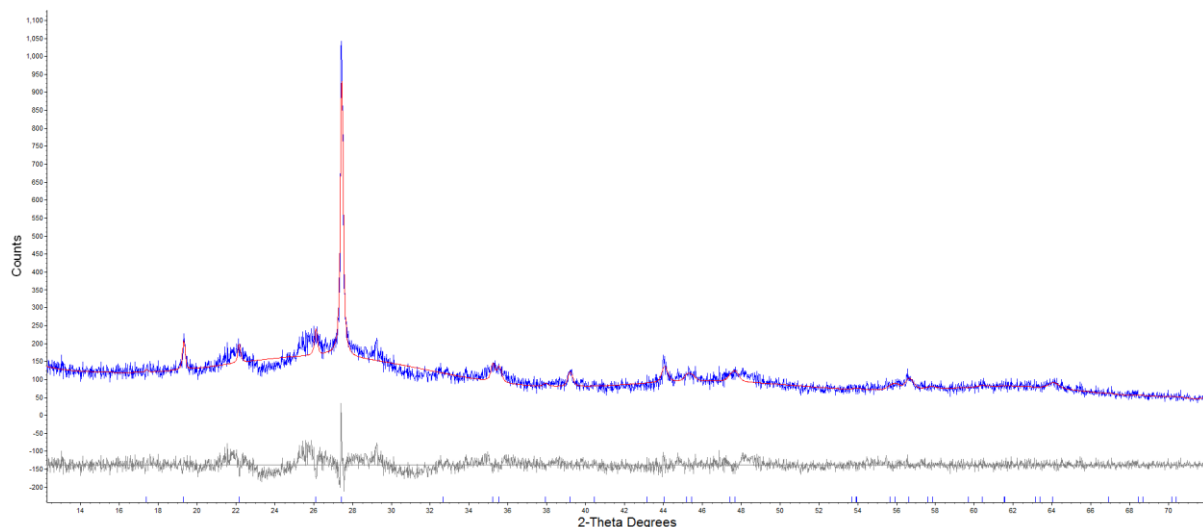


Figure 5.2 – Pawley fit of Ce/Cs competitive ion-exchange with pure Ti-natisite.

Figure 5.3 shows the diffraction pattern of Co/K competitive ion-exchange 20% Zr natisite. This competitive ion-exchange had the lowest level of K exchange due to the fast rate of Co exchange with the Zr-containing natisite sample. The diffraction pattern shows a higher background associated with the fluorescence of Co.

The lattice parameters again have changed from the 20% Zr single Co ion exchange, showing an increase of the *ab* parameter from 6.4629(35) to 6.4799(15) and an increase in the *c* parameter from 5.0314(25) to 5.0792(25). This marginal increase of lattice parameter can be attributed to the exchange of both the ions from solution.

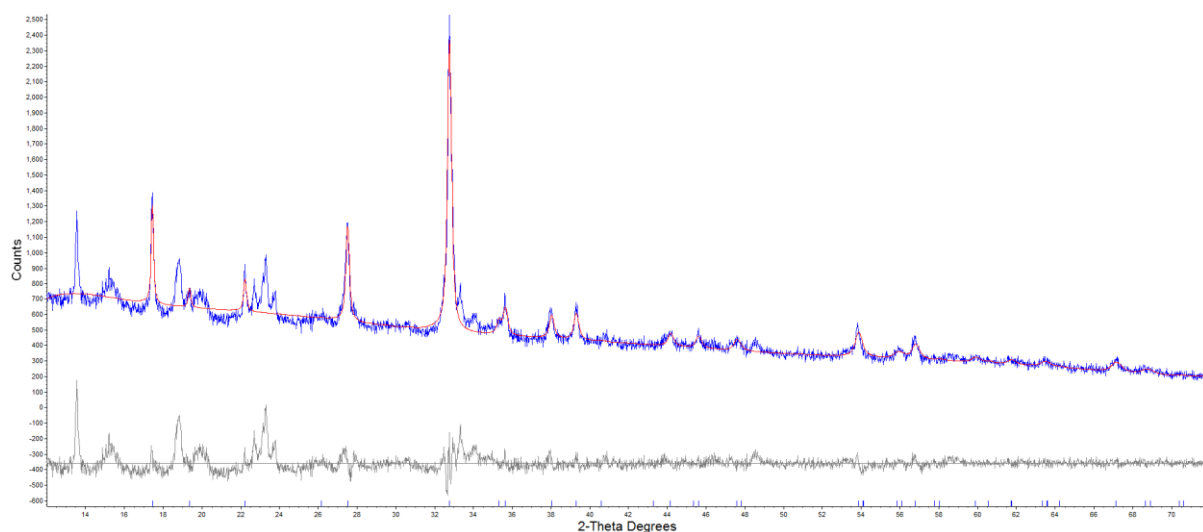


Figure 5.3 – Pawley fit of Co/K competitive ion-exchange with 20% Zr natisite.

Figure 5.4 shows the 10% Zr Cs/Sr competitive ion-exchange. The increased exchange of Cs seems to have little effect on the diffraction pattern, keeping the long-range order of the material intact. This exchange showed an increase exchange of 33% with respect to Cs compared to the single 10% exchange, with a 3% increase of Sr exchange also being observed. It would have been expected that the level of both Cs and Sr to remain low due to the low levels of removal of these ions in the single ion-exchanges. However, the presence of a competing ion dramatically increases the removal of both Cs and Sr.

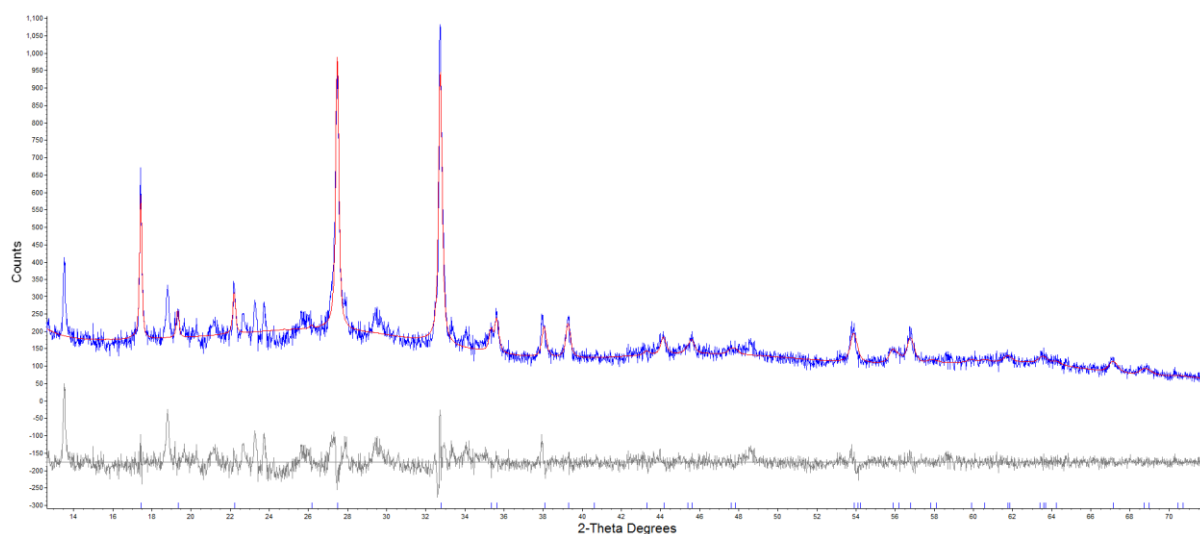


Figure 5.4 - Pawley fit of Cs/Sr competitive ion-exchange with 10% Zr natisite.

Figure 5.5 shows a Pawley fit of 10% Zr natisite Nd/Sr competitive ion-exchange. From the diffraction pattern, again a loss of crystallinity is observed, similar to the results found with regards to the single Nd ion-exchanges. Suggesting again that the large Nd ion is disrupting the long-range order of that material, but not to the same extent with that seen with Ce exchanges. Despite the level of Zr doping or competing ion, the level of Nd exchange is around 15% where-as the competing ions fluctuate from 14% to 37%, indicating that the rate of Nd exchange may be slower than that of competing ions, and therefore only allowing a relatively small percentage of Nd to exchange.

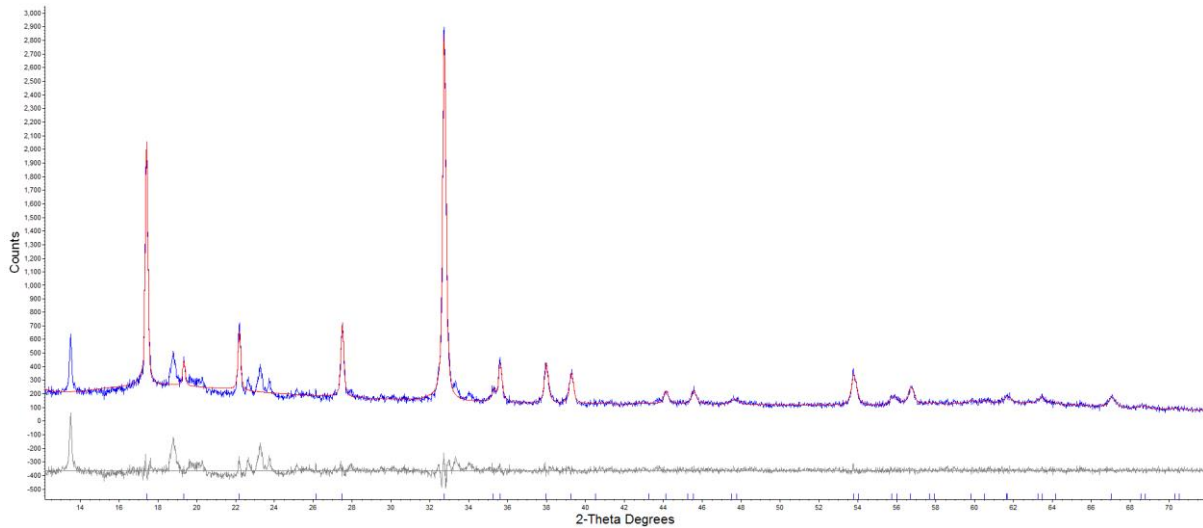


Figure 5.5 - Pawley fit of Nd/Sr competitive ion-exchange with 10% Zr natisite.

### 5.2.2.3: XRF

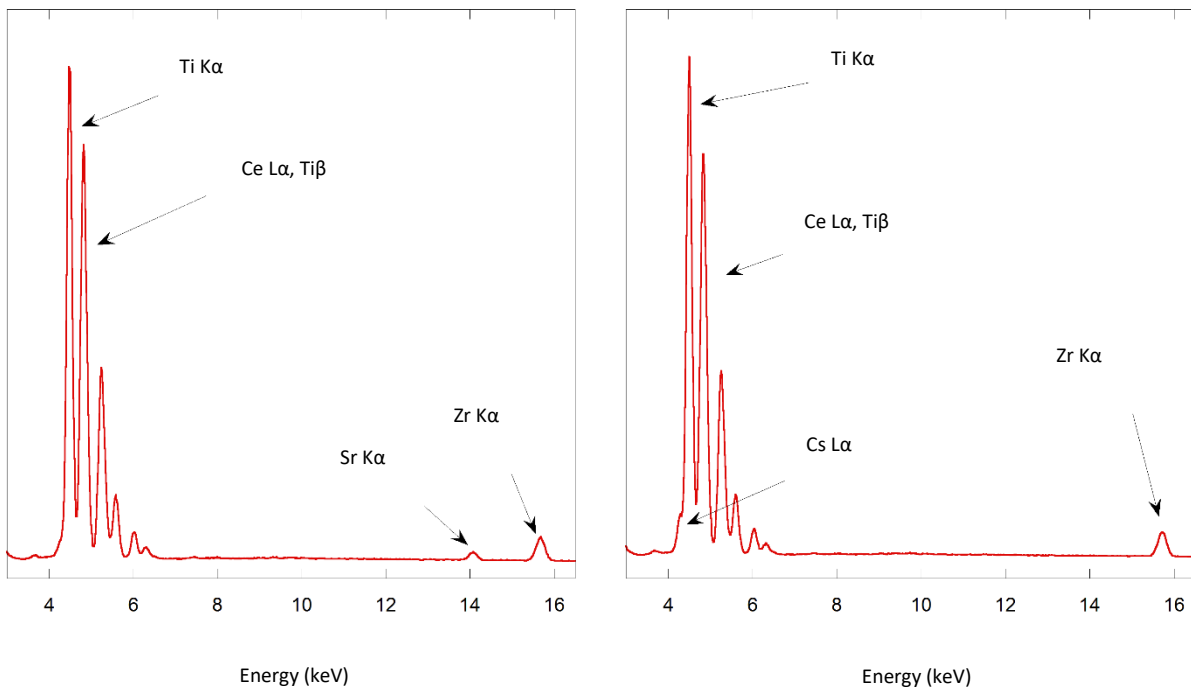


Figure 5.6 – XRF spectra of (Left) 10% Zr natisite Ce/Sr exchange and (Right) 10% Zr natisite Ce/Cs.

With the Ce/Cs and Ce/Sr despite the higher levels of Cs and Sr exchange, there are still relatively small signals for those elements observed from the XRF. For Cs figure 5.6 (right) the possible reason is due to the overlap of the Cs L line and the Ti K line. The XRF used in this

work is unable to detect the Cs K line. Similarly, the Sr K line signal is again small but could be attributed to the large signal from both the Ti K line and Ce L line causing this peak to appear smaller than the ICP data would have suggested it to be, potentially due to matrix effects.

### 5.3: Summary

The competitive ion-exchanges shows that the level of exchange of certain ions is altered in the presence of competing ions. K is the most preferred competing cation in the exchanges apart from with Co is the competing ion. However, K is not found in such high concentrations in natural water systems or in nuclear waste streams, therefore the level of K exchange is not such an issue. The levels of Ca and Mg exchange are relatively low compared to the ions of choice, suggesting that the materials can successfully remove cations of choice whilst leaving these competing ions in solution.

Increases in the amount of Cs and Sr removal of the undoped material are observed regardless of the competing ion, indicating that the competing ions help facilitate the exchange of both Cs and Sr to much higher levels than the singles exchanges allow.

The levels of Ce and Nd removal are lower than those seen in the single exchanges but a loss of crystallinity is still observed in the XRD patterns. Also, where Ce or Nd is a competing ion, it allows higher levels of exchange of the competing ions than the level of exchange found in single exchanges.

The XRF used in this work is unable to provide qualitative. The results showed signals from both of the competing ions indicating that there has been successful exchange of both cations from solution. As this technique was unable to provide detailed information on levels

of exchange, and is susceptible to experimental bias, it was not extensively used in the determination of levels of exchange in the competitive ion-exchange work.

# *CHAPTER SIX*

## *Variable pH Ion-Exchanges*

### 6.1: Introduction

As discussed in chapter one, titanium silicates have been used within the nuclear industry due to their increased stability in extreme pH conditions compared to zeolites. Natural and synthetic zeolites undergo dealumination, the process of stripping aluminium from the framework, and therefore can no longer ion-exchange, which renders the materials as unusable in certain conditions. Titanium silicates however are more stable in both high and low pH conditions providing a viable alternative to the zeolites which have traditionally been used. Basic pH conditions are commonly used within the nuclear industry as a way to control the breakdown of nuclear products. Therefore, a material which could effectively exchange ions of choice at both acidic and basic conditions would be an advantage. Acidic conditions can also be found in high level nuclear waste reprocessing streams.

All previous ion-exchange experiments detailed in this work have been conducted at a neutral pH. It was therefore necessary to conduct a series of ion-exchange experiments in both acidic and basic conditions both to determine if natisite, 10% Zr and 20% Zr natisite would remain stable at these extreme pH conditions and if the order of affinity or level of exchange would be affected.

## 6.2: Acidic pH Ion-exchange

### 6.2.1: Sample Preparation

A 0.1 M solution of each nitrate ion was prepared in 125 ml di-water at room temperature. The pH of the solution was then adjusted to pH 3 using concentrated nitric acid. Each solution was mechanically stirred at 300 rpm with the use of a glass coated magnetic follower. 0.5 g of natisite was added to the acidic ion containing solution and left for a period of 18 hours. The resulting powder was collected by filtration and washed with copious amounts of di-water.

### 6.2.2: Analysis

#### 6.2.2.1: XRD

XRD patterns of the acidic ion-exchanges are shown in figure 6.2 with refined lattice parameters obtained by Pawley phase fitting shown in table 6.1.

The diffractions patterns show that crystallinity is maintained even at pH 3 with no notable differences to the pH7 exchanges (figure 6.1), with the exception of the Ce ion-exchange. As explained in previous chapters, is due to the formation of CeO<sub>2</sub> nanoparticles causing a loss of long range order. The stability of natisite at this pH shows that the material can still be effective in conditions that the traditionally used zeolites would start to degrade.

There are no notable differences between the diffraction patterns of the ion-exchanges at pH 3 and of those conducted at a neutral pH. No changes are again observed with respect to the Cs exchanges, suggesting from the XRD data alone that the level of Cs exchange remains relatively low at both pH 3 and pH 7

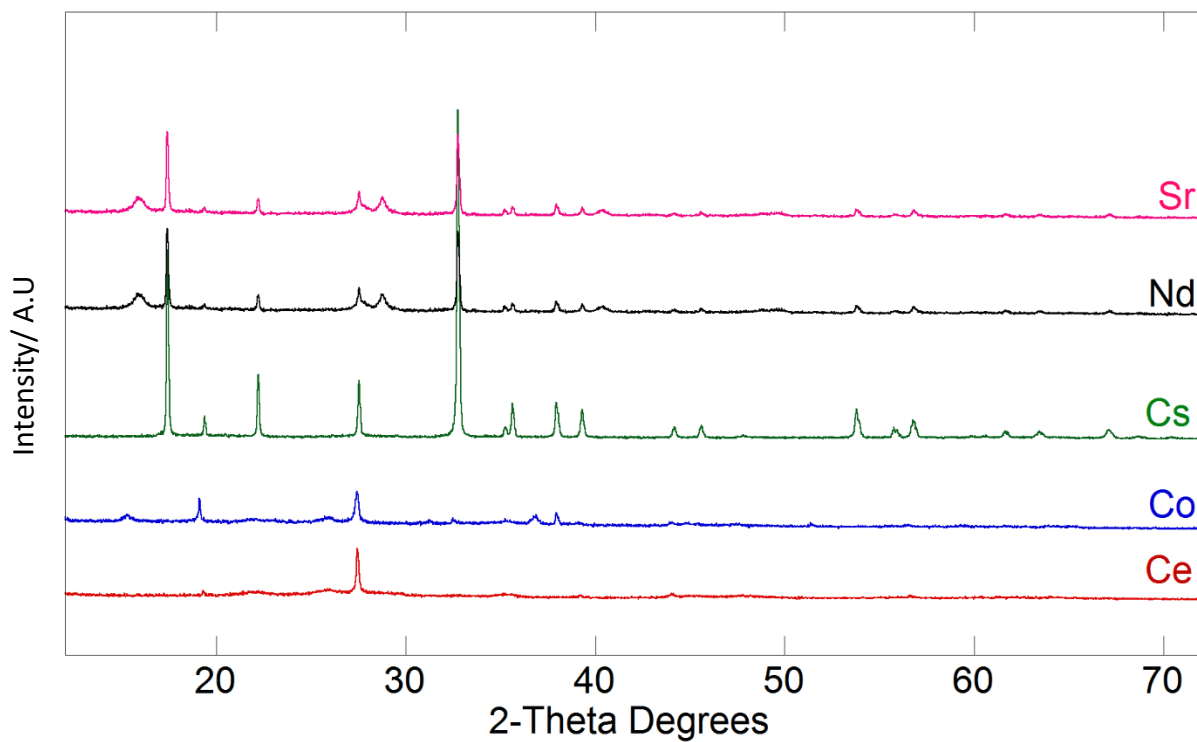


Figure 6.1 – XRD patterns of ion-exchanged natisite at pH 7.

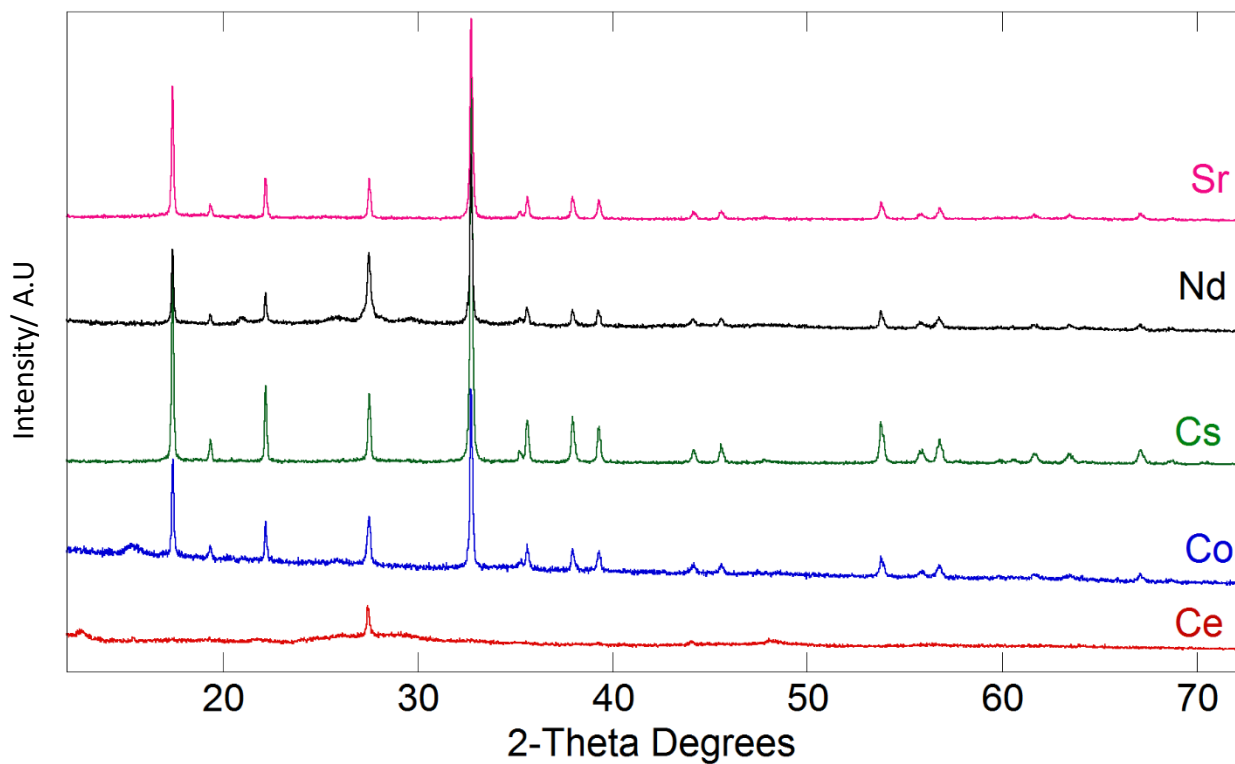


Figure 6.2 – XRD patterns of ion-exchanged natisite at pH 3.

Table 6.1 – Refined lattice parameters of ion-exchanged natisite at pH 3.

Ion	<i>ab</i>	<i>c</i>	RwP %	Difference to Synthesised Natisite	
				<i>a</i> / Å	<i>c</i> / Å
<b>Natisite</b>	6.4849(2)	5.0936(2)	12.807	-	-
<b>Ce</b>	6.5017(27)	5.1172(25)	11.922	0.01684	0.02354
<b>Co</b>	6.4853(4)	5.0893(6)	6.156	0.00038	-0.00435
<b>Cs</b>	6.4839(7)	5.0923(5)	9.927	-0.00104	-0.00134
<b>Nd</b>	6.4849(4)	5.0893(6)	10.925	-0.00003	-0.00433
<b>Sr</b>	6.4823(5)	5.0928(7)	10.748	-0.00265	-0.00085

There is slightly higher background associated with the pH 3 Co ion-exchange compared to the neutral exchange due to either the slight increase of Co exchange from 19% to 22% at pH 3 or the Co exchange and acidic conditions introducing more strain on the framework. The pH 3 Nd ion exchange shows a near identical *ab* parameter but a large difference in the *c* parameter, suggesting that again the large Nd ion is causing disruption in the way the layers are stacking, but not to the extent seen with the Ce exchanges.

Figure 6.4 and 6.5 show the diffraction patterns of 10% Zr and 20% Zr natisite ion-exchanges at pH 3 respectively. Again, few changes are observed between the neutral pH and the acidic pH, indicating that the Zr doped materials also remain stable in these conditions.

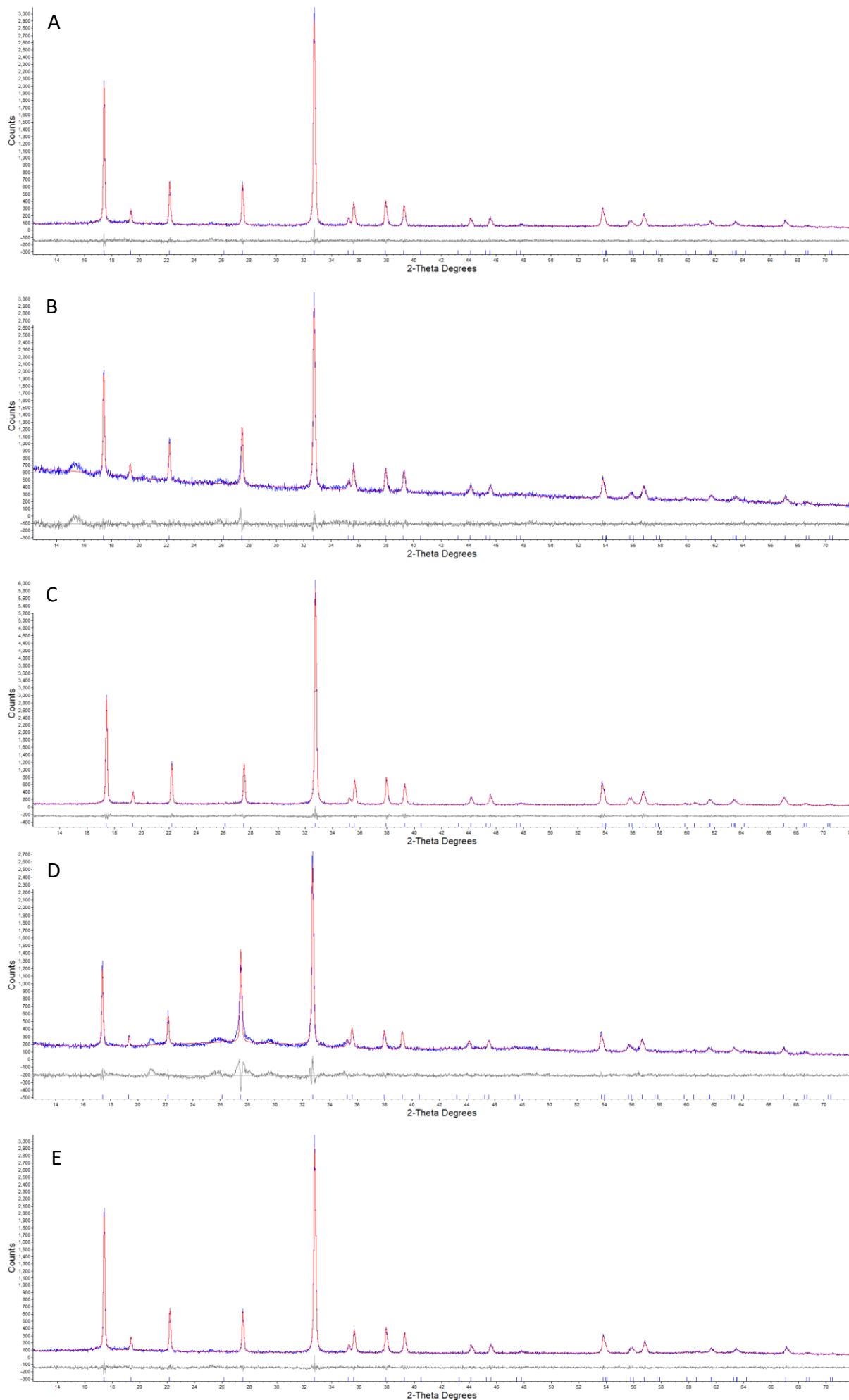


Figure 6.3 – Pawley fits of (A) Ce pH 3, (B) Co pH 3, (C) Cs pH 3, (D) Nd pH 3, (E) Sr pH 3 exchanged natisite.

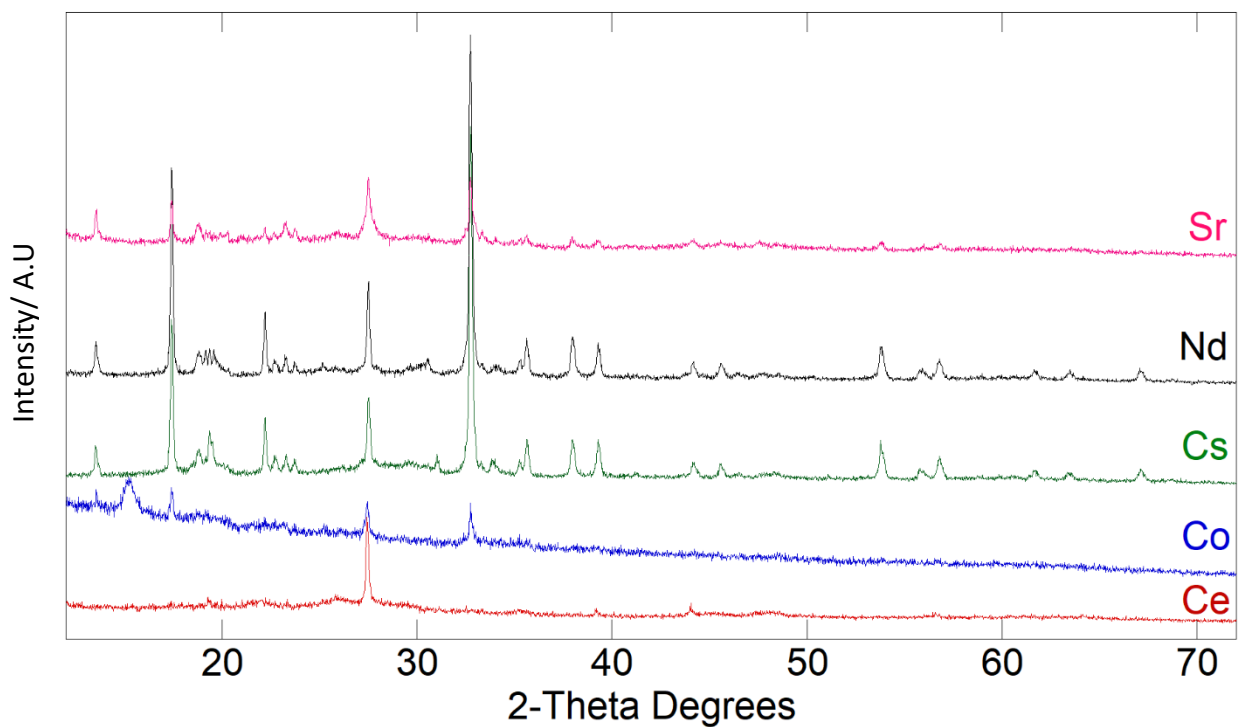


Figure 6.4 – XRD patterns of ion-exchanged 10% Zr natisite at pH 3.

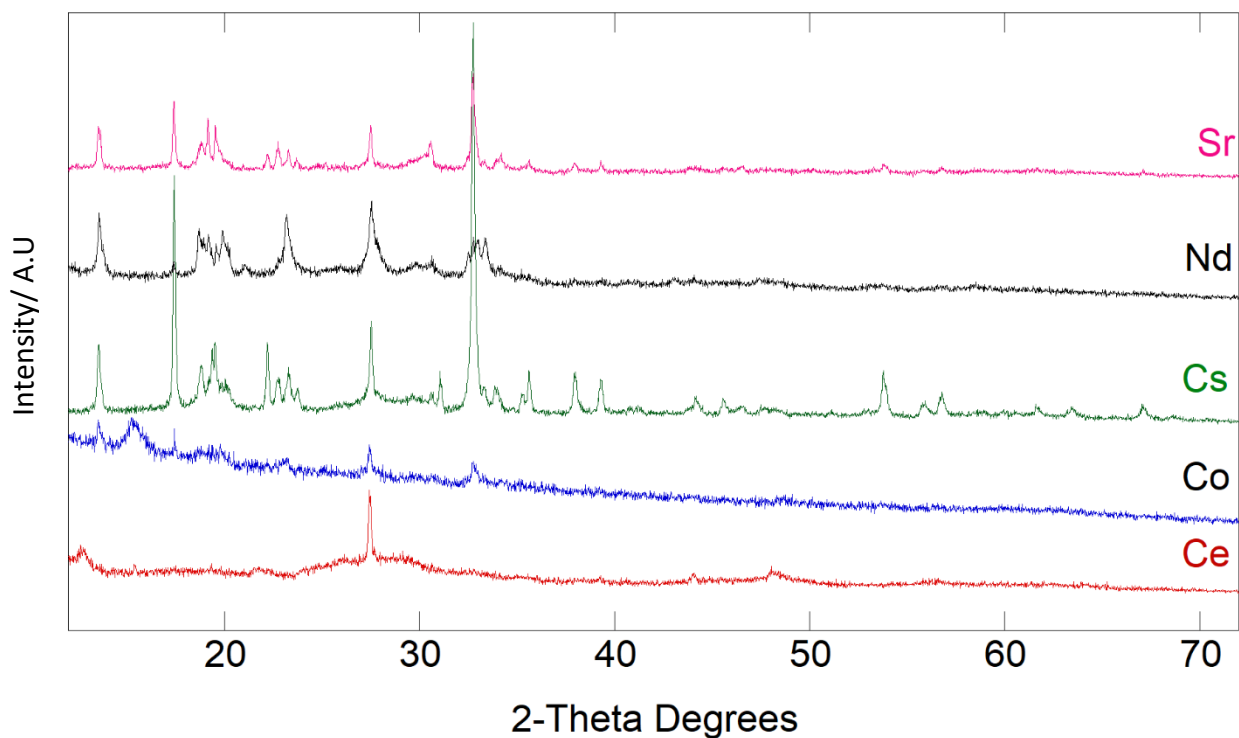


Figure 6.5 – XRD patterns of ion-exchanged 20% Zr natisite at pH 3.

## 6.2.2.2: ICP-MS

The same method for ICP-MS and the analysis detailed in previous chapters was used here. Table 6.2 shows the percentage exchange of natisite, 10% Zr natisite and 20% Zr natisite.

**Table 6.2 – Comparison of percentage exchange for natisite, 10% Zr natisite and 20% Zr natisite at pH 3.**

<b>Ion</b>	<b>Natisite % Exchange (pH7) ±1%</b>	<b>Natisite % Exchange (pH3) ±1%</b>	<b>10% Zr Natisite % Exchange (pH3) ±1%</b>	<b>20% Zr Natisite % Exchange (pH3) ±1%</b>
<b>Ce</b>	52	60	15	15
<b>Co</b>	19	22	31	35
<b>Cs</b>	4	9	45	50
<b>Nd</b>	27	35	17	15
<b>Sr</b>	6	13	28	30

The results show that exchange of all ions is still successful at pH 3. The level of Ce exchange however drops significantly when Zr is in the framework reducing the level of exchange from 60% to just 15%. In neutral conditions the levels of exchange with respect to the Zr doped analogues is much higher than those found in acidic conditions reducing from 60% with the 10% Zr natisite and from 67% with the 20% Zr natisite material. The Nd exchanges show a similar trend decreasing from 59% and 47% to 17% and 15% with the 10% Zr and 20% Zr natisite samples respectively. The other notable difference is the increased level of Cs exchange, increasing from 7% with respect to the 10% Zr material up to 45% in acidic conditions, with a further increase from 39% to 50% with 20% Zr natisite.

## 6.3: Basic pH Ion-Exchange

### 6.3.1: Sample Preparation

A 0.1 M solution of each nitrate ion was prepared in 125 ml di-water at room temperature. The pH of the solution was then adjusted to pH 10 using concentrated tertiary butyl ammonium hydroxide (TBAH). TBAH was chosen as a base which has a large bulky counter ion which was believed would not interfere with the ion-exchange process or effect the ICP-MS results. Each solution was mechanically stirred at 300 rpm with the use of a glass coated magnetic follower. 0.5 g of natisite was added to the basic ion containing solution and left for a period of 18 hours. The resulting powder was collected by filtration and washed with copious amounts of di-water.

### 6.3.2: Analysis

#### 6.3.2.1: XRD

XRD patterns of the basic ion-exchanges are shown in figure 6.6 with refined lattice parameters obtained from Pawley phase fitting shown in table 6.3.

The XRD patterns show that crystallinity is maintained at pH 10 with all samples apart from the Ce and Co. As seen at pH3 there was a loss of crystallinity associated with the Co exchange. This trend has continued at pH 10 with less crystallinity observed. This can be attributed to the solid Co which precipitated out of solution, increasing the amount of Co in the sample analysed by XRD increasing the fluorescence seen and therefore causing a high background. There is also a large change in the lattice parameter and errors compared to that of the unchanged natisite indicating a breakdown of the structure. Figure 6.7 and 6.8 show

the diffraction patterns of 10% Zr natisite and 20% Zr natisite ion-exchanges at pH 3 respectively.

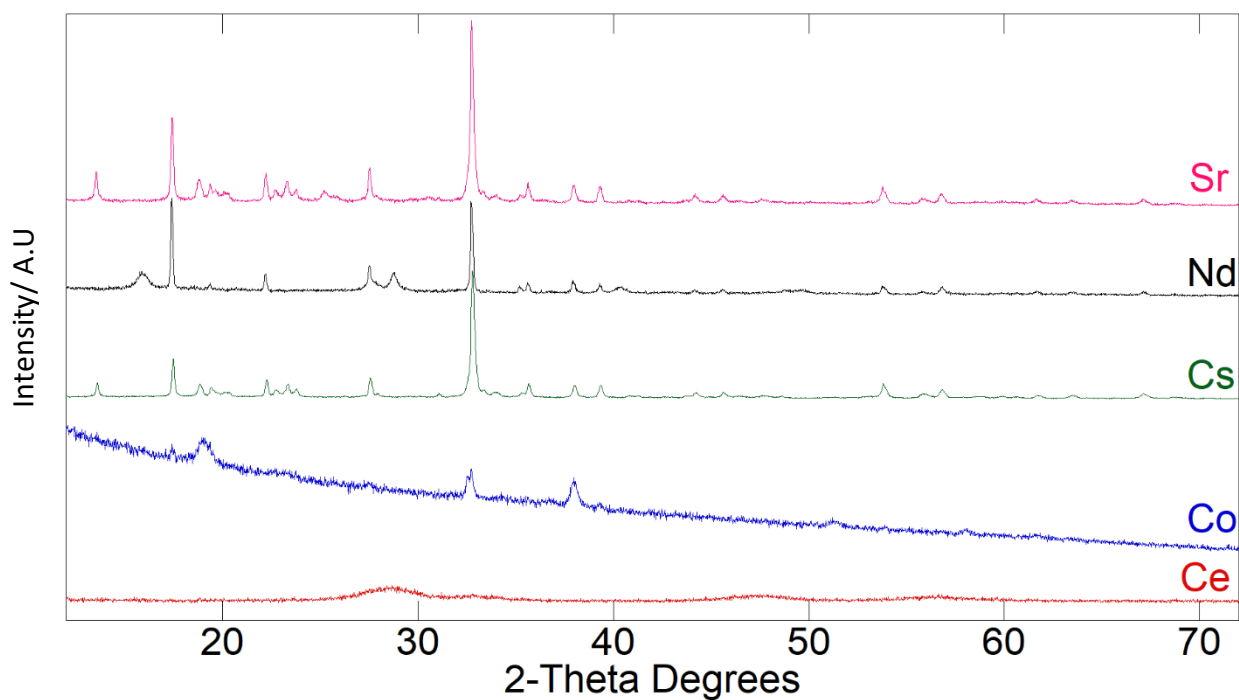


Figure 6.6 – XRD patterns of ion-exchanged natisite at pH 10.

Table 6.3 – Refined lattice parameters of ion-exchanged natisite at pH 10.

Ion	$ab$	$c$	RwP %	Difference to Synthesised Natisite	
				$a/\text{\AA}$	$c/\text{\AA}$
Natisite	6.4849(2)	5.0936(2)	12.807	-	-
Ce	6.486(20)	5.0997(30)	19.864	0.00178	0.00608
Co	6.4646(46)	5.0614(21)	4.083	-0.02027	-0.0322
Cs	6.4882(6)	5.0950(2)	9.816	0.00330	0.00140
Nd	6.4800(10)	5.0940(10)	17.299	-0.00488	0.00044
Sr	6.48387(2)	5.0929(3)	13.183	-0.00112	0.00071

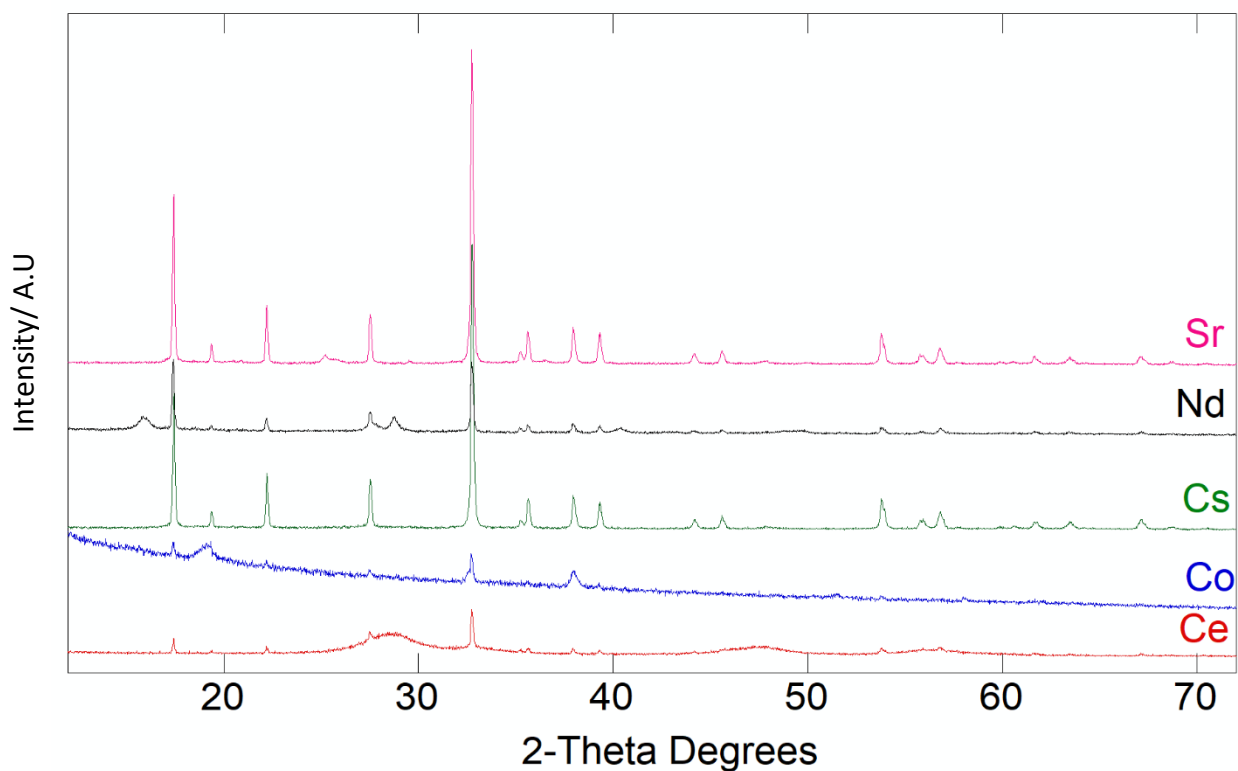


Figure 6.7 – XRD patterns of ion-exchanged 10% Zr natisite at pH 10.

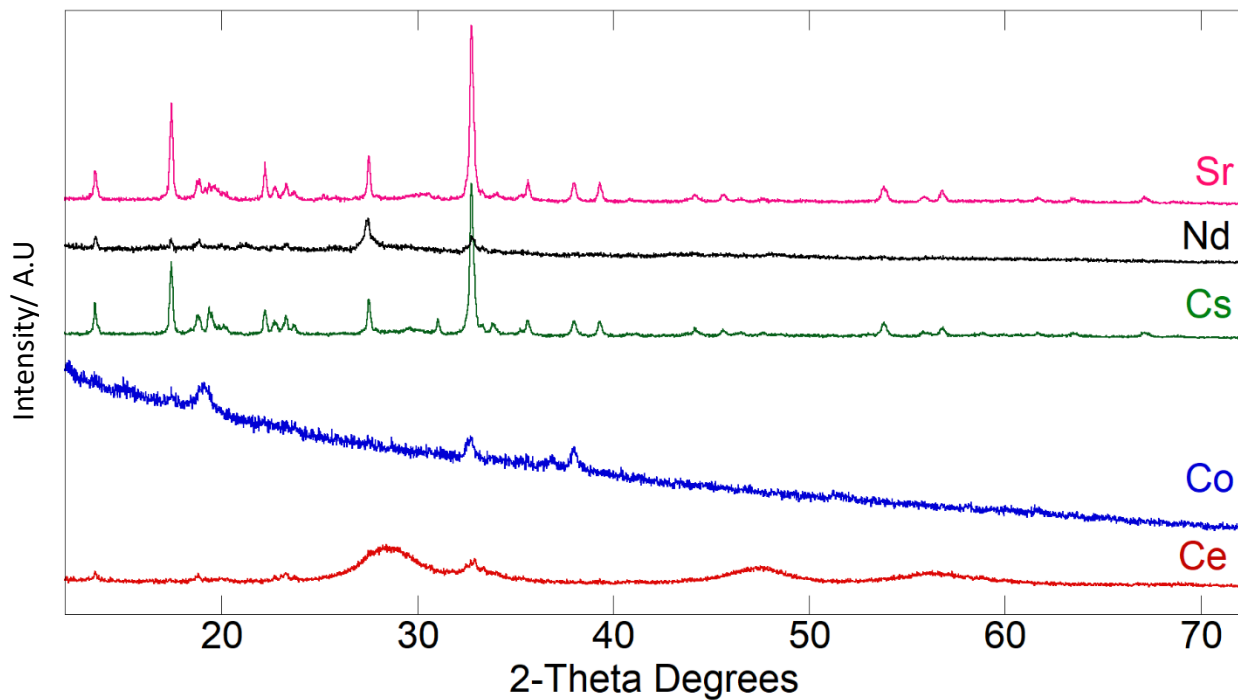


Figure 6.8 – XRD patterns of ion-exchanged 20% Zr natisite at pH 10.

### 6.3.2.2: ICP-MS

The same method for ICP-MS and the analysis detailed in previous chapters was attempted here. As stated earlier, the nuclear industry uses basic conditions to limit the breakdown of nuclear fuel stored in water. At the basic conditions used in this work, most of the metal ions precipitated out of solution, meaning that the use of ICP-MS as an analytical tool was no longer viable as the liquid phase no longer contained unexchanged the metal ions. It is therefore unknown to what extent the material was able to exchange with the ions in solution before they crashed out of solution. It was observed that the metal ions were solidifying upon contact with the base, so levels of exchange would be expected to be low.

## 6.4: Summary

Natisite, 10% Zr and 20% Zr remain stable in both acidic and basic conditions with the exception of Ce, where the mechanism has already been discussed in previous chapters, and Co, where at pH 10 the Co crashes out of solution, increasing the amount of Co within the sample causing an increase in the florescence seen by the XRD. There is a significant increase in the level of Cs exchange at acidic pH, however the reason for this increase to date is unclear. Large changes are observed in the lattice parameters post Co ion-exchange, indicating again that there is a potential breakdown of the structure with the Co.

The new order of affinities at pH 3 are:

For natisite: Cs < Sr < Co < Nd < Ce

For 10% Zr natisite: Ce < Nd < Sr < Co < Cs

For 20% Zr natisite: Ce  $\approx$  Nd < Sr < Co < Cs

# *CHAPTER SEVEN*

## *Clinoptilolite*

### 7.1: Introduction

Clinoptilolite is a naturally occurring zeolite commonly used as an insoluble ion-exchanger in the nuclear industry. Clinoptilolite, one of the most abundant natural zeolites, possess the heulandite (HEU) framework <sup>[85]</sup> and has large interconnecting channels where large cations are able to pass through. <sup>[86, 87]</sup>

The use of clinoptilolite in the nuclear industry has been widely adopted and is one of the main ion-exchange materials used due to its high cation exchange capacity and specificity for Cs. <sup>[88]</sup> <sup>137</sup>Cs is one of the most abundant radionuclides in the nuclear fission products that is either purposely or accidentally released. <sup>[88-90]</sup> Also it was found that clinoptilolite can readily exchange with Cs at low temperatures (20°C) at the expense of its charge balancing cations Na and K. <sup>[91]</sup>

Clinoptilolite is currently used in the Sellafield Ion Exchange Effluent Plant (SIXEP) process at Sellafield Ltd which is designed to remove soluble radioactive caesium and strontium from nuclear fuel storage pond water. This is due to the materials relatively high Si/Al compositional ratio allowing for a high ion-exchange selectivity for large monovalent cations. <sup>[92]</sup> Clinoptilolite has been extensively used at both Chernobyl and Fukushima in an attempt to help clean up the radioactive waste released into the environment. Specifically at Chernobyl, clinoptilolite had several applications from, the addition in detergents, animal

feeds, sewage waters and in the decontamination of milk <sup>[93]</sup> where the intake of radiocontaminated food was one of the main pathways for radiation exposure.<sup>[94, 95]</sup> Clinoptilolite was also used at Fukushima Daiichi, where it was observed that 96% of Cs was adsorbed from contaminated soil by clinoptilolite. <sup>[96]</sup> A potential downside of the use of clinoptilolite is its reduced efficiency at high pH, where it was found that on top of the material being unstable, Cs is also less mobile.<sup>[97]</sup>

The chemical composition of clinoptilolite varies from the location in which it is mined. <sup>[98-100]</sup>. The clinoptilolite used for the SIXEP process is mined from one location in the Mojave Desert, and is found to be particularly selective towards <sup>137</sup>Cs and <sup>90</sup>Sr.<sup>[101]</sup> However, clinoptilolite is no longer able to be mined from this location as it has been deemed a protected area for natural conservation reasons.

Despite the ion-exchange chemistry being extensively investigated, the only way to compare the ion-exchange capacity would be to conduct ion-exchanges under the same conditions. It would be useful to compare the effectiveness of the materials used in this work to clinoptilolite to determine which ion-exchange material has the higher capacity for each of the cations investigated.

## 7.2: Clinoptilolite Ion-Exchange

This chapter compares the ion-exchange capacity and selectivity of natisite, 10% Zr and 20% Zr doped natisite to that of clinoptilolite. While the ion-exchange chemistry of clinoptilolite has already been investigated, and reported previously, by conducting the ion-exchange in the same laboratory conditions as the natisite ion-exchanges, a direct comparison can be made.

### 7.2.1: Sample Preparation

A batch of clinoptilolite was acquired from the Sellafield LTD site. A 0.1 M solution of each nitrate ion was prepared in 125 ml di-water at room temperature. Each solution was mechanically stirred at 300 rpm with the use of a glass coated magnetic follower. 0.5 g clinoptilolite was added to the ion containing solution and left for a period of 18 hours. The resulting powder was collected by filtration and washed with copious amounts of di-water. A small sample of the waste solution was obtained for analysis.

### 7.2.2: Analysis

#### 7.2.2.1: SEM/EDX

The SEM results (prior to any ion-exchange work) at 3103x magnification shows a microcrystallite of around 20 $\mu$ m in size. EDX was performed on figure 7.1 and the results shown in table 7.1.

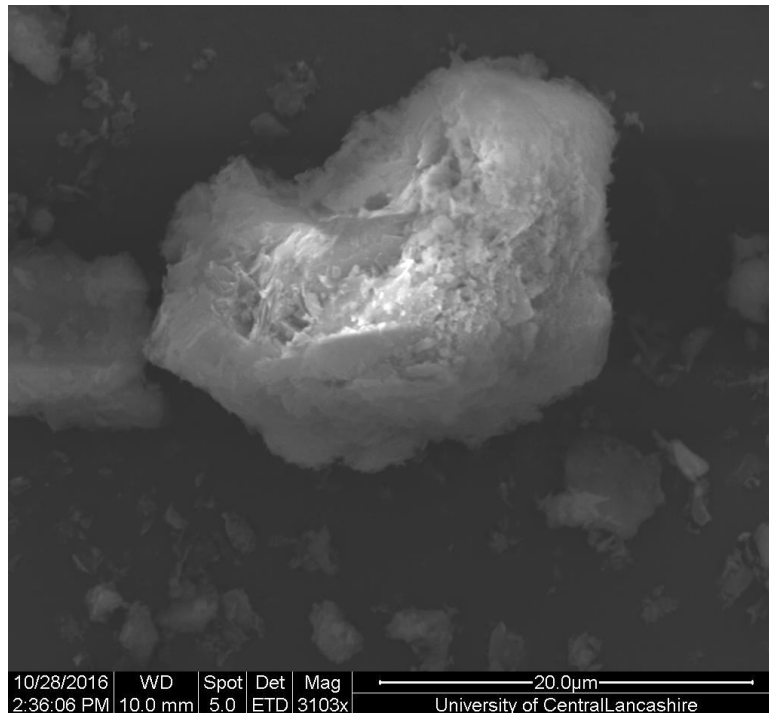


Figure 7.1 – SEM Image for clinoptilolite.

Table 7.1 – Elemental composition of clinoptilolite acquired from EDX.

<i>Element</i>	<i>Measured Weight %</i>	<i>Measured Atom %</i>	<i>Measured Molar ratio (Normalised to Si)</i>
<i>O</i>	60.33	73.01	1.04
<i>Na</i>	0.54	0.45	0.0064
<i>Al</i>	2.69	1.93	0.027
<i>Si</i>	33.6	69.67	1
<i>K</i>	1.36	2.03	0.029
<i>Ca</i>	1.45	2.12	0.03

The Si:Al ratio is 12.5:1. This high ratio is to be expected. The O content obtained by the EDX is unreliable due to the relative inaccuracy of EDX determining the low O energy. The EDX results show that in addition to Na, there is also Ca and K which can act as charge balancing cations. The elemental composition is typical and does not contain any Fe, which can also be found in clinoptilolite.

#### 7.2.2.2: XRD

Clinoptilolite crystallises in the monoclinic space group  $C 12/m 1$  where  $a = 17.641(40) \text{ \AA}$ ,  $b = 18.031(40) \text{ \AA}$ ,  $c = 7.402(2) \text{ \AA}$ ,  $\alpha = \gamma = 90^\circ$ ,  $\beta = 116.43(2)^\circ$ .<sup>[102]</sup> Figure 7.2 shows a Pawley fit of the unexchanged clinoptilolite with table 7.1 showing the refined lattice parameters of the ion-exchanged clinoptilolite samples. Overall there is a good agreement between the calculated and observed patterns, with a small quartz impurity (labelled \* on figure 7.2).

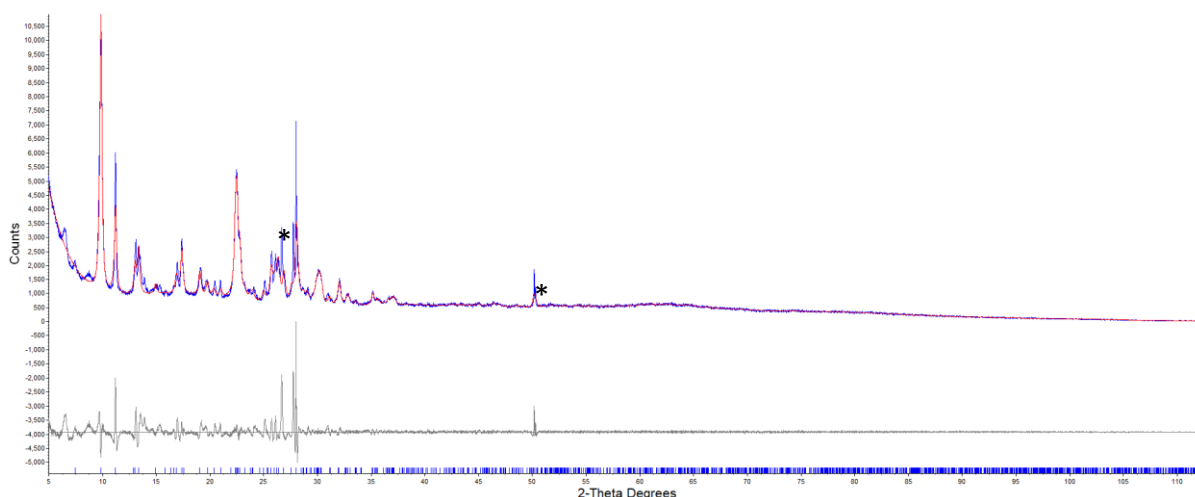


Figure 7.2 – Pawley fit of Clinoptilolite.

The largest difference in unit cell parameters and  $\beta$  angle is with the Ce ion-exchange. This is a similar trend found with the natisite ion-exchanges, indicating that the uptake of Ce has been successful. Also, the large  $\text{Ce}^{4+}$  ion is having an effect on the materials framework, in particular the  $0\ 2\ 0$  peak has reduced in intensity significantly, but unlike natisite, clinoptilolite remains crystalline (figure 7.3 A).

Table 7.2 – Refined lattice parameters of clinoptilolite and Ion-exchanged Clinoptilolite.

Ion	$a$	$b$	$c$	$\beta$	RwP %	Difference to Clinoptilolite			
						$a$	$b$	$c$	$\beta$
Clino	17.6787 (55)	17.9674(81)	7.42412(14)	116.665(14)	11.144	-	-	-	-
Ce	17.6641(76)	18.0021(98)	7.4311(21)	116.113(25)	10.920	0.0145	-0.0347	0.00693	0.55232
Co	17.6509(55)	17.9761(57)	7.39500(19)	116.419(23)	14.322	0.02774	0.00869	0.0292	0.2462
Cs	17.6786(79)	17.9911(99)	7.4413(22)	116.368(18)	9.167	5E-05	0.02372	0.01716	0.29705
Nd	17.6673(84)	17.9848(24)	7.3989(24)	116.503(27)	10.275	0.01131	0.01735	0.02523	0.16198
Sr	17.6792(84)	18.0124(113)	7.4211(254)	116.239(25)	10.970	0.00055	0.04503	0.00308	0.42548

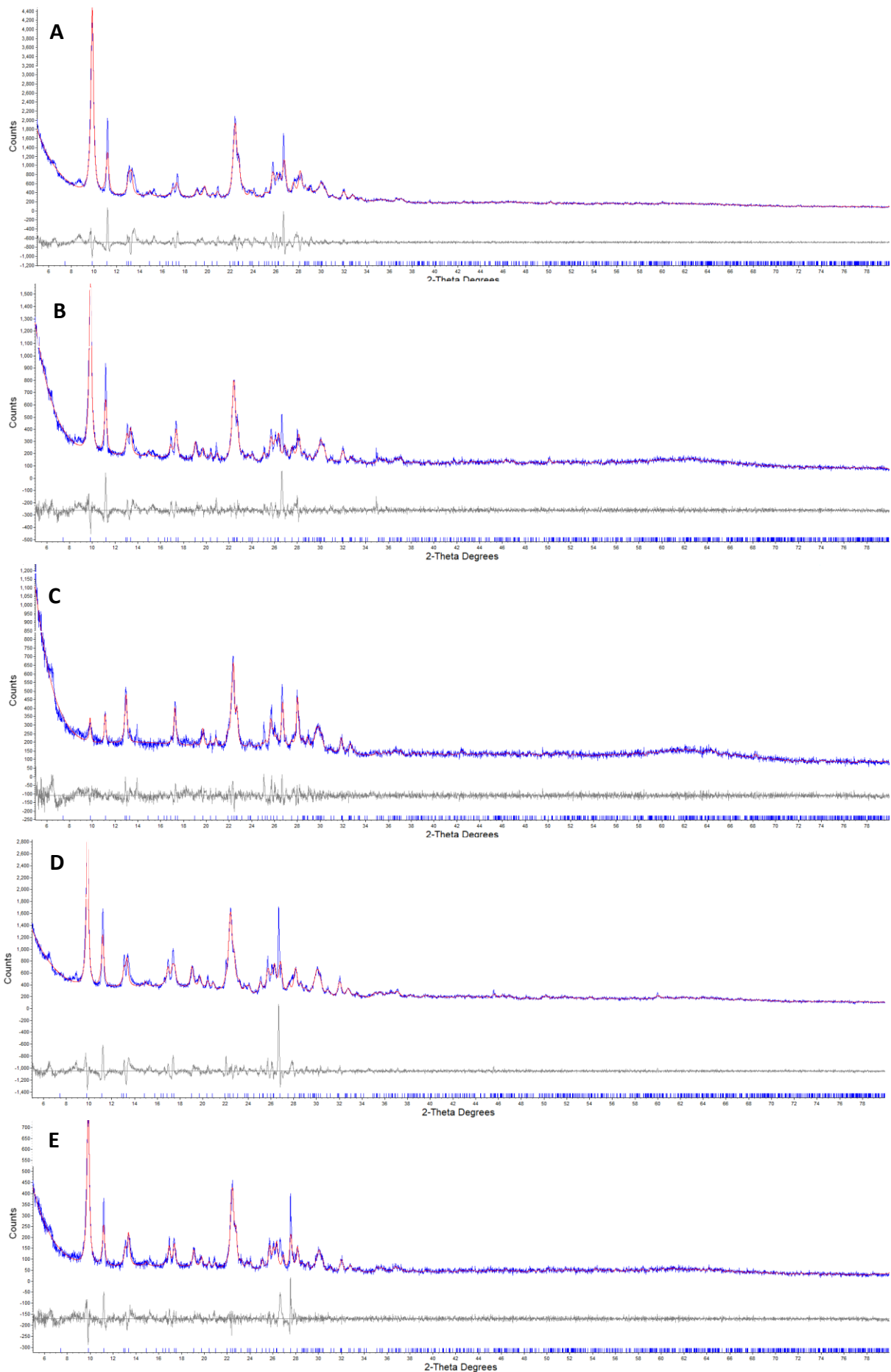


Figure 7.3 – Pawley fit of Ion-exchanged Clinoptilolite. (A) Ce, (B) Co, (C) Cs, (D) Nd, (E) Sr.

Figure 7.3 shows the Pawley fits of the clinoptilolite ion-exchanges. The data shows that clinoptilolite remains crystalline after exchange with all cations. The Cs exchange shows a higher background compared to the other exchanges and a large decrease in the peak at  $9^\circ$  corresponding to the (0 2 0) reflection. The SIXEP process at Sellafield uses clinoptilolite for the uptake of Cs so this large change in diffraction pattern is to be expected. The Sr exchange, also a key element in the SIXEP process, shows the largest change in lattice parameters and relative intensities, indicating that there has been successful uptake of Sr however the reduction of the 0 2 0 peak is not observed. There is less fluorescence seen by the XRD with respect to the Co exchange with clinoptilolite compared to the natasite materials, suggesting from the XRD data alone that natasite has a higher affinity towards Co compared to clinoptilolite.

### 7.2.2.3: ICP-MS

The same method of ICP-MS analysis was used in this chapter. The quantification formula shown in chapter three was adjusted to take into account the molecular weight of clinoptilolite. Quantitative analysis of the waste solutions was determined by ICP-MS. The results are shown in table 7.3.

Table 7.3 – Calculated percentage ion-exchange from ICP-MS results for clinoptilolite.

Ion	ppm left in solution	Percentage exchange/ $\pm 1\%$
Ce	10.932	5
Co	5.139	19
Cs	3.265	48
Nd	10.025	13
Sr	4.857	35

As the same ions are being investigated, the same calibration curve (shown in chapter three) can be used in the analysis of the clinoptilolite ion-exchanges. The ppm results show the concentration of each ion found in solution post ion-exchange. As the concentration of each ion in solution is 0.1 M, any reduction in this found by the ICP-MS can be attributed to the exchange of cations onto the framework.

From the ICP-MS results, an order of affinity can now be made.



The results show that clinoptilolite has a low affinity toward Ce exchanging at just 5%, whilst having a high affinity towards Cs, exchanging at 48%. The Ce XRD data shows the largest change in the  $\beta$  angle at an increase of  $0.522^\circ$ . Despite the low levels of exchange with respect to Ce, there are structurally large differences being caused. Suggesting that a small amount of Ce is exchange but distorting the framework. There is also the potential that the Ce ions are blocking the pores preventing further ion-exchange.

Sr is the next highest cation exchanged at 35%. The XRD data showed that this exchange caused the worst fit of any of the cations with an Rwp of 10.97 %, higher than the 9.167 % seen with the Cs exchanges, suggesting that while levels of Sr exchange are lower than those seen of Cs, Sr is causing more structural changes. A relatively large angle of  $0.425^\circ$  is observed in the  $\beta$  angle with the Sr exchange, indicating that the framework is being distorted due to the presence of Sr in the pores.

A direct comparison can now be made between clinoptilolite and natisite, 10% Zr natisite and 20% Zr natisite. A comparison table is shown in figure 7.4.

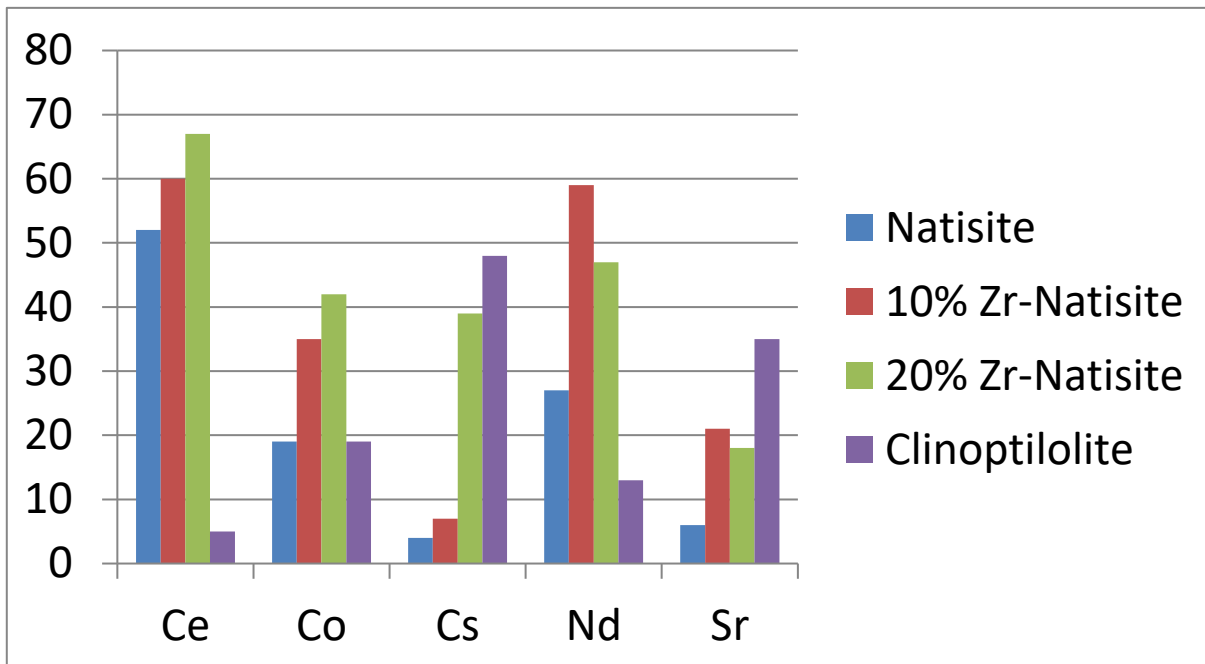


Figure 7.4 – Comparison table of the percentage ion-exchange of each cation.

From the results, we can see that 20% Zr doped natisite is the best exchanger for Ce, Co, while 10% Zr is superior for Nd exchange. Whilst Clinoptilolite is still better at removing both Cs and Sr from solution, the presence of Zr in the framework increase the amount of exchange of Cs and Sr to levels much more comparable to that of clinoptilolite.

### 7.3: Summary

Clinoptilolite can successfully exchange with all ions investigated, ranging from Ce exchange at just 5% to Cs exchange at 48%. Clinoptilolite is the superior ion-exchange material for the exchange of Cs and Sr, but the Zr containing natisite samples are at much higher levels for all other ions, especially Ce where levels of exchange reach up to 67%. The presence of Zr in the natisite framework also increases the level of exchange of Cs and Sr to levels similar to those found by clinoptilolite. Table 7.4 shows the material with the highest affinity for each cation.

Table 7.4 – Optimum ion-exchange material for each of the ions of interest.

<b>Ion</b>	<b>Ion-Exchange Material</b>
Ce	20% Natisite
Co	20% Natisite
Cs	Clinoptilolite
Nd	10% Zr Natisite
Sr	Clinoptilolite

# *CHAPTER EIGHT*

## *Conclusions and Future Work*

### 8.1: Conclusions

Natisite can be successfully synthesised using hydrothermal methods, from a previously reported synthetic route for sitinakite. All the analytical techniques used showed good agreement to previously published literature. This was with the exception of the morphology, where slight differences were observed, suggesting that the morphology is extremely susceptible to change with synthetic conditions. The ion-exchange work at neutral conditions showed that natisite has the highest affinity towards Ce, however the formation of CeO<sub>2</sub> causes a loss of crystallinity, supported by the XRD data where it showed the layers themselves remained intact but there was no long-range order in the stacking of the layers. Natisite also had a low affinity towards Cs and Sr in neutral conditions.

10% and 20% Zr can be substituted into the natisite framework, with the presence of a small Zr containing phase. It should therefore be noted that due to the impurity phase that actual amount of Zr in natisite will be slightly less than 10% and 20%. Zr Natisite can be successfully synthesised using hydrothermal methods. XAS was used to determine the local coordination environment around both Ti and Zr. Decreases in the amplitude of the Ti pre-edge feature and changes in the interatomic distances, show that substitution of Zr into the framework has been successful. The natisite XAS data can be successfully fitted and modelled. However, this is only out to a short range, approximately 5 Å, due to the outgoing XAS signal

being artificially damped by the incoming signal, producing no XAS spectra further out than the first two coordination shells. The lack of changes seen in the Zr edge ion-exchange data suggests that the exchangeable cations prefer sites closer to Ti than Zr and that Zr in the framework is more rigid and makes the process of exchange at Ti sites much more facile.

Also, there have been significant changes seen in the ion-exchange results, such as the increased rate of Co exchange, where upon contact with the Co containing solution both 10% and 20% Zr natisite undergo a near instant reaction, observed by the white powder turning instantly green. Such a change would not have been observed if the differences were due to the impurity phase. Also, no Ti-natisite spheres with the crosses are observed in the SEM of the Zr natisite products. The ion-exchange results show that the order of affinity has not been changed in the 10% Zr natisite sample. In the 20% Zr natisite ion-exchanges, only Cs and Sr had changed in the order of affinity. It was however the level of exchange that had differed significantly, with all ions increasing the amount exchanged. The increased level of exchange in the Zr containing natisite samples suggest that the presence of Zr in the framework is facilitating exchange of Na between the silicate layers. The lack of crystallinity observed with Ce and Nd exchanges is again observed in both the 10% and 20% Zr natisite samples.

When two or more cations are in the same solution, the level of exchange is altered. From the ICP-MS results it is shown that K is the most preferred cation, except for when Co is the competing ion. As K is not found in such high concentrations naturally as were used in this work, the increases affinity towards K would not pose an issue in the majority of industrial applications but would not be a good option when K concentration are a consideration. Ca and Mg levels of exchange are relatively low compared to the main cations of interest, indicating that natisite, 10% Zr natisite and 20% Zr natisite can selectively remove the cations

of choice whilst leaving the competing ions of Ca and Mg in solution. Lower levels of exchange are observed with Ce and Nd compared to the single ion-exchanges, but a loss of crystallinity is still observed in the diffraction data. Where Ce and Nd are the competing ions, the level of exchange of the other cation in solution is increased, suggesting that Ce and Nd facilitate higher levels of exchange of competing ions. In the single exchanges, the level of Cs and Sr on natisite were less than 7%. However, when in a solution of two cations, there is an increased level of Cs and Sr exchange indicating that the competing ion helps facilitate higher levels of Cs and Sr compared to the singles exchanges. This observed property may be of interest for applications when Cs and Sr species need to be removed from waste streams when related actinides species are present. Such a waste stream is generated on the Sellafield site through fuel reprocessing operations and is currently treated by the Enhance Actinide Removal Plant (EARP).

Natisite, 10% Zr and 20% Zr natisite crystallinity is maintained at both pH 3 and at pH 10. There is no change in order of affinity at pH 3, with the order of affinity at pH 10 being unable to be determined using the methods available in this work. There is however an increase in the amount of Cs exchange at acidic pH.

Clinoptilolite remains the best ion-exchange material for both Cs and Sr in single ion solutions whereas 10% natisite is better for Nd and 20% Zr natisite is preferred for both Ce and Co removal. Clinoptilolite can however exchange with each of the ions investigated but is a poor exchange material for Ce where just 5% was removed from solution. Competitive clinoptilolite ion exchanges will need to be investigated to see if the selectivity towards these cations is changed.

Whilst microwave synthesis has been shown to be a viable route to the synthesis of natisite and crystalline sitinakite there currently is no viable industrial scale up route that will be able to utilise microwave technology.

To conclude, natisite and its zirconium doped analogues remain stable in both acidic and basic conditions, can selectively remove the cations of choice whilst leaving competing ions in solution, and have a higher affinity for all but Cs and Sr compared to that of clinoptilolite. Natisite is therefore a viable alternative to clinoptilolite for use in the nuclear industry. If accidents were to occur, natisite and its zirconium doped analogues could be used as materials that could selectively remove radioactive cations from solution quickly.

### 8.2: Future Work

Future work on this project will be split into two sections. One, where the mechanism of the ion-exchanges will be investigated and two, the geological disposal of the ion exchange materials.

#### 8.2.1: Ion-Exchange Mechanism Future Work

*In-situ* ion-exchange work will be conducted in order to determine the mechanism of the formation of CeO<sub>2</sub> nanoparticles. As previously discussed, Ce-nitrate upon contact with water forms CeO<sub>2</sub> which forms between the layers, forcing them apart and as a consequence, losing crystallinity in the diffraction data. However, to-date the mechanism for this formation within the context of this work is unknown. *In-situ* liquid XAS could be utilised to not only on the Ce edge to determine the rate of formation of the Ce nanoparticles but also on the Ti edge to determine how this formation effects the local environment around Ti. Also,

Transmission electron microscopy (TEM) can be utilised to investigate the CeO<sub>2</sub> nanoparticles and the layer structure of natisite.

Timed ion-exchanges would also be conducted to determine the optimum time for each exchange, and at what level the process of back exchange would occur. This would be particularly relevant with respect to the Co exchanges, where it was observed that the rate of Co removal from solution was drastically increased with the Zr containing materials.

While ICP-MS provided quantitative analysis on the percentage exchange of each cation, this was the only technique used in this work to determine the level of exchange. Quantitative XRF would provide an alternate technique to determine the concentration of each ion within the powdered sample. As the material are all washed with copious amount of di-water, it can be assumed that the level of each cation found by the XRF is a result of ion-exchange and not simply surface adsorption. Alternatively, digestion of the solid material and ICP-MS analysis conducted could be another technique employed to determine the level of exchange.

Competitive clinoptilolite ion-exchanges would also be conducted in order to determine if the order of affinity and capacity would change in the presence of a competing ion. The results from that natisite competitive exchanges show that both the affinity and percentage exchange can change. Also timed clinoptilolite ion-exchanges could be conducted in order to determine the optimum time of exchange for each of the ions investigated, and at what point the process of back exchange takes place. The results from the competitive and times clinoptilolite ion-exchanges could again be directly compared to natisite to determine the more effective ion-exchange material.

### 8.2.2: Geological disposal

This section of the future work will focus on the testing of the material to see how viable it is for geological disposal or long term storage.

Leach testing will be carried out on all ion-exchange samples to determine how well each of the materials can keep the cations within the structure and what percentage of the exchanged cations leach back out. This will be achieved by stirring the powdered ion-exchanged samples in water and testing the water for any traces for the cations. This would be conducted at both neutral and basic conditions, as geological disposal usually entails the material will be likely to be encapsulated in cement for storage due to the microporous nature of cement and its alkaline character where the pH is around 13.<sup>[103]</sup> It will also be useful to compare to the industrially used clinoptilolite to determine if there are any differences in the leach testing data.

Also, most ion-exchange materials post exchange are heat treated in an attempt to encapsulate the cations within the structure. More potential work will focus on the heat treatment of the ion-exchange materials both before and after ion-exchange to see the effect it has on the materials and if the exchanged cations are “trapped” within the collapsed framework.

Hot isostatic pressing (HIPing) could also be conducted. HIPing causes the internal pores within the solid to collapse and weld up, creating a homogeneous material with a near 100% density at low temperatures. Leach testing after HIPing of both natasite and the Zr doped analogues together with clinoptilolite would provide useful information to the nuclear industry as to the geological disposal of the materials.

As the ion-exchange materials investigated in the work are potentially useful in the nuclear industry, it is important to identify if that materials are stable to ionising radiation. Therefore, radiation stability experiments will be conducted to determine if the materials are still able to ion-exchange with either radioactive elements in solution, or if there is any radiation damage to the framework, which would be determined by XRD. The most common radiation stability experiments are the  $^{60}\text{Co}$  gamma radiation experiments, where the sample is placed inside a stainless-steel reaction vessel inside a closed system. The sample is irradiated at similar levels found within the nuclear industry and analysed to determine any structural damage caused by the radiation. <sup>[104]</sup>

Again, after this has been conducted it would be important to again determine the leach rates/ ion mobility to determine the overall effect of radiation damage to all the ion-exchange materials studied in this work. It will also be important to not only investigate the the leaching of ions from the materials but also the cations decay products. As Ce and Nd were used in this work as inactive surrogate for Pu and U respectively, it would be important to determine leach rates of both Pb and Bi.

# References

1. Cundy, C.S. and P.A. Cox, *The hydrothermal synthesis of zeolites: Precursors, intermediates and reaction mechanism*. Microporous and Mesoporous Materials, 2005. **82**(1–2): p. 1-78.
2. Walls, J., *Chapter 1 Nuclear Power Generation - Past, Present and Future*, in *Nuclear Power and the Environment*. 2011, The Royal Society of Chemistry. p. 1-39.
3. Goldwhite, H., *The Manhattan Project*. Journal of Fluorine Chemistry, 1986. **33**(1): p. 109-132.
4. Taylor, D.J., *30<sup>th</sup> anniversary of GLEEP*. Atoms, 1977. **9**: p. 196-198.
5. Bohr, N. and J.A. Wheeler, *The Mechanism of Nuclear Fission*. Physical Review, 1939. **56**(5): p. 426-450.
6. Sharrad, C.A., L.M. Harwood, and F.R. Livens, *Chapter 2 Nuclear Fuel Cycles: Interfaces with the Environment*, in *Nuclear Power and the Environment*. 2011, The Royal Society of Chemistry. p. 40-56.
7. AGENCY, I.A.E., *Nuclear Power Reactors in the World*. Reference Data Series. 2017, Vienna: INTERNATIONAL ATOMIC ENERGY AGENCY.
8. Dawson, J.I. and R.G. Darst, *Meeting the challenge of permanent nuclear waste disposal in an expanding Europe: Transparency, trust and democracy*. Environmental Politics, 2006. **15**(4): p. 610-627.
9. Landa, E.R., *Uranium mill tailings: nuclear waste and natural laboratory for geochemical and radioecological investigations*. Journal of Environmental Radioactivity, 2004. **77**(1): p. 1-27.
10. World Nuclear Association: <http://www.world-nuclear.org/info/Nuclear-Fuel-Cycle/Nuclear-Wastes/Radioactive-Waste-Management/>.
11. Abdelouas, A., *Uranium Mill Tailings: Geochemistry, Mineralogy, and Environmental Impact*. Elements, 2006. **2**(6): p. 335-341.
12. Turekian, K.K., *Uranium Decay Series*. Reviews in Mineralogy and Geochemistry, 2003. **52**(1): p. iv-v.
13. The World Nuclear Association: <http://www.world-nuclear.org/information-library/nuclear-fuel-cycle/fuel-recycling/processing-of-used-nuclear-fuel.aspx>.
14. Bowman, C.D., E.D. Arthur, P.W. Lisowski, G.P. Lawrence, R.J. Jensen, J.L. Anderson, B. Blind, M. Cappiello, J.W. Davidson, T.R. England, L.N. Engel, R.C. Haight, H.G. Hughes Iii, J.R. Ireland, R.A. Krakowski, R.J. LaBauve, B.C. Letellier, R.T. Perry, G.J. Russell, K.P. Staudhammer, G. Versamis, and W.B. Wilson, *Nuclear energy generation and waste transmutation using an accelerator-driven intense thermal neutron source*. Nuclear Instruments and Methods in Physics Research Section A: Accelerators, Spectrometers, Detectors and Associated Equipment, 1992. **320**(1–2): p. 336-367.
15. Deng, Y., J.B. Harsh, M. Flury, J.S. Young, and J.S. Boyle, *Mineral formation during simulated leaks of Hanford waste tanks*. Applied Geochemistry, 2006. **21**: p. p.1392-1409.
16. SARKKA, P., *Rock engineering characteristics of the investigated sites for final disposal of spent nuclear fuel in Finland*. 13-17 March 2000, 2000: p. 115.
17. Slovic, P., M. Layman, N. Kraus, J. Flynn, J. Chalmers, and G. Gesell, *Perceived Risk, Stigma, and Potential Economic Impacts of a High-Level Nuclear Waste Repository in Nevada*. Risk Analysis, 1991. **11**(4): p. 683-696.
18. Patel, P., *Yucca Mountain, deemed safe, still faces long road ahead*. MRS Bulletin, 2015. **40**(1): p. 10-11.
19. Dyer, A., *Zeolite Molecular Sieves*. 1988, Sussex: Wiley.
20. Baerlocher, C.H. and L.B. McCusker. *Database of Zeolite Structures*: <http://www.iza-structure.org/databases/>. 09/06/2014].

21. Smart, L.E. and E.A. Moore, *Solid State Chemistry- An Introduction*. Vol. Fourth Edition. 2012, Florida: CRC Press.
22. Kapko, V., C. Dawson, M. Treacy, and M. Thorpe, *Flexibility of ideal zeolite frameworks*. *Physical Chemistry Chemical Physics*, 2010. **12**(30): p. 8531-8541.
23. Write, P., *Microporous Framework Solids*. 2008, The Royal Society of Chemistry: Cambridge. p. 1-6.
24. Mondale, K.D., R.M. Carland, and F.F. Aplan, *The Comparative Ion Exchange Capacities of Natural Sedimentary and Synthetic Zeolites*. *Materials Engineering*, 1995. **8**: p. p535.
25. Xu, R., W. Pang, J. Yu, Q. Huo, and J. Chen, *Chemistry of Zeolites and Related Porous Materials: Synthesis and Structure*. 2007, Singapore: Wiley. 13-15.
26. Jones, J.B., *Al-O and Si-O tetrahedral distances in aluminosilicate framework structures*. *Acta Cryst.*, 1968. **B24**: p. 355-358.
27. Bekkum, H.v., E.M. Flanigen, P.A. Jacobs, and J.C. Jansen, *Introduction to Zeolite Science and Practice*. Vol. 2. 2001, Amsterdam: Elsevier.
28. Cejka, J., A. Corma, and S. Zones, *Zeolites and Catalysis: Synthesis, Reactions and Applications*. 2010, Weinheim: Wiley-VCH.
29. Flanigen, E.M., *Molecular Sieve Zeolite Technology*. *Pure & Appl. Chem.*, 1980. **52**.
30. Wright, P., *Microporous Framework Solids*. 2008, Cambridge: Royal Society of Chemistry. p.33-34.
31. Taramasso, M., G. Perego, and B. Notari, *Preparation of porous crystalline synthetic material comprised of silicon and titanium oxides*. 1983, Google Patents.
32. Notari, B., *Microporous Crystalline Titanium Silicates*. 1996, London: Academic Press.
33. Medvedev, D.G., A. Tripathi, A. Clearfield, A.J. Celestian, J.B. Parise, and J. Hanson, *Crystallization of sodium titanium silicate with sitinakite topology: Evolution from the sodium nonatitanate phase*. *Chemistry of Materials*, 2004. **16**(19): p. 3659-3666.
34. Tripathi, A., D.G. Medvedev, M. Nyman, and A. Clearfield, *Selectivity for Cs and Sr in Nb-substituted titanosilicate with sitinakite topology*. *Journal of Solid State Chemistry*, 2003. **175**(1): p. 72-83.
35. Kramer, S. and A.J. Celestian, *Effects of Hydration during strontium exchange into nanoporous hydrogen niobium titanium silicate*. *Inorganic chemistry*, 2012. **51**(11): p. 6251-6258.
36. Chitra, S., S. Viswanathan, S.V.S. Rao, and P.K. Sinha, *Uptake of cesium and strontium by crystalline silicotitanates from radioactive wastes*. *Journal of Radioanalytical and Nuclear Chemistry*, 2011. **287**(3): p. 955-960.
37. Kuznicki, S.M., V.A. Bell, S. Nair, H.W. Hillhouse, R.M. Jacubinas, C.M. Braunbarth, B.H. Toby, and M. Tsapatsis, *A titanosilicate molecular sieve with adjustable pores for size-selective adsorption of molecules*. *Nature*, 2001. **412**(6848): p. 720-724.
38. Braunbarth, C., H.W. Hillhouse, S. Nair, M. Tsapatsis, A. Burton, R.F. Lobo, R.M. Jacubinas, and S.M. Kuznicki, *Structure of strontium ion-exchanged ETS-4 microporous molecular sieves*. *Chemistry of Materials*, 2000. **12**(7): p. 1857-1865.
39. Marathe, R., S. Farooq, and M. Srinivasan, *Effects of site occupancy, cation relocation, and pore geometry on adsorption kinetics in ETS-4*. *The Journal of Physical Chemistry B*, 2005. **109**(8): p. 3257-3261.
40. Pavel, C.C., D. Vuono, O.L. Catanzaro, P. De Luca, N. Bilba, A. Nastro, and J.B. Nagy, *Synthesis and characterization of the microporous titanosilicates ETS-4 and ETS-10*. *Microporous and Mesoporous Materials*, 2002. **56**(2): p. 227-239.
41. Anderson, M.W., O. Terasaki, T. Ohsuna, A. Philippou, S.P. MacKay, A. Ferreira, J. Rocha, and S. Lidin, *Structure of the microporous titanosilicate ETS-10*. *Nature*, 1994. **367**(6461): p. 347-351.
42. Ferdov, S., V. Kostov-Kytin, and O. Petrov, *Improved powder diffraction patterns for synthetic paranatisite and natisite*. *Powder Diffraction*, 2002. **17**(3): p. 234-237.

43. Kostov-Kytin, V., S. Ferdov, and O. Petriv, *Hydrothermal Synthesis and Successive Transformation of Paranatisite into Natisite*. Tome, 2001(2): p. 61.
44. Peng, G.W. and H.S. Liu, *FT-IR AND XRD CHARACTERIZATION OF PHASE-TRANSFORMATION OF HEAT-TREATED SYNTHETIC NATISITE (NA<sub>2</sub>TiOSiO<sub>4</sub>) POWDER*. Materials Chemistry and Physics, 1995. **42**(4): p. 264-275.
45. Zagorodni, A.A., *Ion Exchange Materials: Properties and Applications*. 2007, Amsterdam: Elsevier.
46. Dyer, A., A. Chimedtsogzol, L. Campbell, and C. Williams, *Uptake of caesium and strontium radioisotopes by natural zeolites from Mongolia*. Microporous and Mesoporous Materials, 2006. **95**(1): p. 172-175.
47. Howden, M. *British Nuclear Fuel's site ion exchange effluent plant*. in *Effluent treatment in the process industries. Symposium organised by the Institution of Chemical Engineers jointly with the Royal Society of Chemistry and co-sponsored by the Filtration Society. Held at the University of Technology, Loughborough, 12-14 April 1983*. 1983.
48. Tompsett, G.A., W.C. Conner, and K.S. Yngvesson, *Microwave synthesis of nanoporous materials*. ChemPhysChem, 2006. **7**(2): p. 296-319.
49. Somani, O.G., A.L. Choudhari, B.S. Rao, and S.P. Mirajkar, *Enhancement of crystallization rate by microwave radiation: synthesis of ZSM-5*. Materials Chemistry and Physics, 2003. **82**(3): p. 538-545.
50. Prasad, M.R., G. Kamalakar, S. Kulkarni, K. Raghavan, K.N. Rao, P.S. Prasad, and S. Madhavendra, *An improved process for the synthesis of titanium-rich titanium silicates (TS-1) under microwave irradiation*. Catalysis Communications, 2002. **3**(9): p. 399-404.
51. Serrano, D., M. Uguina, R. Sanz, E. Castillo, A. Rodriguez, and P. Sanchez, *Synthesis and crystallization mechanism of zeolite TS-2 by microwave and conventional heating*. Microporous and mesoporous materials, 2004. **69**(3): p. 197-208.
52. Chandrasekhar, S. and P. Pramada, *Microwave assisted synthesis of zeolite A from metakaolin*. Microporous and Mesoporous Materials, 2008. **108**(1): p. 152-161.
53. Elder, F.R., A.M. Gurewitsch, R.V. Langmuir, and H.C. Pollock, *Radiation from Electrons in a Synchrotron*. Physical Review, 1947. **71**(11): p. 829-830.
54. Calvin, S., *XAFS for Everyone*. 2013: CRC press.
55. Kiani, A., N.J. Lakhkar, V. Salih, M.E. Smith, J.V. Hanna, R.J. Newport, D.M. Pickup, and J.C. Knowles, *Titanium-containing bioactive phosphate glasses*. Philosophical Transactions of the Royal Society A: Mathematical, Physical and Engineering Sciences, 2012. **370**(1963): p. 1352-1375.
56. Newville, M., *Fundamentals of xafs. consortium for advanced radiation sources*. University of Chicago, Chicago, IL, 2004.
57. Rehr, J.J., J.J. Kas, M.P. Prange, A.P. Sorini, Y. Takimoto, and F. Vila, *Ab initio theory and calculations of X-ray spectra*. Comptes Rendus Physique, 2009. **10**(6): p. 548-559.
58. Ravel, B. and M. Newville, *ATHENA, ARTEMIS, HEPHAESTUS: data analysis for X-ray absorption spectroscopy using IFEFFIT*. Journal of Synchrotron Radiation, 2005. **12**(4): p. 537-541.
59. Shackley, M.S., *An Introduction to X-Ray Fluorescence (XRF) Analysis in Archaeology*, in *X-Ray Fluorescence Spectrometry (XRF) in Geoarchaeology*, M.S. Shackley, Editor. 2011, Springer New York: New York, NY. p. 7-44.
60. Yakubovich, O., O. Mel'Nikov, and V. Urusov. *Paraframework of a mixed nature in the crystalline structure of Na<sub>3</sub> {Fe<sub>2</sub>F (3)[PO<sub>4</sub>] 2}, a new homeotype in the natisite series*. in *Physics-Doklady*. 1995.
61. Peng, G.-W., S.-K. Chen, and H.-S. Liu, *Infrared Absorption Spectra and Their Correlation with the Ti-O Bond Length Variations for TiO<sub>2</sub> (Rutile), Na-Titanates, and Na-Titanosilicate (Natisite, Na<sub>2</sub>TiOSiO<sub>4</sub>)*. Applied Spectroscopy, 1995. **49**(11): p. 1646-1651.

62. Cherry, B.R., M. Nyman, and T.M. Alam, *Investigation of cation environment and framework changes in silicotitanate exchange materials using solid-state  $^{23}\text{Na}$ ,  $^{29}\text{Si}$ , and  $^{133}\text{Cs}$  MAS NMR*. Journal of Solid State Chemistry, 2004. **177**(6): p. 2079-2093.
63. AXS, B., *TOPAS V3.0: General Profile and Structure Analysis Software for Powder Diffraction Data*. Karlsruhe, Germany.
64. Nyman, H., M. O'Keeffe, and J.O. Bovin, *Sodium titanium silicate,  $\text{Na}_2\text{TiSi}_2\text{O}_5$* . Acta crystallographica B, 1978. **24**: p. 905-906.
65. Ferdov, S., *Organic-Free and Selectively Oriented Recrystallization for Design of Natisite Microstructures*. Crystal Growth & Design, 2011. **11**(10): p. 4498-4504.
66. Ferdov, S., *A Comparative Rietveld Refinement Study of Natisite Prepared in Different Morphology*. Journal of Chemical Crystallography, 2013. **43**(8): p. 443-447.
67. Beall, G., W. Milligan, D. Dillin, R. Williams, and J. McCoy, *Refinement of neodymium trihydroxide*. Acta Crystallographica Section B: Structural Crystallography and Crystal Chemistry, 1976. **32**(7): p. 2227-2229.
68. Treushnikov, E. and B. Grechushnikov, *VV Ilyukhin, and NV Belov*. Sov. Phys. Crystallogr.(Engl. Transl.), 1970. **15**(9).
69. Thomas, J.M., G. Sankar, M.C. Klunduk, M.P. Attfield, T. Maschmeyer, B.F. Johnson, and R.G. Bell, *The Identity in Atomic Structure and Performance of Active Sites in Heterogeneous and Homogeneous, Titanium–Silica Epoxidation Catalysts*. The Journal of Physical Chemistry B, 1999. **103**(42): p. 8809-8813.
70. Behrens, P., J. Felsche, S. Vetter, G. Schulz-Ekloff, N.I. Jaeger, and W. Niemann, *A XANES and EXAFS investigation of titanium silicalite*. Journal of the Chemical Society, Chemical Communications, 1991(10): p. 678-680.
71. Yakubovich, O.V., V.V. Kireev, and O.K. Mel'nikov, *Refinement of crystal structure of a Ge-analogue of natisite  $\text{Na}_2\{\text{TiGeO}_4\}$  and prediction of new phases with anionic  $\{\text{MTO}_5\}$  radicals*. Crystallography Reports, 2000. **45**(4): p. 578-584.
72. Li, P., I.-W. Chen, and J.E. Penner-Hahn, *X-ray-absorption studies of zirconia polymorphs. I. Characteristic local structures*. Physical Review B, 1993. **48**(14): p. 10063.
73. Mountjoy, G., D.M. Pickup, R. Anderson, G.W. Wallidge, M.A. Holland, R.J. Newport, and M.E. Smith, *Changes in the Zr environment in zirconia–silica xerogels with composition and heat treatment as revealed by Zr K-edge XANES and EXAFS*. Physical Chemistry Chemical Physics, 2000. **2**(10): p. 2455-2460.
74. Farges, F., G.E. Brown, and D. Velde, *Structural environment of Zr in two inosilicates from Cameroon; mineralogical and geochemical implications*. American Mineralogist, 1994. **79**(9-10): p. 838-847.
75. Sanchez, C. and M. In, *Molecular design of alkoxide precursors for the synthesis of hybrid organic-inorganic gels*. Journal of non-crystalline solids, 1992. **147**: p. 1-12.
76. Dunn, P., R. Rouse, B. Cannon, and J. Nelen, *Zektzerite; a new lithium sodium zirconium silicate related to tualite and the osumilite group*. American Mineralogist, 1977. **62**(5-6): p. 416-420.
77. Neeway, J.J., R.M. Asmussen, A.R. Lawter, M.E. Bowden, W.W. Lukens, D. Sarma, B.J. Riley, M.G. Kanatzidis, and N.P. Qafoku, *Removal of  $\text{TcO}_4^-$  from Representative Nuclear Waste Streams with Layered Potassium Metal Sulfide Materials*. Chemistry of Materials, 2016. **28**(11): p. 3976-3983.
78. Simmance, K., G. Sankar, R.G. Bell, C. Prestipino, and W. van Beek, *Tracking the formation of cobalt substituted ALPO-5 using simultaneous in situ X-ray diffraction and X-ray absorption spectroscopy techniques*. Physical Chemistry Chemical Physics, 2010. **12**(3): p. 559-562.
79. Seddon, J., E. Suard, and M.A. Hayward, *Topotactic reduction of  $\text{YBaCo}_2\text{O}_5$  and  $\text{LaBaCo}_2\text{O}_5$ : square-planar Co (I) in an extended oxide*. Journal of the American Chemical Society, 2010. **132**(8): p. 2802-2810.

80. Vogt, T., P. Woodward, P. Karen, B. Hunter, P. Henning, and A. Moodenbaugh, *Low to high spin-state transition induced by charge ordering in antiferromagnetic YBaCo<sub>2</sub>O<sub>5</sub>*. Physical review letters, 2000. **84**(13): p. 2969.
81. Lin, H.-K., H.-C. Chiu, H.-C. Tsai, S.-H. Chien, and C.-B. Wang, *Synthesis, characterization and catalytic oxidation of carbon monoxide over cobalt oxide*. Catalysis letters, 2003. **88**(3): p. 169-174.
82. Chen, L., *Hydrothermal synthesis and ethanol sensing properties of CeVO<sub>4</sub> and CeVO<sub>4</sub>-CeO<sub>2</sub> powders*. Materials Letters, 2006. **60**(15): p. 1859-1862.
83. Pettinger, N., R. Williams, J. Chen, and B. Kohler, *Crystallization Kinetics of Cerium Oxide Nanoparticles Formed by Spontaneous, Room-temperature Hydrolysis of Cerium (IV) Ammonium Nitrate in Light and Heavy Water*. Physical Chemistry Chemical Physics, 2017.
84. Readman, J.E., *Unpublished work*. 2017.
85. Tanaka, H., N. Yamasaki, M. Muratani, and R. Hino, *Structure and formation process of (K,Na)-clinoptilolite*. Materials Research Bulletin, 2003. **38**(4): p. 713-722.
86. Bish, D.L. and J.M. Boak, *Clinoptilolite-heulandite nomenclature*. Reviews in mineralogy and geochemistry, 2001. **45**(1): p. 207-216.
87. Mumpton, F.A., *Clinoptilolite redefined*. American Mineralogist, 1960. **45**(3-4): p. 351-369.
88. Ames Jr, L., *The cation sieve properties of clinoptilolite*. Am. Mineralogist, 1960. **45**.
89. Mercer, B. and L. Ames, *Zeolite ion exchange in radioactive and municipal wastewater treatment*. Natural zeolites; occurrences, properties, uses. Pergamon Press, Oxford, 1978: p. 451-462.
90. Song, K.-C., H.K. Lee, H. Moon, and K.J. Lee, *Simultaneous removal of the radiotoxic nuclides Cs 137 and I 129 from aqueous solution*. Separation and purification technology, 1997. **12**(3): p. 215-227.
91. Smyth, J., A. Spaid, and D. Bish, *Crystal structures of a natural and a Cs-exchanged clinoptilolite*. Cell, 1990. **3**(2097.06): p. 2106.23.
92. Dyer, A. and K.J. White, *Cation diffusion in the natural zeolite clinoptilolite*. Thermochemica Acta, 1999. **340**: p. 341-348.
93. Campbell, L.S. and B. Davies, *Experimental investigation of plant uptake of caesium from soils amended with clinoptilolite and calcium carbonate*. Plant and Soil, 1997. **189**(1): p. 65-74.
94. YÜCEL, H. and A. ÖZMEN, *Migration of 137Cs extracted from contaminated tea in sandy clay soil*. Journal of nuclear science and technology, 1995. **32**(6): p. 547-555.
95. Kaminski, M., L. Nunez, M. Pourfarzaneh, and C. Negri, *Cesium separation from contaminated milk using magnetic particles containing crystalline silicotitanates*. Separation and purification technology, 2000. **21**(1): p. 1-8.
96. Sato, K., S. Takiuchi, M. Kakuta, R. Suzuki, H. Sasaki, and N. Sakamoto, *Removal and adsorption of radioactive cesium from contaminated soil caused by the Fukushima Daiichi Nuclear Power Station accident*. Bunseki Kagaku (Japan Analyst), 2013. **62**(6): p. 535-540.
97. Livens, F. and P. Loveland, *The influence of soil properties on the environmental mobility of caesium in Cumbria*. Soil Use and Management, 1988. **4**(3): p. 69-75.
98. Bish, D.L., *Effects of exchangeable cation composition on the thermal expansion/contraction of clinoptilolite*. Clays and Clay Minerals, 1984. **32**(6): p. 444-452.
99. Araya, A. and A. Dyer, *Studies on natural clinoptilolites—II: Cation mobilities in near homoionic clinoptilolites*. Journal of Inorganic and Nuclear Chemistry, 1981. **43**(3): p. 595-598.
100. Araya, A. and A. Dyer, *Studies on natural clinoptilolites—I: Homoionic clinoptilolites*. Journal of Inorganic and Nuclear Chemistry, 1981. **43**(3): p. 589-594.
101. Juoi, J. and M. Ojovan. *Characterisation and durability of glass composite waste forms immobilising spent clinoptilolite*. in *Waste Management Conference Proceeding, Tucson, AZ, USA*. 2007.
102. Alberti, A., *The crystal structure of two clinoptilolites*. Tschermaks mineralogische und petrographische Mitteilungen, 1975. **22**(1): p. 25-37.

103. Glasser, F.P., *Progress in the immobilization of radioactive wastes in cement*. Cement and concrete research, 1992. **22**(2-3): p. 201-216.
104. Allen, D., G. Baston, A.E. Bradley, T. Gorman, A. Haile, I. Hamblett, J.E. Hatter, M.J.F. Healey, B. Hodgson, R. Lewin, K.V. Lovell, B. Newton, W.R. Pitner, D.W. Rooney, D. Sanders, K.R. Seddon, H.E. Sims, and R.C. Thied, *An investigation of the radiochemical stability of ionic liquids*. Green Chemistry, 2002. **4**(2): p. 152-158.